

Abhishek Rawat

Coupled Hydro-mechanical Behavior of a Compacted  
Bentonite-Sand Mixture: Experimental and Numerical  
Investigations

Bochum 2019

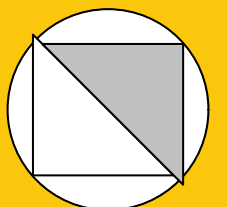
Heft 69

---

Schriftenreihe des Lehrstuhls für  
Grundbau, Boden- und Felsmechanik

Herausgeber: Tom Schanz

ISSN 2190-3255



Ruhr-Universität Bochum

Schriftenreihe Grundbau, Boden- und Felsmechanik

Heft 69

Herausgeber:

Prof. Dr. -Ing. habil. Tom Schanz

Ruhr-Universität Bochum

Fakultät für Bau- und Umweltingenieurwissenschaften

Lehrstuhl für Grundbau, Boden- und Felsmechanik

44801 Bochum

Telefon: 0234/ 3226135

Telefax: 0234/ 3214236

Internet: [www.gbf.ruhr-uni-bochum.de](http://www.gbf.ruhr-uni-bochum.de)

ISSN 2190-3255

© 2019 der Herausgeber

# **Coupled Hydro-mechanical Behavior of a Compacted Bentonite-Sand Mixture: Experimental and Numerical Investigations**

**Dissertation**

as a requirement of the degree of  
Doktor-Ingenieur (Dr.-Ing.)

at the  
Faculty of Civil and Environmental Engineering  
Ruhr-Universität Bochum

by  
**Abhishek Rawat**

Reviewers

Prof. Dr. rer. nat. Jörg Renner, Ruhr-Universität Bochum, Germany

Prof. Dr. Robert Charlier, University of Liege, Belgium

Dr. Snehasis Tripathy, Cardiff University, United Kingdom

Bochum, May 2019



# Vorwort des Herausgebers

Die vorliegende Arbeit von Herrn Abhishek Rawat entstand im Rahmen eines DFG-Forschungsprojektes zum Thema “Transient water transport in expansive soils under coupled hydraulic, mechanical and thermal boundary conditions”, welches von Prof. Tom Schanz initiiert und geleitet wurde. Prof. Tom Schanz verstarb am 12. Oktober 2017 völlig unerwartet. An der Fortsetzung und dem Abschluss der Arbeit hatten Herr Dr. Snehasis Tripathy (Cardiff University) und die Kooperation mit der Forschungsgruppe um Prof. Robert Charlier der Universität Liège einen entscheidenden Anteil.

Das Thema der Promotionsarbeit von Herrn Abhishek Rawat ist im Bereich der Forschung zur Entsorgung von wärmeentwickelnden radioaktiven bzw. toxischen Abfällen in tiefen geologischen Formationen bis zu 800 m Tiefe angesiedelt. Sogenannte Verschlussbauwerke (Schacht- und Streckenverschlüsse) bilden eine der Komponenten, welche innerhalb des Multibarrierenkonzeptes neben dem Kanister, einer angrenzenden Pufferzone aus hochverdichtetem Bentonit sowie dem Wirtsgestein die Abdichtung des Ablagerungsbereiches gegenüber der Geosphäre sicherstellen sollen.

Vor diesem Hintergrund beschäftigt sich die vorliegende Arbeit mit dem hydromechanischen Verhalten hochverdichteter Bentonit-Sand-Gemische als potenziell geeignetes Material für Verschlussbauwerke. Herr Rawat implementierte eine neuentwickelte Versuchssäule im Technikumsmaßstab. Sie ermöglicht es, Randwertprobleme auf einer mittleren Skala zwischen Elementversuch und großmaßstäblichem Versuch mit einem relativ geringen Aufwand im Vergleich zu in-situ Versuchen zu untersuchen. Die maßgebenden physikalischen Parameter relative Feuchte, Temperatur, Wassergehalt sowie axiale und radiale Spannung werden kontinuierlich in mehreren Messquerschnitten erfasst. Die Randbedingungen Temperatur und hydraulischer Druck können kontrolliert werden.

Herr Rawat führte einen isothermen Langzeitversuch bei relevanten hydromechanischen Belastungen und kontrollierten Randbedingungen durch. Im zweiten Teil seiner Arbeit führte er numerische Berechnungen auf Basis der Finite-Elemente-Methode durch, wobei verschiedene existierende Konstitutivmodelle, welche die hydraulische Kopplung beschreiben, verglichen wurden. Der wissenschaftliche Wert der Arbeit von Herrn besteht darin, dass er mithilfe der Versuchssäule eine zuverlässige Datengrundlage geschaffen hat, welche im Zusammenhang mit den numerischen Berechnungen Aufschluss über das transiente, gekoppelte hydromechanische Verhalten einer Bentonit-Sand-Mischung gibt. Es

steht nun ein adäquates experimentelles Werkzeug in Form der Bochumer Thermosäule zur Verfügung, welches zukünftig auch für andere ingenieurmäßige Fragestellungen genutzt werden kann.

Bochum, May 2019

Dr.-Ing. Wiebke Baille

*This work is dedicated to my mentor*

*Prof. Tom Schanz,*

*my parents, my wife Smita and my daughter Aarini*





# Acknowledgment

First and the foremost, I would like to thank my supervisor Prof. Dr.-Ing. habil. Tom Schanz who accepted me as a PhD student under his supervision and provided me the opportunity to work on the novel and interdisciplinary research topic. Unfortunately, he left this world on 12<sup>th</sup> October 2017. His scientific approach and personality will always inspire me. His memories and thoughts will be with me forever.

I would like to thank Prof. Jörg Renner for his support to evaluate this PhD work.

I sincerely thank Dr. Snehasish Tripathy (Cardiff School of Engineering, United Kingdom) for his active co-supervision and valuable scientific contributions. His critical and constructive comments significantly improved this work.

A special thanks to Prof. Robert Charlier, Prof. Frederic Collin (University of Liege) and Dr. Anne Catherine Dieudonne (Technical University, Delft, The Netherland) for giving me the opportunity to join their team during my research stays.

My sincere gratitude also goes to Dr. Wiebke Baille and Dr. Diethard König (Chair of Foundation Engineering, Soil and Rock Mechanics, Ruhr-Universität Bochum) for their continuous help and lots of constructive suggestions during my research work.

I would like to thank Mr. Joachim Blazytko, Werner Müller, Bernhard Sperl and Mr. Ralf Schudy from Soil Mechanical Laboratory (IDN) for supporting me during my experimental work. I also want to thank Mr. Michael Skubisch from Clay Laboratory (IC) for helping me during my small-scale experiments.

I also would like to appreciate the financial support by the Deutsche Akademische Austauschdienst (DAAD) and RUB research school for providing me the financial support for my research stays at Cardiff School of Engineering, United Kingdom and at Technical University, Delft, The Netherland.

Last but not least, there are no words to say thanks my beloved parents, my wife Smita, my sister Nidhi and my daughter Aarini for their love, support, understanding and for their continuous emotional support during my PhD.

Bochum, May 2019

Abhishek Rawat



## Abstract

In Germany, a bentonite-sand mixture (50:50) compacted to bricks is proposed to be used as a backfill material in nuclear waste repositories. As an expansive clay, bentonite swells on exposure to water and fills the available constructional gaps and technical voids. For the mechanical stability of the entire disposal system, the rate of saturation and the resulting swelling pressure are crucial from the design point of view. Hence, an understanding of the coupled hydro-mechanical behavior of backfill materials and the ability to model their behavior is paramount for ensuring long-term safety. The present PhD work aims at improving the understanding of the hydro-mechanical behavior of compacted bentonite-sand mixtures at conditions relevant for repositories using a holistic approach combining experimental, theoretical and numerical investigations.

A column-type experimental device was designed to investigate the behavior of soil subjected to a repository-relevant hydraulic gradient. The experimental device facilitates the transient measurements of swelling pressure in both axial and lateral directions, and the simultaneous measurements of temperature, water content and relative humidity at various pre-selected locations. Validation tests were performed to ensure the reliability of transient measurements. A water infiltration test was performed with the pre-compacted sample of a Calcigel bentonite-sand mixture (50:50) using the newly designed device for a period of 349 days. The experimental set-up mimics the transient hydration of backfill material in a nuclear waste repository. The test results highlighted the hydration-induced heterogeneity in the material and its effect on the lateral swelling pressure development along the height of soil sample. The axial swelling pressure measurements revealed the factors that affect the stress-transfer mechanism between both the ends. The simultaneous measurements of relative humidity and water content indicated the porosity redistribution close to the hydration-end during the test.

A fully coupled hydro-mechanical analysis of the water infiltration test was conducted using the finite element method. The modified Barcelona Basic Model (BBM) was used to describe the mechanical behavior of soil along with the double-structure water retention model for an indirect coupling. Based on the available elementary test results (i.e., water retention tests under constant volume condition, suction-controlled oedometer tests and microstructural investigations) for the Calcigel bentonite-sand mixture (50:50), the model parameters were identified in a sequential manner and calibrated. The simulation results successfully captured the water transport mechanism in the material and agreed well with the experimental measurements (i.e., water content, relative humidity and the rate of water infiltration). Considering the mechanical behavior, the modified Barcelona Basic

Model successfully predicted the axial swelling pressure evolution at the wetting-end. On the other hand, the model did not predict the measured lateral swelling pressure correctly for measurement sections away from wetting-end. A comparative analysis of experimental and numerical investigations provides key inputs to improve the existing constitutive models for a fully coupled hydro-mechanical analysis.

# Zusammenfassung

Bentonit-Sand-Mischungen werden in Deutschland als Verfüll- und Abdichtungsmaterial für untertägige Endlager in Betracht gezogen, zum Beispiel in Form von vorkompaktierten Formsteinen. Bentonit ist ein quellfähiger Ton mit sehr geringer Durchlässigkeit, der aufgrund der Quellfähigkeit in der Lage ist, bei Wasserzutritt mögliche vorhandene konstruktionsbedingte Spalten zu verschließen. Für das Design des Dichtbauwerks im Hinblick auf die Langzeitsicherheit sind die zeitlichen Verläufe der Sättigung sowie der Quelldruckentwicklung entscheidend. Für eine hinreichend genaue Modellierung zur Vorhersage des Langzeitverhaltens der Dichtbauwerke ist das Verständnis der bei der Aufsättigung stattfindenden gekoppelten hydromechanischen Prozesse unabdingbar.

Die vorliegende Arbeit hat zum Ziel, mittels experimenteller, theoretischer und numerischer Untersuchungen ein besseres Verständnis der gekoppelten hydromechanischen Prozesse bei den relevanten Randbedingungen zu erlangen. Dazu wurde ein innovativer Säulenversuchsstand verwendet, mithilfe dessen bei kontrollierten thermischen und hydraulischen Randbedingungen das zeitabhängige, gekoppelte hydromechanische Verhalten von Böden erfasst werden kann. Der Versuchsstand ermöglicht dazu die kontinuierliche Messung des Quelldrucks in axialer und radialer Richtung, sowie der Temperatur, des Wassergehaltes und der relativen Feuchte an ausgewählten Probenquerschnitten. Die Funktionalität der Versuchssäule und der verwendeten Messsysteme konnte durch eine Reihe von Kalibrierungs- und Validierungsversuchen gezeigt werden. Es wurde ein Hydratationsversuch an einer hochverdichteten Bentonit-Sand-Probe mit einer Versuchsdauer von 349 Tagen durchgeführt. Die Ergebnisse zeigten die infolge Hydratation entstehende Heterogenität des Materials (lokale Porositätsänderung) und deren Einfluss auf die Entwicklung der lokalen radialen Spannungen (Quelldrücke) in den Messquerschnitten. Des Weiteren wurden anhand der Messung der lokalen axialen Spannungen in den Messquerschnitten entlang der Probenhöhe wesentliche Erkenntnisse über den Verlauf der Spannungsübertragung innerhalb des Materials infolge der Hydratation gewonnen werden.

Es wurde eine gekoppelte hydromechanische Modellierung unter Verwendung der finiten Elemente-Methode durchgeführt. Das modifizierte Barcelona-Basic-Modell (BBM) in Verbindung mit einem double-structure-Modell zur Beschreibung des hydraulischen Verhaltens wurde dazu verwendet. Die erforderlichen Modellparameter wurden anhand von Ergebnissen aus verschiedenen Elementversuchen identifiziert und kalibriert. Die Simulationsergebnisse zeigen eine gute Übereinstimmung mit den experimentellen Ergebnissen

der Säulenversuche, sowohl im Hinblick auf die Zeitverläufe der hydraulischen Parameter (Wassergehalt und relative Feuchte), als auch im Hinblick auf das mechanische Verhalten. Die Simulation konnte die Entwicklung des lokalen axialen Quelldrucks sehr gut abbilden, die Entwicklung der radialen Quelldrücke jedoch nicht. Basierend auf den Ergebnissen der vorliegenden Arbeit wurden Empfehlungen für weitere Untersuchungen abgeleitet.

# Contents

<b>Vorwort des Herausgebers</b>	<b>iii</b>
<b>Acknowledgements</b>	<b>vii</b>
<b>Abstract</b>	<b>ix</b>
<b>Zusammenfassung</b>	<b>xi</b>
<b>1 Introduction</b>	<b>1</b>
1.1 Motivation . . . . .	1
1.2 Objectives . . . . .	8
1.3 Outline of thesis . . . . .	8
<b>2 Literature review</b>	<b>11</b>
2.1 General . . . . .	11
2.2 Basics of clay mineralogy . . . . .	11
2.3 Physico-chemical forces in clay mineral-water system . . . . .	14
2.3.1 Van der Waals long-range interactions . . . . .	14
2.3.2 Diffuse double layer repulsion . . . . .	15
2.3.3 Short-range interaction forces . . . . .	16
2.3.4 Net force in a clay mineral-water system . . . . .	19
2.4 Hydration of clays and influencing factors . . . . .	20
2.4.1 Hydration mechanism . . . . .	20
2.4.2 Influencing factors . . . . .	21
2.5 Soil-water total potential (soil total suction) . . . . .	23
2.5.1 Components of soil total suction . . . . .	23
2.5.1.1 Matric suction . . . . .	24
2.5.1.2 Osmotic suction . . . . .	25
2.5.2 Soil suction measurement techniques . . . . .	26
2.5.2.1 Direct suction measurement techniques . . . . .	26

2.5.2.2	Indirect suction measurement techniques . . . . .	27
2.5.3	Errors in soil suction measurements . . . . .	28
2.6	Factors influencing soil water retention characteristics . . . . .	31
2.7	Swelling pressure of bentonite-based materials . . . . .	32
2.7.1	Standard laboratory test methods . . . . .	32
2.7.2	Phenomenological soil testing approach . . . . .	36
2.8	Constitutive modeling in unsaturated soils . . . . .	40
2.8.1	The Barcelona Basic Model (BBM) . . . . .	40
2.8.2	Limitations and modification in the original BBM . . . . .	41
2.8.2.1	The choice of stress state variables . . . . .	41
2.8.2.2	Variation in soil stiffness with suction . . . . .	43
2.8.2.3	Prediction of elastic swelling . . . . .	43
2.8.3	Modeling of coupled flow and deformation problem . . . . .	44
2.9	Summary . . . . .	45
<b>3</b>	<b>Material and methods</b>	<b>47</b>
3.1	General . . . . .	47
3.2	Basic Geotechnical properties . . . . .	47
3.3	Physico-chemical properties . . . . .	48
3.3.1	Specific surface area . . . . .	48
3.3.2	Cation Exchange Capacity (CEC) . . . . .	49
3.3.3	Mineralogy and chemical composition . . . . .	49
3.4	Compaction characteristics . . . . .	50
3.4.1	Standard and modified Proctor compaction characteristics . . . . .	50
3.4.2	Static uniaxial compaction curves . . . . .	51
3.5	Method for producing the pre-compacted blocks . . . . .	53
3.6	Experimental devices . . . . .	58
3.6.1	High-pressure oedometer device . . . . .	58
3.6.2	UPC isochoric cell . . . . .	61
3.7	Experimental techniques and methods . . . . .	63
3.7.1	Techniques for controlling and measuring the soil suction . . . . .	63
3.7.1.1	Vapour equilibrium technique . . . . .	63
3.7.1.2	Osmotic technique . . . . .	64
3.7.1.3	Chilled-mirror hygrometer . . . . .	66
3.7.2	Suction-controlled oedometer tests . . . . .	68
3.7.3	Water retention tests under constant volume condition . . . . .	71



---

3.8	Summary . . . . .	72
<b>4</b>	<b>Column-type experimental device: design, validation and implementation</b>	<b>75</b>
4.1	Introduction . . . . .	75
4.2	Column-type experimental device: design features . . . . .	75
4.2.1	Top and bottom plugs . . . . .	76
4.2.2	Sample rings . . . . .	77
4.2.3	Stainless steel confining cell and rigid frame . . . . .	79
4.2.4	Sensors and monitoring instrumentations . . . . .	81
4.2.4.1	Sensors for temperature measurements . . . . .	81
4.2.4.2	Sensors for total stress measurement . . . . .	84
4.2.4.3	Sensors for water content measurement . . . . .	86
4.2.4.4	Sensors for relative humidity measurement . . . . .	88
4.3	Calibration of sensors and monitoring instruments . . . . .	92
4.4	System compliance tests . . . . .	94
4.4.1	Response of Load cells under pressure and thermal loading conditions	95
4.4.2	Volumetric Thermal Expansion at Elevated Temperature . . . . .	98
4.4.3	Test with fine sand . . . . .	100
4.4.4	Test with the compacted bentonite-sand blocks . . . . .	104
4.5	Summary . . . . .	110
<b>5</b>	<b>Water-infiltration test</b>	<b>113</b>
5.1	Introduction . . . . .	113
5.2	Sample preparation and testing program . . . . .	115
5.3	Test results . . . . .	116
5.4	Discussion . . . . .	121
5.4.1	Evolution of state variables . . . . .	123
5.4.2	Swelling behavior . . . . .	126
5.4.3	Soil water retention behavior . . . . .	131
5.5	Summary . . . . .	132
<b>6</b>	<b>Numerical simulation of the water infiltration test</b>	<b>135</b>
6.1	Introduction . . . . .	135
6.2	Finite element formulation . . . . .	136
6.2.1	Balance equations . . . . .	136
6.2.1.1	Mass balance of water . . . . .	136
6.2.1.2	Mass balance of air . . . . .	136

6.2.1.3	Balance of heat . . . . .	137
6.2.1.4	Momentum balance for the medium . . . . .	138
6.2.2	Constitutive equations: Mechanical behavior . . . . .	138
6.2.2.1	Formulation for isotropic stress states: saturated case . . .	138
6.2.2.2	Formulation for isotropic stress state: unsaturated case . .	139
6.2.2.3	Influence of suction change . . . . .	141
6.2.2.4	Formulation for triaxial stress state . . . . .	142
6.2.2.4.1	Elastic strains in triaxial stress state . . . . .	142
6.2.2.4.2	Yield surface . . . . .	142
6.2.2.4.3	Flow rules . . . . .	143
6.2.3	Constitutive equations: Hydraulic behavior . . . . .	143
6.2.4	Clay-microstructure based water retention model . . . . .	145
6.3	Identification and calibration of model parameters . . . . .	148
6.3.1	Parameter identification and calibration for BBM . . . . .	148
6.3.2	Identification and calibration of double-structure water retention model parameters . . . . .	153
6.3.3	Identification and calibration of hydraulic parameters . . . . .	156
6.4	Features of numerical simulation . . . . .	157
6.5	Results and discussion . . . . .	159
6.5.1	Evolution of state variables . . . . .	159
6.5.2	Material swelling behavior . . . . .	163
6.5.3	Soil water retention behavior . . . . .	169
6.6	Summary . . . . .	169
<b>7</b>	<b>Conclusions and recommendations</b>	<b>171</b>
7.1	Summary and conclusions . . . . .	171
7.2	Recommendations . . . . .	174
	<b>Bibliography</b>	<b>175</b>

# List of Figures

1.1	Schematic illustration of deep geological disposal concept and system components, (a) setting up the facility in stable deep geological formation (host-rock), (b), (c) vertical and horizontal disposal of waste canister and (d) sectional view (vertical disposal) and (e) sectional view (horizontal disposal). . . . .	2
1.2	Application of compacted bentonite-based material as a backfill material at deep geological repository (Hansen et al., 2009). . . . .	3
1.3	(a) Application of bentonite-based material in multilayer-engineered barrier system, (b) water ingress from the host rock and (c) evolution of swelling pressure in vertical direction against the host-rock and in horizontal direction against the sealing plug. . . . .	4
1.4	Application of bentonite-based materials in multilayer-engineered barrier system as a buffer material (Colin Leung, 2014). . . . .	5
1.5	Multiscale and multi-physical processes in the compacted buffer material at the nuclear waste repository. . . . .	5
2.1	Diagrammatic sketch of tetrahedral and octahedral units (Baille, 2014; Grim, 1968): (a) single silica tetrahedron (left), sheet of tetrahedra arranged in a hexagonal network (right) and (b) single octahedron (left), di- and trioctahedral sheets (right). . . . .	12
2.2	Diagrammatic sketch and charge distribution of montmorillonite (Baille, 2014; Grim, 1968): (a) diagrammatic sketch of the montmorillonite structure, (b) charge distribution on montmorillonite. . . . .	13

2.3	Schematic representation of the electrochemical interactions at the surface of clay mineral particle. This figure also shows the evolution of the electric potential as a function of the distance to this surface. The terms IHP and OHP indicate "Inner Helmholtz Plane" and "Outer Helmholtz Plane." $Q_0$ , $Q_b$ , and $Q_s$ ( $C - m^{-2}$ ) indicate charge densities at the surface of the particle, in the Stern layer, and in the diffuse layer, respectively. $\psi_0$ , $\psi_b$ , $\psi_d$ ( $V$ ) indicate the electrical potential at the surface and at the planes $\beta$ (IHP) and $d$ (OHP), respectively. TrP is the truncation plane situated at a distance $x_{Tr}$ from the particle surface (Goncalves et al., 2015). . . . .	17
2.4	Hexagonal cavity with tetrahedral sheet, $a_0$ and $b_0$ refer to unit cell parameters (van Olphen, 1977; Sposito et al., 1984). . . . .	18
2.5	Schematic illustration of repulsive, attractive and net forces as a function of inter particle distance (modified from van Olphen (1977)). . . . .	20
2.6	Plausible hydration sequence in Li- and Na- montmorillonites (modified after Salles et al. (2008)) at different relative humidity (RH) levels. . . . .	22
2.7	Schematic representation of capillary mechanism, (a) saturated soil, (b) three-phase interface system in an unsaturated soil and (c) capillary tube analogy. . . . .	25
2.8	Soil suction measurement techniques and devices. . . . .	26
2.9	(a) Chilled mirror dew-point potentiometer (b) schematic view. . . . .	29
2.10	Error in the total suction measurement due to temperature gradient only (Agus & Schanz, 2007). . . . .	30
2.11	Error in the total suction measurement of bentonite (B) sand (S) mixtures due to temperature gradient using relative humidity sensors (Agus, 2005). . . . .	30
2.12	Effect of sample initial dry density and the applied volume constraint on soil water retention behavior of (a) compacted Boom clay (Romero et al., 1999) and (b) compacted FEBEx bentonite (Lloret et al., 2003). . . . .	32
2.13	Different laboratory test methods for determining the swelling pressure (modified after Sridharan et al. (1986)). . . . .	33
2.14	Schematic representation of fundamental concept for determining swelling pressure from diffuse double layer theory. (modified after van Olphen (1963)). . . . .	35

2.15	Generalized stress paths observed in the multistage swelling pressure tests (a) Lloret et al. (2003) (b) Yigzaw et al. (2016), (legends: OCVG1 = test with G-bentonite using osmotic technique, VCVG2 = test with G-bentonite using vapor equilibrium technique, OCVMX1 = test with MX-80 bentonite using osmotic technique, and VCVMX2 = test with MX-80 bentonite using vapor equilibrium technique). . . . .	36
2.16	Swelling pressure development with decreasing suction during multistage swelling pressure test (Agus et al., 2013). . . . .	37
2.17	(a) Full-scale Engineered-barrier Experimental (FEBEx) performed at the Grimsel Test Site (GTS, Switzerland) (Villar et al., 2005) and (b) full-scale mock-up test in laboratory (Martin & Barcala, 2005). . . . .	38
2.18	Schematic illustration of column-type testing concept, (a) deep geological disposal concept, (b) and (c) compacted blocks as a buffer material between waste canister and host rock (1 = host rock; 2 = compacted blocks; 3 = technical gap between blocks; 4 = gap between blocks and host rock; 5 = Waste canister, T = applied temperature, H = hydration from host rock). . . . .	39
2.19	Characteristic features of Barcelona Basic Model (Alonso et al., 1990). . . . .	41
3.1	Grain size distribution curves of the Calcigel bentonite and sand (Lang, 2019). . . . .	48
3.2	Standard and modified Proctor compaction curve of Calcigel bentonite-sand mixture with equal dry mass proportion. . . . .	51
3.3	Uniaxial static compaction device and compaction mould. . . . .	52
3.4	Uniaxial static compaction characteristics of Calcigel bentonite sand mixture with 6 % initial water content (a) applied vertical stress versus axial strain (b) applied stress versus mixture bulk density, (c) applied stress versus mixture dry density and (d) applied stress versus bentonite dry density in mixture. . . . .	54
3.5	Uniaxial static compaction characteristics of Calcigel bentonite sand mixture with 9 % initial water content (a) applied vertical stress versus axial strain (b) applied stress versus mixture bulk density, (c) applied stress versus mixture dry density and (d) applied stress versus bentonite dry density in mixture. . . . .	55
3.6	Schematic view: extrusion of compacted block from the mould and resulting shear stresses at the edges. . . . .	56

3.7	Compaction induced heterogeneity in the compacted Calcigel bentonite sand mixture (dry density distribution along the sample height), (a) with 6 % initial mixture water content and (b) with 9 % initial mixture water content. . . . .	57
3.8	High pressure oedometer device with schematic of cell (left) and actual view of test set-up (right) (Baille, 2014). . . . .	60
3.9	Deformation characteristics of the high stress oedometer device (Lang, 2019). 61	
3.10	The isochoric cell, (a) actual view, (b) schematic view of design details and (c) different components of the cell (Agus, 2005) . . . . .	62
3.11	Vapor equilibrium technique for controlling the soil suction (a) schematic illustration and (b) application in the laboratory (Lang, 2019). . . . .	64
3.12	Relationship between mass ratio and Brix and between Brix and the applied soil matric suction for the PEG solutions used in this study (Lang, 2019). .	66
3.13	Chilled-mirror hygrometer used in this study (a) actual view and (b) schematic view. . . . .	67
3.14	Stress paths for unsaturated oedometer tests on compacted sand-bentonite mixture . . . . .	68
3.15	Test set-up for the suction-controlled oedometer tests on the compacted Calcigel bentonite sand mixture (a) saturated condition and (b) unsaturated condition (Lang, 2019). . . . .	70
3.16	Equipments for preparing sample for element tests (Lang, 2019). . . . .	70
3.17	Experimental set-up for multistage wetting test with UPC isochoric cell using osmotic technique (legends: 1 = peristaltic pump, 2 = PEG solution, 3 = magnetic stirrer, 4 = isochoric cell, 5 = digital display for load cell reading) (Lang, 2019). . . . .	71
4.1	Constructional details of the newly designed column-type experimental set-up, (a) and (b) vertical and horizontal sectional views, and (c) a photograph of the device. . . . .	76
4.2	Constructional details of top/bottom plug, (a) actual view, (b) PVDF encapsulation rings, (c) schematic view and (d) load-transferring mechanism (legends: 1 = loading piston; 2, 3 = air outlet/water inlet; 4, 5 = for heating fluid circulation; 7 = metallic chamber and 8 = porous base). . . .	78
4.3	Test set-up for investigating the effect of inter-facial friction between the top/bottom plug and the encapsulation rings on the load transferring mechanism. . . . .	79

---

4.4 Constructional details of PVDF sample rings, (a) schematic view, (b) actual view with monitoring sensors (legend: 1 = lateral load cell, 2 = TDR based water content measurement sensor, 3 = Pt100 sensor and KYOWA pressure transducer and 4 = RH sensor) and (d) measurement sections (X1, X2 and X3). . . . . 80

4.5 (a) Stainless steel confining cell and installation of Pt100 sensors and (b) installation of lateral load cell with confining cell . . . . . 81

4.6 Sensors and monitoring instrumentations, (a) sensors with PVDF adapters (legend: 1 = lateral load cell, 2 = TDR sensor for water content measurement, 3 = Pt100 sensor with KYOWA pressure transducer and 4 = relative humidity sensor), (b) Huber external thermostat, (c) and (d) top and bottom load cells and (e) Graphtech GLS820 data logger. . . . . 82

4.7 Sensors for measuring temperature, (a) Pt100 sensors for measuring the room temperature and for measuring soil temperature at sections X1, X2 and X3 and (c) installation of Pt100 sensors with confining cell. . . . . 84

4.8 Lateral load cell installation details, (a) load cell along with accessories and (b) installation at measurement sections X1, X2 and X3 along the height of soil sample, (c) A photograph of compacted sand-bentonite mixture sample (for sample rings S1 or S2) showing seating space for a miniature pressure transducer (1-compacted block, 2-seating space), and (b) pressure transducer installation in a compacted sample. . . . . 85

4.9 TDR sensors installation details, (a) TDR along with accessories and (b) a schematic showing positions of the sensors along the height of the sample. 87

4.10 TRIME internal measuring procedure. . . . . 88

4.11 VAISALA HMT337 relative humidity sensors with additional Pt100 sensors 89

4.12 Accuracy of Pt100 sensors associated with VAISALA HMT337 RH sensor (modified from Vaisala-Oyi, 2011). . . . . 90

4.13 Installation of Rotronic RH sensor in the embedded position inside the compacted soil sample during the trial tests. . . . . 90

4.14 Schematic illustration of the closed-vapour chamber concept for measuring relative humidity. . . . . 91

4.15 (a) Condensation at the higher relative humidity levels based on the difference in the soil/ambient temperature and the temperature inside the closed vapor chamber and (b) Trial tests: Rotronic sensors with closed-chamber concept. . . . . 92

4.16 (a) Installation of VAISALA HMT337 RH probe with an additional Pt100 probe in closed-vapor chamber. . . . .	93
4.17 Test set-up for material specific calibration at (a) room temperature and (b) at elevated temperature. . . . .	94
4.18 Temperature dependent calibration curve for TDR sensor. . . . .	95
4.19 A schematic view of the test set-up for verifying response of load cells under pressure and thermal loading conditions. . . . .	96
4.20 Test results showing response of load cells to pressure and thermal loading conditions in the presence of a dummy wood sample, (a) applied temperature at opposite ends of the dummy, (b) applied air pressure in annular space, (c) measured axial total stress, and (d) measured lateral total stress. . . . .	97
4.21 A schematic view of the test set-up for quantifying the volumetric thermal expansion of the device in the presence of a stainless-steel dummy. . . . .	99
4.22 Schematic views of test set-up for testing the moist sand under an applied hydraulic gradient (test 1) and under an applied thermal gradient (test 2). . . . .	101
4.23 Test with fine sand under the applied hydraulic gradient (a) evolution of water content and (b) evolution of relative humidity over time along the height of soil sample. . . . .	102
4.24 Test with fine sand under the applied temperature gradient (a) evolution of temperature and (b) evolution of relative humidity along the height of soil sample. . . . .	103
4.25 (a) A schematic view of test set-up in the presence of compacted bentonite-sand blocks and (b) monitoring sensors. . . . .	104
4.26 Elapsed time vs. temperature plot for the test with the compacted sand-bentonite mixture. . . . .	106
4.27 (a) Temperature profile and (b) temperature gradient at 7, 9 and 64 days. . . . .	106
4.28 (a) Elapsed time vs. relative humidity and (b) elapsed time vs. water content plots at salient levels along the height of the sample. . . . .	107
4.29 Profiles of (a) relative humidity and (b) water content at 7, 9, and 64 days. . . . .	108
4.30 Development of (a) axial stress and (b) lateral stress at various salient levels of the sample. . . . .	109
4.31 Post-experimental observation: deformation in cable connection of KY-OWA miniature pressure transducer installed at position B1 (close to heating end). . . . .	110



---

5.1	(a) Deep geological disposal concept for disposing the high level radioactive waste, (b) transient hydration of backfill material and resulting swelling pressure pressure in vertical and horizontal directions against the host-rock and sealing plugs ( $P_s$ = swelling pressure), (c) sectional view along the X1-X2 axis (legends: 1 = host rock, 2 = compacted blocks, 3 = constructional gaps between the compacted blocks, 4 = gap between the compacted blocks and host rock), (d) flow and displacement boundary conditions for the backfill element during the mock-up test, and (d) transient measurements during the mock-up test. . . . .	114
5.2	Schematic view, (a) test setup for water infiltration test and (b) cross sectional view and installation of monitoring sensors. . . . .	116
5.3	(a) Elapsed time vs. relative humidity and (b) elapsed time vs. water content plots at salient levels along the height of the sample. . . . .	117
5.4	(a) Elapsed time vs. soil total suction and (b) elapsed time vs. degree of saturation plots at salient levels along the height of the sample. . . . .	119
5.5	(a) Elapsed time vs. soil total suction and (b) elapsed time vs. degree of saturation plots at salient levels along the height of the sample. . . . .	120
5.6	Installation of KYOWA miniature pressure transducer in floating condition, (a) KYOWA miniature pressure transducer with PVDF adapter (b) compacted block and sitting-space for installing the sensor, (c) and (d) installation of sensor between two blocks (legends: 1 = PVDF sample ring, 2 = compacted block, 3 = KYOWA sensor). . . . .	122
5.7	Elapsed time vs. water potential gradient along the height of soil sample. .	123
5.8	(a) Volumetric water content isochrones at different selected time intervals and (b) measured and calculated infiltrated-water volume into the soil sample.	125
5.9	(a) Lateral total stress profiles along the height of soil sample and (b) lateral total stress vs. soil suction for measurement sections X1, X2 and X3.	128
5.10	Material physical state before and after the test. . . . .	129
5.11	Transient soil water retention profiles along the sample height during the hydration process, (a) gravimetric water content versus suction and (b) degree of saturation versus suction. . . . .	130

6.1	Characteristic features of Barcelona Basic Model (Alonso et., 1990), (a) extension of the Modified Cam-clay model for saturated to unsaturated state taking suction as a hardening parameters with the assumption of constant slope of critical state lines, (b) yield surface, (c) features of BBM (Alonso et al., 1990) and (d) loading path and collapse deformation of an unsaturated as-compacted sample. . . . .	140
6.2	Stress paths for unsaturated oedometer tests on compacted sand-bentonite mixture . . . . .	149
6.3	Suction-controlled oedometer tests results for compacted sand-bentonite mixture (50:50) with Barcelona Basic Model parameters. . . . .	150
6.4	Determination of the BBM parameters, (a) slope of suction dependent normal compression lines, (b) applied net stress vs. specific volume at different applied suction-levels, (c) applied suction vs. specific volume at different applied net mean stress and (d) loading-collapse curve. . . . .	152
6.5	Calibration of BBM model parameters using suction-controlled oedometer test results. . . . .	154
6.6	Evolution of micro-void ratio with water void ratio for compacted Calcigel bentonite-sand mixture (50:50) from Agus (2005). . . . .	156
6.7	Calibration of water retention models against the experimental data on Calcigel bentonite-sand mixture (50:50) at two different dry densities (wetting path under confined condition). . . . .	157
6.8	Sample initial porosity versus intrinsic permeability of compacted Calcigel bentonite-sand mixture (50:50): experimental data and the predicted values using Kozeny-Carman model. . . . .	159
6.9	Features of numerical simulation, (a) geometry with global force and displacement boundary conditions, (b) mesh formation and (c) specifications of 2D isoparametric quadrilateral element with 5 degree of freedoms. . . . .	160
6.10	Experimental vs. simulation results: elapsed time vs. relative humidity values along the height of soil sample. . . . .	160
6.11	Experimental vs. simulation results: elapsed time vs. water content along the height of soil sample. . . . .	161
6.12	Experimental vs. simulation results: elapsed time vs. infiltrated water volume. . . . .	162
6.13	Numerical simulation results (a) evolution of void ratio and (b) evolution of micro and macro void ratio according to Dieudonne water retention model (Dieudonne et al., 2017). . . . .	164

---

6.14	Numerical simulation results: evolution of hydraulic conductivity (m/s) over time for measurement section X1, X2 and X3. . . . .	165
6.15	Experimental vs. simulation results: elapsed time vs. axial total stress. . .	165
6.16	Experimental vs. simulation results: elapsed time vs. lateral total stress. .	166
6.17	Numerical simulation results (a) saturated preconsolidation stress vs. soil suction and (b) evolution of loading-collapse curve along the sample height.	167
6.18	Comparison between the experimental and simulation results: soil suction vs. gravimetric water content. . . . .	169



# List of Tables

3.1	Comparison of mineral constituents of Calcigel bentonites. . . . .	50
3.2	Properties of Calcigel bentonite, sand and bentonite-sand mixture (50:50). . . . .	59
3.3	Specifications of saturated salt solutions and the range of applied soil total suction (Lang, 2019). . . . .	65
3.4	Specifications of PEG solution and the applied soil matric suction (Lang, 2019). . . . .	66
3.5	The initial conditions and the applied soil suction during the water retention tests with the Calcigel bentonite-sand mixture (50:50) under constant volume condition ( $\rho_d$ = sample initial dry density, $w$ = initial water content, $S_r$ = initial degree of saturation, $\psi_t^*$ = applied total suction and $\psi_t$ = initial total suction of soil sample). . . . .	72
4.1	Details of the monitoring sensors and instruments used in the device. . . . .	83
4.2	Calculation for volumetric thermal expansion of column-type experimental set-set-up ( $\alpha_v$ = coefficient of volumetric thermal expansion, $V$ = volume at 20 °C and $\Delta V$ = change in the volume due to a temperature change from 20 to 80 °C). . . . .	100
6.1	Barcelona Basic Model parameters for compacted bentonite-sand mixture (50:50). . . . .	153
6.2	Hydraulic parameters for compacted sand- Calcigel bentonite mixture having equal dry mass ratio. . . . .	158



# Nomenclature

$\alpha$	Parameter for van Genuchten water retention model
$\beta_D$	Similarity constant in Dubinin's adsorption theory
$\chi$	Bishop's effective stress parameter
$\kappa$	Slope of loading-unloading lines of soil in unsaturated state for changes in mean net stress
$\kappa_0$	Slope of loading-unloading lines of soil in saturated state for changes in mean net stress
$\kappa_s$	Slope of wetting-drying lines of soil for changes in suction
$\lambda$	Slope of normal compression line
$\nu$	Poisson's ratio
$\Omega_M$	Total volume of macro-pores
$\Omega_m$	Total volume of micro-pores
$\Omega_{wM}$	Volume of water stored in macro-pores
$\Omega_{wm}$	Volume of water adsorbed in micro-pores
$\phi$	Soil friction angle
$\pi$	Osmotic pressure
$\psi_c$	Potential due to capillary forces
$\psi_e$	Potential due to short-range electrical fields

---

$\psi_f$	Potential due to van der Waal's fields
$\psi_m$	Soil matric suction
$\psi_o$	Osmotic potential
$\psi_t$	Total potential (soil total suction)
$\rho_c$	Effective bentonite density in mixture
$\rho_d$	Dry density of bentonite-sand mixture
$\rho_w$	Density of water
$\sigma_t$	Tensor of total (Cauchy) stress
$\tau_v$	Tortuosity
$\varepsilon_{sv}^*$	Volumetric swelling strain of montmorillonite
$A_h$	Halmaker constant
$b$	Body force vector in momentum balance equation
$c$	Soil cohesion value
$C_{ads}$	Fitting parameter for microstructural water retention domain
$d$	Half the distance between two charged surfaces
$D_{atm}$	Molecular diffusion coefficient
$E$	Young's Modulus
$e$	Void ratio of soil
$e_{M0}$	Initial macrostructure void ratio
$e_{m0}$	Initial microstructure void ratio
$e_w$	Soil-water ratio
$F_A^{vdW}$	van der Waals attractive force



---

$G$	Shear modulus of soil
$G_c$	Specific gravity of sand
$G_{mix}$	Specific gravity of mixture
$G_s$	Specific gravity of bentonite
$H$	Henry's constant
$K$	Bulk modulus
$K_{int}$	Intrinsic permeability coefficient
$m$	Fitting parameter for van Genuchten water retention model
$M_\theta$	Slope of critical state line
$n$	Fitting parameter for van Genuchten water retention model
$n_{ads}$	Fitting parameter for microstructural water retention domain
$p$	Net mean stress
$p_0$	Preconsolidation stress of soil in unsaturated state
$p_c$	Reference pressure
$q$	Deviatoric stress
$Q_0$	Charge densities at the surface of the particle
$Q_b$	Charge densities in the Stern layer
$Q_s$	Charge densities at the surface of the particle
$R$	Universal gas constant
$r$	BBM loading-collapse curve fitting parameter
$R_{DDL}$	Repulsive double-layer pressure
$RH$	Relative humidity

$s$	Soil total suction
$s_0$	Threshold suction (Yield suction)
$S_r$	Degree of saturation
$S_{rM}$	Degree of saturation of macrostructure
$S_{rm}$	Degree of saturation of microstructure
$T$	Soil temperature
$u_a$	Pore air pressure
$u_w$	Pore water pressure
$u_{atm}$	Atmospheric pressure
$p_0^*$	Preconsolidation stress of soil in saturated state

# 1 Introduction

## 1.1 Motivation

Radioactive isotopes are used in various applications such as in energy production, in medical treatments, in agriculture and in the scientific research (IAEA, 2006). All these applications generate radioactive wastes that are hazardous to living beings and the environment. As per the IAEA (2009) general safety guidelines, the nuclear waste is classified into different categories depending upon the half life period of radionuclides in the waste. The intermediate and high-level radioactive wastes contain long-lived radionuclides and are highly radiotoxic. Thus, their disposal needs long-term isolation.

Several options have been considered for the safe disposal of high and intermediate level radioactive waste (Lennemann, 1978). Among many other options, the deep geological disposal concept is accepted worldwide as a viable option for the safe disposal of high level radioactive waste (OECD, 1995; NEA, 2000, 2008; IAEA, 2011). Figure 1.1 presents the schematic illustration of deep geological disposal concept. The disposal facility (repository) consists of a network of disposal galleries located at several hundred meters below the surface in a stable geological formation (host rock), where the waste canisters are placed vertically in boreholes or horizontally in drifts (Fig. 1.1b, c). The disposal concept may vary depending upon the geological features and nuclear waste characteristics (Sellin & Leupin, 2013).

A vertical shaft passing through the geological formations connects these disposal galleries with the surface facilities. The excavation process and resulting stress redistribution change the rock properties (Delage et al., 2010). As a result, the excavation activities may connect the water bearing fractures located in the upper geological formations and initiate the water flow towards the waste canisters through preferential flow paths, which is not desirable for a long-term isolation of waste from near-field and far-field biosphere (Vazaios & Vlachopoulos, 2017). Hence, the multilayer-engineered barriers are deployed to delay the water ingress towards the waste canister (Fig. 1.1d, e). A multilayer-engineered

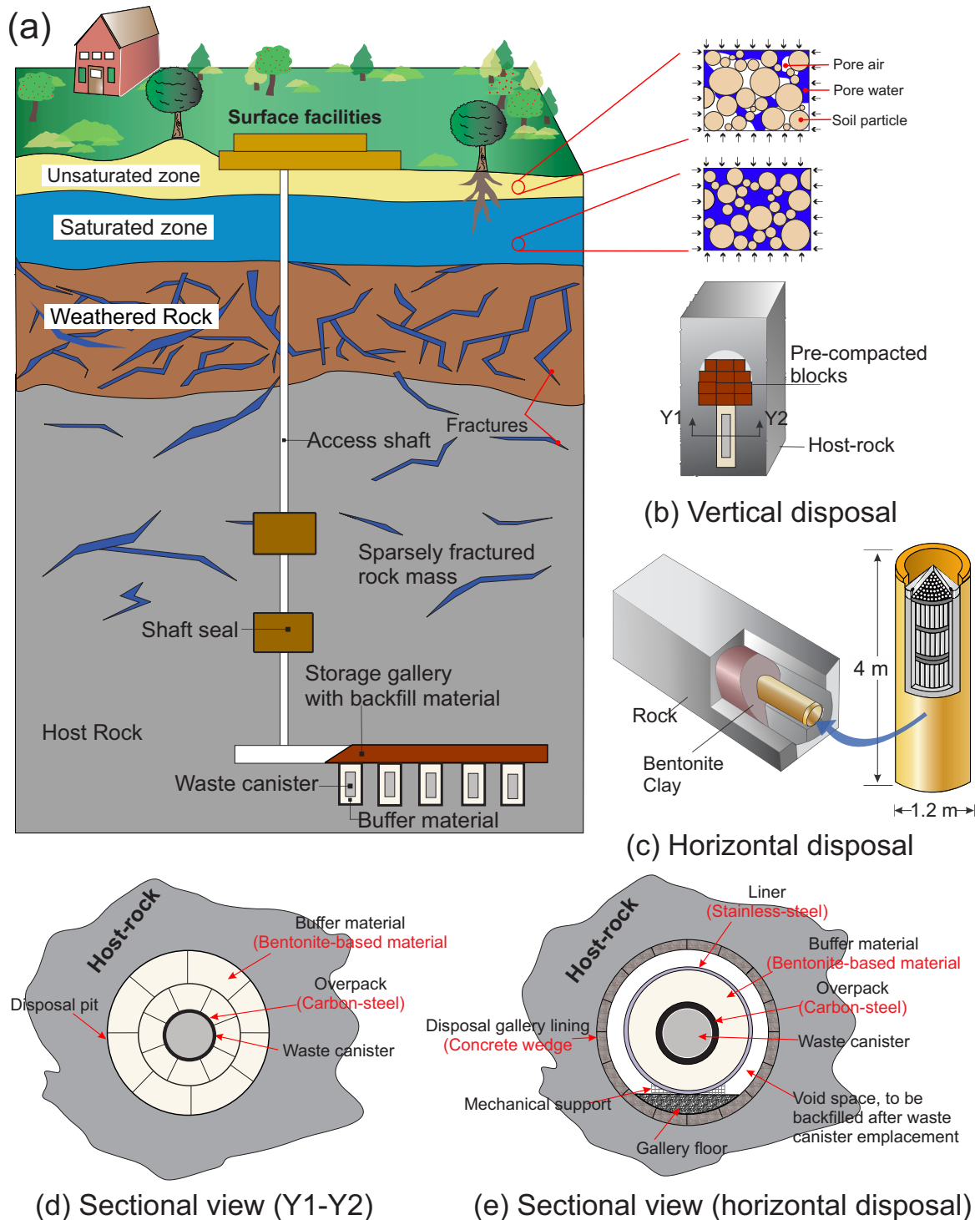


Figure 1.1: Schematic illustration of deep geological disposal concept and system components, (a) setting up the facility in stable deep geological formation (host-rock), (b), (c) vertical and horizontal disposal of waste canister and (d) sectional view (vertical disposal) and (e) sectional view (horizontal disposal).

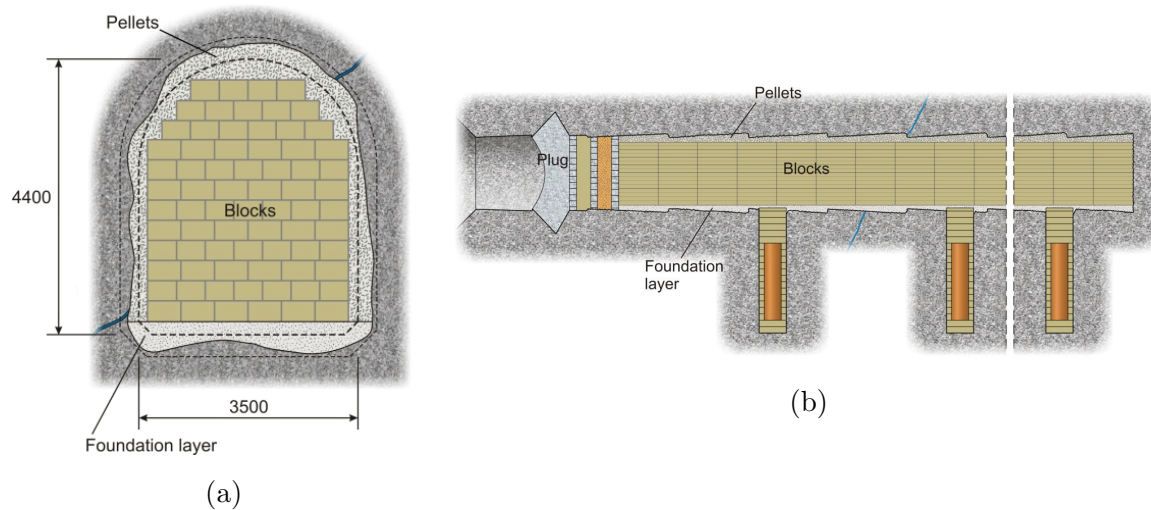


Figure 1.2: Application of compacted bentonite-based material as a backfill material at deep geological repository (Hansen et al., 2009).

barrier system (EBS) comprises natural and man-made physical entities, such as the waste form, packaging, buffer material, backfill material, the host environment and the geological formation.

As a key component of an EBS, bentonite-based mixtures are proposed to be used as a backfill, sealing and buffer material due to having favorable engineering properties such as low permeability, high swelling potential and good radionuclide retention properties. According to the KBS-3V vertical disposal concept at Olkiluoto repository site in Finland, bentonite-based compacted blocks are proposed to be used as a backfill material in the access tunnels, shaft and drifts (Fig. 1.2) (Hansen et al., 2009).

The primary function of sealing and backfill material is to create a low-permeability zone for delaying the water infiltration towards the waste canister from the host rock. In the field, the initially unsaturated pre-compacted blocks are subjected to hydration due to water ingress from the host rock (Fig. 1.3). In the early stage of hydration, the external part of backfill material hydrates first and fills the available constructional gaps between the host rock and backfill material and also between the pre-compacted blocks. Once the existing constructional gaps are filled, the swelling pressure develops in both lateral and axial direction under constant volume condition. For the mechanical stability of the entire disposal system, the rate of saturation and resulting swelling pressure of bentonite-based materials are of prime importance. For instance, the swelling pressure due to the hydration of pre-compacted blocks should be less than in-situ stresses in the host rock and the compressive strength of a waste canister, at the same time it should be high

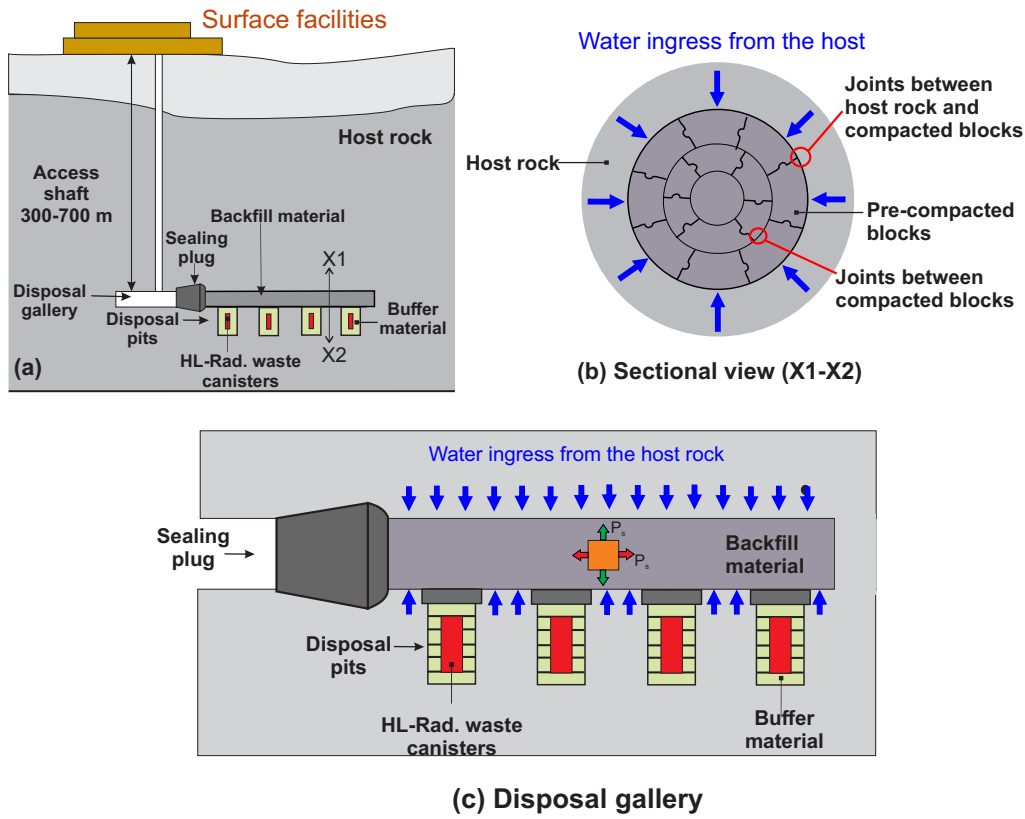


Figure 1.3: (a) Application of bentonite-based material in multilayer-engineered barrier system, (b) water ingress from the host rock and (c) evolution of swelling pressure in vertical direction against the host-rock and in horizontal direction against the sealing plug.

enough to seal the minor fractures in the excavation damaged zone in the vicinity of the underground openings (Juvankoski & Marcos, 2010).

As a buffer material, the compacted blocks are placed in the deposition hole between waste canister and host rock (Fig. 1.4) (Colin Leung, 2014). In the lifetime of repository, the buffer material is subjected to high temperature due to radiogenic heat production.

The design temperature depends on several factors such as the type of waste. Hence, depending on the arrangements, different maximum values are expected for the canister temperature shortly after deposition (Mattsson, 1981). For instance, the Swedish Nuclear Fuel Safety Project (KBS) has specified a maximum canister temperature of 70-80 °C shortly after the deposition in a crystalline host rock (Mattsson et al., 1978; Mattsson, 1980). A very high temperature can generate mechanical failure of host rock, chemical degradation and transformation of the buffer and rock, water vaporization and condensa-

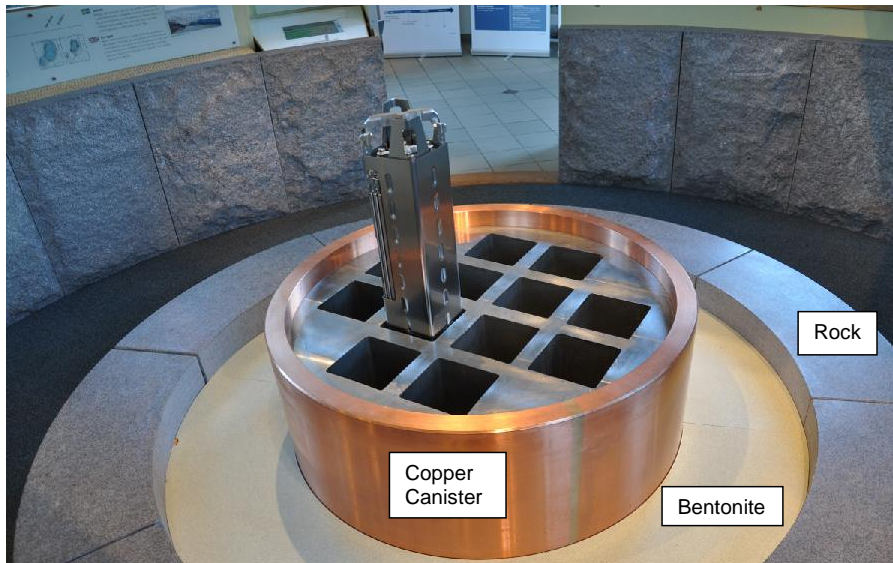


Figure 1.4: Application of bentonite-based materials in multilayer-engineered barrier system as a buffer material (Colin Leung, 2014).

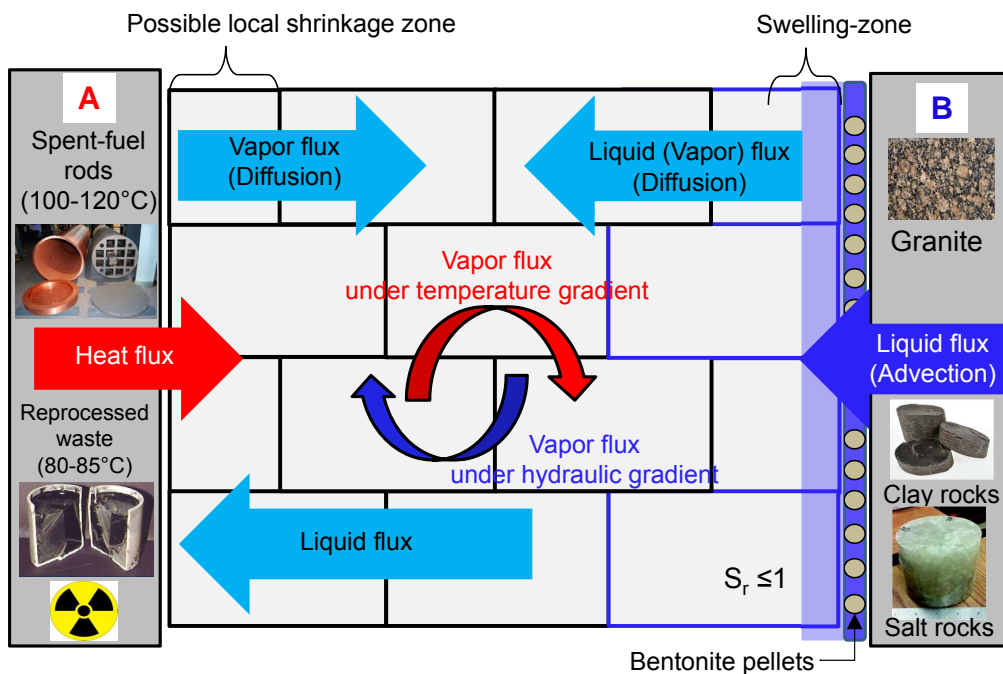


Figure 1.5: Multiscale and multi-physical processes in the compacted buffer material at the nuclear waste repository.

tion. In many countries, a maximum temperature of less than 100 °C has been selected, in order to avoid these issues (Goblet & Marsily, 2000). At the host rock end, the ground water interacts with the compacted buffer blocks. With these loading scenarios, different multi-physical and multiscale processes take place in the compacted buffer blocks (Fig. 1.5). An applied thermal gradient initiates water-vapor migration from the warmer section towards the colder sections, whereas the hydraulic gradient instates water migration towards the inner sections. Under the competing effects of heat and moisture migrations, the material is subjected to water flow, thermal flux and volumetric deformations in terms of soil swelling and shrinkage, which are highly coupled.

Studies on the swelling behavior of compacted bentonite-based materials highlighted various aspects of material swelling behavior (Gray et al., 1984; Dixon et al., 1985; Komine, 1994; Komine & Ogata, 2003; Mollins et al., 1996; Tripathy et al., 2004; Agus & Schanz, 2008; Schanz & Tripathy, 2009). For instance, the final swelling pressure of the compacted bentonite-sand mixture primarily depends upon the bentonite dry density in the compacted mixture (Gray et al., 1984; Dixon et al., 1985; Komine, 1994), the applied volume constraint governs the swelling pressure dynamics and the final swelling pressure (Sridharan et al., 1986; Wang et al., 2012; Al-Badran et al., 2017), material exhibits anisotropic swelling behavior in compacted state (Börgesson et al., 1995; Cho et al., 2000; Lee et al., 2012; Saba et al., 2014, 2016). The above-mentioned studies were performed with small-scale samples using oedometer type testing devices.

In the conventional soil testing methods, it is not possible to conduct the test under thermal or hydraulic gradients due to the small sample size. Hence, several mock-up tests have been conducted on both full-scale and reduced-scale for investigating the soil under repository relevant boundary conditions either in the Underground Research laboratory (URL) or in the surface laboratory (Alonso et al., 2005; Gens et al., 2009; Villar et al., 2005; Martin & Barcala, 2005). In addition to the initial installation cost, the surface laboratory-based investigations have various advantages over the URL-based studies such as a precise control over the applied thermal/hydraulic gradient, efficient data monitoring and a legitimate testing period. In this regard, a number of reduced-scale tests have been performed using column-type experimental device (Cuevas et al., 1997; Yong et al., 1997; Börgesson et al., 2001; Pintado et al., 2002; Åkesson et al., 2009; Schanz et al., 2013; Tripathy et al., 2015; Saba et al., 2016; Villar et al., 2016). In column-type experiments, a radial element of the buffer/backfill is subjected to repository relevant thermal/hydraulic gradient. In general, the experimental device facilitates the transient measurements of key state variables such as temperature, water content, relative humidity, soil suction, and



swelling pressure. An understanding of the coupled processes in the repositories on account of thermal and hydraulic loadings demands measurements of the axial total stresses at both warmer and cooler regions, the lateral stress, and simultaneous measurements of the water content. These aspects have not been explored in detail in the past.

Numerical analysis has become a powerful tool to predict the coupled hydro-mechanical behavior of soils. The Barcelona Basic Model (Alonso et al., 1990) is the pioneer elastoplastic model for unsaturated soil. The model was developed in 1990 originally for low to moderate expansive soils. However, several extensions of the original BBM have been proposed to satisfactorily reproduce the swelling pressure developed by bentonite samples upon water saturation (Delahaye & Alonso, 2002; Vaunat & Gens, 2005; Zandarin et al., 2013; Sánchez et al., 2012). Some key issues related to the BBM are also highlighted in the literature (Jommi, 2000; Gens et al., 2006). For instance, in the original BBM, Alonso et al. (1990) observed that the slope of normal compression lines (NCL) for low to moderate expansive soils decreases with an increase in soil total suction, it signifies that the NCLs for different values of suction diverge with increasing applied net mean stress level. While, the experimental data on the compacted speswhite kaoline tested by Wheeler & Sivakumar (1995) exhibited the opposite behavior.

Regarding a fully coupled flow and deformation problem, an indirect coupling is introduced by incorporating the soil water retention model, which features the description of soil suction and degree of saturation relationship in the mechanical constitutive model. The classical soil water retention models (Brooks & Corey, 1964; Van Genuchten, 1980; Fredlund & Xing, 1994) are capable to capture the dependency of degree of saturation on soil suction for non-deformable soils in which the pore size distribution remains constant during wetting or drying path. For the deformable soils, several models have been proposed (Gallipoli, Wheeler & Karstunen, 2003; Nuth & Laloui, 2008; Tarantino, 2009; Gallipoli, 2012). The above-mentioned models correlate the air entry/air expulsion suction with the void ratio or dry density of soil. Additionally, the double-structure water retention models have been proposed particularly for the compacted bentonite-based materials (Romero & Vaunat, 2000; Della Vecchia et al., 2015; Dieudonne et al., 2017) based on the microstructural characteristics of bentonite in the compacted state. Clays in compacted form have multi-scale porosity domains (Cui et al., 2002; Lloret et al., 2003; Delage et al., 2006). Depending upon the mineralogy and the associated force fields, clay-water interaction mechanisms differ in these porosity domains. Based on these characteristics features, Dieudonne et al. (2017) proposed a phenomenological model, which considers different water retention mechanisms in each structural levels of the compacted bentonite-based

materials. One of the major challenges in a fully coupled analysis is the identification of model parameters. For instance, in case of the BBM, a single parameter controls more than one aspects of soil behavior. In this regard, a systematic study is require to identify the model parameters for a fully coupled hydro-mechanical analysis and the effect of soil water retention model on the simulation results.

## 1.2 Objectives

The present research work aims to deal with the above mentioned limitations and challenges with respect to the coupled hydro-mechanical behavior of bentonite-sand mixture as a backfill material in nuclear waste repository. It is aimed to generate the reliable experimental data for calibrating the existing constitutive models for predicting the material coupled behavior. The main objectives of the present study are as follows:

- To design, implement and validate a new column-type experimental device for investigating the soil behavior under repository relevant thermal and hydraulic gradients.
- To identify the coupled hydro-mechanical processes in the compacted bentonite-sand mixture experimentally by mimicking the hydration process of backfill material under an applied hydraulic gradient.
- To conduct a fully coupled hydro-mechanical analysis using finite element method for calibrating the existing constitutive models.

## 1.3 Outline of thesis

The thesis consists of seven chapters, which are organized as follows:

- **Chapter 1** introduces the general background of the research topic, motivation and research objectives.
- **Chapter 2** presents the key findings in the context of current research topic. The chapter covers the basic knowledge of bentonite, forces involved in bentonite-water interaction and soil total suction components along with the existing measurement techniques. Further, the major findings and key studies in the context of water retention and the swelling behavior of bentonite-based materials are presented. Finally, a brief overview of the constitutive modeling approach in unsaturated expansive soils is presented.

- **Chapter 3** is dedicated to the material characterization and the description of testing methods used in this study. In the material characterization, relevant geotechnical and physico-chemical properties of the investigated materials are presented. The chapter also deals with the compaction characteristics, sample preparation method and the compaction induced heterogeneities in the compacted samples.
- **Chapter 4** focuses on the development, calibration and implementation of newly designed column-type experimental device. For mimicking the initial heating phase of buffer material, a test was performed on compacted Calcigel bentonite-sand mixture (50:50) to investigate the thermo-hydro-mechanical behavior of material under an applied temperature gradient.
- **Chapter 5** presents the water infiltration test results using the newly designed column-type experimental set-up. The investigated material was a compacted mixture of Calcigel bentonite and sand having equal dry mass fractions. The test conditions mimic the transient hydration of backfill material under repository relevant boundary conditions.
- **Chapter 6** aims at the numerical simulation of water infiltration test using finite element method. The Barcelona Basic Model (Alonso et al., 1990) for describing the mechanical behavior of unsaturated bentonite-based material was adopted along with the recently developed soil water retention model based on clay micro structural features in compacted state (Dieudonne et al., 2017). The simulation results were compared with classical soil water retention model (Van Genuchten, 1980).
- **Chapter 7** concludes the thesis with conclusions and outlooks for future works.



## 2 Literature review

### 2.1 General

This chapter summarizes the key findings in the context of the current research topic. The chapter covers the basic knowledge of physico-chemical properties of bentonite, forces involved in the clay-water interaction and soil water potential along with the soil suction measurement techniques. The key studies and major finding in the context of water retention and swelling behavior of bentonite-based materials are summarized. Finally, a brief overview of the constitutive modeling approaches in the unsaturated expansive soils is presented.

### 2.2 Basics of clay mineralogy

Clay minerals are crystalline hydrated phyllosilicates, which are composed of a specific combination of two basic structural units i.e., the silica tetrahedral sheet (see Fig. 2.1a) and the aluminum or magnesium octahedral sheet (Fig. 2.1b). In a silica tetrahedron, a silicon atom is equidistant from four surrounding oxygens (or hydroxyls, if needed to balance the structure). In an octahedron unit, an aluminum, iron or magnesium atom is equidistant from six hydroxyl or oxygen atoms. A unit-layer may consist of one or more tetrahedral sheets and an octahedral sheet.

Clay minerals may be grouped in four types i.e., the kaolinite, smectite, illite and chlorite group. Swelling-clays like bentonites mainly have smectite group minerals like montmorillonite depending on the arrangement of tetrahedral and octahedral sheets. For example, 1:1 clay mineral would have one tetrahedral and one octahedral sheet per clay layer; 2:1 clay mineral would have an octahedral sheet between two opposing tetrahedral sheets per clay layer. In 2:1 clay minerals like montmorillonite, layers may be separated from one another by interlayer cations, hydrated cations, organic molecules, and hydroxide octahedral groups and sheets (see Fig. 2.2).

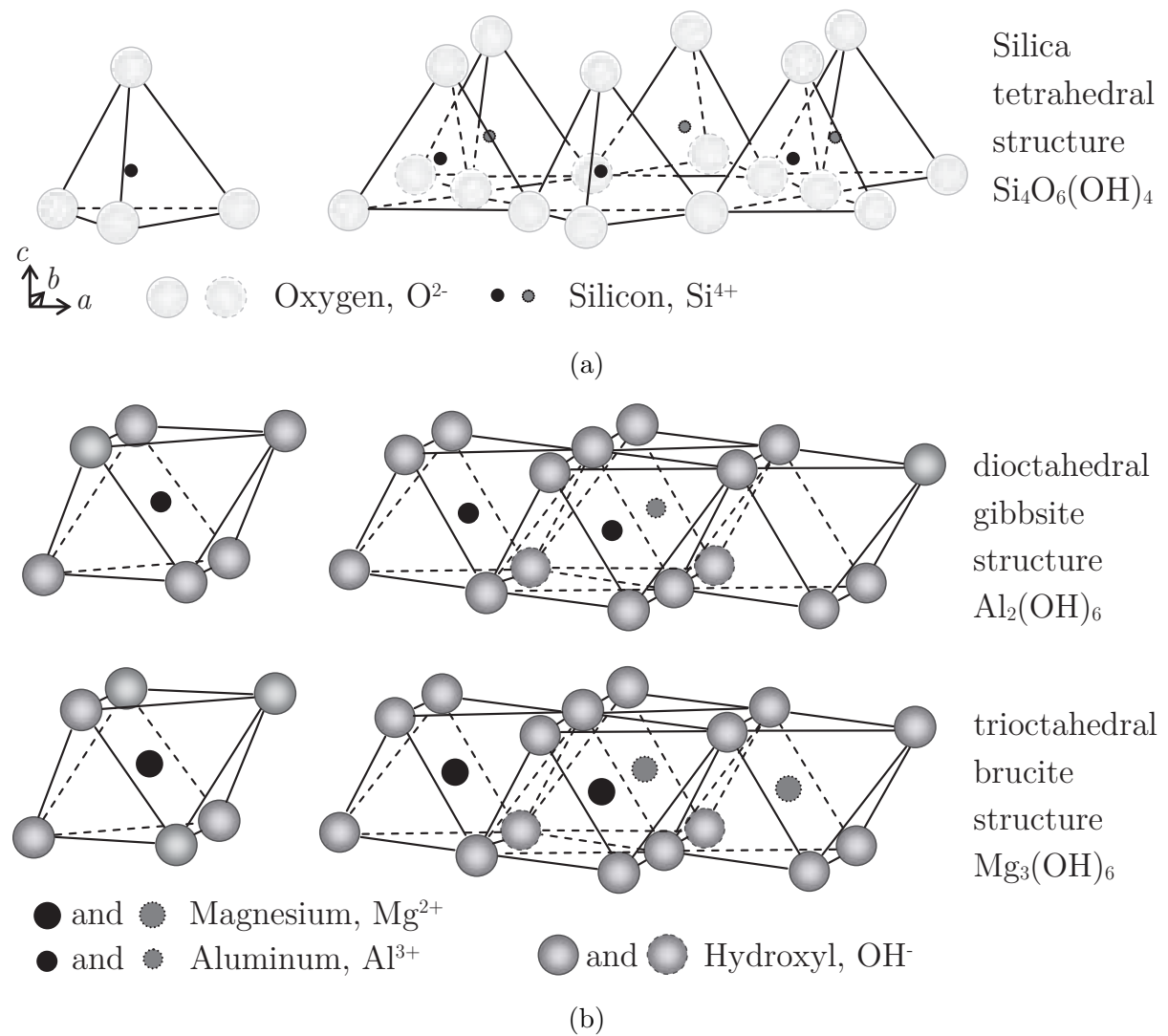


Figure 2.1: Diagrammatic sketch of tetrahedral and octahedral units (Baille, 2014; Grim, 1968): (a) single silica tetrahedron (left), sheet of tetrahedra arranged in a hexagonal network (right) and (b) single octahedron (left), di- and trioctahedral sheets (right).

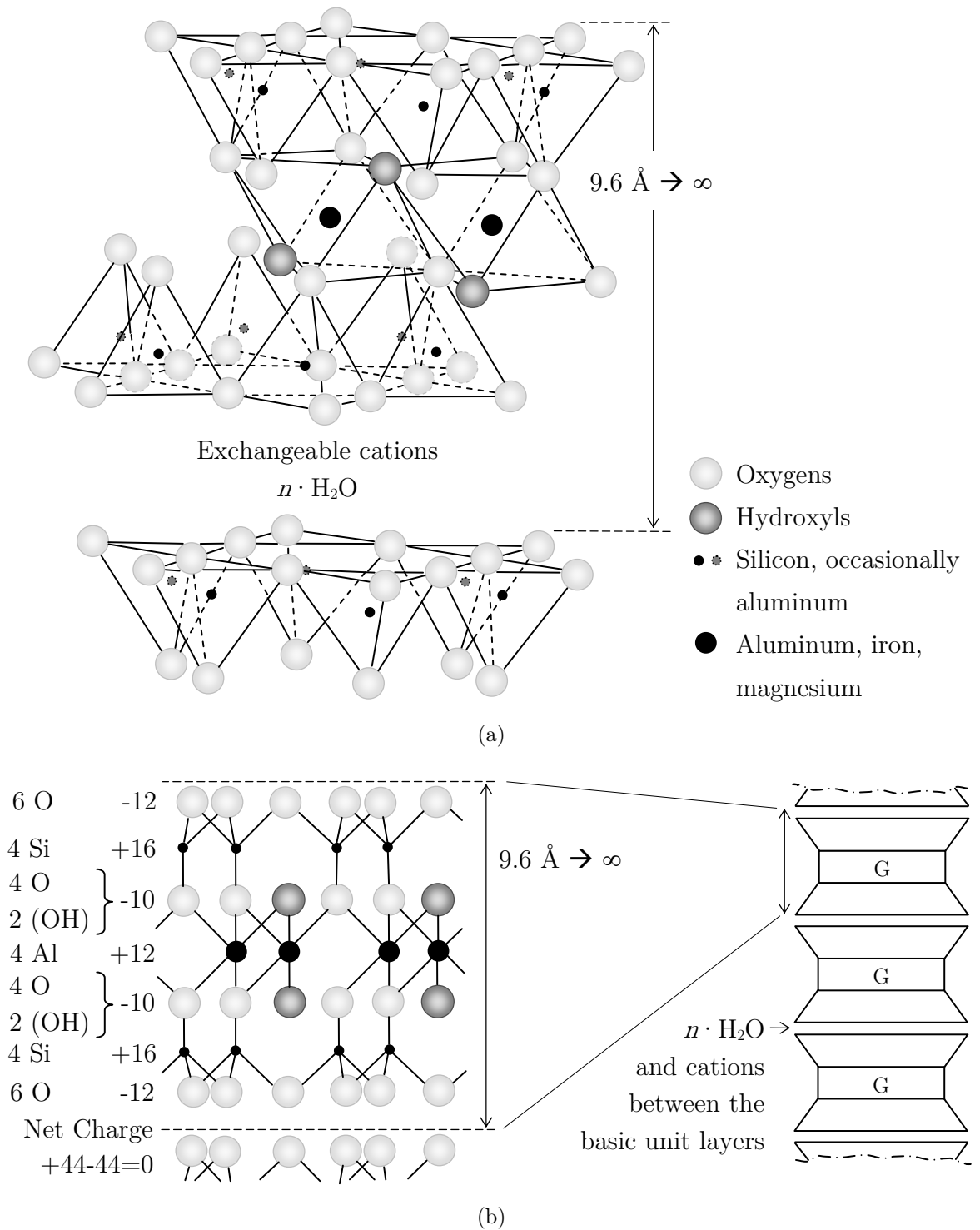


Figure 2.2: Diagrammatic sketch and charge distribution of montmorillonite (Baille, 2014; Grim, 1968): (a) diagrammatic sketch of the montmorillonite structure, (b) charge distribution on montmorillonite.

A unit or unit-structure is the total assembly of the layer and the available interlayer species. A particle is formed by a number of stacked layers (Tessier & Pedro, 1976; Bergaya & Lagaly, 2013). The number of layers in a single clay particle depend mainly upon the mineral type and the interlayer species. In a crystal lattice, the replacement of ions of one type by the ions of another type having the same or different valence without changing the crystal structure is termed isomorphous substitution (Grim, 1968). The type, amount and the location of isomorphous substitution may differ within and among the clay mineral groups. The common examples for substitutions in the clay minerals are aluminum in place of silicon in tetrahedral sheets, magnesium instead of aluminum, and iron for magnesium in octahedral sheets. The isomorphous substitution is the source of the net negative charge of clay mineral surfaces, thus governs the surface reactivity with other factors such as the nature of the local charge distribution, type of interlayer cations and the chemical composition of wetting fluid.

## 2.3 Physico-chemical forces in clay mineral-water system

### 2.3.1 Van der Waals long-range interactions

The Van der Waals forces originate from the interactions between the ions, atoms or molecules suspended in a medium (i.e., air or water). The net charge of an atom at any specific location and at any given moment is due to the revolving electrons around the nucleus at a high frequency. The electron's revolving around the nucleus generates dipole moment fluctuation at a frequency of  $10^{15}$  to  $10^{16}$  Hz per second, consequently two atoms are attracted towards each other (Overbeek, 1952). The dipole moment continuously fluctuates, a net attractive force develops between the induced and inducing dipoles (De Boer, 1936). The clay particle as a macroscopic body with flat surfaces interacts with each other in the presence of different mediums. Considering  $d$  as a half distance between the surfaces of two parallel clay particles, the Van der Waals attractive force can be calculated using the following equation,

$$F_A^{vdW} = \frac{A_h}{6\pi (2d^3)} \quad (2.1)$$

where  $F_A^{vdW}$  is the Van der Waals attractive force (N/mm<sup>2</sup>),  $A_h$  is the Halmaker constant (J), and  $2d$  is the inter particle distance (m).



Sridharan & Jayadeva (1982) proposed the following equation, which accounts for the thickness of the clay platelets ( $\delta$ ).

$$F_A^{vdW} = \frac{A_h}{48\pi} \left[ \frac{1}{d^3} + \frac{1}{(d + 0.5\delta)^3} - \frac{2}{(d + 0.5\delta)^3} \right] \quad (2.2)$$

According to the above equations, the Van der Waals forces depend upon the Hamaker constant ( $A_h$ ) and the inter particle distance ( $d$ ).

The Van der Waals interaction between any two atoms in a fluid (air or water as a medium) is always attractive. Considering an example when air is the pore fluid, the Hamker constant ( $A_h = 19.2$ ) is higher than the case where water is the pore fluid ( $A_h = 6.11$ ) for montmorillonite clay mineral, it signifies that attractive forces should increase as the clay system changes from saturated to unsaturated state. Sridharan (1968) established a relationship for the Hamaker constant as a function of degree of saturation. The Van der Waals attractive forces are considered as the long-range forces, hence describe the behavior of clays for a particle distance between 1 to 2 nm (Ninham, 1980).

### 2.3.2 Diffuse double layer repulsion

The dissolved ions of salts in the solution are attracted towards the negatively charged clay mineral surfaces in a colloidal suspension for compensating it. The charge compensating process induces a chaotic Brownian motion in the solution (Sposito et al., 1984). The surface charge of the clay particle and the adsorbed compensating charge arising from the counter-ions together are called double layer, and due to the diffusive nature of the ion charge, it is termed as the diffuse double layer. The net charge of a clay-water solution may be positive, negative or zero depending upon the pH of solution. The zero charge of the system could be observed in well-dispersed phase, where particles collide and move away from each other. A high concentrations of cations can be observed close to the surface and diffuse towards the bulk water solution to neutralize the concentration, however the free movement of these cations are restricted by electrostatic attraction of clay surface and known as immobile Stern layer, which is held very strongly by the clay particle surface (or basal surface). It is also known as the adsorbed water, which have more viscosity than the pure water and give the soil their plastic properties.

The second layer is created by anions present in the solution, these anions are attracted to cations around the clay particles, but these are loosely adsorbed to the first layer and they diffuse inside in bulk solution. These interactions create a non-uniform potential in the solution with the maximum potential on the clay surface and a zero potential at a large

separation distance. Figure 2.3 shows the schematic representation of the electrochemical interactions at the clay mineral surface (Goncalves et al., 2015). It also shows the evolution of the electric potential as a function of distance from the clay mineral surface.

The balance between a negatively-charged surface and the distributed ions around the surface creates a double layer (Chang & Sposito, 1996). The thickness of the double layer mainly depends upon the type of clay mineral and the chemistry of the pore water, it can go up to  $10^{-5}$  cm to  $10^{-4}$  cm in dilute solutions. Gouy (1910) and Chapman (1913) presented a theory for the distribution of the counter ions near a charged surface based on the Boltzmann distribution. In their proposed theory, the clay sheets were considered as infinitely long sheets, the size of double layer ions was neglected and considered as point charges, whereas the surface charge was assumed to be uniformly distributed. Stern (1924) united the models of Helmholtz and Gouy-Chapman, supposing that some of the counter-ions are fixed to the charged surface by considering the finite dimensions of clay sheets along with the finite distance between the charged surfaces and the counter ion.

In a clay-water electrolyte system, the repulsive double layer forces arise from the overlapping of the double layers of adjacent clay particles can be calculated in several ways. One of them is the solution of the Poisson-Boltzmann equation, which relates the electric potential, charge and the separation distance as per following equation,

$$\frac{d^2\phi}{dx^2} = \frac{2\eta_0\nu e}{\varepsilon} \sinh \frac{\nu e\phi}{k_B T} \quad (2.3)$$

where  $\phi$  is the electric potential (V),  $x$  the distance from particle surface (m),  $\eta_0$  the bulk fluid equilibrium concentration ( $\text{m}^3$ ),  $\nu$  the valency of the ions (-),  $e$  is the electron charge ( $1.602 \times 10^{-19}$  C),  $\varepsilon$  is the permittivity of the medium ( $\text{C}^2/\text{J}^{-1}\text{m}^{-1}$ ).

According to the theory, the inter particle distance  $2d$  will increase when the ions are replaced by the ions of a higher valency or when bulk solution concentration decreases. Based on the theory for single particle, for bulk fluid concentrations of  $10^{-5}$  and  $10^{-3}$  mol/l, the calculated thickness of the double layer was found to be about 100 nm and 10 nm for monovalent ions, and 50 nm and 5 nm for divalent ions (van Olphen, 1977).

### 2.3.3 Short-range interaction forces

The short range forces act mostly in the interlayer space, which are mainly the hydration (solvation) forces and the Born repulsion. In montmorillonite,  $\text{SiO}_4$  tetrahedra are arranged in a hexagonal pattern through sharing three of the four corners (O atoms) to

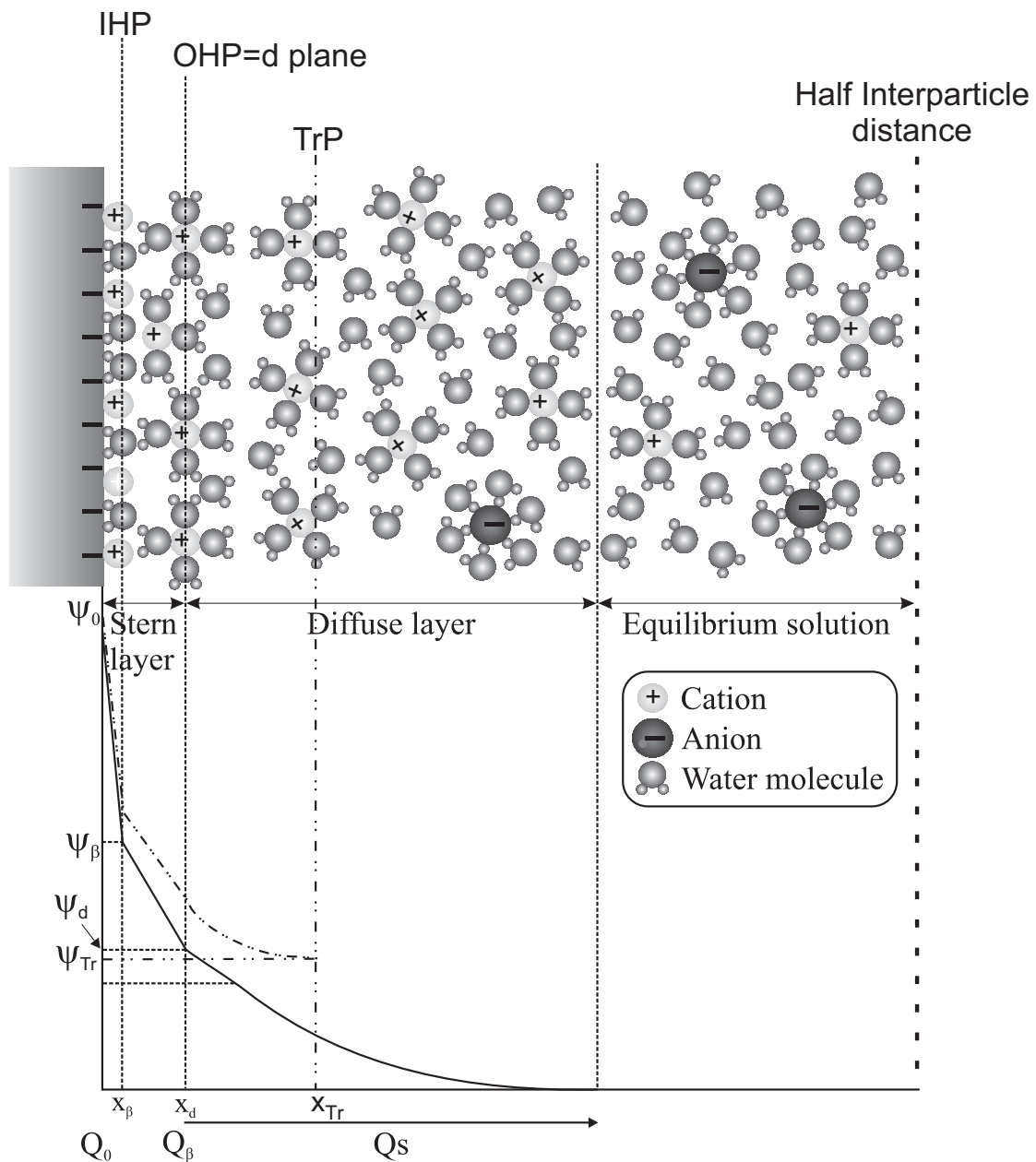


Figure 2.3: Schematic representation of the electrochemical interactions at the surface of clay mineral particle. This figure also shows the evolution of the electric potential as a function of the distance to this surface. The terms IHP and OHP indicate "Inner Helmholtz Plane" and "Outer Helmholtz Plane."  $Q_0$ ,  $Q_b$ , and  $Q_s$  ( $C - m^{-2}$ ) indicate charge densities at the surface of the particle, in the Stern layer, and in the diffuse layer, respectively.  $\psi_0$ ,  $\psi_b$ ,  $\psi_d$  (V) indicate the electrical potential at the surface and at the planes  $\beta$  (IHP) and  $d$  (OHP), respectively. TrP is the truncation plane situated at a distance  $x_{Tr}$  from the particle surface (Goncalves et al., 2015).

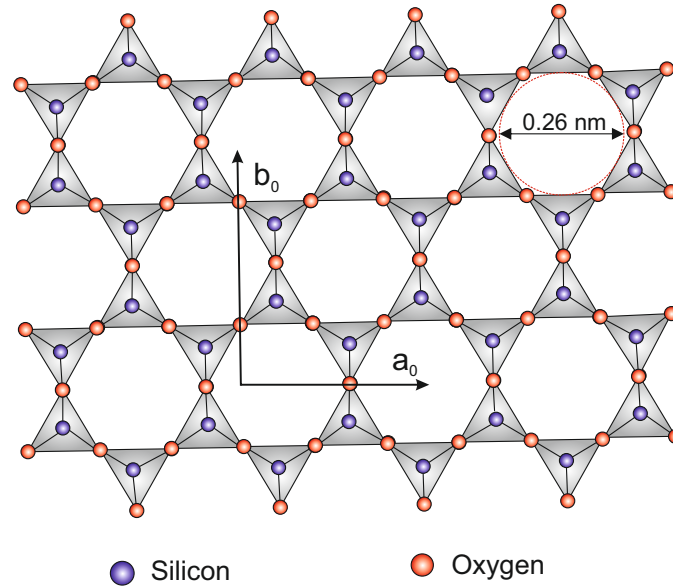


Figure 2.4: Hexagonal cavity with tetrahedral sheet,  $a_0$  and  $b_0$  refer to unit cell parameters (van Olphen, 1977; Sposito et al., 1984).

form a clay sheet. As a result, hexagonal cavities (see Fig. 2.4) are formed at the basal plane of the silica tetrahedrons in 2:1 montmorillonite clay mineral (Mitchell, 1993).

In the dry-state, the interlayer cations try to orient themselves as close to the negative charge as possible. However, the exact location depends upon the nature of interlayer cations. In case of monovalent cations, for example, sodium ( $\text{Na}^+$ ), it would go into the hexagonal hole, whereas the divalent calcium ( $\text{Ca}^{+2}$ ) would go into the hole nearest to one negative charge. The above condition implies a strong interaction between the interlayer cation and the clay mineral surface, which traps the cation in the hexagonal cavity. Consequently, a high resulting activation energy is needed for cations to escape into the interlayer space. In contrast, the larger cations cannot penetrate inside the cavity, the cation-framework interactions are weaker and the activation energy required to displace them is smaller. In this regard, the interlayer spacing for montmorillonites was investigated in dry state (Sato et al., 1992; Ferrage, 2004) and the test results revealed the role of size of interlayer cations in the interlayer spacing. For  $\text{Li}^+$  and  $\text{Na}^+$  montmorillonites at the dry state, the basal spacing ( $d_{001}$ ) values were small ( $\approx 9.6 \text{ \AA}$ ), which corresponds to a close contact between the two layers. In contrast, for  $\text{K}^+$  and  $\text{Cs}^+$  montmorillonites, the interlayer distances were larger ( $\approx 10.6$  and  $11.6 \text{ \AA}$ , respectively).

In the cation hydration process, the position of cation in the dry state plays a significant role as the hydration of cation is easier if it is more accessible and mobile. Following the statement, the cations  $\text{Li}^+$  and  $\text{Na}^+$  are the least accessible cations in the interlayer structure. In the hydrated state, the activation energy is lower than the dry state for all homo-ionic systems as the cation mobility increases due to hydration. The sequence of the activation energy at hydration state is the following:  $\text{Li}^+ \sim \text{Na}^+ > \text{Cs}^+ > \text{K}^+$ . The interactions between the hydrated-cations and the clay mineral surface are weaker, because of the existence of the hydration shell around the cation. In general, the mono ionic small cations ( $\text{Li}^+$ ,  $\text{Na}^+$ ) leaves the hexagonal site during the hydration and their mobility is made easier when the interlayer distance increases due to the hydration process as the water molecules modify the equilibrium between the surface layer and cation.

### 2.3.4 Net force in a clay mineral-water system

The theory proposed by Derjaguin, Landau, Verwey, and Overbeek (DLVO-theory) in the 1940s (Derjaguin & Landau, 1941; Verwey & Overbeek, 1948) explains the net interaction energy as a function of inter particle distance in the presence of repulsive and attractive force fields. The theory was based on the assumption that the repulsive double layer forces and the Van der Waals forces are independent and therefore can be superimposed or added (see Fig. 2.5).

The ionic strength of the suspension controls the range of double layer interaction; on the other hand, the Van der Waals forces are independent from ionic strength. Considering the role of separation distance, the Van der Waals attraction is an inverse power law function of the separation distance while the double layer force decays exponentially with the separation distance. Adding the Van der Waals attraction and the electrostatic repulsion gives the total interaction energy at a particular separation distance. For a low ionic strength, the net interaction force is repulsive at the large and intermediate separation distance. In contrast, at high ionic strength, the range of the Van der Waals force is larger and the interaction energy is slightly attractive at a large separations with a repulsive energy barrier at medium separations (see Fig. 2.5). The key feature of a high-ionic strength solution is the formation of secondary minimum, this energy barrier is relatively lower and the particles overcome it easily. In general, the double layer repulsive force resists soil particles aggregation whilst the Van der Waals attractive force induces aggregation.

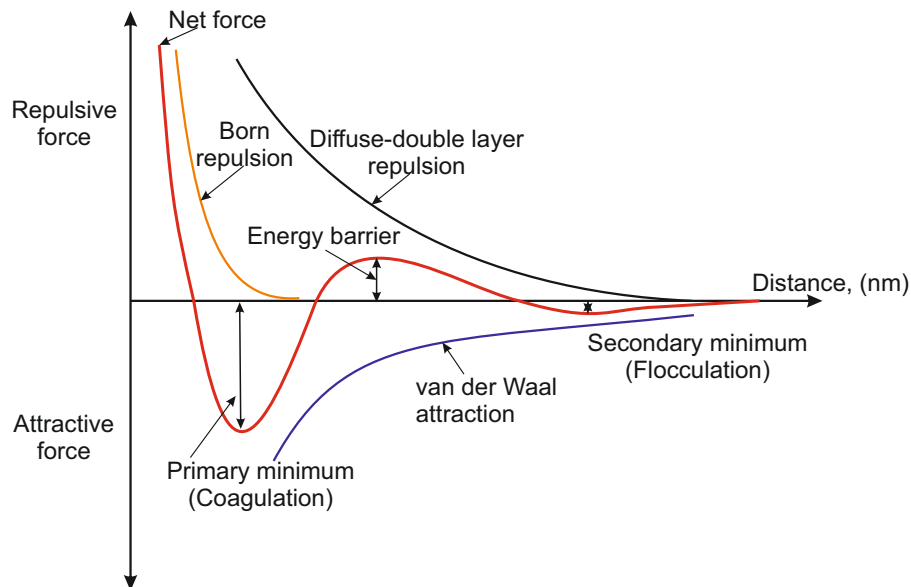


Figure 2.5: Schematic illustration of repulsive, attractive and net forces as a function of inter particle distance (modified from van Olphen (1977)).

## 2.4 Hydration of clays and influencing factors

### 2.4.1 Hydration mechanism

The clay microscopic structure consists negatively charged silicate layers and interlayer species. In the presence of different long and short-range interactions in a clay-water system, two different hydration mechanisms may be distinguished in swelling clays i.e., interlayer hydration and surface hydration. In the interlayer hydration, the water molecules are adsorbed in the form of successive monolayers in the interlayer space and also at the inner siloxane surfaces depending upon the chemical potential of bi-polar water molecules. The amount of adsorbed water or the number of monolayers in the interlayer space mainly depends upon the nature of cations and their location in the interlayer space. The volume change during the interlayer hydration is known as the crystalline swelling.

In the surface hydration, the negatively charged siloxane exterior surfaces and edges of clay particles react with the bi-polar water molecules, as a result the thickness of clay particles increases. The surface hydration also contribute in the volume change due to the diffuse double-layer repulsion by which the particles or the layers may be pushed further apart (osmotic swelling).

### 2.4.2 Influencing factors

The relative importance of the interlayer and surface hydration mechanisms depends on nature of exchangeable cations (i.e.,  $\text{Na}^+$  or  $\text{Ca}^{+2}$ ). For instance, Cases et al. (1997) found that the crystalline swelling in Ca-rich bentonite during the hydration was completed at a relative humidity of about 70 %. Saiyouri et al. (2000, 2004) found that the crystalline swelling in Ca-rich bentonite completed, when a transition in interlayer spacing from 1.56 nm corresponding to two monomolecular layers of water to 1.86 nm corresponding to three monomolecular layers of water, which occurred at a suction of about 4 MPa. The Ca-rich bentonite has a considerable range of stability with two molecular layer of water and it has substantially no expansion beyond a basal spacing of about 1.9 nm (Aylmore & Quirk, 1959). However, it may continue to accommodate more water on the particle's outer surfaces and result in to the inter-particle osmotic swelling (Madsen & Müller-Vonmoos, 1989; Segad et al., 2010).

For the basal spacing ( $d_{001}$ ) more than 22 Å, the surface hydration energy is no longer important, and the electrical double layer repulsion comes in to the picture as a major repulsive force between the clay plates. According to the diffuse-double theory, a saturated clay-water system is in equilibrium when the difference in osmotic pressures at the central plane between two particles and in the bulk fluid is balanced by the external pressure. The external pressure is usually termed as the repulsive pressure or swelling pressure (Bolt, 1956; Mitchell, 1993). This concept was used to determine the swelling pressures of compacted bentonites (Komine & Ogata, 1996; Tripathy et al., 2004). In these studies, the swelling pressure at equilibrium (i.e., at the end of saturation) was considered to be equal to diffuse-double layer repulsive pressure with an assumption that the double-layer repulsive force is the single operating force in the clay-water system. However, in case of the divalent montmorillonite at a close clay particle distance with restricted diffuse double-layer swelling, the hydration energy due to surface and ion hydration are the dominating factors for the swelling pressure development (van Olphen, 1977; RN, 1999).

Regarding the sequence of clay-hydration process and the resulting volume change behavior, Salles et al. (2008) conducted the thermoporometry in combination with X-ray diffraction and showed that the hydration of montmorillonite saturated with sodium or other cations is a multiscale process in which all scales are involved in the evolution of the clay microstructure. Authors also shown that in the montmorillonite saturated with  $\text{Li}^+$  and  $\text{Na}^+$  ions, the mesoscopic pore space is saturated by water and mesoscopic swelling begins. On the other hand, the interlayer space is filled with only one layer of water molecules (see Fig. 2.6).

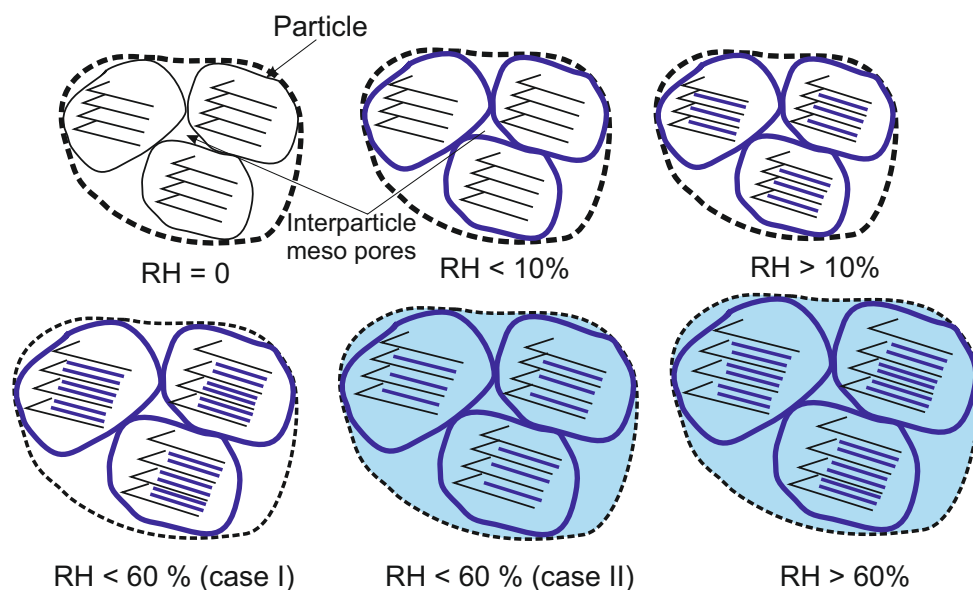


Figure 2.6: Plausible hydration sequence in Li- and Na- montmorillonites (modified after Salles et al. (2008)) at different relative humidity (RH) levels.

At the lower relative humidity levels ( $RH < 10\%$ ), the particle surfaces (or “external” surfaces) have one layer of water molecules. For the relative humidity higher than 10%, the water molecules first enter in the interlayer space for hydrating the cations and partially the “internal surfaces”, where the oxygen atoms and the hexagonal rings have a great importance. For further increase in relative humidity ( $RH < 60\%$ ), the water fills interlayer space with two monomolecular layers (case 1). In another possibility, the water molecules first fill the mesoscopic porosity completely (case 2). With further hydration ( $RH > 60\%$ ), the interlayer space is completely filled along with the mesoscopic porosity, which results in to an increase in the interlayer distance (crystalline swelling), the breaking of particles into smaller particles (exfoliation), and concurrently the increase of the volume of the mesoscopic porosity (osmotic swelling). The results indicated that the mesoscopic swelling begins well before the end of the interlayer swelling.

In contrast to the above observations, the infrared spectroscopic studies of smectite (Prost, 1975; Poinسیون & Fripiat, 1978) revealed that the first stage of water adsorption was due to the solvation of exchangeable cations, which was confirmed by the density functional theory (DFT) calculations performed by Emmerich et al. (2015) with Na-exchanged montmorillonite. After the solvation of cations, the water molecules start to reorient and form hydrogen bonds. In two monolayers of water, the water molecules form an octahedral complex with 6 water molecules surrounding the Na-ion (Emmerich et al., 2015;



Ferrage, 2016). A part of H<sub>2</sub>O molecules forms a hydration shells around the interlayer cation while remaining H<sub>2</sub>O molecules fill the space between them. It should be noted here that the observed hydration sequence by Salles et al. (2008) is only valid for Li and Na montmorillonites.

## 2.5 Soil-water total potential (soil total suction)

The state of water in the unsaturated soil can be described based on the theory of thermodynamics and varies according to the physicochemical forces of variable origin and intensity. In 1974, the second terminology committee of the International Society of Soil Science (ISSS) adopted the total potential as an energy concept to express the state of water in the soil. The total potential ( $\psi_t$ ) or soil total suction of the constituent water in the soil at temperature (T) is the amount of work per unit mass of pure water that must be done by means of externally applied forces to transfer reversibly and isothermally an infinitesimal amount of water from the state ( $S_0$ ) to the soil liquid phase at the point under consideration. The soil-water total potential can be expressed as energy per unit mass (chemical potential in J/kg), or as energy per unit volume (pressure potential) in J/m<sup>3</sup> = Pa), or as energy per unit weight (head potential in J/N = m). In the geotechnical engineering, soil total suction is the preferred term and refers to the pressure potential.

### 2.5.1 Components of soil total suction

The soil total suction  $\psi_t$  can be expressed as per the following equation (Fredlund & Rahardjo, 1993; Lu & Likos, 2004),

$$\psi_t = \psi_c + \psi_o + \psi_e + \psi_f \quad (2.4)$$

where  $\psi_t$  is the total potential,  $\psi_c$  is the potential due to the capillary forces including the negative pore water pressure,  $\psi_o$  is the osmotic potential due to the concentration of solutes contained in the pore water,  $\psi_e$  is the potential due to the short-range electrical fields of the soil solid, and  $\psi_f$  is the potential due to the Van der Waals fields. The latter two components ( $\psi_e$  and  $\psi_f$ ) signify the short-range interactions between the bi-polar water molecules and soil solids.

The soil total suction is related to the relative humidity of the pore volume inside the soil and the temperature by Kelvin's law:

$$s = - \left( \frac{\rho_w RT}{M_w} \right) \ln \left( \frac{RH}{100} \right) \quad (2.5)$$

where,  $s$  is soil total suction (MPa),  $\rho_w$  is the water unit mass ( $1 \text{ Mg/m}^3$ );  $R$  is the universal (molar) gas constant ( $8.31432 \text{ J/mol-K}$ );  $T$  is the absolute temperature ( $273.15 + t \text{ }^\circ\text{C}$ )  $^\circ\text{K}$ ;  $M_w$  is the molecular mass of water vapour ( $18.016 \text{ kg/kmol}$ ) and  $RH$  is the relative humidity in (%).

### 2.5.1.1 Matric suction

The potentials arising from the short-range forces and capillarity together correspond to the matric potential. Hence,

$$\psi_m = \psi_c + \psi_e + \psi_f \quad (2.6)$$

where  $\psi_m$  is the matric suction,  $\psi_e$  is the potential due to the short-range electrical fields of the soil solid, and  $\psi_f$  is the potential due to the Van der Waals fields.

The unsaturated soil is a special case of saturated state, where the pore water is partially replaced with air. By this definition, the matric suction component is related to the air-water interface (or surface tension) giving rise to the capillary phenomenon. The capillary component of matric suction is defined as the difference between pore-air pressure ( $u_a$ ) and pore-water pressure ( $u_w$ ) in the soil. The capillary component of matric suction arises from surface tension effects occurring at the air-water interface and may be described by drawing an analogy to water in a capillary tube at equilibrium. Figure 2.7 depicts this analogy. As depicted in Figure 2.7, the air-water interface exists as a result of a difference in the air pressure above the interface ( $u_a$ ) and the water pressure below the interface ( $u_w$ ). In general, the pore air pressure ( $u_a$ ) is atmospheric in unsaturated soils, whereas the water pressure ( $u_w$ ) is negative according to the capillary tube analogy as depicted in Figure 2.7c.

Due to the pressure difference ( $u_a - u_w$ ), a concave interface or meniscus emerges. In the context of unsaturated soil system, the radius of curvature is dependent on the pore fabric (i.e., particle size and arrangement) and the characteristics of liquid and solid which affect the contact angle. However, the expression for matric suction i.e.,  $u_a - u_w$  is only valid in unsaturated soil above the soil water cavitation pressure. The range of cavitation pressure for pore water in soil varies between 100-400 kPa (Frydman & Baker, 2009). Below the cavitation pressure, water starts to cavitate inside the pores and there will be no capillary water anymore. Hence, the definition of matric suction beyond the cavitation pressure needs some additional mechanisms to incorporate in the definition of matric suction.

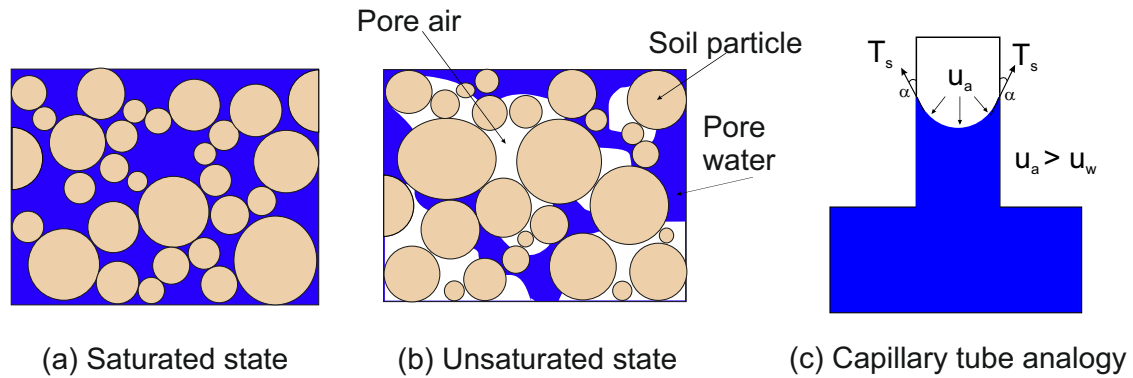


Figure 2.7: Schematic representation of capillary mechanism, (a) saturated soil, (b) three-phase interface system in an unsaturated soil and (c) capillary tube analogy.

The definition of matric suction in case of expansive soils requires modification in the Yong-Laplace equation (Philip, 1977; Nitao & Bear, 1996) as per the following equation,

$$u_m = -2T\kappa + A(h) \quad (2.7)$$

where  $u_m$  is matric suction,  $T$  is surface tension,  $\kappa$  is mean curvature of the air-water interface and  $h$  is the thickness of the adsorbed water film on the particle surface. The second term (i.e.,  $A(h)$ ) states that the energy associated with the adsorption process is a function of water film thickness  $h$ . Like the first term i.e., capillarity, the second term also provides the negative water pressure, thus indicates a lower energy state for the adsorbed water as compared to the free water.

### 2.5.1.2 Osmotic suction

Osmotic suction is due to the presence of dissolved salts in the pore-fluid, which may present in both saturated and unsaturated state. In a saturated state, the osmotic suction remains constant, whereas in case of unsaturated state, it can change significantly due to an increase in the concentration of dissolved salts. For instance, as the soil loses water during the evaporation process, the concentration of dissolved salts increases, consequently the osmotic suction also increases. The measurement techniques for osmotic suction are based on the extraction of pore water from the soil sample. The pore fluid squeezing technique is most common method for measuring the osmotic suction. In this methods, the soil sample is squeezed to extract the pore water and then measuring its electrical conductivity for the entire range of soil osmotic suction. The technique was used by several

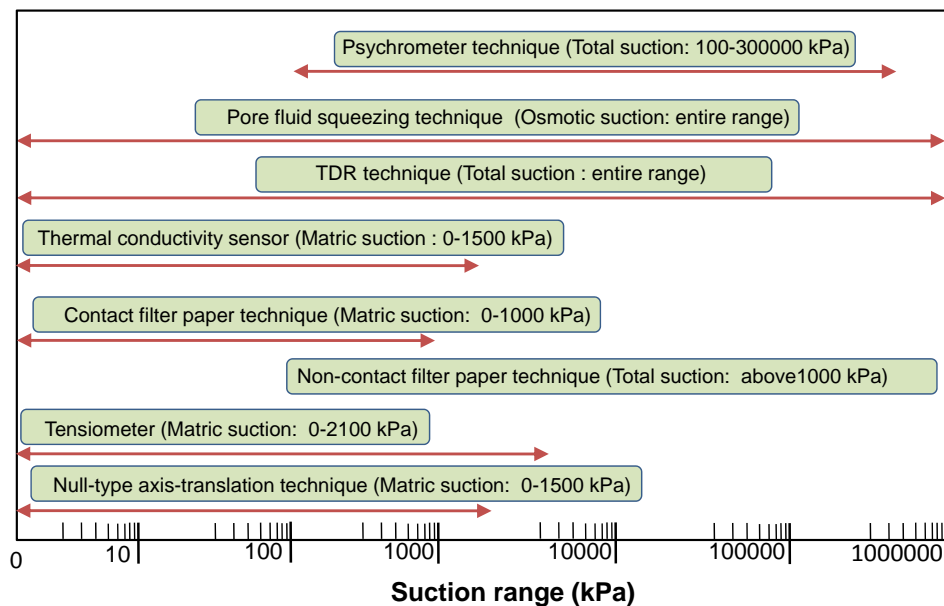


Figure 2.8: Soil suction measurement techniques and devices.

researchers (Krahn & Fredlund, 1972; Leong et al., 2003), however the measurement is sensitive to the applied squeezing pressure and the type of soil.

## 2.5.2 Soil suction measurement techniques

Figure 2.8 presents soil suction measurement techniques and devices. In general, these techniques can be classified in two major categories i.e., direct and indirect suction measurement techniques. The direct suction measurement techniques provide the matric suction, whereas the indirect suction measurement techniques provide the soil total suction.

### 2.5.2.1 Direct suction measurement techniques

The direct suction measurement methods measure the negative pore-water pressure and mainly include the axis translation technique, contact-filter paper method and the application of tensiometers. These techniques require a separation between water and air phase, which is achieved by means of a ceramic disk in the axis-translation technique or a ceramic cup in tensiometers. The continuity in water phase b/w the pore water and the device is one of the key requirements for measuring soil matric suction. Hence, the maximum value of soil matric suction that can be measured directly is limited by the air entry value of the ceramic disk or the ceramic cup used and the cavitation process.

Tensiometers measure the negative pore-water pressure of soil. A ceramic transducer, which is located in the tensiometer measures the equilibrated soil water pressure. Since a semi-permeable membrane for soluble salts does not exist in tensiometer, the effect of osmotic component of suction can not be measured. Hence, the measurement only provides the soil matric suction component. Due to the cavitation problem, the application of a ceramic cup with a higher air entry value will not increase the maximum value of soil matric suction that can be measured directly. A considerable efforts have been made to enhance the measurement range of tensiometer (Ridley & Burland, 1993; Guan & Fredlund, 1997; Tarantino & Mongiovi, 2003; Ridley et al., 2003) by modifying either the air entry value of ceramic cup or the form of construction.

The axis-translation technique is also known as null-type-axis-translation technique. In the working principle, water pressure in the pressure chamber is maintained close to zero, and it translates the origin of reference from the standard atmospheric condition to the final air pressure in the chamber. According to Hilf (1956) and Olson & Langfelder (1965), under a constant water mass condition, an increase in the applied air pressure inside the pores of unsaturated soil systems that possess sufficient continuity of air phase will increase the pore-water pressure in equal amount. Therefore, the difference between the applied air pressure and the pore-water pressure (i.e., matric suction) remains constant regardless of the translation of both the pore-air and pore-water pressures. In the measurement, an unsaturated soil specimen is placed on top of a saturated ceramic disk (air-entry value: 0.5-1.5 MPa) in an air pressure chamber.

### 2.5.2.2 Indirect suction measurement techniques

The indirect suction measurement methods correlate the soil water potential with the material physical properties which are moisture dependent such as relative humidity, electrical resistance, thermal conductivity, di-electric constant etc. A number of techniques are available to measure the soil total suction indirectly such as, the use of psychrometers, chilled-mirror hygrometer, thermal and electrical conductivity sensors, the filter paper technique and time domain reflectrometry (TDR) technique. The comprehensive reviews of suction measurement techniques are available in literature (Ridley & Wray, 1996; Rahardjo & Leong, 2006), only some of the relevant techniques such as chilled-mirror methods and relative humidity measurements are discussed here in detailed.

The Kelvin's equation correlates the soil total water potential with the relative humidity and temperature measurements of soil samples (Fredlund & Rahardjo, 1993). Hence, the

relative humidity sensors along with the temperature probes can be used for measuring soil total suction. Recently, Polymer capacitance technology is used in the relative humidity sensors, which provides a precise relative humidity measurement (Wiederhold, 2012). The polymer capacitance sensor consists of two electrodes that are separated by a thermoset polymer film. According to the RH level of surrounding environment, the film adsorbs or releases water. The RH value is determined by measuring the change in the capacitance of polymer film. With this technology, a rapid response of the sensor in measuring relative humidity is obtained.

The chilled-mirror hygrometer technique was first introduced to measure relative humidity of food products (Hand, 1994; Zhang et al., 1996) and pharmaceuticals (Ahlneck & Zografis, 1990; Friedel & Cundell, 1998). In geotechnical applications, the technique has been used for measuring total suction of soils (Leong et al., 2003; Albrecht et al., 2003).

The chilled-mirror hygrometer measures the dew point temperature and ambient temperature of the head-space above the soil specimen (see Fig. 2.9). The specimen is placed in a special closed/sealed chamber. The dew point temperature is measured using a mirror, photo-detector cell and a thermoelectric cooler. Temperature of the mirror is precisely controlled by a thermoelectric cooler. A light beam directed onto the mirror is used to detect the first appearance of water vapour condensation on the mirror. A photo-detector cell measures the change in reflectance of the mirror caused by the condensed water vapour. The temperature of the soil specimen is considered same as the temperature of vapour space, which is measured via an infrared thermocouple. The relative humidity or the water activity of the specimen is computed from the measured dew point and temperature. To speed up the equilibration time, an internal fan is used in the device to circulate the water vapour in the vapour space above the specimen. Leong et al. (2003) reported that the technique could be used to quantify total suction as low as about 150 kPa.

### **2.5.3 Errors in soil suction measurements**

Agus & Schanz (2005) assessed four methods for measuring soil total suction in the laboratory: the non-contact filter paper method, the psychometric technique, the relative humidity (RH) sensor and the chilled-mirror hygrometer technique. The assessment was made using the bentonite-sand mixtures. It was concluded that the chilled-mirror hygrometer technique gives the most accurate results and therefore used as a benchmark for assessing the accuracy of the other methods.

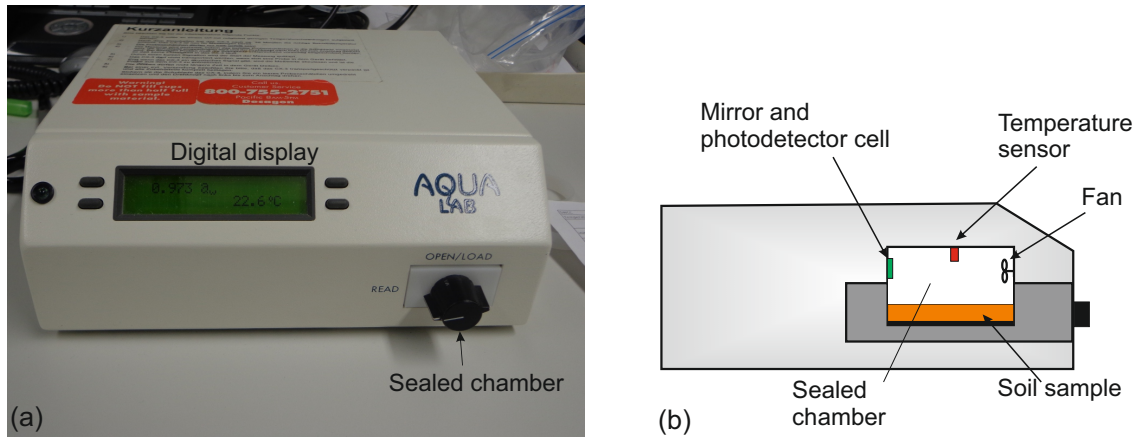


Figure 2.9: (a) Chilled mirror dew-point potentiometer (b) schematic view.

The investigations pertaining to the application of relative humidity sensors for measuring soil total suction revealed that the involved errors in the total suction measurements can be classified into three categories:

- Errors which are induced due to the inaccuracy of sensors,
- Errors due to the thermal gradient between the vapour space, the soil, and the sensor used, and
- Errors due to excessive condensation of water vapour on the measuring device.

Errors due to the inaccuracy of the devices and temperature gradient can be quantified while the errors due to excessive water vapour condensation on the measuring devices and the operator-related errors cannot be quantified. The error due to the temperature gradient can be estimated by taking the first derivative of Kelvin's equation with respect to temperature according to

$$\frac{d(\ln s_t)}{dT} = \frac{1}{T} - \frac{1}{u_{v0} \ln(RH)} \frac{d(u_{v0})}{dT}. \quad (2.8)$$

Equation (2.8) calculates the error involved in the soil total suction measurement due to the temperature gradient b/w the soil specimen and sensor (Fig. 2.10). If the error is limited, for instance, to 30 % of the measured value, the measurement of total suction will be limited to a value of about 850 kPa assuming that a 0.5 °C temperature gradient exists between the specimen and the vapour space. The temperature gradient of 0.5 °C can likely be maintained in a temperature-controlled laboratory, whereas the determination of low total suctions in the field by measuring relative humidity will most likely result

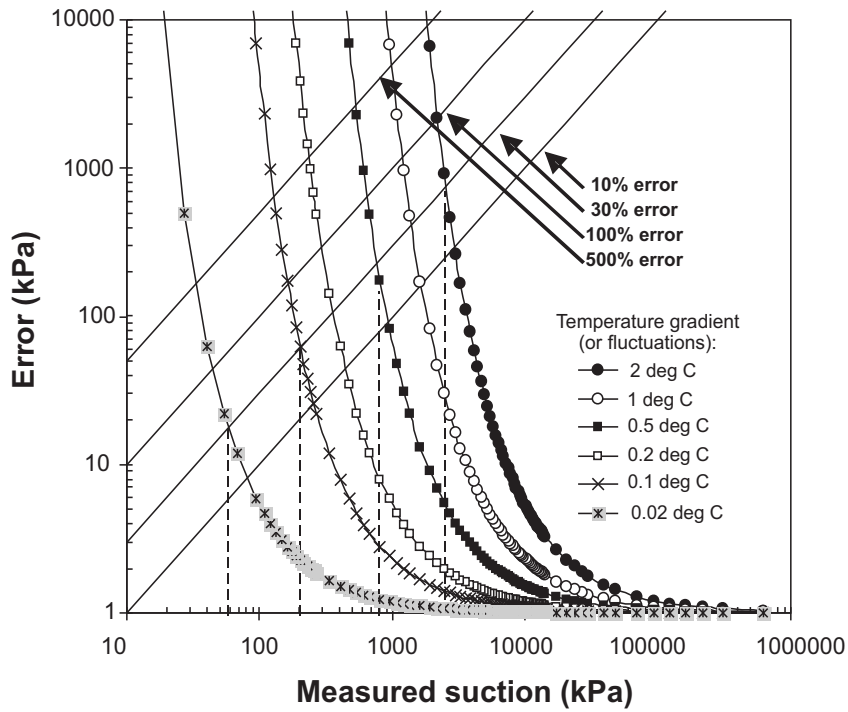


Figure 2.10: Error in the total suction measurement due to temperature gradient only (Agus & Schanz, 2007).

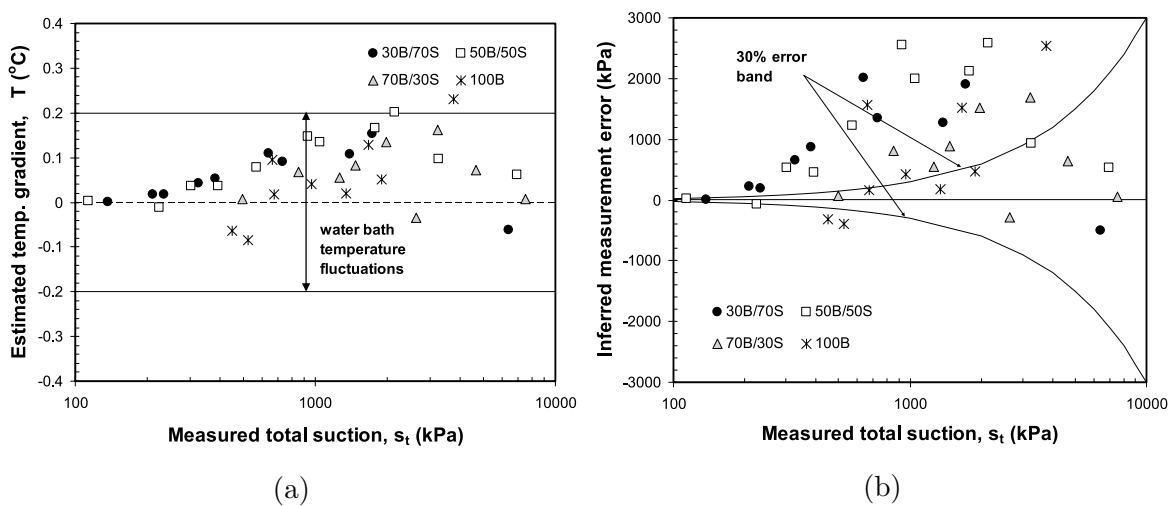


Figure 2.11: Error in the total suction measurement of bentonite (B) sand (S) mixtures due to temperature gradient using relative humidity sensors (Agus, 2005).



in inaccurate values due to the fundamental limitations of the techniques. The accurate measurement of total suction as low as 100 kPa with 30 % error requires a means to control temperature within  $\pm 0.04$  °C according to Eq. (2.8).

Agus (2005) estimated the temperature gradients b/w the compacted sand-bentonite mixtures and the RH sensor by considering the chilled-mirror hygrometer measurements as a reference case. The estimated temperature gradients values were almost positive in the entire range of total suction measured as depicted in Figure 2.11a. The errors involved in the soil total suction measurement error can be inferred from the estimated temperature gradient using Eq. (2.8) as shown in Figure 2.11b.

## 2.6 Factors influencing soil water retention characteristics

The soil water retention characteristics at the higher suction-levels is governed by the physicochemical properties of the clay minerals and independent from the material initial-state (i.e., dry density and water content) and the applied volume constraint (Romero et al., 1999; Lloret et al., 2003; Villar, 2007; Agus et al., 2013; Seiphoori et al., 2014; Gatabin et al., 2016). For instance, Romero et al. (1999) stated that the water at the higher suction-level mainly adsorbed at the surface of the clay particles or in the intra-aggregate pores; whereas, at the lower suction-levels, the water is stored in the macropores, which are affected by changes in the initial dry density as shown in Figure 2.12a. Similar observations were reported for the FEBEx bentonite (Lloret et al., 2003; Villar, 2007), for the Calcigel bentonite-sand mixtures (Agus et al., 2013) and for granular MX-80 bentonite Seiphoori et al. (2014). For instance, Lloret et al. (2003) presented the water retention curves of compacted FEBEx bentonite under both confined and unconfined conditions. The test results revealed that the SWRC is independent from the initial dry density upto a suction of 30 MPa, while for the lower suction levels, it becomes dry density dependent as depicted in Figure 2.12b.

The effect of applied volume constraints on the soil water retention characteristics of compacted expansive soils has been investigated by Wang et al. (2013a) and Gatabin et al. (2016). Wang et al. (2013a) determined the water retention behavior of compacted mixture of MX-80 bentonite and sand. Samples having initial dry density of  $1.67 \text{ Mg/m}^3$  were subjected to wetting under both confined and unconfined conditions. Gatabin et al. (2016) used the same mixture and material with higher density ( $2.03 \text{ Mg/m}^3$ ) and the

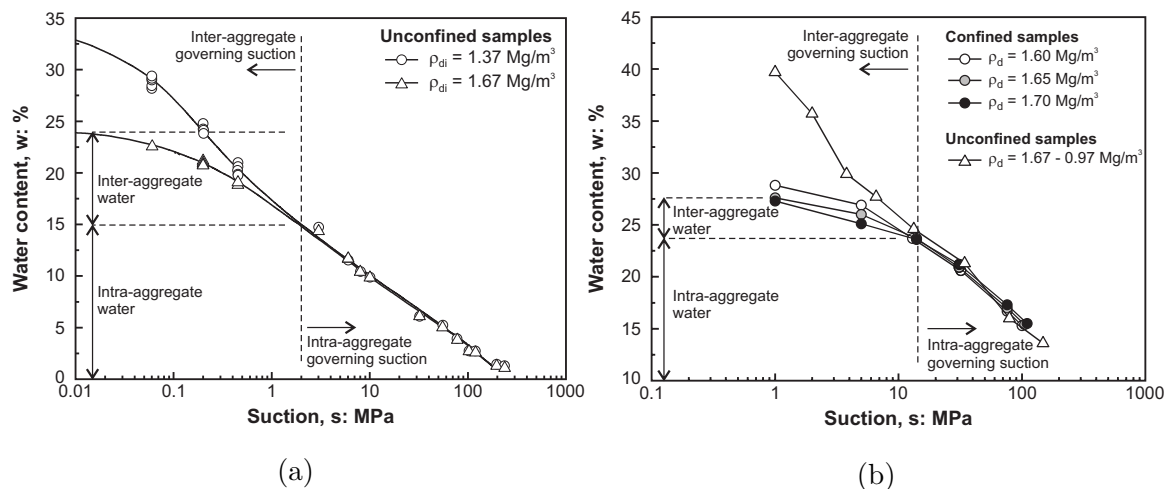


Figure 2.12: Effect of sample initial dry density and the applied volume constraint on soil water retention behavior of (a) compacted Boom clay (Romero et al., 1999) and (b) compacted FEBEx bentonite (Lloret et al., 2003).

samples were subjected to wetting under both confined and unconfined conditions. The test results revealed that, for a given suction, the amount of water in the mixture is higher in unconfined wetting condition than the confined wetting condition, particularly in lower suction range. While in higher suction levels, soil water retention behavior does not depend upon the applied volume constraints.

## 2.7 Swelling pressure of bentonite-based materials

The swelling pressure of compacted bentonite-based materials plays a key role in the long-term satisfactory performance of the engineered barrier systems. From the perspective of swelling pressure measurements, the relevant studies are reported in two parts. In the first part, the standard laboratory test methods for determining the swelling pressure are discussed along with the performed studies. In the second part, the phenomenological experimental for investigating the coupled hydro-mechanical behavior of bentonite-based materials under the repository-relevant boundary conditions are discussed.

### 2.7.1 Standard laboratory test methods

The standard laboratory methods for determining the swelling pressure are classified into three main categories: namely the constant volume, swell-under load and swell-load

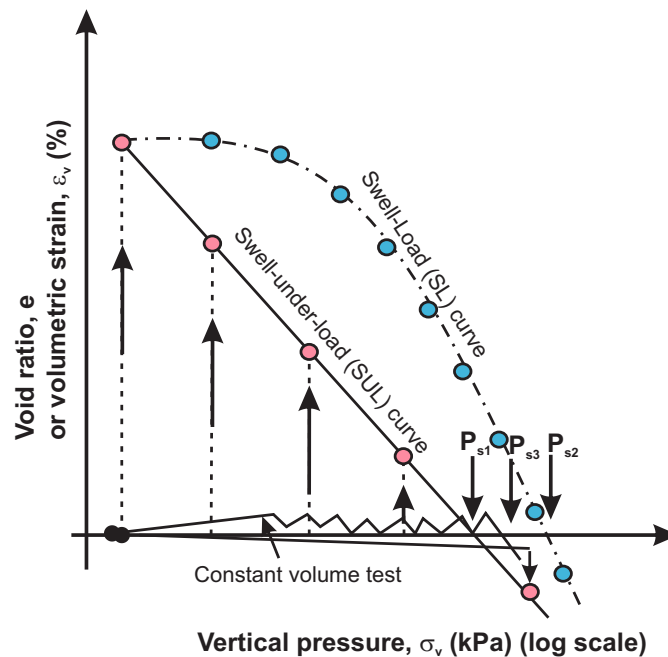


Figure 2.13: Different laboratory test methods for determining the swelling pressure (modified after Sridharan et al. (1986)).

method (Sridharan et al., 1986). Figure 2.13 shows the different measurement methods and the measured swelling pressure in a comparative manner.

In the constant volume method, swelling pressure can be measured by saturating the specimen with hydrating fluid under the rigid cell boundary conditions. In the swell-under-load (SUL) method (equilibrium void ratios method), a number of soil specimens having similar initial state are subjected to different vertical stress levels in the oedometer cells. In the next step, once the equilibrium is achieved under an applied vertical stress, the specimens are subjected to the hydration. With the hydration induced swelling or collapse under the applied vertical stress, the specimen attains a new equilibrium void ratio. The equilibrium void ratio versus applied vertical stress of different soil specimens tested will form a curve (normally a straight line) on a semi-logarithmic plot. The line intersects the horizontal line drawn through the average initial void ratio (or the zero volume change) at a certain point (i.e., point  $P_{s1}$  in Figure 2.13). The vertical pressure corresponding to this point is called swelling pressure determined from the swell-under-load method.

The swell-load (SL) method for determining swelling pressure is normally performed along with the conventional oedometer test. A soil specimen is allowed to swell usually under a

seating load of approximately 7 kPa. After the swelling has reached its equilibrium value, the soil specimen is subsequently loaded and unloaded to determine its compression and rebound curves (see Fig. 2.13). The compression curve intersects the horizontal line drawn through the initial void ratio (or the zero volume change) at point  $P_{s2}$  in Figure 2.13 which signifies the swelling pressure measured by the swell-load method.

A large number of studies have been reported based on the above-mentioned standard test methods (Gray et al., 1984; Dixon et al., 1985; Komine, 1994; Komine & Ogata, 2003; Mollins et al., 1996; Tripathy et al., 2004; Agus & Schanz, 2008; Schanz & Tripathy, 2009; Sun et al., 2013). These investigations highlighted several key aspects of material swelling behavior. Several researchers highlighted the effect of sample initial dry density and water content on the final swelling pressure (Gray et al., 1984; Dixon et al., 1985; Komine, 1994). These investigations revealed that the final swelling pressure of bentonite-sand mixture primarily depends upon the effective bentonite dry density in the mixture. Gray et al. (1984) performed the pioneer study in this field and provided the expression of the effective clay/bentonite density in the statically compacted bentonite-sand mixture defined as

$$\rho_c = \frac{G_c}{\left[1 + \left(\frac{G_{mix}}{\rho_d} - 1\right) \left(1 + \frac{G_c}{P.G_s}\right)\right]} \quad (2.9)$$

where  $\rho_c$  is the effective bentonite density in compacted sand bentonite mixture,  $G_c$  is the specific gravity of bentonite,  $G_{mix}$  is specific gravity of mixture,  $\rho_d$  is the mixture dry density,  $P$  is mass ratio of bentonite to sand and  $G_s$  is the specific gravity of sand.

Dixon et al. (1985) and Agus & Schanz (2008) validated the theory of effective bentonite dry density in the compacted bentonite-sand mixtures. Later, following the approach proposed by Gray et al. (1984), Komine & Ogata (1999) incorporated the clay mineralogical aspects and proposed the parameter “swelling volumetric strain of montmorillonite ( $\varepsilon_{sv}^*$ )” as a simplified evaluation of the swelling pressure of compacted sand-bentonite mixtures. With further modification, Komine & Ogata (2003) proposed a set of new equations for evaluating the swelling behavior of compacted bentonite and bentonite sand mixture that can accommodate the influence of the bentonite-sand mass ratio and the exchangeable-cation composition of bentonite with the consideration of Gouy-Chapman diffuse double layer theory and of the Van der Waals force.

For predicting the final swelling pressure, several researchers used the Gouy-Chapman diffuse double layer theory (Bolt, 1956; van Olphen, 1963; Sridharan & Jayadeva, 1982; Tripathy et al., 2004; Schanz & Tripathy, 2009). In the early era of research on this topic, Bolt (1956) expressed the swelling pressure as a difference between the osmotic pressure

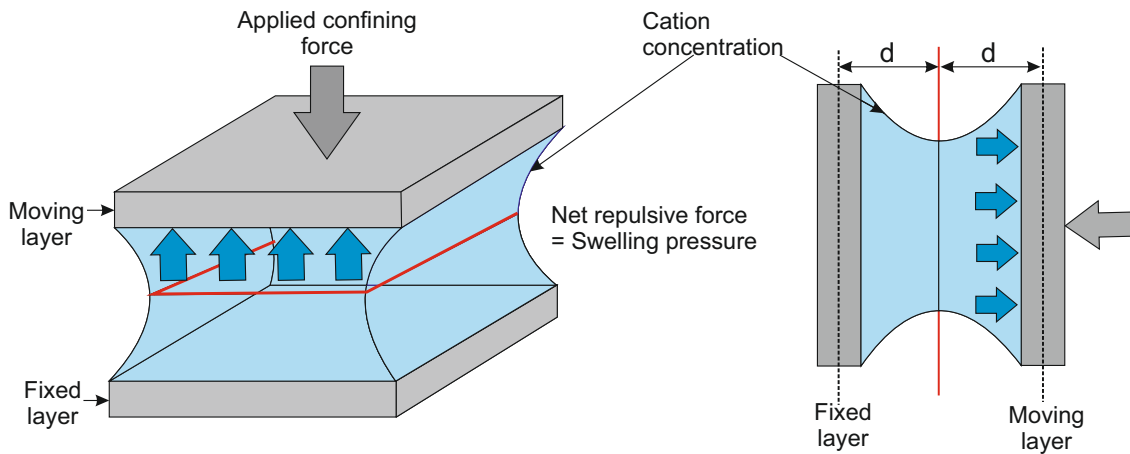


Figure 2.14: Schematic representation of fundamental concept for determining swelling pressure from diffuse double layer theory. (modified after van Olphen (1963)).

in the central plane between the clay platelets and the osmotic pressure in the equilibrium solution. van Olphen (1963) defined swelling pressure as the net repulsive force per unit area at the given distance. The swelling pressure was determined by measuring the equal confining force which must be applied externally to the moving layer to keep the layers at the given distance. Figure 2.14 depicts the schematic representation of the fundamental concept to determine the swelling pressure using diffuse double layer theory.

For investigating the role of soil suction in the development of swelling pressure, multistage swelling pressure tests have been performed with compacted bentonite-based materials (Lloret et al., 2003; Agus et al., 2013; Yigzaw et al., 2016). For instance, Lloret et al. (2003) performed the suction-controlled swelling pressure tests with a compacted Ca-rich bentonite under constant volume condition. Statically compacted samples (initial dry density:  $1.63 \pm 0.01 \text{ Mg/m}^3$  at  $13.7 \pm 1.3 \%$  hygroscopic water content) were subjected to the suction reduction phase in order to achieve a range of initial conditions for the constant volume swelling phase. The test results (see Fig. 2.15a) revealed three distinguish swelling zones. Similar test results were observed by Yigzaw et al. (2016) as shown in Figure 2.15b. Regarding the three different swelling zones as observed by Lloret et al. (2003) and Yigzaw et al. (2016), the zone I depicted an increase in swelling pressure due to the suction reduction; then, in zone II, a decrease in suction induced collapse of macrostructure that was manifested by a reduction in the measured swelling pressure; and finally, in the zone III at lower suction level, the swelling pressure increased again due to the microstructural rearrangement in bentonite.

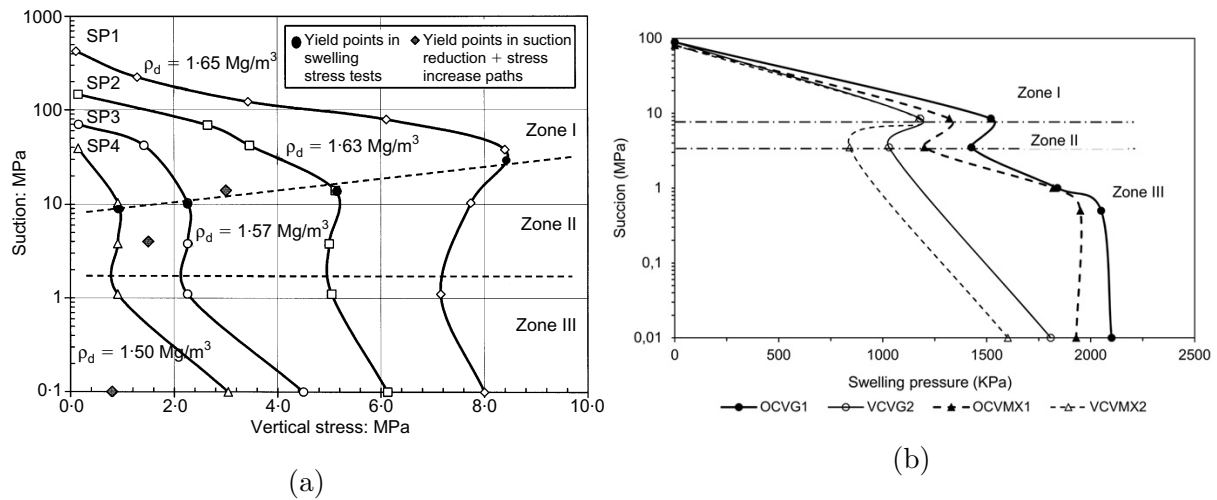


Figure 2.15: Generalized stress paths observed in the multistage swelling pressure tests (a) Lloret et al. (2003) (b) Yigzaw et al. (2016), (legends: OCVG1 = test with G-bentonite using osmotic technique, VCVG2 = test with G-bentonite using vapor equilibrium technique, OCVMX1 = test with MX-80 bentonite using osmotic technique, and VCVMX2 = test with MX-80 bentonite using vapor equilibrium technique).

Agus et al. (2013) also conducted a series of multistage swelling pressure tests on the compacted bentonite sand mixtures under constant volume condition. The test results are shown in Figure 2.16 along with sample initial conditions. It can be seen from the test results that Agus et al. (2013) did not observe any collapse of macrostructure and the microstructural rearrangement upon suction reduction during the multistage swelling pressure tests. Although three distinct zones can also be distinguished in the test results presented in Figure 2.16, in all cases a majority of the swelling pressures were found to be developed in the central zone. A reduction in the swelling pressure was not observed in this study; rather, all specimens exhibited maximum swelling pressures upon saturation with water or when the applied suction was null. The development of swelling pressure with decreasing suction for the specimens showed threshold suctions below which a further reduction in suction yields an increase in swelling pressure of the same magnitude. The magnitude of threshold suction was found to be a function of bentonite content in compacted specimens.

## 2.7.2 Phenomenological soil testing approach

In the standard swelling pressure test methods, it is not possible to conduct the test under the thermal and thermal-hydraulic gradients due to the small sample size. On the other

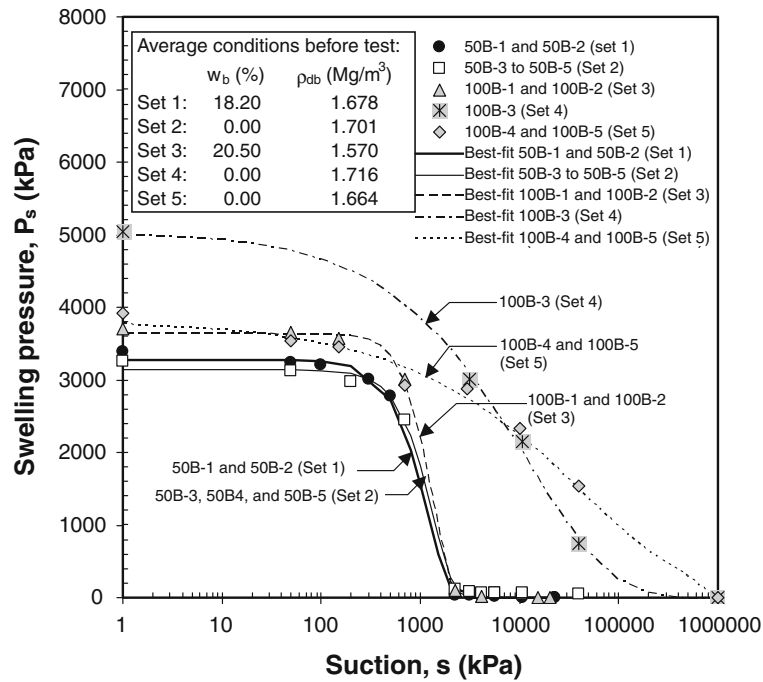


Figure 2.16: Swelling pressure development with decreasing suction during multistage swelling pressure test (Agus et al., 2013).

hand, the experimental device for investigating the coupled hydro-mechanical behavior of material under repository-relevant boundary conditions should be able to test the soil sample under the coupled thermo-hydro-mechanical (THM) boundary conditions identical to the field application. In this regard, several phenomenological tests have been conducted on both full-scale and reduced-scale.

A number of full-scale tests have been conducted either in the field or in the laboratory under the coupled THM loading scenarios relevant to the high-level radioactive waste disposal (Alonso et al., 2005; Gens et al., 2009; Villar et al., 2005; Martin & Barcala, 2005). For instance, the **F**ull-scale **E**ngineered **B**arriers **E**xperiment (FEBEx) was installed at the Grimsel underground research laboratory in Switzerland (Alonso et al., 2005; Gens et al., 2009; Villar et al., 2005). The test set-up is shown in Figure 2.17a. Meanwhile, a full-scale mock-up test was conducted as a forerunner of FEBEx field test under the controlled boundary conditions in laboratory (Martin & Barcala, 2005) as depicted in Figure 2.17b.

Apart from the initial installation cost, the reduced-scale experiments in the laboratory have certain advantages over the full-scale investigations such as a precise control over the applied thermal/hydraulic gradient, the efficient data monitoring and a legitimate testing



Figure 2.17: (a) Full-scale Engineered-barrier Experimental (FEBEx) performed at the Grimsel Test Site (GTS, Switzerland) (Villar et al., 2005) and (b) full-scale mock-up test in laboratory (Martin & Barcala, 2005).

period. In this regard, a number of reduced-scale experiments have been performed using the column-type experimental devices (Cuevas et al., 1997; Yong et al., 1997; Börgesson et al., 2001; Pintado et al., 2002; Åkesson et al., 2009; Schanz et al., 2013; Tripathy et al., 2015; Saba et al., 2016; Villar et al., 2016).

Figure 2.18 illustrates the column-type testing concept for investigating the material behavior under the repository relevant boundary conditions. The bentonite-based materials are key components of multilayer engineered barrier system in form of sealing, backfill and buffer material. Based on the application, these materials are subjected to the elevated temperature arising from the radioactive decay heat, the hydration through the host rock and the mechanical stress due to the hydration under confined condition. Under these boundary conditions, the material behavior is governed by the coupled thermal-hydro-mechanical (THM) processes.

The main objective in the phenomenological column-type experimental approach is to capture these coupled processes in the material under the applied loading scenarios (Figs. 2.18b, c). The identification of coupled processes during the experiment relies on the measurement capabilities of experimental device, in general the time history of temperature, relative humidity, pore water pressure and material mechanical response (swelling pressure) are monitored during the test.

In the reported column-type investigations (Cuevas et al., 1997; Yong et al., 1997; Börgesson et al., 2001; Pintado et al., 2002; Åkesson et al., 2009; Schanz et al., 2013; Tripathy et al., 2015; Saba et al., 2016; Villar et al., 2016), the swelling pressure measurements were



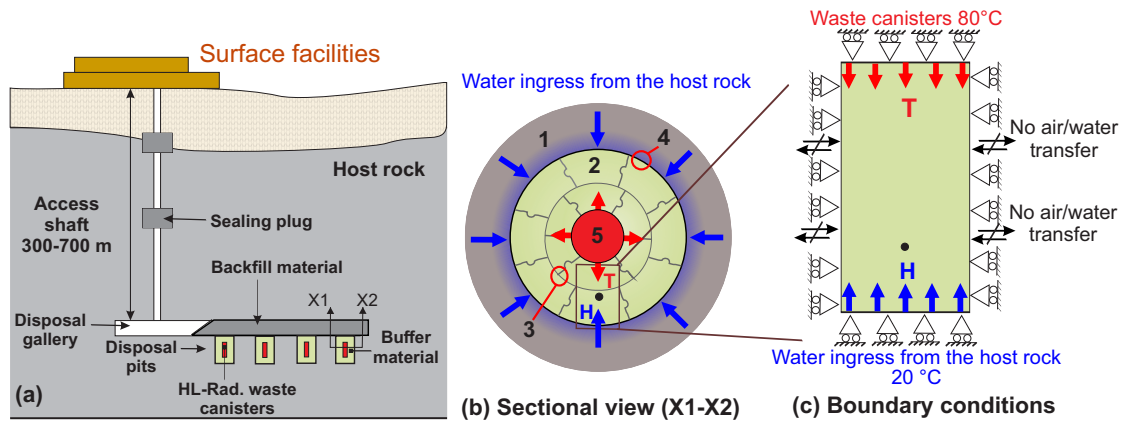


Figure 2.18: Schematic illustration of column-type testing concept, (a) deep geological disposal concept, (b) and (c) compacted blocks as a buffer material between waste canister and host rock (1 = host rock; 2 = compacted blocks; 3 = technical gap between blocks; 4 = gap between blocks and host rock; 5 = Waste canister, T = applied temperature, H = hydration from host rock).

performed at the hydration-end only. A limited number of researchers (Åkesson et al., 2009; Saba et al., 2016) performed the swelling pressure measurements in the lateral direction during the test. The key process variables such as the water content and porosity of the soil samples were determined after the termination of the tests (Tripathy et al., 2015; Saba et al., 2016; Villar et al., 2016).

During the early phase of the repository life time, the impact of thermal loading on the hydro-mechanical behavior of the materials is of significant interest (Sellin & Leupin, 2013; Tripathy et al., 2017). A difference in the temperature between the high-level waste canisters and the surrounding barrier materials causes a redistribution of the water content and leads to volumetric deformations in the soil. Under the restrained condition, a development of the swelling pressure occurs, which in turn provides the desired structural stability to the repositories (Pusch & Yong, 2014). The magnitude of swelling pressure that gets developed during the thermal loading phase depends upon the vapour-phase continuity in the system and the stiffness of the boundary (restraint), that may differ in both axial and lateral directions. Therefore, an understanding of the coupled processes in the repositories on account of thermal loading demands measurements of the axial total stresses at both warmer and cooler regions, the lateral stress, and simultaneous measurements of the water content. These aspects have not been explored in detail in the past.

## 2.8 Constitutive modeling in unsaturated soils

A constitutive model is a fundamental tool to reproduce the material behavior using the suitable constitutive laws, which are developed based on the laboratory investigations. As stated by Gens et al. (2006), “there is nothing special in an unsaturated soil apart from the simple fact that some part of the pore space is occupied by air”. The above statement provides the consistency between the fully saturated state to unsaturated state. Accordingly, constitutive models for unsaturated soils have been proposed based on the elastoplastic framework for the saturated soils (Roscoe & Burland, 1968; Alonso et al., 1990; Loret & Khalili, 2002; Wheeler et al., 2003; Gallipoli, Gens, Sharma & Vaunat, 2003; Sheng et al., 2004). One of the main objectives of the developments of constitutive models was to predict the behavior of unsaturated soils based on the past developments in saturated soil mechanics. The Barcelona Basic Model (Alonso et al., 1990) is the pioneer elastoplastic model for unsaturated soils. Later, several other elastoplastic models have been proposed based on the characteristics features of the Barcelona Basic Model (Loret & Khalili, 2002; Wheeler et al., 2003; Gallipoli, Gens, Sharma & Vaunat, 2003; Sheng et al., 2004).

### 2.8.1 The Barcelona Basic Model (BBM)

The Barcelona Basic Model proposed by Alonso et al. (1990) is one of the first elastoplastic models for describing the mechanical behavior of slightly or moderately expansive soils, such as sands, silts and low plasticity clays. It uses the concepts of the plasticity theory and the critical state soil mechanics. The model is an extension of the Modified Cam-Clay Model (MCCM) (Roscoe & Burland, 1968) to an unsaturated state by considering soil suction  $s$  as an additional stress state variable. The characteristics features of Barcelona Basic Model (BBM) with three yield surfaces in the  $(p - q - s)$  space are illustrated in Figure 2.19, where  $p$  is the mean net stress and  $q$  is the deviatoric stress. The model includes suction-induced hardening (isotropic) by generalizing the definition of preconsolidation stress in an unsaturated state to account the influence of suction  $s$ . The first yield surface lies in the  $(p - q)$  plane for the saturated case ( $s = 0$ ), the yield surface corresponds to the Modified Cam Clay ellipse. The second yield curve exhibits an increase in the elastic domain as soil suction increases and designated as loading-collapse (LC) curve, which is one of the fundamental characteristics of the model. While, the third yielding surface describes the suction-induced plastic strains.

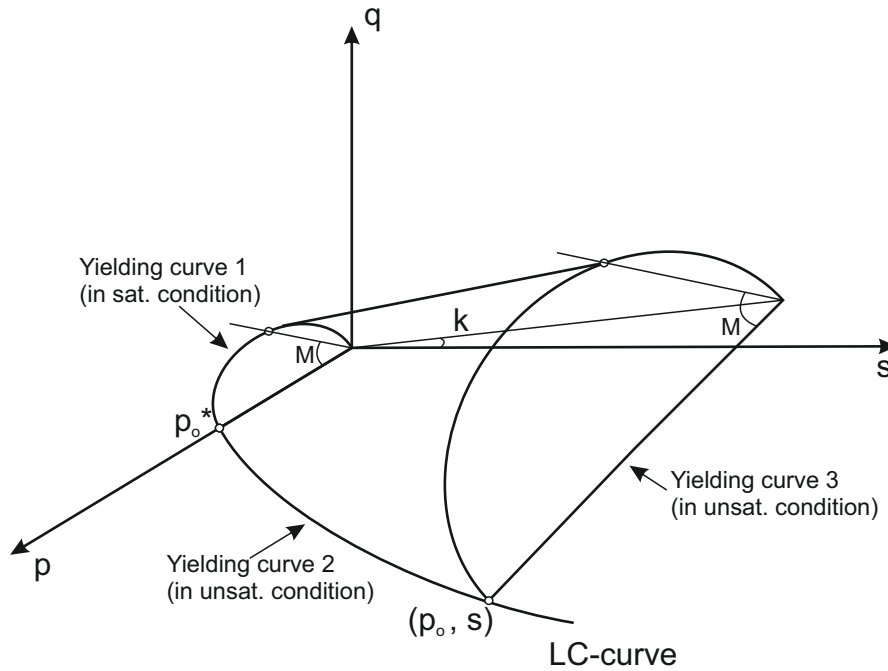


Figure 2.19: Characteristic features of Barcelona Basic Model (Alonso et al., 1990).

## 2.8.2 Limitations and modification in the original BBM

The Barcelona Basic Model is an elastoplastic model and considers soil suction as a stress-variable in an unsaturated state. While, in the saturated state, the model essentially coincides with the Modified Cam-Clay Model. Therefore, it has all the limitations or the characteristic features associated with the MCCM. For instance, the model is not able to represent the viscous behavior and the dependency of shear strength on the loading direction (Potts et al., 2001). Some key issues related to the BBM are highlighted by Jommi (2000) and Gens et al. (2006), such as:

### 2.8.2.1 The choice of stress state variables

The choice of stress state variables plays a key role in the constitutive modeling approach. According to Gens (1996), most of the unsaturated constitutive models can be expressed as,

$$(\sigma_{ij} - u_a \delta_{ij}) + \mu_1(s, \dots) \quad (2.10)$$

$$\mu_2(s, \dots) \quad (2.11)$$

where  $\sigma_{ij}$  is total stress,  $\delta_{ij}$  is Kronecker's delta,  $u_a$  is pore-air pressure,  $\mu_1$  and  $\mu_2$  are functions of soil suction and, sometimes, of other variables as well. In fact, these functions signify the role of air-water interface in the soil mechanical behavior.

Based on the definition of  $\mu_1$ , three main classes of models can be distinguished as per the following equation,

$$\mu_1 = \begin{cases} 0 & \text{Class I} \\ f(s) & \text{Class II} \\ f(s, S_r) & \text{Class III} \end{cases} \quad (2.12)$$

where  $s$  is soil suction and  $S_r$  is the degree of saturation.

Class I models are defined within the net stress framework. The Barcelona Basic Model falls under this category. According to Gens et al. (2006), although it is the simplest and most practical choice in terms of stress path representation, it poses difficulties when trying to incorporate hydraulic hysteresis effects. In addition, this class of models requires an explicit variation of apparent cohesion with soil suction. This type of formulation may encounter difficulties in the transition between the saturated to unsaturated states. Concerning the Barcelona Basic Model, Vaunat et al. (1997) suggested special numerical techniques to overcome the issue of transition between the saturated and unsaturated states.

In class II models, the definition of constitutive stress includes explicitly the soil suction but not the degree of saturation (Loret & Khalili, 2002). The increase in the strength with soil total suction is implicit in the definition of constitutive stress and hence, it does not need additional specific relationship. The stress-path representation is comparatively complex than Class I models. Transition between the saturated to unsaturated states is not straightforward, even when the air-entry suction value is adopted as a baseline.

In Class III models, the definition of constitutive stress includes explicitly the soil suction and degree of saturation (Wheeler & Sivakumar, 1995; Wheeler, 1996; Sheng et al., 2004). Hydraulic hysteresis effects are also naturally incorporated and the strength increase with suction results directly from the definition of the constitutive stress. Naturally, the representation of stress paths is now more complex and it becomes impossible if, as it is often the case, data on water content is not available or unreliable. The classical Bishop's equation (Eq. (2.13)) for effective stress is an example of Class III type of constitutive stress, where the effective stress parameter,  $(\chi)$  is expressed as a function of degree of saturation, hence

$$(\sigma_{ij})_c = (\sigma_{ij} - u_a \delta_{ij}) + \chi (u_a - u_w) \delta_{ij} \quad (2.13)$$

In any case, all constitutive models as mentioned above share the same core of assumptions (Gens et al., 2006): (1) use of two independent stress variables, (2) formulation of some type of LC yield surface, and (3) use of a saturated model as a limiting case.

### 2.8.2.2 Variation in soil stiffness with suction

In the original BBM, Alonso et al. (1990) assumed that the slope of normal compression lines (NCLs) for samples having different suction decreases with an increase in soil total suction, it signifies that the NCLs for different values of suction diverge with increasing applied net mean stress level. The above statement is valid for the soil having low to medium swelling potential. While, the oedometer test results shows the converging behavior of normal compression lines under applied net mean stress levels. Wheeler et al. (2002) proposed a procedure for selecting the BBM parameter values ( $r$  and  $p_c$ ) to model the behavior of such soils where the NCLs converge with increasing applied stress.

### 2.8.2.3 Prediction of elastic swelling

The original formulation of BBM (Alonso et al., 1990) overestimates the elastic swelling (Gens and Sánchez, 2014). In order to overcome this shortcoming, the approach adopted by the Barcelona research group consists in introducing suction and/or stress dependent elastic parameters  $k$  and  $k_s$  (Delahaye & Alonso, 2002; Vaunat & Gens, 2005; Zandarin et al., 2013; Sánchez et al., 2012). Accordingly, the slope of unloading-reloading line for changes in the mean net stress varies as per the following equation,

$$k = k_0 \left[ 1 + \alpha_1 s + \alpha_2 \ln \left( \frac{s + u_{atm}}{u_{atm}} \right) \right] \quad (2.14)$$

where  $k_0$  is the elastic stiffness in saturated conditions,  $\alpha_1$  and  $\alpha_2$  are model parameters and  $u_{atm}$  is the atmospheric pressure.

While, the slope of reversible wetting-drying line on mean net stress,  $k_s(p)$  is given as

$$k_s(p) = k_{s,0} \left[ 1 + \alpha_p \ln \left( \frac{p}{p_{ref}} \right) \right] \exp(\alpha_s p) \quad (2.15)$$

where  $k_{s,0}$ ,  $\alpha_p$  and  $\alpha_s$  are the material parameters and  $p_{ref}$  is the reference pressure.

In the present work, Class I constitutive model (BBM) is used to predict the hydro-mechanical behavior of compacted expansive soil based material as the main focus is on the prediction of stress path evolution following the wetting path. Also, the present work does not deal with the cycles of wetting-drying processes.

### 2.8.3 Modeling of coupled flow and deformation problem

In the original Barcelona Basic Model, the mechanical model is defined in terms of net stresses and consequently there is no direct coupling between the hydraulic and mechanical model (Gens et al., 2006). In other words, the BBM can not be used as a solution of coupled flow and deformation problem. Additionally, the model can not predict the unsaturated soil behavior under undrained (constant water content) loading condition (Wheeler, 1996) because under the undrained conditions the variation of suction is not externally specified but is determined by the requirement that the water content remains constant. The original elastoplastic stress-strain frame work (Alonso et al., 1990) was not consistent with the concept of work-conjugate proposed by Houlsby (1997). According to work input to an unsaturated soil (Houlsby, 1997), each stress variable introduced within the constitutive framework must be work conjugate with the increment of a corresponding strain variable. More precisely, if a mechanical constitutive stress variable (e.g., net stress in Class I model) and a capillary stress variable (e.g., soil suction in Class II model) are introduced in constitutive model, they should be related respectively to a mechanical strain variable and a capillary strain variable. To overcome this issue, the indirect coupling is introduced by introducing the soil water retention model to feature the description of soil suction and degree of saturation relationship ( $s - S_r$ ), commonly known as soil water characteristics curve (SWCC) or soil water retention curve (SWRC).

The classical models provide a unique relationship between soil suction and normalized water content/volumetric water content/degree of saturation based on some curve fitting parameters, which are linked with pore size distribution (Brooks & Corey, 1964; Van Genuchten, 1980; Fredlund & Xing, 1994). The mentioned classical soil water retention models are capable to capture the dependency of degree of saturation on suction for non-deformable soils or pore size distribution remains constant during wetting or drying path.

The void ratio dependent water retention models have been proposed by relating the air entry suction with the initial dry density of soil (Huang et al., 1998; Vanapalli et al., 1999; Ng & Pang, 2000; Kawai et al., 2000; Karube & Kawai, 2001; Gallipoli, Wheeler & Karstunen, 2003; Assouline, 2006; Nuth & Laloui, 2008; Tarantino, 2009; Sheng & Zhou, 2011; Gallipoli, 2012). For instance, Gallipoli, Wheeler & Karstunen (2003) and Gallipoli (2012) proposed a void-ratio dependent hysteric WRC model by incorporating a power function of the void ratio in the van Genuchten model. Summarizing the above-mentioned void ratio based WRC models, the dependency of air-entry value on the void ratio implicitly describe the role of microstructure on the hydraulic properties. The fabric

developed during compaction is evolutionary along the repository relevant loading paths and should be accounted to describe the water retention behavior of compacted bentonite-based materials.

To incorporate the microstructural characteristics, several water retention models have been proposed (Simms & Yanful, 2004; Romero et al., 2011; Hu et al., 2013; Romero & Vaunat, 2014; Dieudonne et al., 2017). Simms & Yanful (2004) proposed a method to develop the water retention model from the pore size distribution data. Romero et al. (2011) and Della Vecchia et al. (2015) provided a comprehensive picture of the evolution of the aggregated fabric along the hydraulic and mechanical paths. Dieudonne et al. (2017) proposed a water retention model for compacted bentonite-based material. The proposed model considers different water retention mechanisms in each structural levels, namely adsorption in the intra-aggregate pore space and capillarity in the inter-aggregate pores.

## 2.9 Summary

The physico-chemical properties of bentonite-based material govern its macroscopic response during the hydration process. The knowledge of these properties is necessary when dealing with the application of compacted bentonite-based materials in the engineered barrier system (EBS) in nuclear waste repositories. The effective bentonite density governs the final swelling pressure in a compacted bentonite-sand mixture. Hence, the mixture composition and the degree of compaction should be optimized according to the design swelling pressure values in axial and lateral direction. The mixture should be optimized in such a way that it exhibits the sufficient swelling potential to fill all the technical voids and constructional gaps, at the same time it should be lower than the in-situ stresses in the host rock and the compressive strength of the waste canister.

For investigating the soil subjected to repository-relevant boundary conditions, several full-scale and reduced-scale experimental investigations have been reported in past. In the reduced-scale experimental investigations, several column-type tests have been conducted for investigating the behavior of an unsaturated bentonite-based material subjected to repository-relevant thermal and hydraulic gradients. The reported studies revealed various aspects of the coupled thermo-hydro-mechanical (THM) behavior of bentonite-based materials in the context of engineered barriers for radioactive waste emplacement. For instance, the effect of an applied thermal/hydraulic gradient on the moisture distribution and resulting volumetric deformations/swelling behavior of buffer and backfill material

have been highlighted. In the reported studies, the swelling pressure was usually measured at the low temperature end, whereas the water content, volumetric, and chemical properties of the tested materials were determined after termination of the tests. However, several aspects should be explored further for assessing the long-term behavior of engineered barrier system. For instance, the effect of an applied thermal and hydraulic gradient on the transient state of material, soil water retention behavior in the transient state and the effect of hydration-induced heterogeneities on the swelling pressure dynamics in both axial and lateral directions. Therefore, an understanding of these aspects requires measurements of the axial total stresses at both ends, the lateral stress, and simultaneous measurements of the water content and relative humidity, which were not performed in the previous studies.

Regarding the modeling of coupled flow and deformation problems in bentonite-based materials, the indirect coupling is introduced by incorporating the soil water retention models to features the description of soil suction and degree of saturation relationship in the existing elastoplastic constitutive models such as the Barcelona Basic Model. In case of reproducing the mechanical behavior of expansive soils, several modifications were suggested in the original formulations of the BBM proposed by Alonso et al. (1990). In this regard, the ability of BBM with its extensions to reproduce the swelling behavior of compacted bentonite-sand mixture upon water saturation, and the influence of water retention model on the simulation results should be explored using the experimental results.



## **3 Material and methods**

### **3.1 General**

The bentonite-based materials are proposed to be used as a hydraulic barrier in the waste disposal projects due to having favorable engineering properties such as low hydraulic conductivity, high swelling potential, good radionuclide retention properties etc. From the design point of view, these engineering properties should be maintained within a desired range during the entire service life for ensuring a long-term safety. For instance, the swelling pressure of the backfill material should not exceed the in-situ stresses and the compressive strength of canister material, at the same time it should be high enough to seal the available preferential flow paths for providing the mechanical support to waste canister and other system components.

The primary selection of bentonite is based on the amount of montmorillonite, nature of exchangeable cation and the geochemistry of in-situ ground water. In most of the commercially available bentonite (e.g., MX-80, Wyoming bentonite etc.), the montmorillonite content is more than 60 %. The mixing ratio of other foreign materials such as sand/graphite/crushed host rock with the bentonite mainly depends upon the site-specific conditions and the required swelling pressure. In the present study, the investigated material is a Calcigel bentonite and quartz sand mixture with equal dry mass proportions. The Calcigel is a commercially available calcium-type bentonite mined in the Southern Germany. This chapter provides an overview of material geotechnical, physicochemical and compaction characteristics and discusses the test methods, which are used in this study.

### **3.2 Basic Geotechnical properties**

The preliminary investigations pertaining to the geotechnical characterization of the proposed mixture of Calcigel bentonite and sand were performed. The grain size analysis

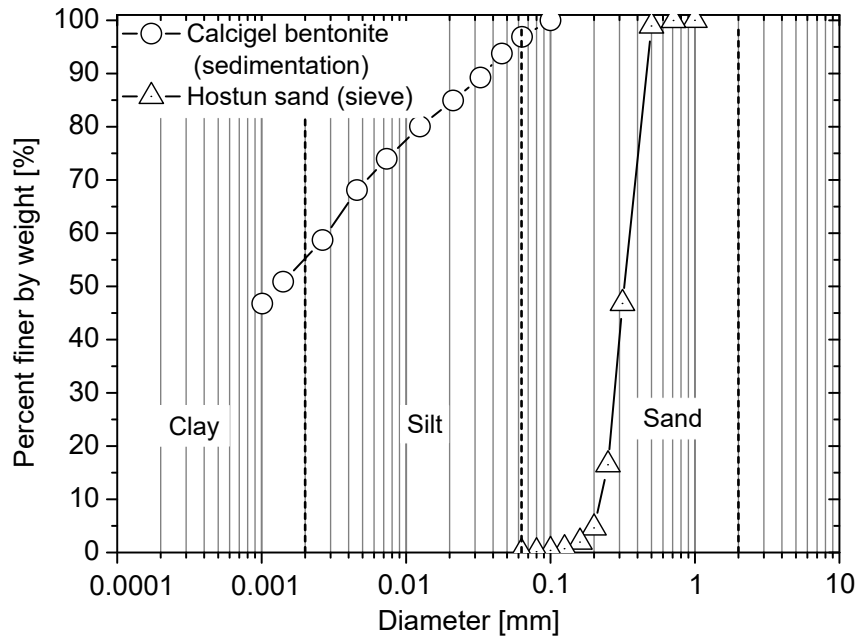


Figure 3.1: Grain size distribution curves of the Calcigel bentonite and sand (Lang, 2019).

was performed using the sedimentation method (ASTM-D3977, 1997) and sieve method (ASTM-D422, 2007) for the Calcigel bentonite and sand, respectively. The grain size distribution curves of Calcigel bentonite and sand are presented in Figure 3.1. The specific gravity of Calcigel bentonite (2.80) and sand (2.65) was determined using the pycnometer method (ASTM-D854, 2002). The Atterberg's limits (i.e., liquid limit, plastic limit and shrinkage limit) were determined according to ASTM-D4318 (2000). The liquid limit, plastic limit and plastic index of Calcigel bentonite were found to be equal to 119, 45 and 74 %, respectively, while, bentonite-sand mixture (50:50) have a liquid limit of 62 %, plastic limit of 26 % and plastic index of 36 %.

### 3.3 Physico-chemical properties

#### 3.3.1 Specific surface area

The specific surface area in clays plays a decisive role in the material swelling behavior. The total specific surface area of Calcigel bentonite was measured by ethylene glycol monoethyl ether (EGME) method (Cerato & Lutenegger, 2002). The measured total specific surface area was equal to  $436 \text{ m}^2/\text{g}$  for the Calcigel bentonite and  $0.3 \text{ m}^2/\text{g}$  for

the sand. Baille (2014) reported the external specific surface area of the Calcigel bentonite close to  $66 \text{ m}^2/\text{g}$  and  $0.25 \text{ m}^2/\text{g}$  for sand using the Brunette-Emmett-Teller  $\text{N}_2$  Adsorption (BET) method (Brunauer et al., 1938).

### 3.3.2 Cation Exchange Capacity (CEC)

The data regarding the cation exchange capacity (CEC) of Calcigel bentonite having similar mineral constituents were collected from the relevant studies (Madsen, 1998; Herbert & Moog, 2002; Steudel & Emmerich, 2013; Baille, 2014). The CEC of Calcigel bentonite reported by Madsen (1998) was determined by the ammonium acetate method at  $\text{pH} = 7$  and was equal to  $62 \text{ cmol}(+)/\text{kg}$  with  $\text{Na}^+$  ( $1.8 \text{ cmol}(+)/\text{kg}$ ),  $\text{K}^+$  ( $0.2 \text{ cmol}(+)/\text{kg}$ ),  $\text{Mg}^{2+}$  ( $22.4 \text{ cmol}(+)/\text{kg}$ ) and  $\text{Ca}^{2+}$  ( $37.6 \text{ cmol}(+)/\text{kg}$ ).

Herbert & Moog (2002) measured the CEC of the bentonite used in this study via Ammonium Acetate method and the reported value was equal to  $49 \text{ meq}/100\text{g}$ . The cation exchange capacity including the type and amount of cations was determined utilizing the Cu-Triethylene tetramine method (Meier & Kahr, 1999) with a weighted sample of 0.08 and 0.12 g. Additionally, the CEC values were determined by the Silver-Thiourea method with calcite saturation (Pleysier & Juo, 1980; Dohrmann, 1997).

Additionally, the CEC reported by Steudel & Emmerich (2013) was measured with the Cu-Triethylene tetramine method (Lorenz, 1999), which was equal to  $63 \text{ cmol}(+)/\text{kg}$  with  $\text{Na}^+$  ( $8 \text{ cmol}(+)/\text{kg}$ ),  $\text{K}^+$  ( $2 \text{ cmol}(+)/\text{kg}$ ),  $\text{Mg}^{2+}$  ( $21 \text{ cmol}(+)/\text{kg}$ ) and  $\text{Ca}^{2+}$  ( $44 \text{ cmol}(+)/\text{kg}$ ). The value of CEC determined by Baille (2014) was  $64 \text{ cmol}(+)/\text{kg}$  with  $\text{Na}^+$  ( $3 \text{ cmol}(+)/\text{kg}$ ),  $\text{K}^+$  ( $2 \text{ cmol}(+)/\text{kg}$ ),  $\text{Mg}^{2+}$  ( $21 \text{ cmol}(+)/\text{kg}$ ) and  $\text{Ca}^{2+}$  ( $50 \text{ cmol}(+)/\text{kg}$ ).

### 3.3.3 Mineralogy and chemical composition

The data pertaining to the mineralogical and chemical composition were supplied by the manufacturing company Süd-Chemie AG, Moosburg, Germany. The reported mineral constituents were compared with the reported data in the literature (Madsen, 1998; Agus, 2005; Steudel & Emmerich, 2013; Baille, 2014) (see Table 3.1).

Baille (2014) performed X-ray diffraction (XRD) and infrared spectroscopy (IR) to determine the mineralogy of the Calcigel bentonite and compared the results based on the detection limits for specific minerals using these two methods. Müller-Vonmoos et al. (1990) investigated the mineralogy of Montigel (earlier name of Calcigel) using X-ray diffraction

Table 3.1: Comparison of mineral constituents of Calcigel bentonites.

Mineral constituents	Content [%]				
	Madsen (1998)	Agus (2005)	Steudel and Emmerich (2013)	Baille (2014)	This study
Montmorillonite	66.3	50-60	63.5	78	60-70
Quartz	8	5-10	5.9	4	6-9
Feldspar	2-4	5-8	-	-	1-4
Kaolinite	-	-	3.8	2	1-2
Illite	-	-	13.7	8	-
Mica	12-15	-	-	-	1-6
Calcite	3.8	1-5	3.3	3.5	2-4
Dolomite		10-15	7.3	3	1-3
Others	2-3	2-29	2.5	1.5	3

technique and found that the bentonite consisted of 66% montmorillonite, 8.3% quartz, 3.8% carbonate, 12-15% muscovite, 2-4% feldspar, 2% kaolinite and some other minerals. Quartz sand used mainly consisted of more than 95% quartz. The mineralogical data (Müller-Vonmoos et al., 1990) show a good agreement with the data reported by Baille (2014).

### 3.4 Compaction characteristics

The swelling potential of the compacted bentonite-based materials primarily depends upon the initial dry density and water content. In this regards, the initial dry density of 1.8 Mg/m<sup>3</sup> with 6 to 9 % initial water content was suggested for the compacted bentonite-sand bricks as a backfill material according to the German reference concept for the disposal of low or intermediate level waste (LILWs) and high level waste (HLWs) (Rothfuchs et al., 2005; Jobmann et al., 2015, 2017). To achieve the desired mixture dry density within the prescribed range, the mixture compaction characteristics were determined.

#### 3.4.1 Standard and modified Proctor compaction characteristics

The standard and modified Proctor compaction curves of bentonite-sand mixture (50:50) were determined as per the procedure described by ASTM-D698 (2007) for the standard

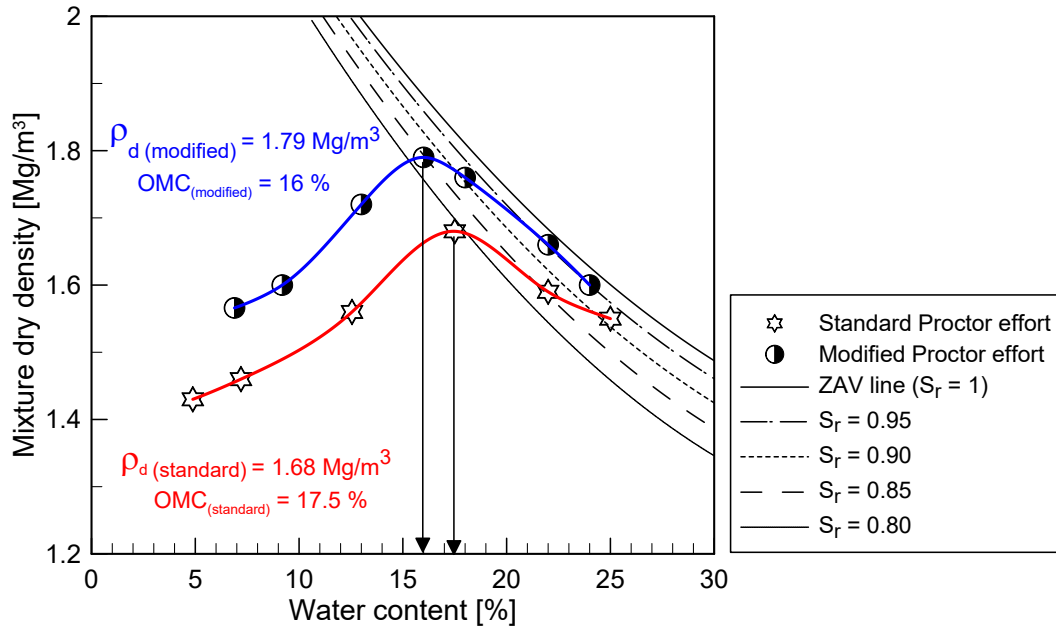


Figure 3.2: Standard and modified Proctor compaction curve of Calcigel bentonite-sand mixture with equal dry mass proportion.

and ASTM-D1557 (2007) for the modified compaction effort. The standard and modified Proctor compaction curves of the Calcigel bentonite-sand mixture are shown in Figure 3.2. According to the standard Proctor compaction method, the optimum water content was close to 17.5 % with the maximum dry density close to 1.68 Mg/m<sup>3</sup>. In the modified Proctor compaction method, the optimum water content was close to 16 % with the maximum dry density close to 1.79 Mg/m<sup>3</sup>. As the achieved mixture dry density values in the standard and modified Proctor compaction methods (i.e., 1.69 and 1.79 Mg/m<sup>3</sup>, respectively) were lower than the targeted mixture dry density (i.e., 1.8 Mg/m<sup>3</sup> at 6 to 9 % initial water content), the static uniaxial compaction method was used to achieve the desired mixture dry density. In this regard, uniaxial static compaction characteristics curves were obtained for the mixture.

### 3.4.2 Static uniaxial compaction curves

The uniaxial static compaction characteristics of Calcigel bentonite-sand mixture were obtained at 6 % and 9 % mixture initial water content. To investigate the effect of the applied lubrication, the compaction curves were obtained for three cases, namely (a) without lubricant, (b) with the Teflon spray, and (c) with the brass foil between

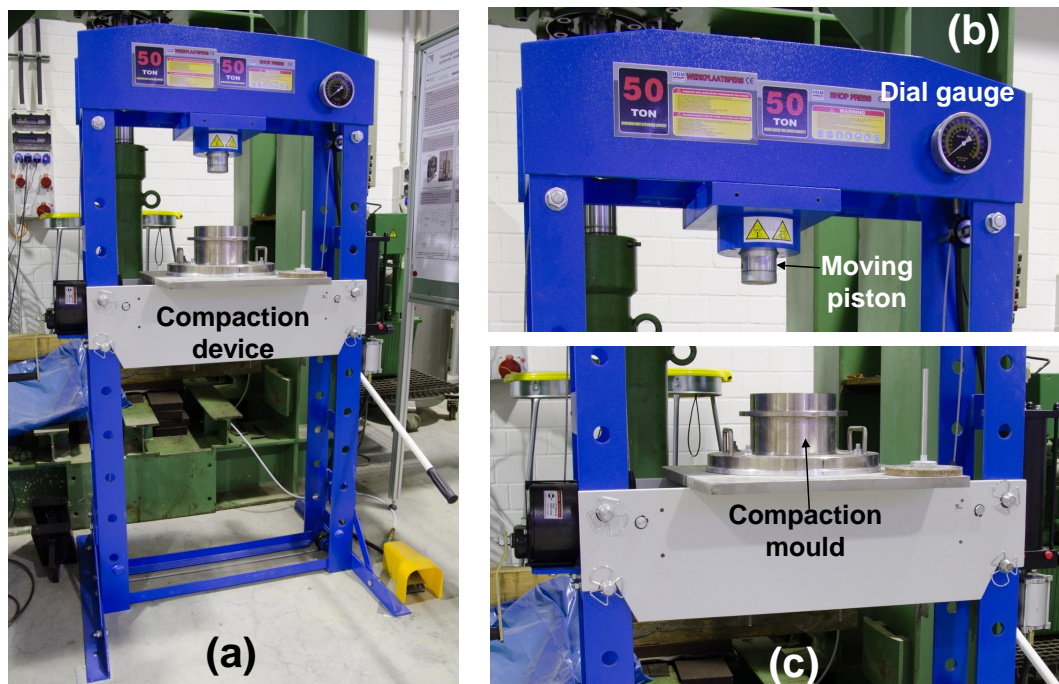


Figure 3.3: Uniaxial static compaction device and compaction mould.

the compaction mould and moist powder. The uniaxial static compaction device (i.e., hydraulic press) and the compaction mould is shown in Figure 3.3. The hydraulic press can be operated either manually or automatically by using the compressed air pressure. The compaction mould is made with the stainless steel with a removable base and the top collar. The mould has the internal diameter of 150 mm and 150 mm height including the height of collar (50 mm).

To obtain the uniaxial static compaction curves, the mixture of Calcigel bentonite sand having equal dry mass fraction were prepared with 6 % and 9 % initial moisture content. It should be noted here that the hygroscopic water content of Calcigel powder under the laboratory climatic conditions (relative humidity = 56 % and temperature = 22 °C) was approximately 9 %. Hence, the mixture with 9 % initial water content was prepared by mixing the Calcigel powder (600 g) with sand (600 g) and the distilled water (54 g). On the other hand, the mixture with 6 % initial water content was prepared by mixing the Calcigel powder (600 g) with sand (600 g) and the distilled water (18 g). Prior to pouring the moist mixture in the compaction mould, the lubricant was applied on the inner surface of the mould and also on the top plate. Later, the moist mixture was poured in the mould and temped slightly under the self weight of top plate. Prior to apply the axial stress, the height of soil sample in the mould was measured with the Vernier caliper. During the

compaction process, the height of the compacted sample was measured by knowing the downward movement of the loading-piston.

The effect of initial water content and the choice of lubricant on the uniaxial compaction characteristics of the moist mixture is evident from Figures 3.4 and 3.5. The achieved density values (bulk, dry or effective bentonite density) were higher for the mixture having 9 % initial mixture water content as compared to 6 %. On the other hand, the application of brass foil between the moist-mixture and the mould enhanced the compaction characteristics in both the cases. These results were obtained from the single layer compaction. In the field, normally the compaction process is performed in different layers to achieve a homogeneous density distribution with the desired dimensions of the compacted blocks. As the compaction in layers is not possible with the brass foil, the Teflon spray is selected as a lubricant during the compaction of compacted blocks. The initial water content of the mixture was selected as 9 %. It was further decided to compact the moist mixture in three layers at 30 MPa compaction stress in downward direction.

### **3.5 Method for producing the pre-compacted blocks**

For preparing the moist mixture, 2 kg of Calcigel powder (with 8-9 % hygroscopic water content) and 2 kg of oven-dried sand were weighed separately. To achieve the targeted mixture water content of 9 %, the required water volume was added to the oven-dried sand. After mixing the required water volume with the sand, the Calcigel powder was added to the wet-sand gradually and mixed properly. Later, the moist-mixture was kept in a sealed plastic bag and stored in an airtight container for at least 28 days to ensure a homogeneous moisture distribution. This procedure provides a small part of the lumps or scale in the mixture (2 % of total weight). During the compaction process, the surface of the compacted layer was scarified prior to place the next layer to ensure a proper homogeneous connection between the different layers. Once the compaction process was over, the compacted block was extruded from the mould.

During the extrusion of compacted blocks from the mould, their diameter slightly increased due to the relaxation of post-compaction residual stresses particularly in the lateral direction (see Fig. 3.6). The diameter increased to 153.6 and 152.8 mm for 6 % and 9 % initial water content, respectively. Under the applied vertical stress, the lateral stress develops during the compaction process. The magnitude of lateral stress mainly depends upon the inter-facial friction between the inner surface of mould and the moist-mixture

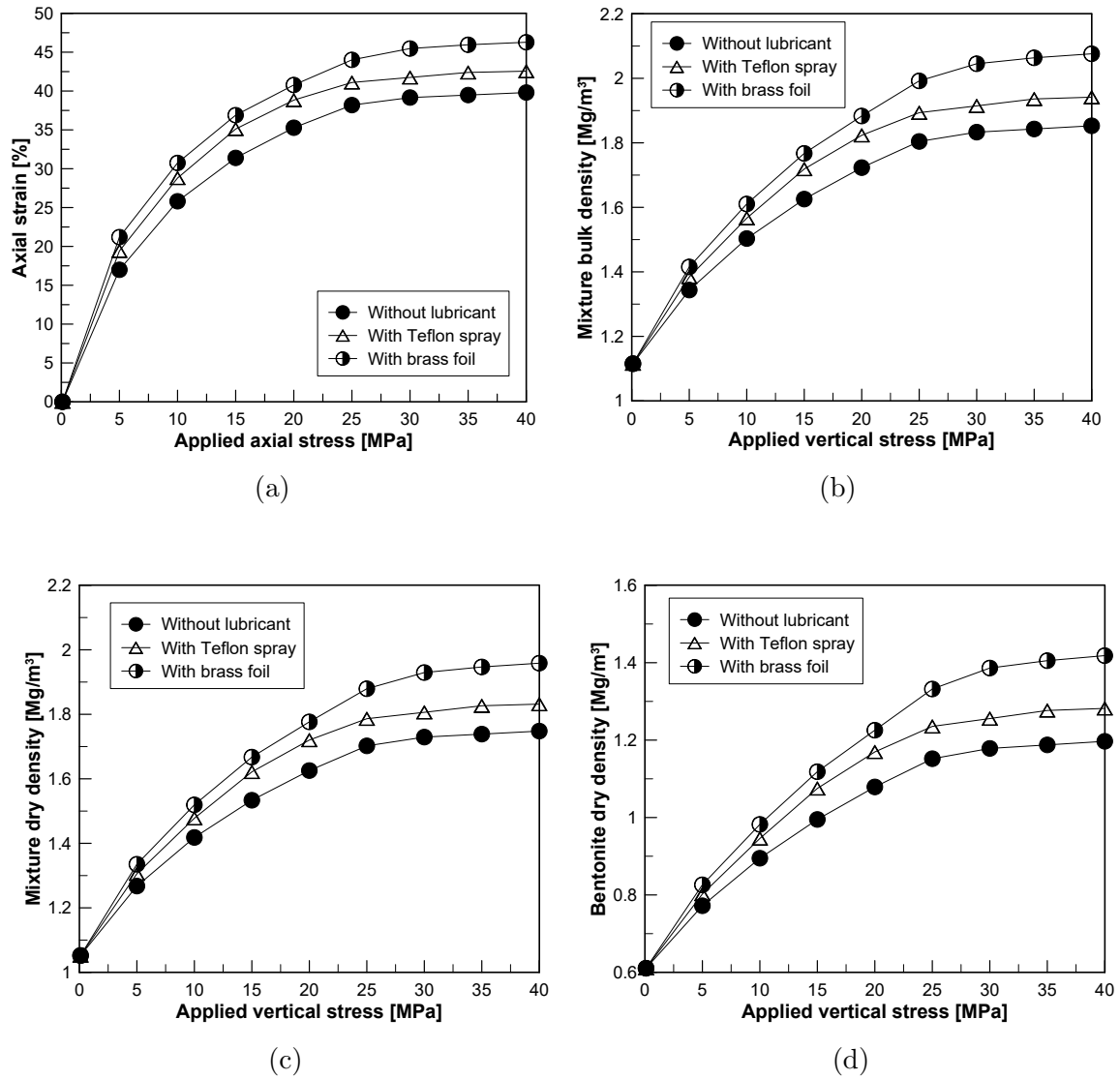


Figure 3.4: Uniaxial static compaction characteristics of Calcigel bentonite sand mixture with 6 % initial water content (a) applied vertical stress versus axial strain (b) applied stress versus mixture bulk density, (c) applied stress versus mixture dry density and (d) applied stress versus bentonite dry density in mixture.



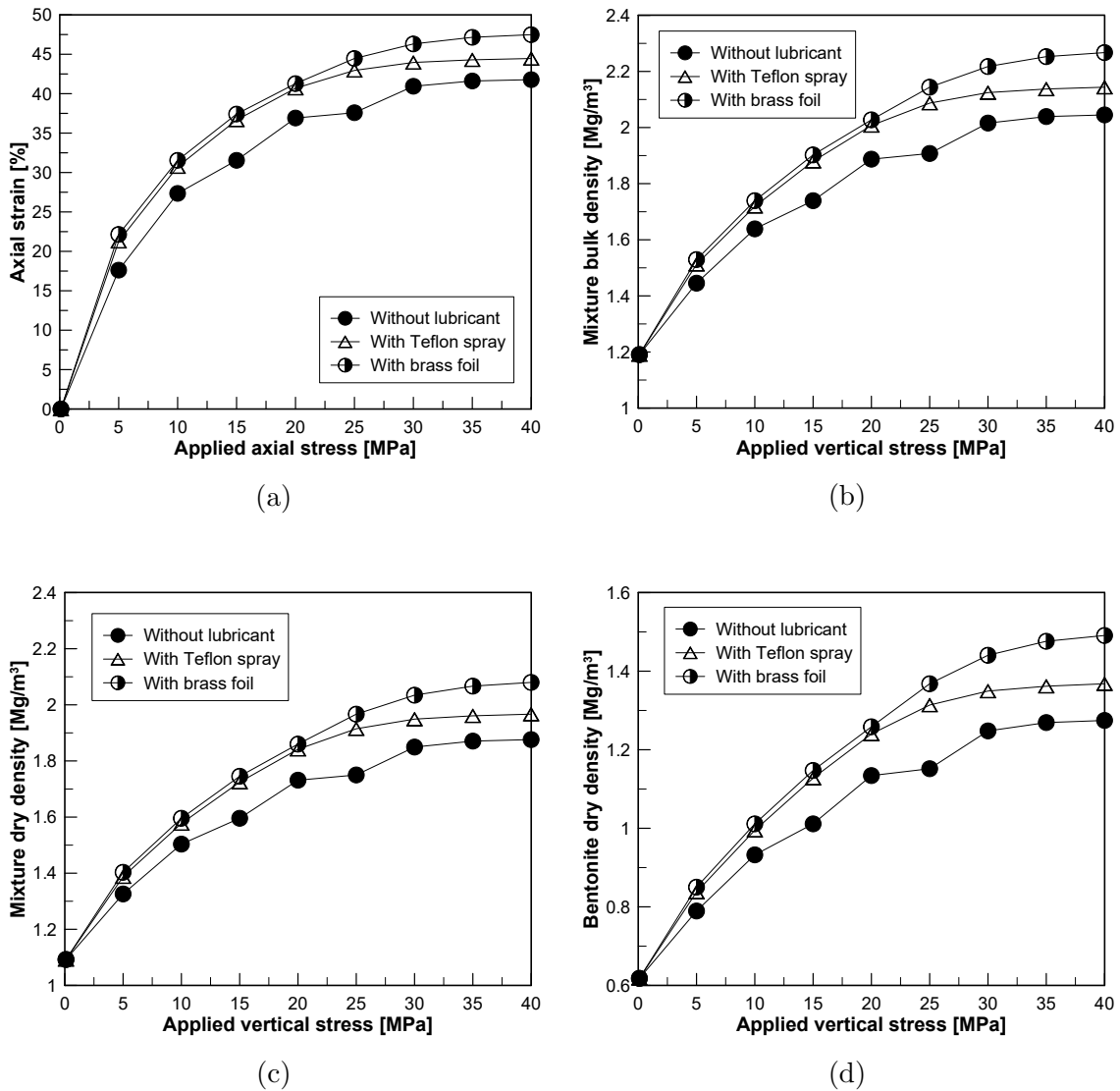


Figure 3.5: Uniaxial static compaction characteristics of Calcigel bentonite sand mixture with 9 % initial water content (a) applied vertical stress versus axial strain (b) applied stress versus mixture bulk density, (c) applied stress versus mixture dry density and (d) applied stress versus bentonite dry density in mixture.

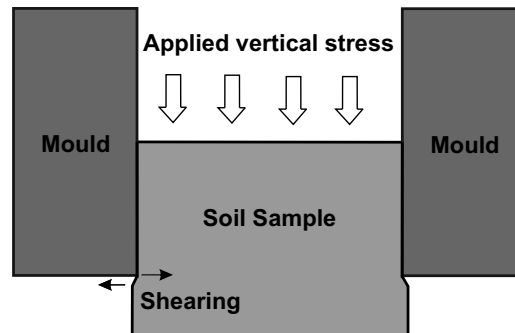


Figure 3.6: Schematic view: extrusion of compacted block from the mould and resulting shear stresses at the edges.

along with the lateral deformation of compacting mould. The compaction induced lateral stress affects the degree of compaction and the density distribution within the block. When the block is extruded from the mould, the lateral stress releases and the block swells and causes shearing stresses in the block at mould edges and may induce cracks or other constructional artifacts in the compacted blocks. Johannesson et al. (1995) indicated a strong influence of the friction between the sample and the walls of the mould on the homogeneity of the sample for compaction with the low water contents (10-11 %). The use of a lubricant (such as Molykote) minimized the friction. At 17-19 % water content, there was no significant difference in the void ratio with and without lubricant. It is recommended that the piston or top plate should also be lubricated to prevent sticking to the moist mixture.

To investigate the degree of homogeneity and the distribution of density within the compacted block, the extruded block was sliced in to three equal layers along the sample height. The height of each slice represents the individual compacted layer. The bulk density and water content were measured for the individual layer and the mixture global void ratio, dry density and effective bentonite dry density were calculated (see Fig. 3.7).

The effect of initial mixture water content and the applied lubrication on the density distribution is evident from Figure 3.7. The compacted block with 9 % initial moisture content showed more homogeneous density distribution as compared to 6 % initial water content. The maximum density was achieved in the bottom layer, while the middle layer exhibited the minimum density. In Figure 3.7, the uniform density values along the sample height were corresponding to the global density of sample inside the compaction mould. As mentioned earlier, the sample diameter increased to 153.6 and 152.8 mm for 6 % and 9 % initial water content, respectively during the extrusion process. So the density decreases

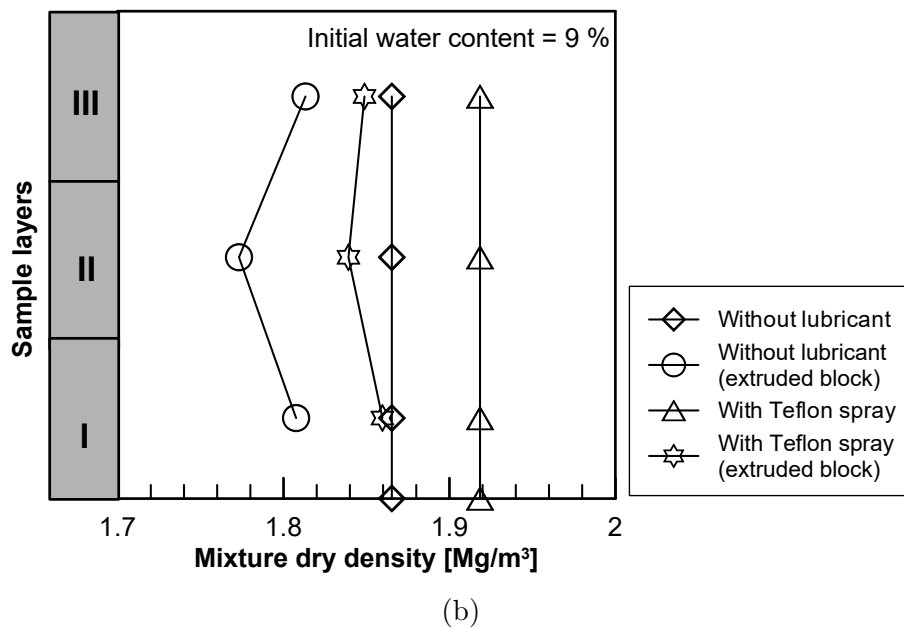
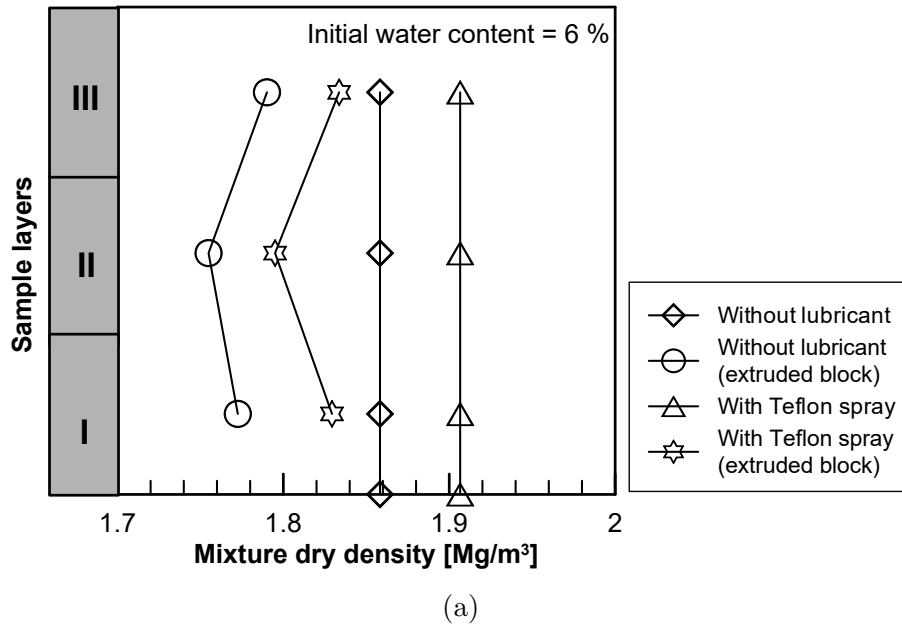


Figure 3.7: Compaction induced heterogeneity in the compacted Calcigel bentonite sand mixture (dry density distribution along the sample height), (a) with 6 % initial mixture water content and (b) with 9 % initial mixture water content.

accordingly. The relevant geotechnical and physicochemical properties of the investigated materials are summarized in Table 3.2 along with the compaction characteristics.

## 3.6 Experimental devices

The experimental work performed in the frame of present study can be categorized in to two subsections.

- Elementary/characterization tests,
- Small-scale water infiltration test using column-type experimental device.

Element/characterization tests were performed by Lang (2019) for identifying the model parameters for the numerical simulation of water infiltration test. In these element tests, the suction-controlled oedometer tests were performed to identify the Barcelona Basic Model parameters (Alonso et al., 1990). Additionally, the water retention tests under constant volume condition were also performed using the isochoric cell to identify the parameters for the van Genuchten (Van Genuchten, 1980) and Dieudonne (Dieudonne et al., 2017) water retention models. Hence, the description of experimental devices mainly includes the the high stress oedometer device and the isochoric cell (Lang, 2019).

### 3.6.1 High-pressure oedometer device

The high-pressure oedometer device is designed for investigating the compressibility behavior of soil in both saturated and unsaturated states at high stress levels (upto 40 MPa). A schematic of the high pressure oedometer device with the design details and a photograph of the test set-up are shown in Figure 3.8. A thick stainless steel base (no. 3) houses a porous stainless steel plate (no. 7) and the bottom water chamber (no. 19). The central part of the device (no. 2) holds a thick-walled specimen ring of height 20 mm and 50 mm in diameter (no. 4) that accommodates a compacted sample (no. 5), and a pressure pad with a porous stainless steel plate (no. 6). The top part carries the loading piston (no. 10) attached with a force transducer (no. 8). The force transducer used in this study had a maximum loading capacity of 50 kN with a precision of 0.001 kN. A strain gauge (no. 9) with a precision of 0.001 mm and a total run of 25 mm was connected directly to the loading piston to record the vertical deformation. The bottom and central part are connected with the help of heavy screws (no. 17), whereas the top part is directly screwed onto the central part. The force transducer together with the

Table 3.2: Properties of Calcigel bentonite, sand and bentonite-sand mixture (50:50).

Properties	Value
<b>Calcigel bentonite</b>	
Specific gravity	2.8
Liquid limit [%]	119
Plastic limit [%]	45
Plasticity index [%]	74
Cation exchange capacity, Ca <sup>+2</sup> as a predominant exchangeable cations [meq/100g]	37.6
Monmorillonite content [%]	60-70
Specific surface area [m <sup>2</sup> /g] by BET	66
Specific surface area [m <sup>2</sup> /g] by EGME	436
<b>Sand</b>	
Specific gravity	2.65
D10 [mm]	0.20
D30 [mm]	0.26
D60 [mm]	0.32
<b>Sand-bentonite mixture (50:50)</b>	
Specific gravity [-]	2.725
Liquid limit [%]	62
Plastic limit [%]	26
Plasticity index [%]	36
Optimum water content (SPT) [%]	18
Maximum dry density (SPT) [Mg/m <sup>3</sup> ]	1.68
Optimum water content (MPT) [%]	16
Maximum dry density (MPT) [Mg/m <sup>3</sup> ]	1.79
Dry density with uniaxial static compaction method [Mg/m <sup>3</sup> ]	1.80 - 1.85
Initial mixture water content of compacted block [%]	9

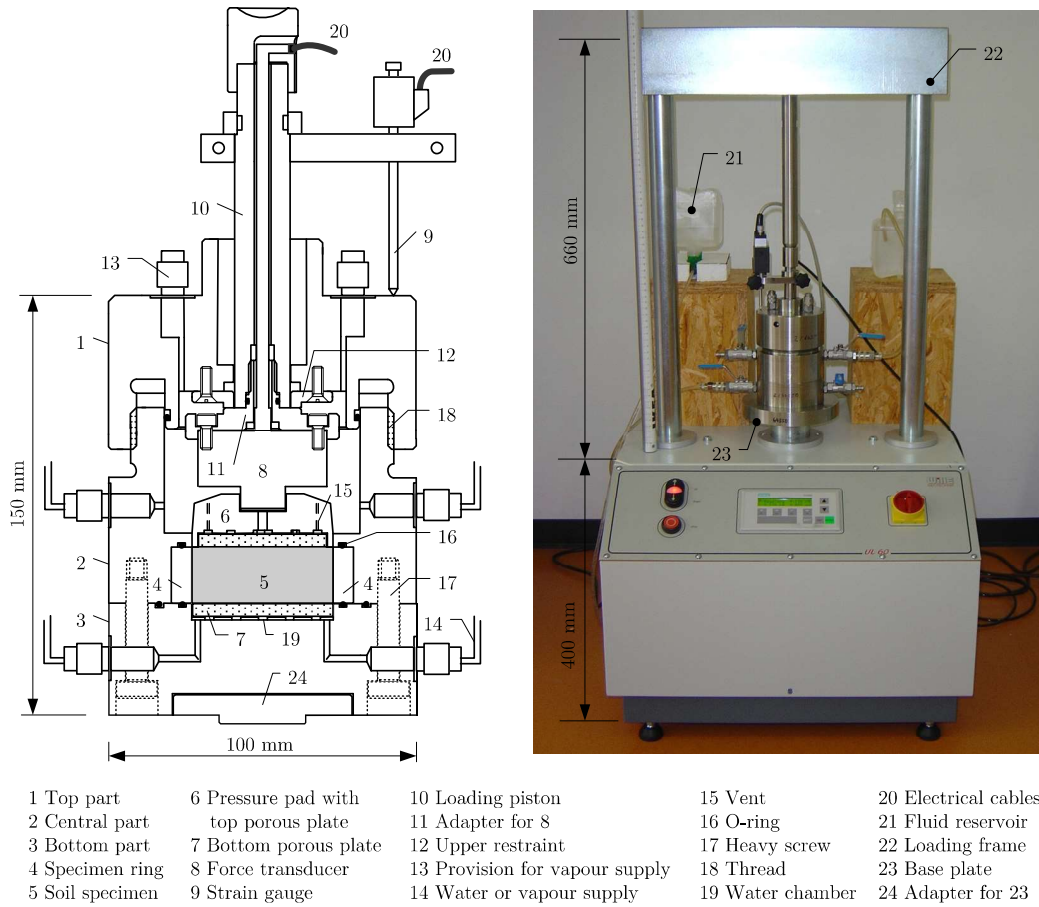


Figure 3.8: High pressure oedometer device with schematic of cell (left) and actual view of test set-up (right) (Baille, 2014).

loading piston becomes fixed between the pressure pad (no. 6) and the upper restraint (no. 12). The device was designed in such a way that upward vertical movement above the initial height of the specimen can be restricted, whereas the loading piston can move downwards. During the unloading process, height changes are restricted above the initial height of the specimen.

The measured deformations during any loading-unloading cycles included the deformation of the loading piston, the transducer, the oedometer cell, and the loading frame, and thus represent the total deformation of the system. Hence, prior to testing with compacted bentonite sand samples, the pressure-deformation characteristic of the oedometer was studied using a steel dummy (diameter = 50 mm; height = 15 mm) following the procedure suggested by ASTM D2435-96 (1996). The dummy together with dry filter papers and porous disks was subjected to loading-unloading paths. In addition, deformation

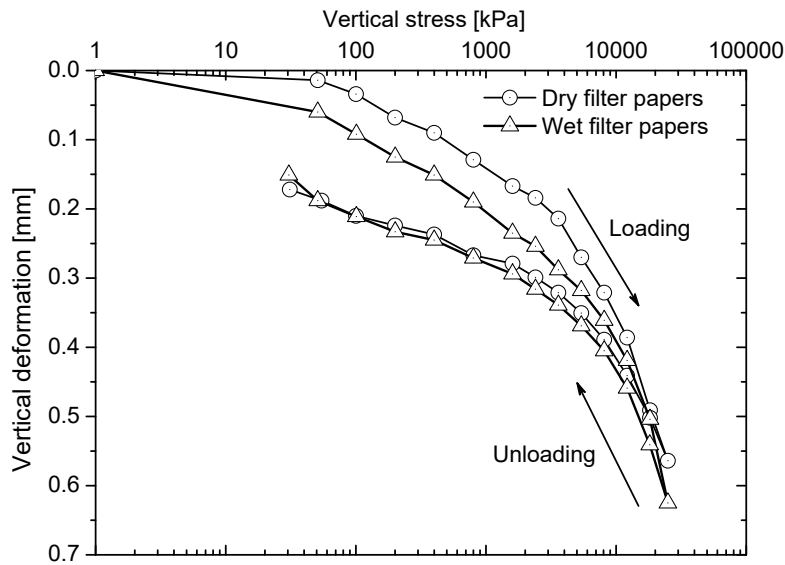


Figure 3.9: Deformation characteristics of the high stress oedometer device (Lang, 2019).

calibration with wet filter papers and porous disks was also performed. The deformation characteristics of the high stress oedometer device are presented in Figure 3.9.

### 3.6.2 UPC isochoric cell

The identification of model parameters to describe the soil water retention behavior requires the soil water retention tests under the constant volume condition. In this regard, the isochoric cell designed by the Technical University of Barcelona (UPC) was used in this study. Earlier, the cell was used to perform constant volume swelling pressure tests at room temperature (Villar, 2000; Agus, 2005). A schematic view of the isochoric cell, the design details and a photograph of the test set-up are shown in Figure 3.10.

The cell mainly consists of a bottom and top part, which are screwed together. The bottom part houses a coarse metal porous disc, which can be replaced with the the high air entry ceramic disk in case of using the device for suction controlled soil testing using the axis translation technique (ATT). The pedestal used for the ATT was designed to have a grooved water compartment where a high-air-entry ceramic disk is seated flushed and glued. The grooves are 3 mm wide and 1.5 mm deep and form a spiral. The ceramic disk used has an air-entry value of 1500 kPa. The top cap has a corrosion resistant metal porous disk. In case of using the vapour equilibrium technique (VET) to apply suction, the cell was equipped with an Erlenmeyer flask and an air pump to circulate water vapor through the specimen bottom and top boundaries. The top part contains

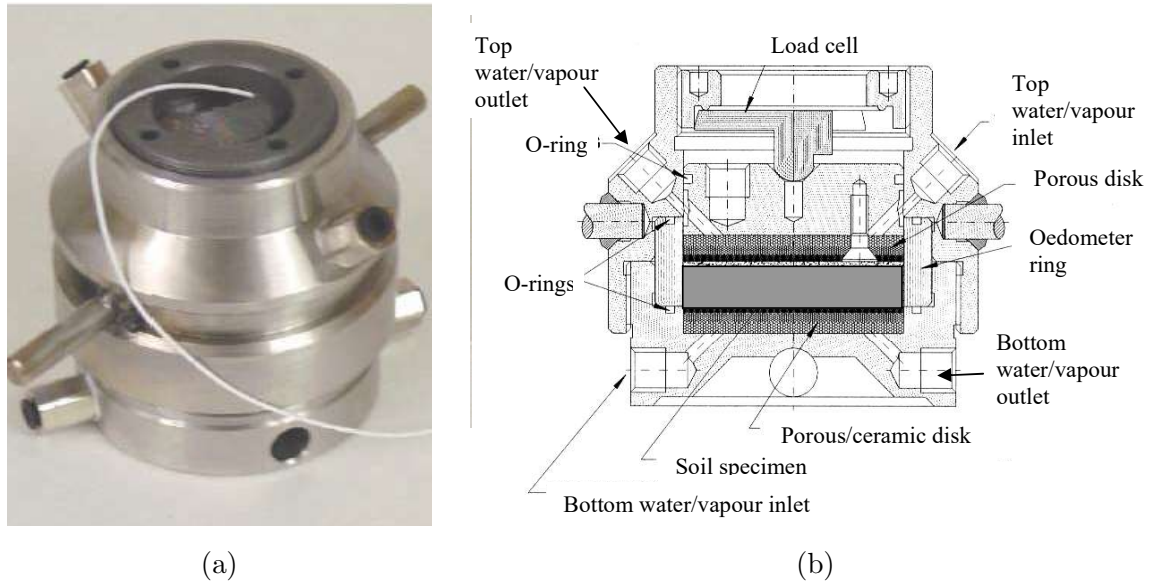


Figure 3.10: The isochoric cell, (a) actual view, (b) schematic view of design details and (c) different components of the cell (Agus, 2005)



the specimen ring, the upper porous disc, and the load cell. The bottom and top porous discs are connected to water/vapour supply. The load cell has a capacity of maximum 22 kN corresponding to about 11 MPa for the specimen diameter of 50 mm. It is screwed into the top part of the cell to ascertain the constant volume testing condition throughout the test and is connected to a readout unit. In the frame of present research work, the multistage wetting tests were conducted, where the as-compacted samples were hydrated by decreasing the soil suction in steps using the osmotic technique (OT).

## **3.7 Experimental techniques and methods**

### **3.7.1 Techniques for controlling and measuring the soil suction**

In element tests, various techniques for controlling and measuring the soil suction were used by Lang (2019). In the suction-controlled oedometer tests, the vapor equilibrium technique was used to control the suction of as-compacted sample. Additionally, the osmotic technique was used in the multistage wetting test using the isochoric cell. For the soil suction measurement, the chilled mirror technique was used in the present study.

#### **3.7.1.1 Vapour equilibrium technique**

The vapor equilibrium technique (VET) is used to control the soil total suction. Fundamentally, this technique controls or creates a desired relative humidity level using the saturated salt solution in a closed space (commonly, a desiccator) (see Fig. 3.11). The soil samples are kept in a desiccator, which is filled with the saturated salt solution. Under the constant temperature, these samples are allowed to attain equilibrium with the surrounding relative humidity, which is actually controlled by the saturated salt solution. Later, the applied total suction can be deduced from the relative humidity and temperature values using the Kelvin's equation.

The water transfer takes place in vapor form between the soil sample and the surrounding environment depending upon the imposed suction level. Hence, a change in the water content during the vapor transfer affects the capillarity as well as the ionic concentration of pore fluid. Since the water transfer from soils occurs in the vapor phase, the compositions of soils remain unchanged during a test. At the higher relative humidity level ( $\geq 98\%$ ), a minor temperature difference/fluctuation may lead to errors in the imposed suction levels. Agus & Schanz (2007) stated that the fluctuation of temperature of 0.5 °C at 850 kPa

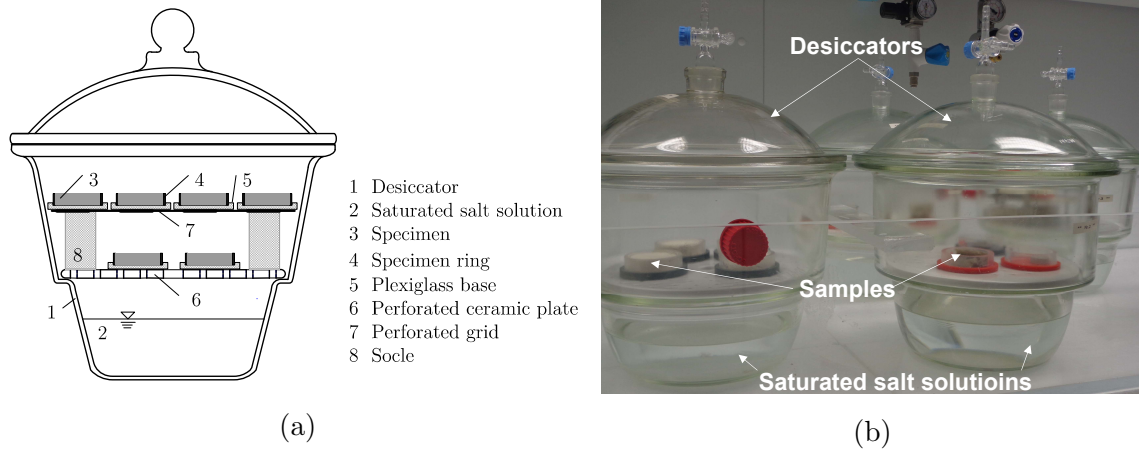


Figure 3.11: Vapor equilibrium technique for controlling the soil suction (a) schematic illustration and (b) application in the laboratory (Lang, 2019).

has an error of 30 %, whereas at a suction of 2 MPa the error would be reduced to 10 % for the same temperature variation.

The salt solutions which are commonly used in the vapor equilibrium technique are presented in Table 3.3 along with the range of applied soil total suction as per ASTM-E104 (2007). The relative humidity of the saturated salt solutions were also monitored with chilled mirror hygroscope or Aqualab (Leong et al., 2003). In general, a slight difference was observed with regard to the prescribed and actual soil total suction. As the Chilled mirror technique measures relative humidity within a precision of 0.1 % and therefore the applied range of soil suction was adopted according to the measured actual soil total suction with Aqualab. In the high pressure oedometer test, a bottle filled with saturated salt solution ( $K_2SO_4$  for 3.39 MPa or  $KNO_3$  for 10 MPa applied total suction) was connected to the oedometer device in a such a way that the sample can only interact with the vapor from the bottle during the test.

### 3.7.1.2 Osmotic technique

The osmotic technique for controlling the soil suction was introduced by Kassiff & Shalom (1971). In this method, the soil sample is placed in contact with a semi-permeable membrane behind which an aqueous solution of large sized molecules of polyethylene glycol (PEG) is circulated continuously in a closed cycle. The semi-permeable membrane does not allow large PEG molecules to pass, while the water can easily pass through the membrane. The PEG solution is continuously circulated in a closed circuit in such a way that

Table 3.3: Specifications of saturated salt solutions and the range of applied soil total suction (Lang, 2019).

Specification	Saturated salt solution and the applied soil total suction [MPa]								
	K <sub>2</sub> SO <sub>4</sub>	KNO <sub>3</sub>	KCl	NaCl	NaNO <sub>2</sub>	Mg(NO <sub>3</sub> ) <sub>2</sub>	MgCl <sub>2</sub>	LiCl	NaOH
ASTM <sup>§</sup>	3.1-4.5	8.2-10	22.9- 23.9	38.7- 39.1	-	86.8- 87.9	152.1- 153.8	-	-
Aqualab <sup>†</sup>	3.39	10	22.3	39.5	58	85.6	153.6	282	346

Notes: <sup>§</sup> determined based on the relative humidity at 25 °C which are given in ASTM-E104 (2007), <sup>†</sup> determined based on the relative humidity at 22.5 °C which are measured by the AquaLab-3TE chilled-mirror hygrometer in the present investigation.

the sample can absorb or release the water depending upon the available difference between the soil pore water and PEG solution. The water transfer between the soil sample and PEG separated by semi-permeable membrane is established until the difference in free energy between two sides dissipates. As the water transfer takes place in the liquid form, the technique essentially controls the soil matric suction. The value of matric suction applied depends on the concentration of PEG solution. The relationship between the PEG solution concentration and the osmotic pressure is used to calculate the applied matric suction. The applicability of osmotic technique for controlling the matric suction as high as 12.6 MPa has been proved by Delage et al. (1998).

The difficulty associated with the osmotic technique is that it requires a sophisticated means for circulating the PEG solution along boundaries of the specimen tested. The concentration of PEG solution used should also be monitored during experiment. Delage et al. (1998) reported that the use of osmotic technique for controlling the high matric suction (or high PEG concentration) required a special care as the PEG solution with a high concentration has a high viscosity. The equilibration time for suction equalization using this method is quite long and can be longer than 10 days (Cuisinier & Masrouri, 2004). Table 3.4 summarizes the specifications of PEG solutions and corresponding suction levels which are commonly used in the unsaturated soil testing.

In the water retention tests using the isochoric cell, PEG solution (molecular weight, MW = 20000) and the semi-permeable membrane (Spectra/Pro: molecular weight cut-off, MWCO = 1000) were used. The specifications of PEG concentration in water (g PEG/100 g H<sub>2</sub>O), which were used in the present study and the corresponding applied matric suction is shown in Table 3.4. The relationship between the mass ratio of PEG

Table 3.4: Specifications of PEG solution and the applied soil matric suction (Lang, 2019).

Osmotic method						
PEG [MW]	20000	20000	20000	20000	20000	20000
Membrane [MWCO]	1000	1000	1000	1000	1000	1000
Concentration [g PEG/100 g H <sub>2</sub> O]	5.22	9.53	16.5	30.2	52.2	96.3
Suction [MPa]	0.03	0.1	0.3	1	3	9

Notes: MW = molecular weight, MWCO = molecular weight cut off

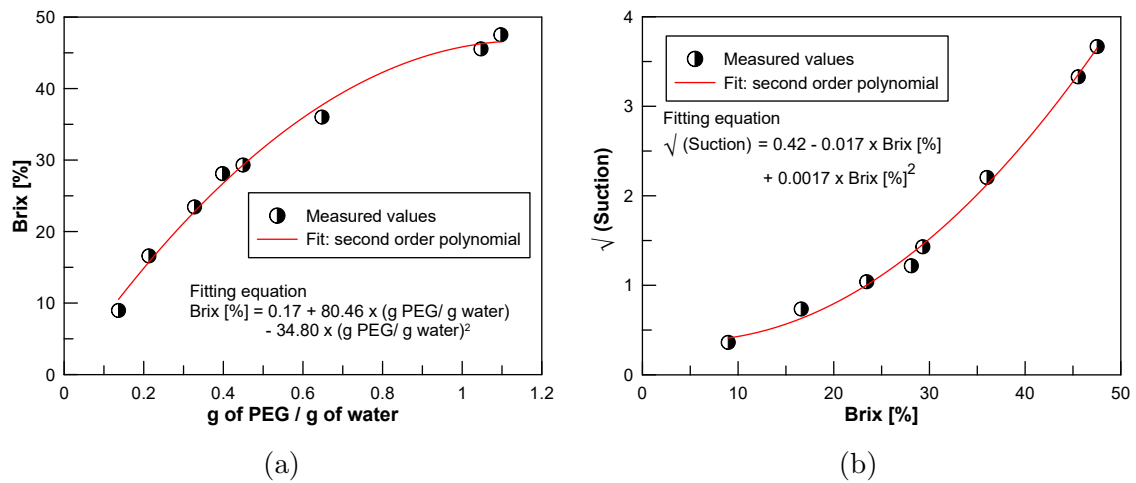


Figure 3.12: Relationship between mass ratio and Brix and between Brix and the applied soil matric suction for the PEG solutions used in this study (Lang, 2019).

to water (g of PEG /g of water), refraction index (brix) and the corresponding matric suction are presented in Figures 3.12a and 3.12b. For a given PEG concentration, it's Brix index and the corresponding matric suction can be determined by a refractometer and the chilled-mirror hygrometer, respectively. The determined Brix index values at pre-measured PEG concentrations were found to agree very well with the values reported by Delage et al. (1998) and Tripathy & Rees (2013).

### 3.7.1.3 Chilled-mirror hygrometer

The chilled-mirror hygrometer, which is also known as water activity meter (Aqualab-3TE) from the Decagon Devices Inc. (Fig. 3.13a) was used in this study to measure the soil total suction. The device measures relative humidity of soil specimen using the dew point technique. As compared to the other methods for soil total suction measurement, for instance the non-contact filter paper method and thermocouple psychrometry, dew point

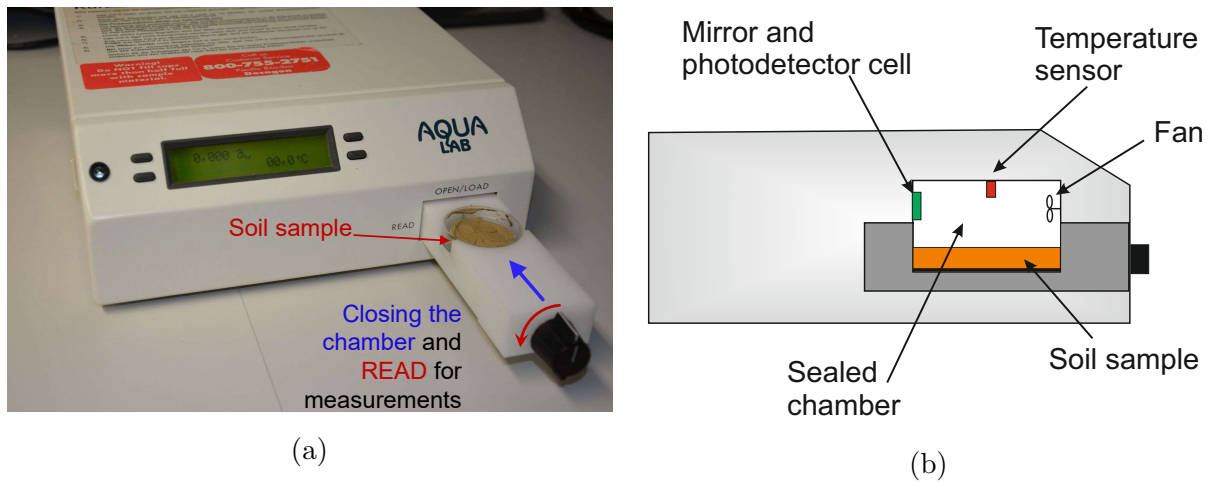


Figure 3.13: Chilled-mirror hygrometer used in this study (a) actual view and (b) schematic view.

technique provides a quick and reliable measurements over a wide suction range (Leong et al., 2003; Agus & Schanz, 2005). A schematic of the device is shown in Figure 3.13b.

For the measurement, the soil sample is enclosed in a sealed chamber and fills about half of the capacity of specimen container. The water vapor in the soil pores equilibrates with the air space above the soil sample inside the sealed chamber. A fan is installed inside the chamber which circulates air in order to reduce the equilibrium time. A mirror whose temperature is precisely controlled by a thermoelectric (Peltier) cooler is fixed inside the chamber. A beam of light, usually from a light-emitting diode (LED), is continuously directed onto the mirror. It is reflected by the mirror onto a photo-detector cell which is able to sense the change in reflectance intensity of the mirror due to condensation of water vapour on the surface of the mirror. The temperature at which condensation occurs (dew point) is maintained constant by a microprocessor circuit and measured by a thermocouple on the mirror. The dew point temperature is then related to the ambient relative humidity. The value of relative humidity and the corresponding temperature are displayed at the end of the measurement. Using the Kelvin's equation, the total suction can be calculated from the measured relative humidity and temperature values. The accuracy of the device (Aqualab-3TE) is in the order of  $\pm 0.3\%$  of relative humidity. The measurement range varies from a minimum relative humidity of  $3\%$  (i.e.,  $\psi_t = 450$  MPa) to  $99.9\%$  ( $\psi_t = 0.1$  MPa). However, the measurements at the higher relative humidity levels (i.e.,  $RH \geq 99\%$ ) are not stable (Lu & Likos, 2004).

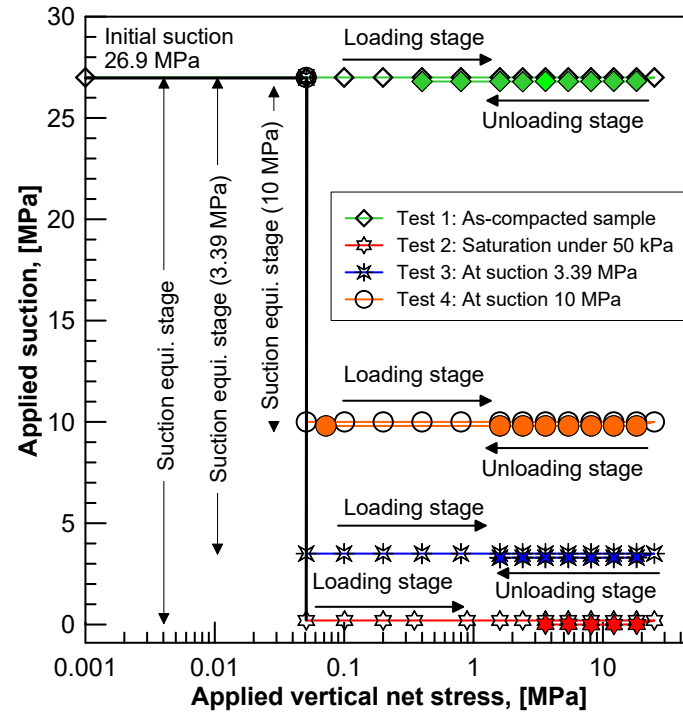


Figure 3.14: Stress paths for unsaturated oedometer tests on compacted sand-bentonite mixture

### 3.7.2 Suction-controlled oedometer tests

The suction-controlled oedometer tests were performed by Lang (2019) with the compacted samples of bentonite-sand mixture (50:50) using the high-pressure oedometer device. The sample initial conditions (i.e., dry density =  $1.80 \text{ Mg/m}^3$ ; water content = 9 %) were similar to the compacted blocks in the water infiltration test. Total four tests were performed with the high-pressure oedometer device, which allowed to perform the test at different suction levels. The samples (dia. = 50 mm; height = 15 mm) were prepared directly inside the oedometer ring using uniaxial static compaction method.

The tests were performed in two stages i.e., the suction-equilibrium stage and the one-dimensional compression-rebound stage (see Fig. 3.14). Prior to initiate the suction-equilibrium stage, the as-compacted samples were subjected to 50 kPa surcharge pressure. Later, the vapor equilibrium technique was used to impose the desired suction level (3.39 and 10 MPa) using the saturated salt solutions. During the suction-equilibrium stage, the vertical deformation of the samples were continuously monitored. Once the sample attained the desired suction level, the second stage i.e., one-dimensional compression-rebound was initiated. For the stress-deformation characteristics of the saturated sample, the distilled water was supplied from the bottom-end under 50 kPa surcharge load prior

to initiate the loading-unloading stage. For the test with as-compacted state, the sample was directly subjected to the one-dimensional compression-rebound stage.

According to the BBM Alonso et al. (1990), the yield surface corresponds to the saturated sample (i.e.,  $s = 0$ ) increases with an increase in soil suction. The rate of increase is represented by the loading-collapse curve, which is one of the fundamental characteristics of BBM. The loading-collapse curve changes its position when the sample undergoes plastic deformation. On the other hand, any combination of the net mean stress and soil suction in the  $(p - s)$  plane inside the elastic domain does not affect the position of loading-collapse curve (LC-curve). Hence, it is essential that the sample should remain in the elastic domain during the suction equilibrium-stage. In the present case, the sample was subjected to 50 kPa surcharge pressure and allowed to attain equilibrium at the imposed suction level (i.e., 3.39 or 10 MPa) under  $K_0$  condition (see Fig. 3.14).

During the saturation, the sample was allowed to swell in the axial direction. As the swelling was not prevented, the height of the sample increased during the saturation process under the applied surcharge pressure of 50 kPa. To ensure the soil stress state  $(p, s)$  with in the elastic domain during the saturation process, the applied surcharge pressure should be lower than the expected swelling pressure of the as-compacted sample during the saturation under constant volume condition. On the other hand, if the swelling is prevented at the global scale during the saturation, the stress path  $(p, s)$  may hit the yield surface in the  $(p - s)$  plane due to an increase in net mean stress and a decrease in the apparent preconsolidation stress during the saturation process. Figure 3.15 shows the test set-up for conducting the test with the saturated (see Fig. 3.15a) and unsaturated soil sample (see Fig. 3.15b).

The soil samples were directly compacted into a stainless steel sample ring using uniaxial static compression (diameter = 50 mm; height = 20 mm). The dimension of compacted samples was also checked by caliper after compaction. Simultaneously, water content and total suction of the mixture were measured by oven and chilled-mirror device, respectively. The equipments for preparing the samples for oedometer tests are shown in Figure 3.16. Sample initial conditions i.e. dry density ( $1.80 \text{ Mg/m}^3$ ), initial water content (9 %) and total suction (26.9 MPa) for as compacted samples were identical in all the tests. Once the oedometer tests were completed, the device was dismantled and total suction and water content of all the samples were determined. For dismantling the test set-up, a syringe was used to flush the bottom and top fluid reservoirs to minimize fluid uptake by samples during unloading. Afterwards, the sample was removed from the device for the soil total suction and water content measurements.

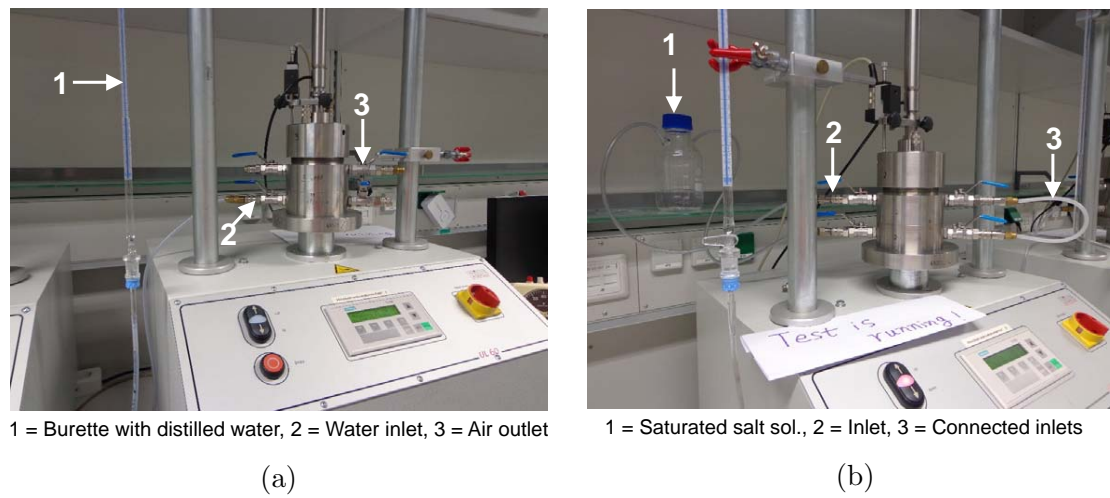


Figure 3.15: Test set-up for the suction-controlled oedometer tests on the compacted Calcigel bentonite sand mixture (a) saturated condition and (b) unsaturated condition (Lang, 2019).

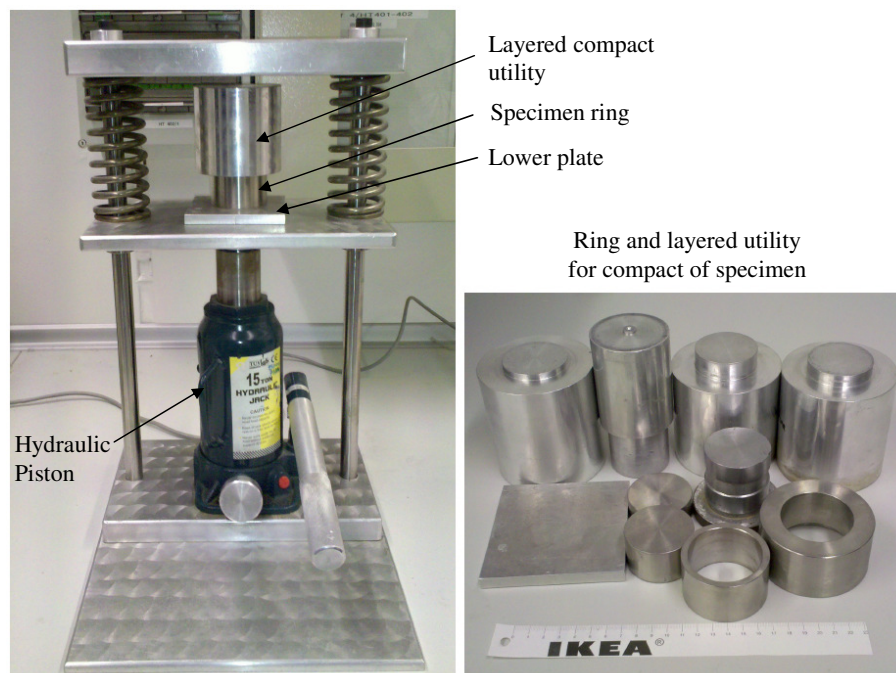


Figure 3.16: Equipments for preparing sample for element tests (Lang, 2019).



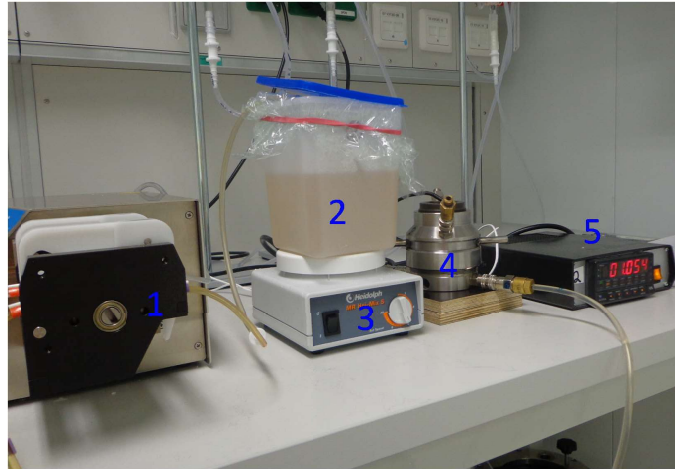


Figure 3.17: Experimental set-up for multistage wetting test with UPC isochoric cell using osmotic technique (legends: 1 = peristaltic pump, 2 = PEG solution, 3 = magnetic stirrer, 4 = isochoric cell, 5 = digital display for load cell reading) (Lang, 2019).

### 3.7.3 Water retention tests under constant volume condition

The water retention tests under the constant volume condition were performed using the isochoric cell by Lang (2019). The samples were compacted directly inside the cell ring (dia. = 50 mm; ht. = 15 mm). The sample initial conditions (i.e., dry density =  $1.80 \text{ Mg/m}^3$  and water content = 9 %) were kept similar to the sample conditions in the water infiltration test. The initial suction of the as-compacted sample (26.9 MPa) was measured with the chilled mirror technique.

The wetting process was initiated by reducing the soil suction in a stepwise manner using the osmotic technique. The schematic diagram of the experimental set-up is shown in Figure 3.17. In osmotic technique for controlling the soil matric suction, the polyethylene glycol (PEG) solution was circulated between the source (label 2) and the isochoric cell (label 4) using a peristaltic pump (label 1). The soil sample and the circulated polyethylene glycol (PEG) solution was separated by a semi-permeable membrane. A magnetic stirrer (label 3) was used to stir the PEG solution continuously. PEG solution with molecular weight (MW) of 20000 and the semipermeable membrane having molecular weight cut off (MWCO) of 1000 were used in this study. Table 3.5 presents the initial conditions of compacted bentonite-sand mixtures samples and applied suction during the tests. Samples were placed in the isochoric cell and subsequently wetted with the applied suctions of 11.45, 11.15, 3.78, 1.12, 0.55, 0.15 and 0.001 MPa. The swelling pressures during the tests were also recorded by a pressure reading unit with a readability of 0.001 kN. It was assumed that equilibrium established when the changes in the measured swelling pressure

Table 3.5: The initial conditions and the applied soil suction during the water retention tests with the Calcigel bentonite-sand mixture (50:50) under constant volume condition ( $\rho_d$  = sample initial dry density,  $w$  = initial water content,  $S_r$  = initial degree of saturation,  $\psi_t^*$  = applied total suction and  $\psi_t$  = initial total suction of soil sample).

Sample ID	Initial sample conditions				
	$\rho_d$ [Mg/m <sup>3</sup> ]	$w$ [%]	$S_r$ [%]	$\psi_t$ [MPa]	$\psi_t^*$ [MPa]
SB-1	1.80	9	48	26.9	0.001
SB-2	1.80	9	48	26.9	0.15
SB-3	1.80	9	48	26.9	0.55
SB-4	1.80	9	48	26.9	1.12
SB-5	1.80	9	48	26.9	3.78
SB-6	1.80	9	48	26.9	11.15
SB-7	1.80	9	48	26.9	11.45

less than 0.01 kN/day. Once the equilibrium was reached, tests were terminated and the samples were removed from the constant volume cell. Finally, the water content and total suction of each sample were measured. The water content measured and the corresponding applied suction were used to establish the wetting WRCs under the constant volume condition.

### 3.8 Summary

Based on the performed geotechnical investigations, Calcigel bentonite can be classified as highly plastic clay according to Unified Soil Classification system. The physicochemical investigations revealed that the total specific surface area of Calcigel bentonite is equal to 436 m<sup>2</sup>/g. The predominant exchangeable cation is Ca<sup>2+</sup> with 60-70 % montmorillonite content. The compaction characteristics of Calcigel bentonite sand mixture with equal dry mass proportions (50:50) were determined using the standard and modified Proctor (SP and MP) compaction methods. The achieved maximum dry density according to the standard and modified Proctor compaction were lower than the prescribed dry density for the compacted bentonite sand blocks as a backfill material as per the German reference concept for the disposal of low or intermediate level waste (LILWs) and the high level waste (HLWs). To achieve the desired mixture dry density, the uniaxial compaction method was used. The static uniaxial compaction characteristics were obtained for the investigated

---

mixture at two different initial water contents (i.e., 6 % and 9 %) with three different lubricants. The desired mixture dry density ( $1.80\text{-}1.85\text{ Mg/m}^3$  at 9 % water content) was achieved under the applied vertical stress of 30 MPa with the Teflon spray as a lubricant. The compaction induced heterogeneity in the compacted blocks were also investigated. It was observed that the density distribution was not uniform along the sample height as the measured values were lower in the middle layer as compared to first and third layer. The heterogeneous mixture dry density depends upon the mixture initial water content and the choice of lubricants. Additionally, the elementary test methods which are used in this study and techniques for measuring and controlling the suction are also discussed. In the next step, a new column-type experimental device is designed and implemented for testing the compacted Calcigel bentonite-sand mixture under thermal and hydraulic gradients.



# **4 Column-type experimental device: design, validation and implementation**

## **4.1 Introduction**

In the following chapter, the design details of the newly designed column-type experimental device are presented. System implementation and validation tests are discussed within the frame of repository-relevant soil testing conditions. In the context of underground storage of nuclear waste, a test is performed with the compacted Calcigel bentonite-sand mixture (50:50) to investigate the thermo-hydro-mechanical behavior of the material under an applied temperature gradient. Thereby, the test results are discussed in terms of temperature-driven processes in the unsaturated compacted soil sample. The interpretation of test data aims at the impact of water vapour release from the material at the opposite end of the heat source on the relative humidity and water content and the resulting changes in soil stiffness.

## **4.2 Column-type experimental device: design features**

The constructional details of the newly designed column-type experimental device are shown in Figure 4.1. The device is comprised of top and bottom plugs (items 1 and 5 in Fig. 2a), sample rings (items S1, S2, and S3 in Fig. 2a), and a confining cell (item 8). A rigid frame (item 9) provides the restraint along the axial direction. The stresses in the axial direction are measured using the load cells (items 6 and 7). The test set-up allows testing cylindrical soil samples (dia. = 150 mm and height = 300 mm) and provides three measurement sections located at various heights from the bottom of the sample, such as

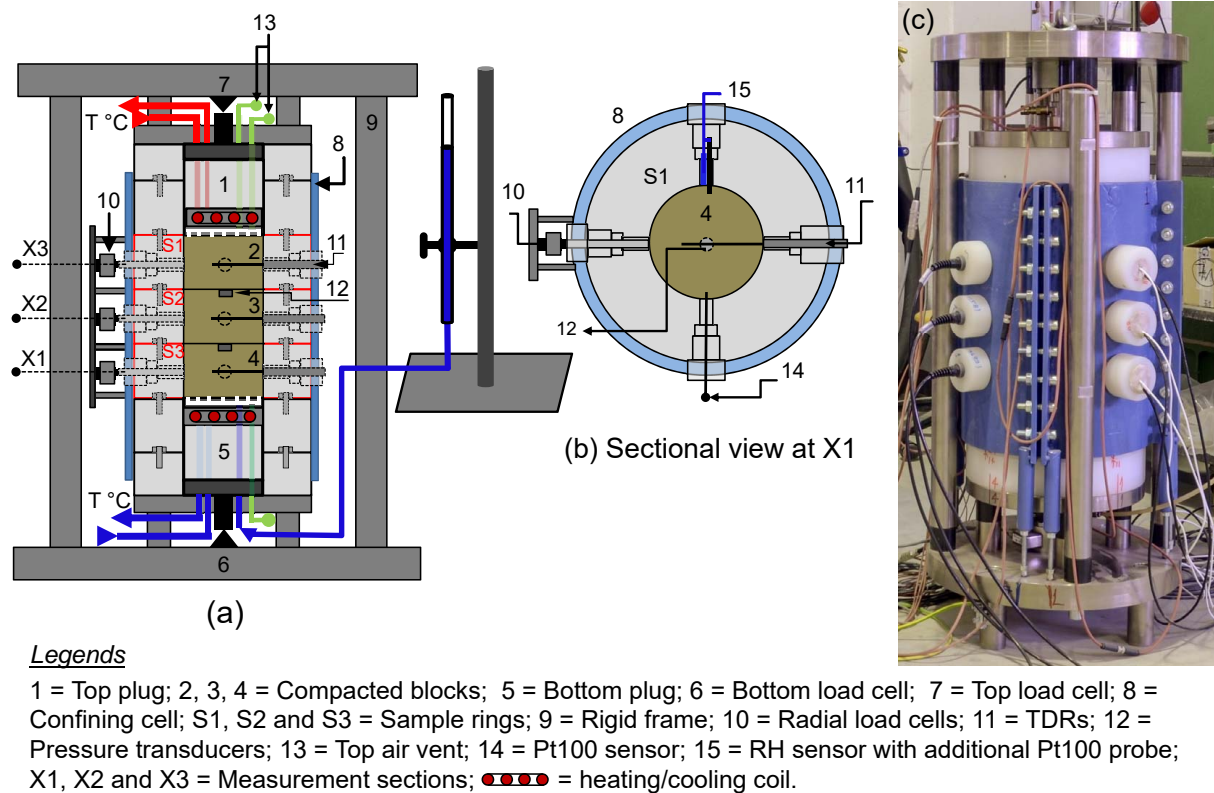


Figure 4.1: Constructional details of the newly designed column-type experimental set-up, (a) and (b) vertical and horizontal sectional views, and (c) a photograph of the device.

X1 (50 mm), X2 (150 mm), and X3 (250 mm) (Fig. 2a). The advantages of the used sensors and monitoring scheme are that, it

- provides the transient water content measurements at three measurement sections,
- facilitates the transient total stress measurements in both axial and lateral directions at various preselected locations, and
- provides the transient soil water retention profiles along the height of the soil sample.

### 4.2.1 Top and bottom plugs

The top and bottom plugs have similar constructional features for applying the thermal and hydraulic gradients along the height of soil sample. Figure 4.2 shows the design features of these plugs. For the mechanical stability and an adequate thermal isolation in the lateral direction, these plugs are encapsulated with Polyvinylidene fluoride (PVDF) rings (outer diameter = 350 mm; inner diameter = 150 mm) as depicted in Figure 4.2b. PVDF

is an opaque, semi-crystalline, thermoplastic fluoropolymer with an excellent chemical stability and a low thermal conductivity (0.13 W/m.K). The high permanent operating temperature up to 140 °C with practically no moisture absorption justifies its application in the long-term experimental investigations at the elevated temperature levels. PVDF is also a good electrical insulator, hence provides minimum disturbance to monitoring instrumentations and electronics.

The plug has a sintered stainless steel base (dia. = 150 mm and thickness = 10 mm) which is connected with water inlet and an air outlet (Fig. 4.2c). The water can be supplied externally to the sintered base via water hose. The plug also has a metallic chamber (dia. = 150 mm and thickness = 20 mm), which is integrated with the sintered stainless steel based. It accommodates the heating/cooling coil and relevant hosing connections for circulating the heating fluid between the chamber and an external thermostat. The heating/cooling temperature can be controlled by circulating the Silicon oil with the precision of 0.1 °C. Two separate thermostats are used for heating and cooling purpose separately. The relevant technical specifications are mentioned in Table 4.1. The cooling thermostat can control temperature in the range of 5 to 35 °C and the heating thermostat in the range of 20 to 95 °C. The integrated design of the metallic chamber with a porous base provide an adequate thermal equilibrium between the heating and hydration systems.

The top and bottom plugs also transfer the load to top and bottom load cells as depicted in Figure 4.2c. For instance, during the hydration under the confined condition, the expansive soil sample exhibits swelling phenomena and the resulting total stress is transferred to top/bottom load cells via these plugs. Some trial tests were conducted at room temperature and at 80 °C to investigate the effect of inter-facial friction between the plug and PVDF encapsulation rings on the load transfer function. The test set-up is shown in Figure 4.3. The volumetric thermal expansion of top/bottom boundary control units were measured and corresponding design changes were made to diminish the effect of temperature dependent inter-facial friction on load transfer function.

### 4.2.2 Sample rings

To accommodate the soil sample, three PVDF encapsulation rings/sample rings (outer dia. = 350 mm, inner dia. = 150 mm, and height = 100 mm) are used (i.e., S1, S2, and S3) (Fig. 4.4). For the low-density samples (dry density < 1.6 Mg/m<sup>3</sup>), the soil can be compacted directly inside the sample ring. For the high-density samples (dry density ≥ 1.6 Mg/m<sup>3</sup>), the compaction should be performed outside the sample ring. Later, the

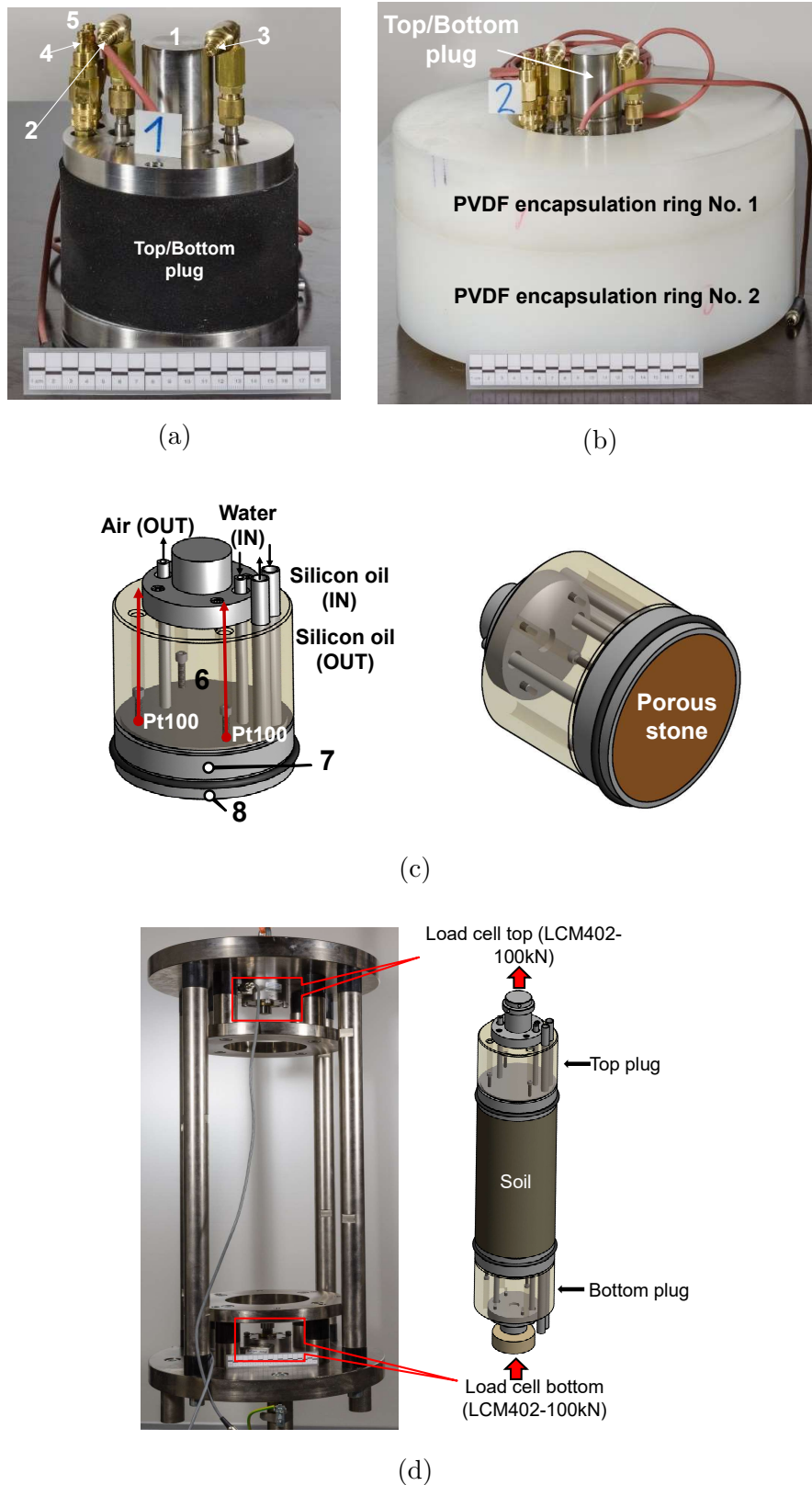
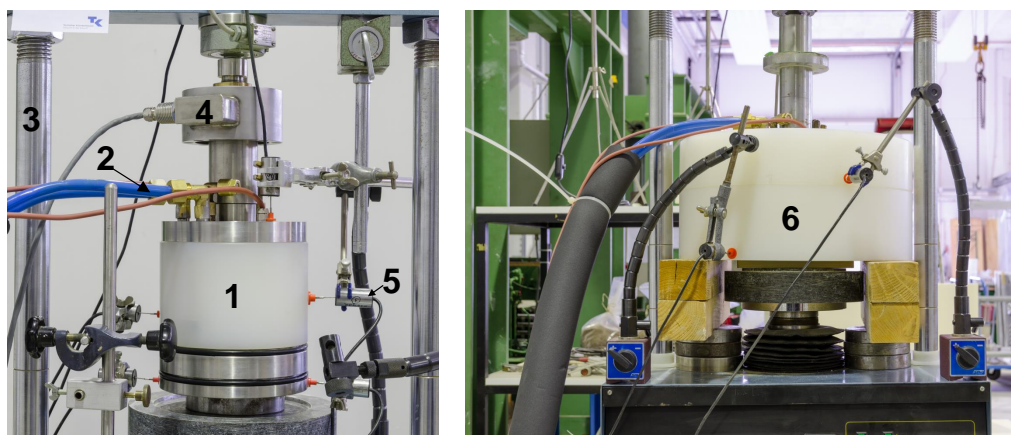


Figure 4.2: Constructional details of top/bottom plug, (a) actual view, (b) PVDF encapsulation rings, (c) schematic view and (d) load-transferring mechanism (legends: 1 = loading piston; 2, 3 = air outlet/water inlet; 4, 5 = for heating fluid circulation; 7 = metallic chamber and 8 = porous base).





Legends: 1 = Top/bottom plug; 2 = Heating oil supply; 3 = loading frame; 4 = load cell; 5 = deformation measurement with high precision LVDTs; 6 = PVDF encapsulation rings.

Figure 4.3: Test set-up for investigating the effect of inter-facial friction between the top/bottom plug and the encapsulation rings on the load transferring mechanism.

pre-compacted blocks can be installed inside the sample ring with the monitoring sensors. The PVDF sample rings assembly provide the mechanical stability, an adequate thermal insulation in the lateral direction, and accommodates the ports for the components of the monitoring sensors.

Each sample ring has four holes at the mid height, but radially positioned at an angle of  $90^\circ$  for installing the sensors that facilitate measuring temperature, relative humidity, water content, and lateral total stress (Figs. 4.4a and 4.4b). The sensors are installed with their respective PVDF adapters for minimizing the heat loss and any possible disturbances to the electronics of the sensors. The provision of O-ring connections along with tightening screws that are made of PVDF provide the air/water tight joints between two consecutive sample rings.

### 4.2.3 Stainless steel confining cell and rigid frame

A stainless-steel confining cell is used to provide the additional resistance against the outward lateral deformation of the sample rings during a test (Fig. 4.5a). It also facilitates the installation of lateral load cells at measurement sections X1, X2 and X3. A vertical stainless steel plate provides a restraint for the lateral load cells (Fig. 4.5b). The stiffness of the measuring system can be expected to be greater in the lateral direction than that in the axial direction, which in turn may influence the development of total stress during

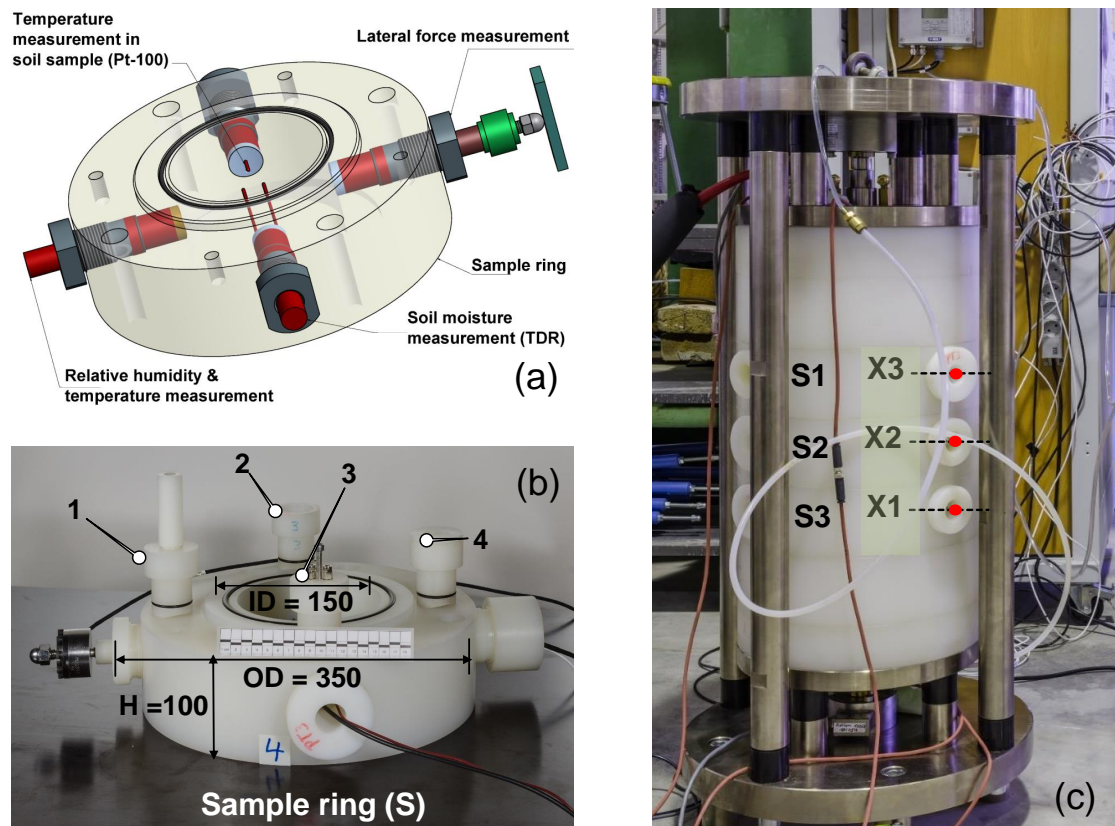


Figure 4.4: Constructional details of PVDF sample rings, (a) schematic view, (b) actual view with monitoring sensors (legend: 1 = lateral load cell, 2 = TDR based water content measurement sensor, 3 = Pt100 sensor and KYOWA pressure transducer and 4 = RH sensor) and (d) measurement sections (X1, X2 and X3).

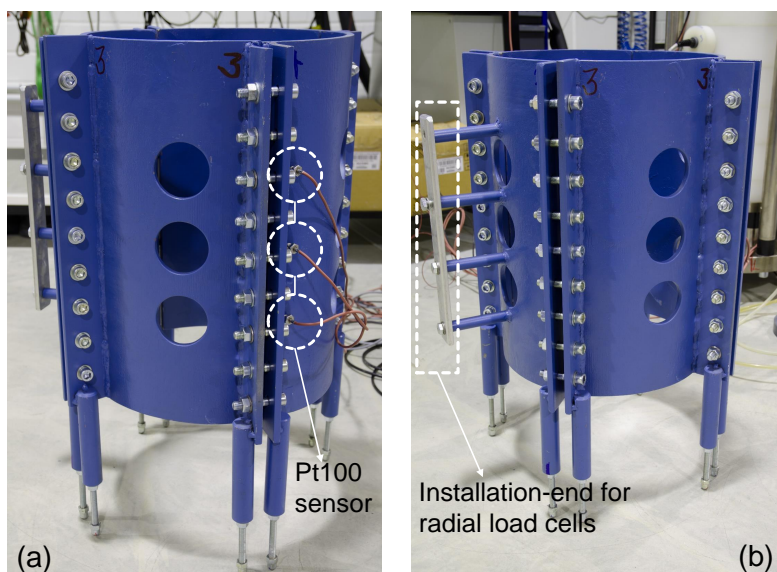


Figure 4.5: (a) Stainless steel confining cell and installation of Pt100 sensors and (b) installation of lateral load cell with confining cell

a test. To monitor the room temperature, three Pt100 sensors are installed at the outer surface of the confining cell.

#### 4.2.4 Sensors and monitoring instrumentations

The newly designed column-type experimental device facilitates the measurements of temperature, relative humidity, water content and stresses in both axial and lateral directions at various pre-selected locations. Sensors and the other monitoring instruments which are used for the measurement purpose are shown in Figure 4.6. The installation details, operating range and accuracy of these sensors are presented in Table 4.1. The accuracies of the relative humidity and water content sensors are expected to affect the interpretation of test results, particularly so when the variations of these parameters are close to the accuracy limits of the sensors.

##### 4.2.4.1 Sensors for temperature measurements

A total of five Pt100 sensors (IP-68) are installed at various locations to monitor the temperature distribution in the experimental set-up (Fig. 4.7). The word IP means "Ingress Protection", IP-68 rated as "dust tight" and protected against complete, continuous submersion in water. Three Pt100 sensors are embedded inside the soil at the measurement

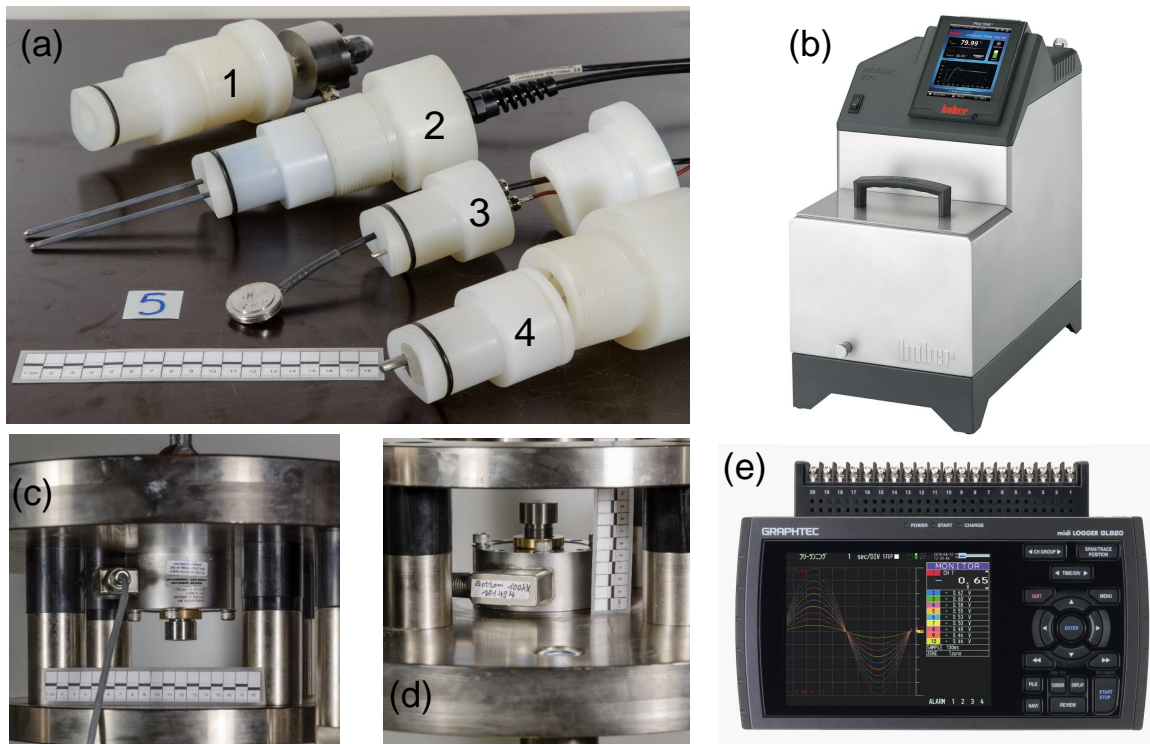


Figure 4.6: Sensors and monitoring instrumentations, (a) sensors with PVDF adapters (legend: 1 = lateral load cell, 2 = TDR sensor for water content measurement, 3 = Pt100 sensor with KYOWA pressure transducer and 4 = relative humidity sensor), (b) Huber external thermostat, (c) and (d) top and bottom load cells and (e) Graphtec GLS820 data logger.

Table 4.1: Details of the monitoring sensors and instruments used in the device.

Sensor type	Nos.	Installation remark	Operating range	Accuracy
Temperature (Pt100)	5	At sections X1, X2, and X3 (3 nos.), at top and bottom plugs (2 nos.); Sensor dia. = 3 mm, embedded length = 10 mm.	-40 to 200 °C	$(0.1 + 0.0015  t )^{\circ}C$
Relative humidity (VAISALA HMT337 with heating option)	3	In closed vapor chambers at sections X1, X2, and X3. Additional Pt100 probe embedded in the sample up to 10 mm.	0-100 % RH	$\pm(1.5 + 0.015 \times \text{reading}) \% \text{ RH}$
Water content (IMKO PICO-32)	3	At sections X1, X2, and X3.	0-100 %	$\pm 2\%$ for 0 – 40% and $\pm 3\%$ for 40 – 70%
Lateral stress (OMEGA Engg.: LCM-203)	3	At sections X1, X2, and X3.	5 kN	$\pm 0.3\%$ incl. non-linearity, hysteresis and repeatability
Axial stress (OMEGA Engg.: LCM-402)	2	At top and bottom ends	100 kN	same as above in lateral stress
Axial stress (KY-OWA BEC pressure transducer)	2	At the interfaces between blocks S1-S2, and S2-S3.	1 MPa	$\pm 0.03 \text{ MPa}$ (incl. nonlinearity and hysteresis) with additional $\pm 0.4\%/^{\circ}C$ due to T effect
Thermostats (Min-istat 230 and CC-202)	2	External units	Cooling = 5-35 °C and Heating = 20-95 °C	Temperature stability $\pm 0.02^{\circ}C/$
Data logger (Graphtech-820)	1	External unit	20 measurement channels	-

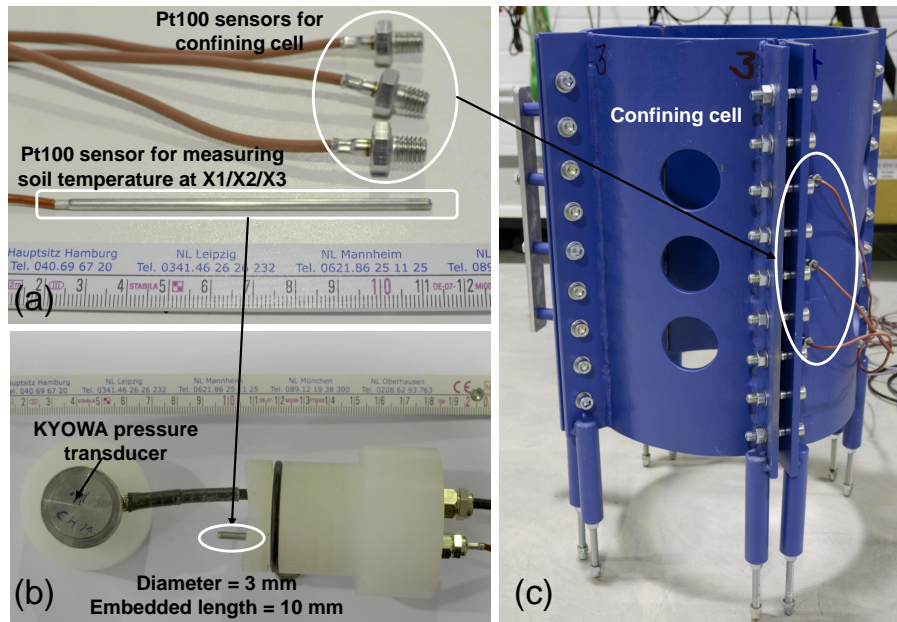


Figure 4.7: Sensors for measuring temperature, (a) Pt100 sensors for measuring the room temperature and for measuring soil temperature at sections X1, X2 and X3 and (c) installation of Pt100 sensors with confining cell.

sections X1, X2 and X3 (dia. = 3 mm and embedded depth = 10 mm). Sensor's adapter and connections are designed for reliable measurements even under adverse conditions such as high-temperature (up to 105 °C) and high relative humidity levels close to saturation. Two Pt100 sensors are installed in the metallic chamber to monitor the heating/cooling temperature. Additionally, three Pt100 sensors are installed at the outer confining cell to monitor room temperature during the test (Fig. 4.7). All the Pt-100 sensors were supplied with the calibration certificate.

#### 4.2.4.2 Sensors for total stress measurement

The newly designed experimental device provides the stress measurements in both axial and lateral directions. The top and bottom load cells (LCM-402 from Omega GmbH) are installed with the rigid frame to measure the axial stress. Additionally, two miniature pressure transducers (KYOWA BEC 1 MPa) are embedded in the soil to measure the axial stress between the compacted blocks. For measuring the lateral total stress, the miniature load cells (LCM-203 from Omega GmbH) are installed at the measurement sections X1, X2 and X3. Figure 4.8 presents the constructional details of installing the lateral load cells and KYOWA miniature pressure transducers.

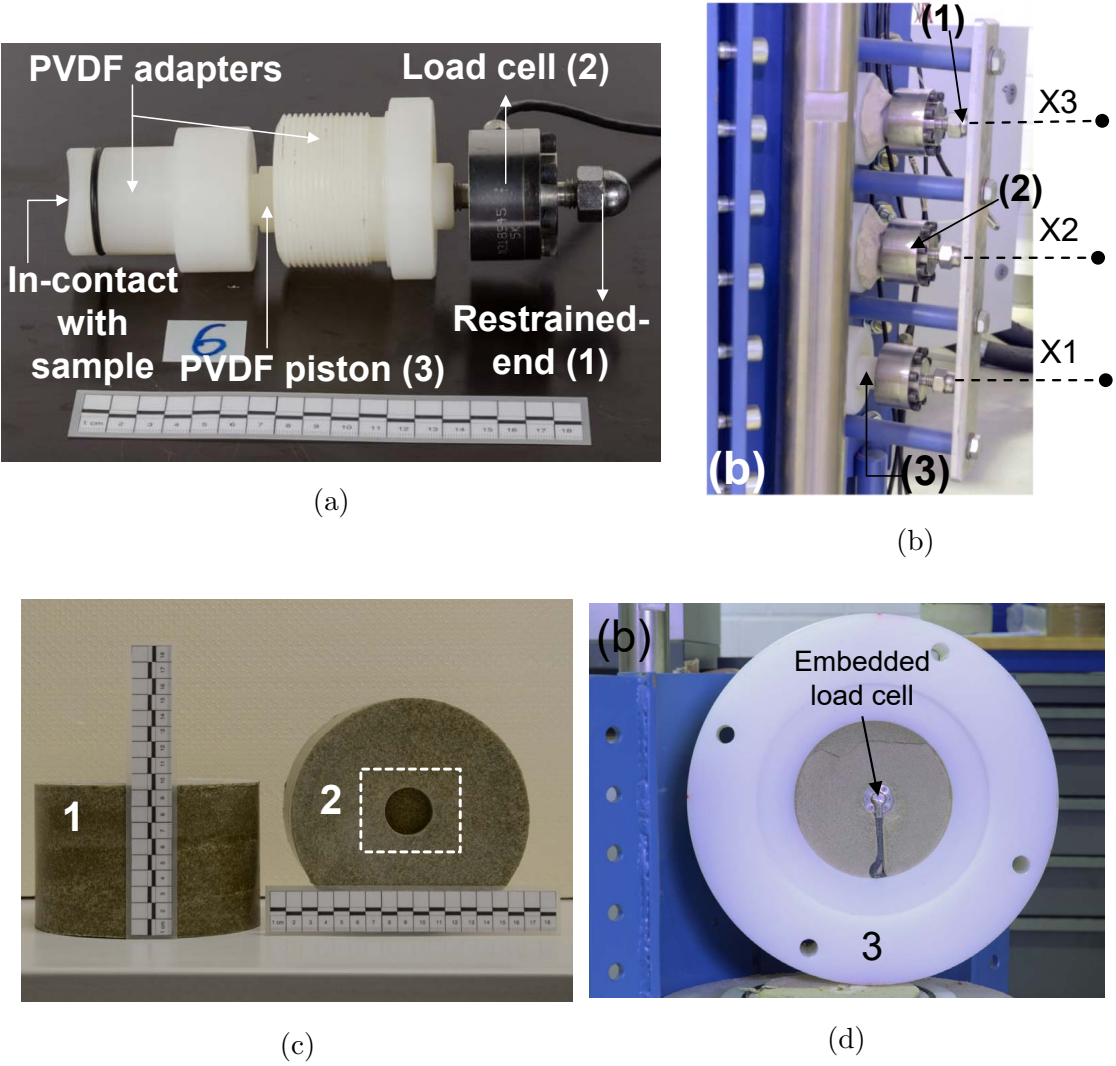


Figure 4.8: Lateral load cell installation details, (a) load cell along with accessories and (b) installation at measurement sections X1, X2 and X3 along the height of soil sample, (c) A photograph of compacted sand-bentonite mixture sample (for sample rings S1 or S2) showing seating space for a miniature pressure transducer (1-compact block, 2-seating space), and (b) pressure transducer installation in a compacted sample.

The technical details of lateral total stress measurement system is shown in Figure 4.8a. These load cells have low height and threaded bolts on both sides. One side of the load cell is restrained against the outer confining cell using a rigid steel plate. On the other hand, the opposite end is attached to load-transferring PVDF piston. This piston is kept in contact with the soil sample. During the hydration, sample exhibits swelling and pushes the piston against the restrained end (Fig. 4.8b). These miniature load cells and the axial load cells from Omega GmbH have a compensated temperature range of + 16 to 71 °C. The rated accuracy of these load cells including the nonlinearity, hysteresis and repeatability is  $\pm 0.3 \%$ .

The miniature pressure transducers (KYOWA BEC-1 MPa) have 3 cm overall diameter with 23 mm diameter of pressure-sensing area. These sensors are embedded in the soil at 100 and 200 mm as shown in Figure 4.8d. The reported safe temperature range is -10 to 60 °C with IP-67, which rated as "dust tight" and protected against immersion. The rated accuracy including nonlinearity and hysteresis at 24 °C is  $\pm 3 \%$  with an additional temperature effect on output ( $\pm 0.4 \%$  / °C).

#### 4.2.4.3 Sensors for water content measurement

The Time domain reflectometry (TDR) based sensors (see Fig. 4.9) are used for measuring the water content of the soil sample during a test. The sensor constitutes of two parallel wave guides or probes (dia. = 3.5 mm and length = 110 mm) made of stainless-steel and are coated with polyvinyl chloride (PVC) for water-proofing. For correct measurements of the water content, the entire length of the probes must be embedded in the soil sample. The wave guides are sensitive to deformation. In the device, the TDR sensors are installed with their respective PVDF adapters (see Fig. 4.9a). Figure 4.9b presents a schematic of a sample along with the positions of the TDR sensors. The rated accuracy of water content measuring sensors (IMKO PICO32) is  $\pm 2 \%$  for volumetric moisture range of 0 - 40 %. The temperature causes a drift of  $\pm 0.3 \%$ .

The TRIME-method (Time Domain Reflectometry with Intelligent Micromodule Elements) is a specially designed TDR-technique to measure the material moisture content. The measuring of the TDR-pulse is carried out by time measurements instead of voltage measurements. The TDR-curve is determined by time measurements at distinct voltage levels. No expensive electronic components, such as track-and-hold units and A/D converters are necessary. Time sampling requires a change of the common TDR-pulse shape of the conventional methods. The level of the reflected pulse must be raised. An increase



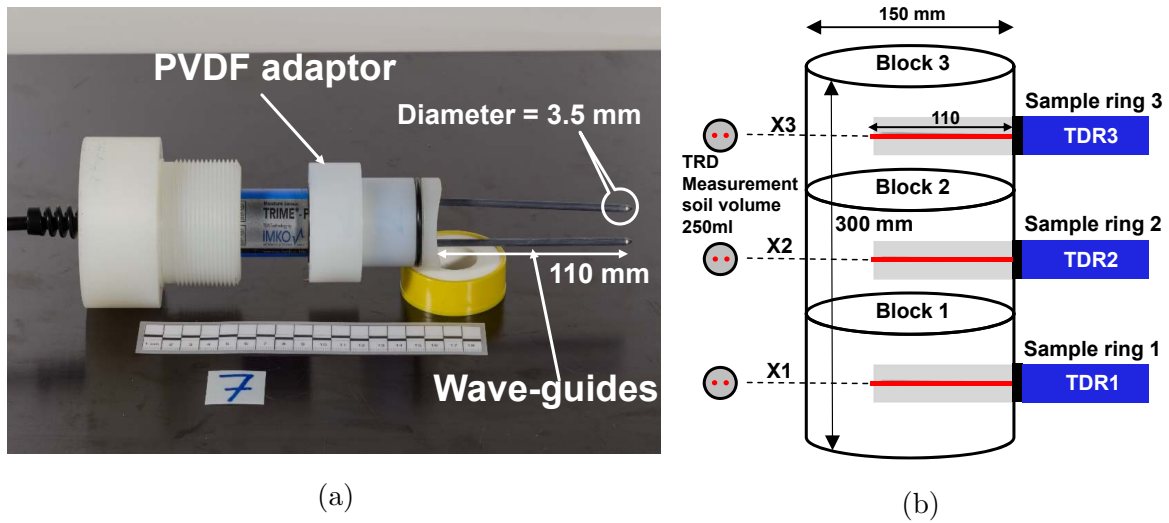


Figure 4.9: TDR sensors installation details, (a) TDR along with accessories and (b) a schematic showing positions of the sensors along the height of the sample.

of the amplitude, i.e. a reduction of the attenuation. This is achieved by a suitable impedance matching between pulse generation output, high frequency (HF) cable, and the probe.

A coating of the metallic probe-rods with plastic (PVC) is the most important measure to get the TDR step-pulse signal. The coating decreases the attenuation similarly to a high-pass filter. Low frequencies, such as the repetition frequency of the TDR-pulse ( $<9$  MHz) are blocked. Only the higher frequencies ( $>300$  MHz) of the electromagnetic wave propagate through the soil or material and are attenuated. Thus the total attenuation is essentially reduced and the amplitude of the reflected TDR-pulse is raised. To evaluate the transit time it is not necessary to scan the whole TDR-signal. A special algorithm in the TRIME-device scans particular points of the curve in order to determine the amplitude of the reflected pulse. The advantages are shorter measuring times and lower power consumption. As per internal measuring procedure, moisture is calculated with the measure transit time in three step as shown in Figure 4.10.

In the first-step, the cable length and probe mechanism tolerance of the probe have to be compensated for a reliable and robust measurement. The compensation is carried out with the help of dry and water saturated glass beads as per the standard procedure suggested in the operating manual (IMKO, 2010). The calibration coefficient  $A$  and  $D$  are automatically calculated by the supplied software (TRIME-WinCal). In the second-step, once having the corrected transit time ( $t_p$ ), one can estimate the soil moisture content by selecting 13 different in-built calibration curves. In special cases such as the soil having

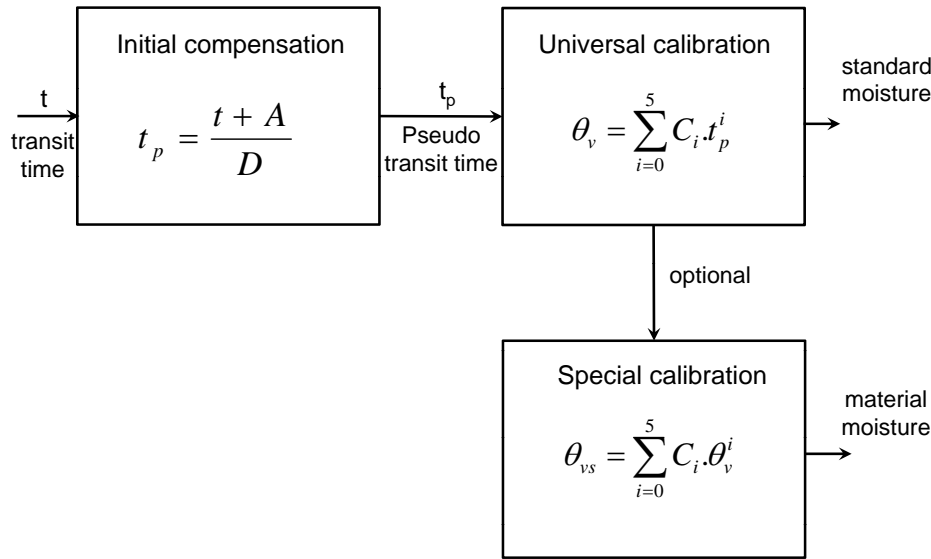


Figure 4.10: TRIME internal measuring procedure.

high active clay content ( $> 50\%$ ), the material calibration must be performed. A wide range of grain size in the soil in-case of a heterogeneous mixture also needs material specific calibration. Hence, the tested material i.e., Calcigel bentonite-sand mixture urges for the material specific calibration of TDRs. The active clays like bentonite have larger surface area of clay minerals, which leads to a high amount of bound water. Hence, an extensive testing program was dedicated to determine the material specific calibration for compacted sand-bentonite mixture and the influence of temperature on the measurement. The detailed information on the TDR material specific calibration is mentioned in section 4.3.1.

#### 4.2.4.4 Sensors for relative humidity measurement

The relative humidity sensors (VAISALA-HMT337) are selected for measuring the relative humidity of soil at measurement sections X1, X2 and X3. The sensors measures relative humidity and temperature and quantifies various optional parameters such as dew point temperature, enthalpy, mixing ratio, absolute humidity and wet bulb temperature. The relative humidity measurement is a challenge task, particularly in the experiments where the material is subjected to competing effect of heat and moisture flows. In such testing conditions, the temperature difference between the probe and the surrounding soil can cause a risk of condensation on the sensor head. For such testing conditions, the warmed probe option prevents the condensation on the probe.



Figure 4.11: VAISALA HMT337 relative humidity sensors with additional Pt100 sensors

Figure 4.11 shows VAISALA-HMT337 probe with an additional Pt100 probe. The accuracy of the humidity sensors including nonlinearity, hysteresis and repeatability is  $(1.5 + 0.015 \times \text{reading})$  % RH in the range of  $-40 \dots +180$  °C. Each sensor is fitted with analogue 2-10 V output for 0-100 % relative humidity and protected by cylindrical stainless steel filter. The rated accuracy of Pt100 temperature sensor is shown in Figure 4.12 (Vaisala-Oyj, 2011). The working temperature for column-experiment investigations ranges between 20 to 80 °C. Hence, the accuracy of the Pt100 sensor varies from  $\pm 0.2$  to  $\pm 0.4$  °C.

The improper installation of RH sensors may affect the quality of relative humidity measurements. Hence, several trial tests were conducted to ensure the quality of measured RH values. In some trial tests, Rotronic sensors were used in the embedded position in the compacted sample as shown in Figure 4.13. It was observed that the installation of RH sensor in the embedded position is not suitable for the long-term experiments due to potential damage of sensor's electronics and induced disturbance to the sample during the retrieval process of the damaged sensor. Considering the impact of the embedded sensing in case of RH probes, the closed-chamber concept was used.

In the closed-chamber concept, a small-space is created inside the sealed chamber, which accommodates the RH sensors and allows the vapor transfer between the soil pores and the sealed chamber through a sintered opening (see Fig. 4.14). An adequate vapor and thermal equilibrium are necessary between the soil pores and the sealed chamber. Considering the role of thermal equilibrium, a temperature difference of 0.5 °C between the soil and sensor

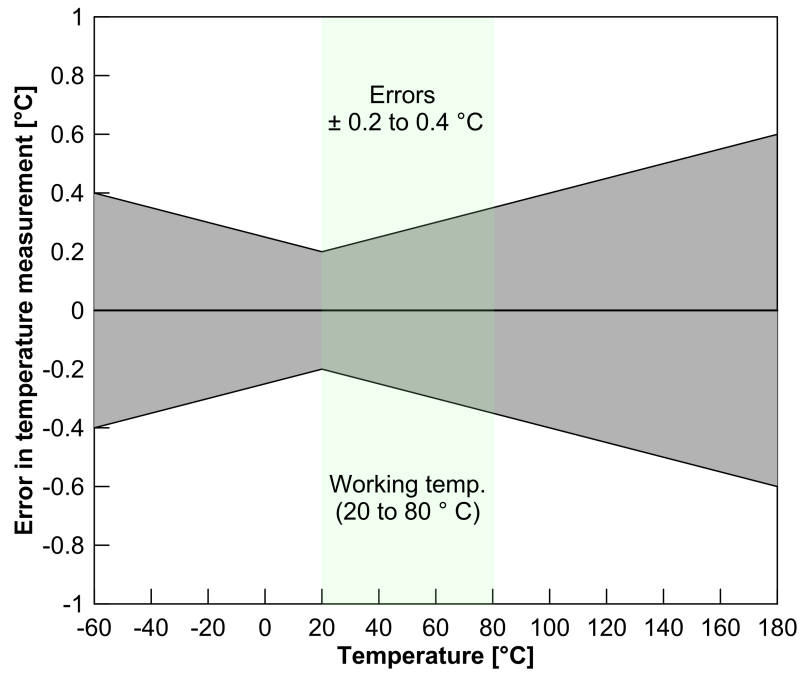


Figure 4.12: Accuracy of Pt100 sensors associated with VAISALA HMT337 RH sensor (modified from Vaisala-Oyi, 2011).

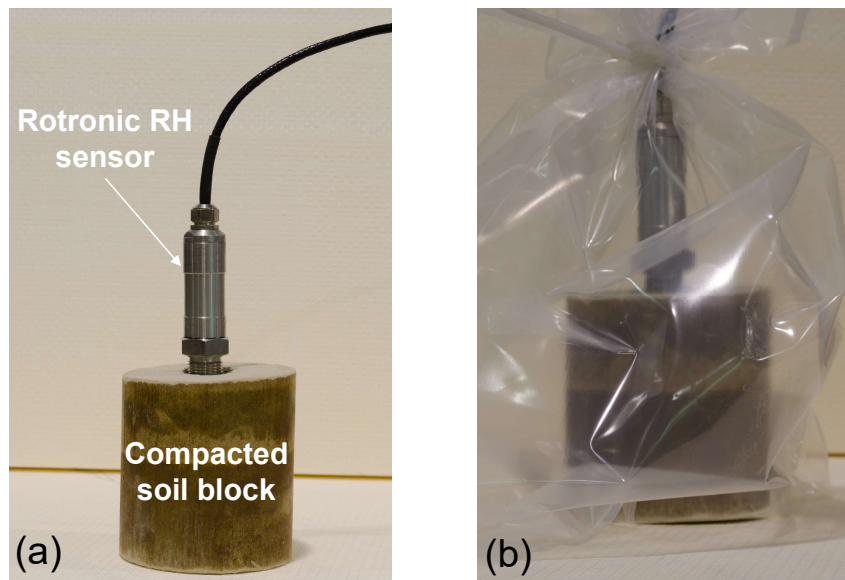


Figure 4.13: Installation of Rotronic RH sensor in the embedded position inside the compacted soil sample during the trial tests.

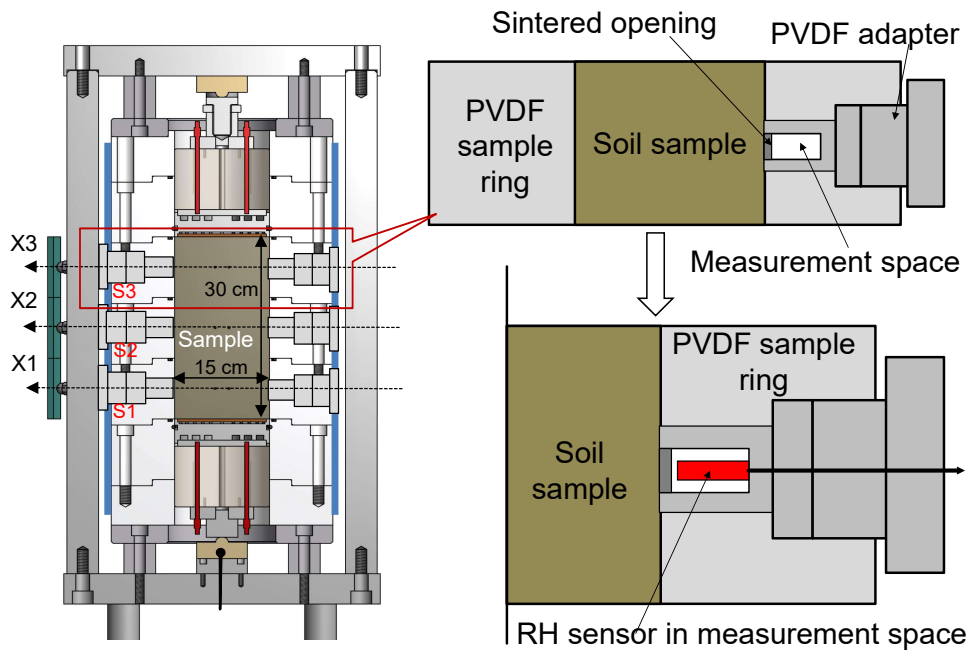


Figure 4.14: Schematic illustration of the closed-vapour chamber concept for measuring relative humidity.

may lead to condensation particularly at higher relative humidity levels ( $> 98\%$ ) as shown in Figure 4.15a. While the difference between the ambient and dew point temperature increases with a decrease in the relative humidity, it signifies that the risk of condensation is less at lower relative humidity levels.

In some trial tests, the Rotronic sensors were installed in the sealed chambers (see Fig. 4.15b) and tested under an applied temperature gradient along the height of soil sample. During the test, condensation occurred inside the chamber particularly at high humidity-levels ( $\geq 98\%$ ) due to the temperature difference between the soil and the chamber. Which was mainly due to the long and extended metallic body of Rotronic RH sensor outside the close chamber.

With a small probe length, VAISALA-HMT337 probe with heating option seems promising for measuring the relative humidity at high relative humidity levels. An additional Pt100 probe measures the ambient temperature, when the heating option is activated. Later, the correct relative humidity value can be calculated from the measured ambient and dew point temperature. As per the installation guidelines, these sensors are not designed for embedded sensing particularly for the long-term experiments. Hence, these sensors are installed in the closed/sealed chambers as shown in Figure 4.16. The

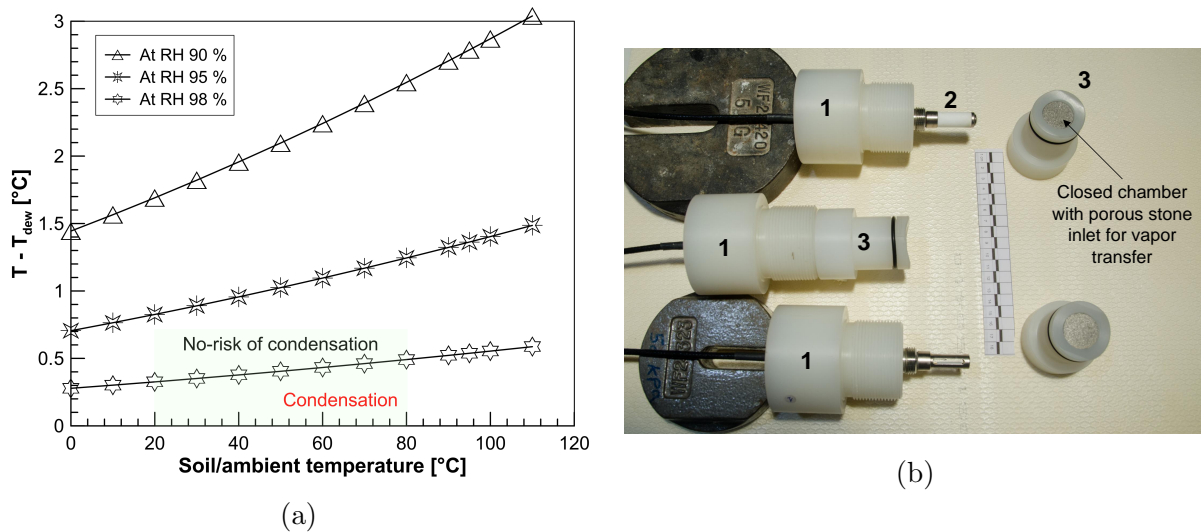


Figure 4.15: (a) Condensation at the higher relative humidity levels based on the difference in the soil/ambient temperature and the temperature inside the closed vapor chamber and (b) Trial tests: Rotronic sensors with closed-chamber concept.

additional Pt100 probe is embedded inside the soil (diameter = 6 mm and length = 10 mm).

During the design phase of the test cell, the number of sensors (Pt100- 6 Nos., TDR- 3 Nos., pressure transducers- 2 Nos.) were considered based on the volume fraction as compared to the sample volume. The volume of the embedment of all sensors was found to be about 0.14 % of the total sample volume. Therefore, the impact of embedment may be considered insignificant. The  $c/c$  distance of the sensors was based upon manufacturer's specification for minimizing the signal interference. Additionally, the TDR wave guides (made of PVC) were sensitive to deformation.

### 4.3 Calibration of sensors and monitoring instruments

The Pt100 sensors, relative humidity sensors, top and bottom load cells, and the lateral load cells were received with the factory calibration certificates. Additional tests were carried out to verify the accuracy of the relative humidity sensors using saturated salt solutions of LiCl, NaCl, and  $K_2SO_4$ . The measured relative humidity values agreed very well with the specified values (ASTM-E104, 2007). Two nos. of pressure transducers were planned to be embedded in the sample to measure axial stresses at heights of 100 and 200 mm from the base of the sample. These pressure transducers are anticipated to operate

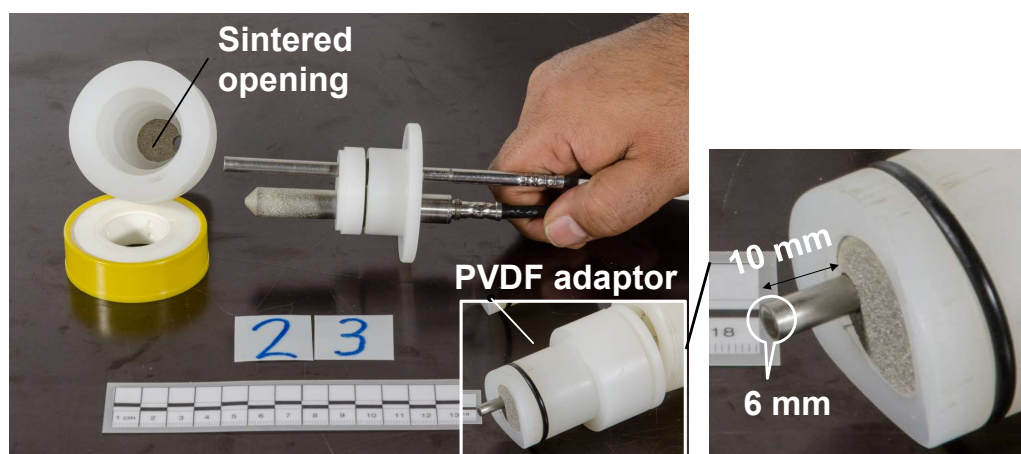


Figure 4.16: (a) Installation of VAISALA HMT337 RH probe with an additional Pt100 probe in closed-vapor chamber.

at elevated temperatures. For these pressure transducers, as suggested by the supplier, a thermal drift of  $\pm 0.4 \text{ \%}/^{\circ}\text{C}$  in terms of the measured voltage for a temperature range of 24 to 60  $^{\circ}\text{C}$  is considered for obtaining the actual pressures.

The TDR probes generate a high-frequency-pulse (up to 1 GHz) that propagates along the wave guides thereby generating an electromagnetic field. At the end of the wave-guides, the pulse is reflected to the source. The transit time ( $t_p$ ) depends upon the dielectric properties of the medium in which the measurement is carried out. It is a common practice to establish the calibration curve (i.e., transit time ( $t_p$ ) vs. water content) for the material under consideration at various temperatures of interest (Topp et al., 1980; Schanz et al., 2010). The minimum sample volume for water content measurement is usually 250  $\text{cm}^3$ .

For establishing the TDR calibration curve in this study, the material specific calibration tests were performed with the compacted bentonite-sand mixture (50:50) having three different initial water contents (5, 10, and 15 %). Samples (dia. 150 mm and height 100 mm) were prepared by statically compacting the mixtures to attain an average dry density of 1.80-1.85  $\text{Mg}/\text{m}^3$ . After the extrusion from the compaction mould, the pre-compacted blocks were covered with layers of plastic film, aluminum foil, and plastic adhesive tape to prevent any moisture loss during the measurements.

The calibration tests were performed at room temperature and at several elevated temperature levels between 25 and 60  $^{\circ}\text{C}$ . For the latter, the tests were carried out in a temperature controlled drying oven. The maximum temperature (i.e., 60  $^{\circ}\text{C}$ ) corresponds

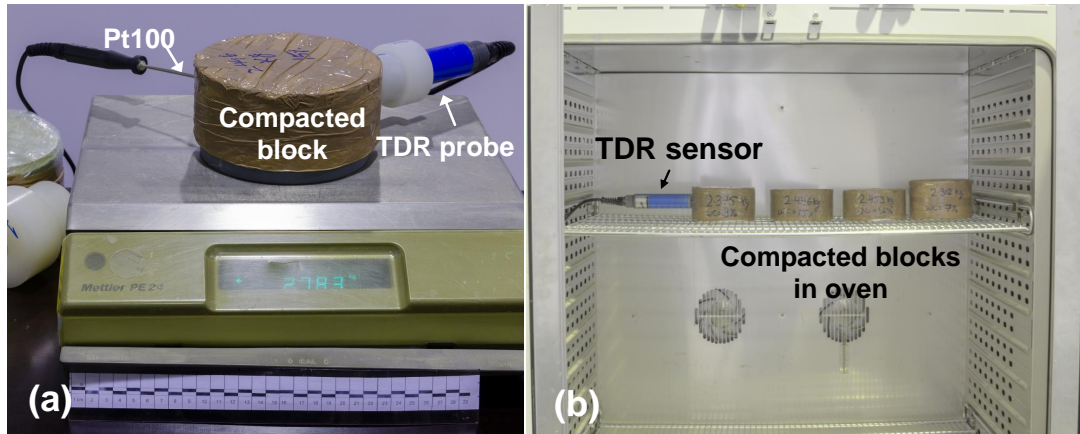


Figure 4.17: Test set-up for material specific calibration at (a) room temperature and (b) at elevated temperature.

to the limit of measurement of the TDR probe. The wave-guides of the sensors were inserted in the pre-drilled holes in the compacted samples. A Pt100 sensor was used to measure temperature during the tests. For the samples that were tested in the oven (Fig. 4.17b), the measurements were performed after the samples attained the desired temperatures. Based on the test results and using an interpolation technique, the calibration test data were plotted as a 3D-surface as depicted in Figure 4.18 with three variables, such as water content, temperature and transit time ( $t_p$ ). A MATLAB program was developed to extract the actual water content from the measured value of  $t_p$  corresponding to any given temperature.

#### 4.4 System compliance tests

Prior to the water infiltration test with the compacted mixture of bentonite-sand (50:50), a series of tests were performed using the device to examine the air and water tightness of constructional joints, to study the response of the load cells, and further for quantifying the temperature-induced volumetric deformation of the test set-up at an elevated temperature. In the test with fine sand, the performance of TDR and relative humidity probes were investigated under the applied hydraulic and temperature gradient, respectively. The test with compacted Calcigel bentonite sand mixture mimics the initial heating phase of the compacted buffer material at the nuclear waste repository. The transient measurements were performed for temperature, relative humidity, water content and total stresses in both axial and lateral directions at various preselected locations during the test.



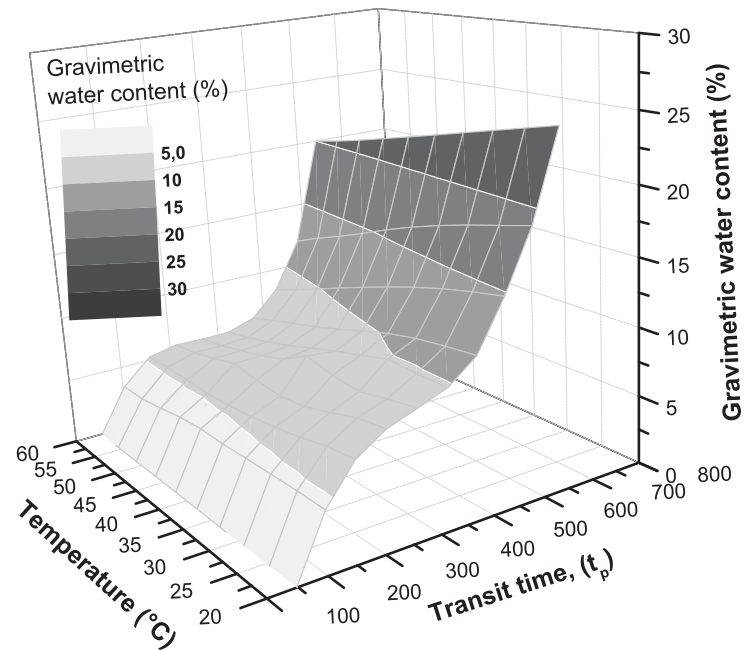


Figure 4.18: Temperature dependent calibration curve for TDR sensor.

#### 4.4.1 Response of Load cells under pressure and thermal loading conditions

For the first two aspects as mentioned above, a test was carried out by using an oak wood dummy sample (dia. = 100 mm and length = 300 mm). The applied temperatures at the opposite ends of the wooden sample were 80 °C (at top) and 20 °C (at bottom). A choice of the elevated temperature of 80 °C ties up with the temperature adopted in case of testing the compacted bentonite-sand mixture sample. A schematic of the test set-up is shown in Figure 4.19. The wooden dummy sample was placed between the top and bottom plugs that prevented the top plug to retreat in to the cell cavity. The dummy also served as an insulator between the top and bottom ends.

Considering the thermal properties of oak wood (thermal conductivity = 0.14 W/mK, coefficient of linear thermal expansion =  $4.86 \times 10^{-6}$  m/m.K parallel to grain) (Avallone & Baumeister, 2017), it was expected that the dummy would exhibit an axial stress under the applied temperature gradient of 0.2 °C/mm. The axial load cells measured the stresses at the top and bottom of the wooden dummy sample. The lateral load cells measured the stresses at levels X1, X2, and X3. Pressurized air was supplied from an

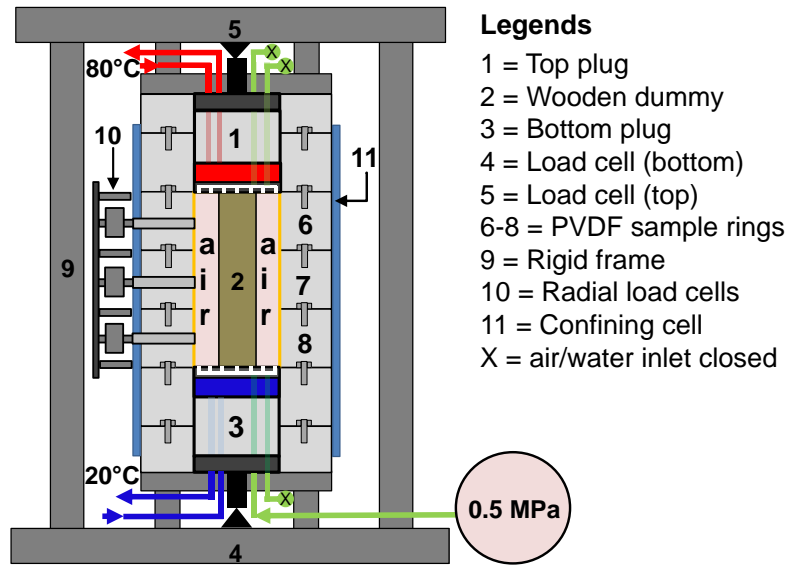


Figure 4.19: A schematic view of the test set-up for verifying response of load cells under pressure and thermal loading conditions.

external air compressor to the annular space between the sample and the inner surface of the sample rings. In case of any air leakage in the system, these load cells are expected to show discrepancies with the applied air pressure.

The test with the wooden dummy was conducted in three phases as depicted in Figure 4.20. Prior to the commencement of the test, the seating pressures for the axial and lateral load cells were 60 and 40 kPa, respectively. In phase 1, the annular space between the PVDF sample rings and wooden dummy was subjected to two successive cycles of compression-decompression using an air pressure of 0.5 MPa at room temperature. In phase 2, the temperature at the top was raised to 80 °C, whereas it was kept constant at 20 °C at the opposite end of the sample. In phase 3, once the thermal equilibrium in terms of the temperature was established, the air pressure was increased to 0.5 MPa and kept constant for a period of five hours. At the end of phase 3 the heating process was terminated, and the air pressure was reduced to zero.

The applied temperatures at both ends of the wooden dummy and the air pressure are shown in Figures 4.20 (a and b), respectively. Figures 4.20 (c and d) show the measured stresses at both ends of the sample and at the three predetermined levels on the circumference of the cell, respectively. As can be seen in Figure 4.20, the measured stress values are similar and agree well with the applied air pressure of 0.5 MPa during phase 1. The load cells responded well when the air pressure was reduced to zero. In phase 2, the

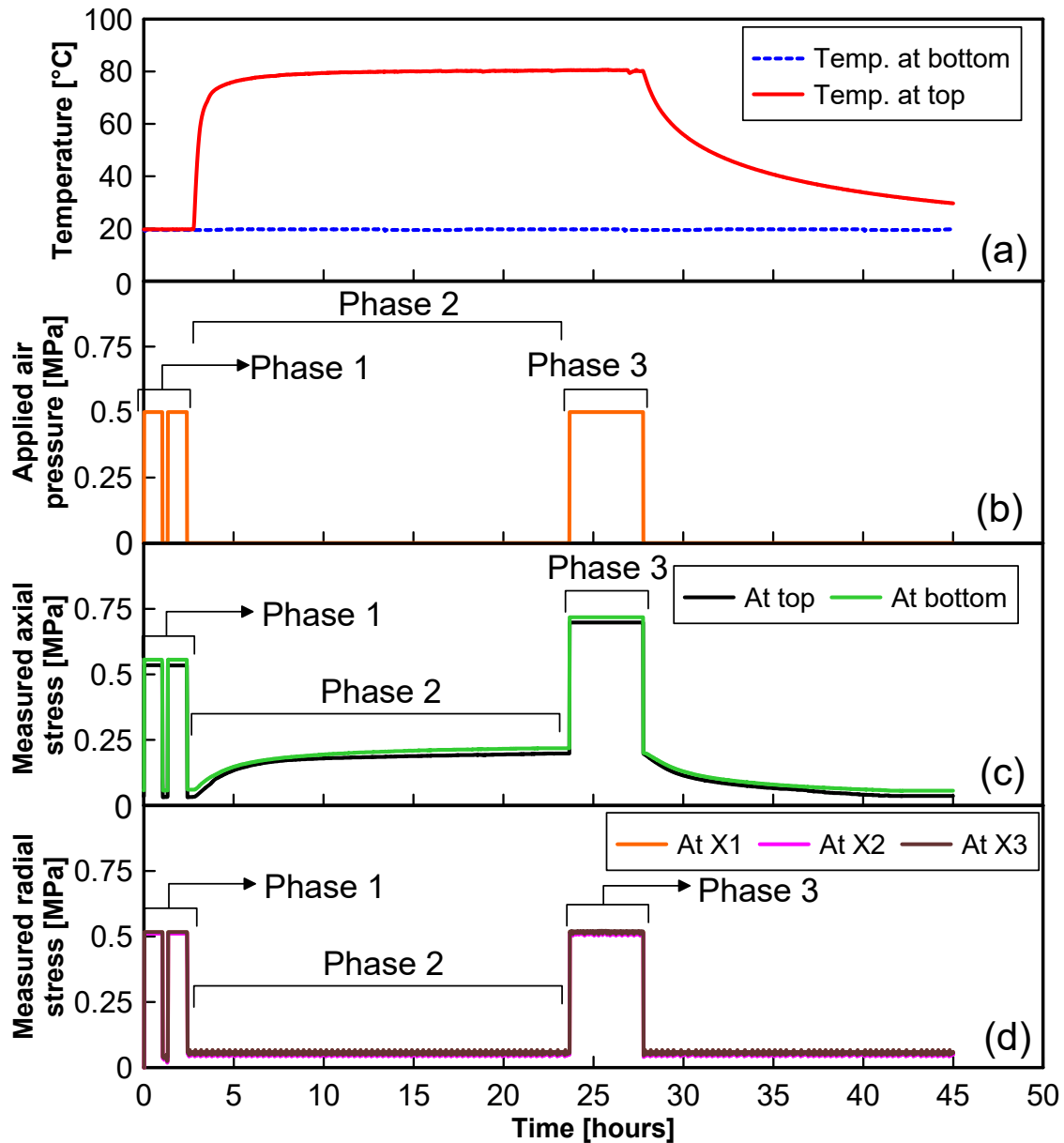


Figure 4.20: Test results showing response of load cells to pressure and thermal loading conditions in the presence of a dummy wood sample, (a) applied temperature at opposite ends of the dummy, (b) applied air pressure in annular space, (c) measured axial total stress, and (d) measured lateral total stress.

measured stresses by the top and bottom load cells were on account of the temperature induced stresses due to the thermal expansion of the wooden dummy since the applied air pressure was zero. The measured axial stresses at the top and bottom ends was about 0.22 MPa. As expected, the stresses measured by the lateral load cells were at seating pressures (Fig. 4.20c) in phase 2. In phase 3, the air pressure in the annular space was increased to 0.5 MPa and further decreased. This occurred when the elevated temperature was applied at the top end. The top and bottom load cells responded well to the elevated air pressure. The measured axial stress value at both ends of the sample was about 0.72 MPa, whereas a net increase in the pressure of 0.5 MPa was noted for the lateral load cells. The test results clearly showed that the device functioned well with no leakage detected under both elevated temperature and pressure conditions and further, the load cells responded well to the elevated temperature and pressure conditions.

#### **4.4.2 Volumetric Thermal Expansion at Elevated Temperature**

One of the major issues of the soil testing at elevated temperature and under K0-condition is the volumetric thermal expansion of test set-up that may lead to change in the stress state of the tested soil sample. A test was conducted in the device to quantify the volumetric thermal expansion of the test set-up at a temperature of 80 °C. To investigate the effect of elevated temperature on thermal expansion of PVDF sample rings, two tests were performed, such as with and without the confining cell.

The view of test set-up is shown in Figure 4.21. A cylindrical stainless-steel dummy (dia. = 100 mm and height = 300 mm) was placed between the top and bottom plugs. The steel dummy provided the mechanical support to the top plug. The annular space between the PVDF sample rings assembly and the steel dummy was filled with water using the bottom inlet port, whereas all other air/water inlets were kept close. A sufficient care was exercised to remove the trapped air bubbles by allowing water to flow from bottom to top. Two nos. of water-filled burettes were connected to the water inlet port (Fig. 4.21) and the water-level in burettes was kept at the level of water inside the cell. The tests were carried out at ambient laboratory temperature of 22 °C. A fluctuation of temperature in the laboratory may cause evaporation of water, which in turn can significantly affect the volume measurements using burettes. To minimize the evaporation of water in burettes, the exposed water surfaces in burettes were covered with a lubricant. The temperature at both the ends of the steel dummy was raised to 80 °C using separate external heating units. The water level in the parallel-burette system was monitored continuously for a period of more than ninety-six hours. In both tests (i.e., with and without the confining

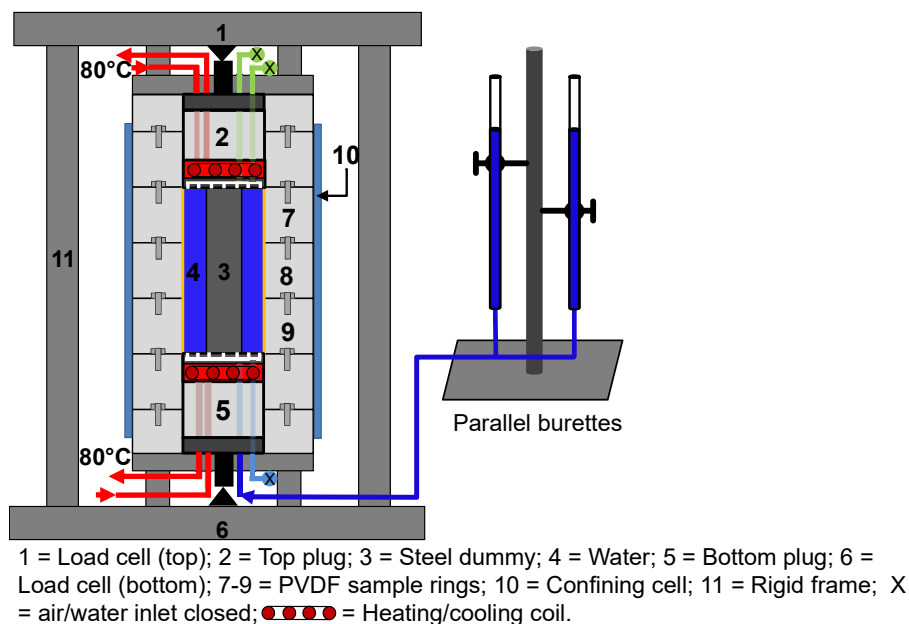


Figure 4.21: A schematic view of the test set-up for quantifying the volumetric thermal expansion of the device in the presence of a stainless-steel dummy.

cell), the water levels burettes was found to be higher than the initial levels indicating that water flow occurred from the cell to burettes.

An increase in the temperature to 80 °C initiates the thermal expansion of stainless-steel dummy, water in the annular space and the PVDF sample rings. Note that the PVDF sample rings assembly was subjected to a temperature gradient along the wall thickness (i.e., 80 °C inside and 22 °C outside). The combined effect of an expansion of various components is expected to affect the water levels in burettes. For example, an increase in the volume of the stainless-steel dummy and the water in the annular space would cause an increase in the water levels in the outside burettes. An expansion of the PVDF sample rings assembly causing an increase in the internal diameter would tend to cause a drop in the water level in burettes.

To quantify the thermal expansion of the PVDF rings assembly, calculations were made in which case the volumetric thermal expansion of the stainless-steel dummy and water was calculated at the applied temperature of 80 °C by considering the appropriate values of coefficient of volumetric thermal expansion of steel ( $\alpha_{steel} = 4.80 \times 10^{-5} \text{ 1/}^\circ\text{C}$ ) and water ( $\alpha_{water} = 2.14 \times 10^{-4} \text{ 1/}^\circ\text{C}$ ). Table 4.2 shows the initial volume and the volume increase due to thermal expansion of the stainless-steel dummy and water, the measured volume change based on the burette readings. The measured water volume was slightly less than

Table 4.2: Calculation for volumetric thermal expansion of column-type experimental set-up ( $\alpha_v$  = coefficient of volumetric thermal expansion,  $V$  = volume at 20 °C and  $\Delta V$  = change in the volume due to a temperature change from 20 to 80 °C).

Test specification	$\alpha_v$ [1/°C]	V [ml]	$\Delta V$ [ml]
<b>Without confining cell</b>			
Steel dummy (SS 316 L grade)	$4.80 \times 10^{-5}$	2356.19	6.78
Water inside the cell volume	$2.14 \times 10^{-4}$	2945.24	37.81
Change in the water-level in burette system	-	-	42.20
Column total internal volume	-	5301.4	2.39
Volumetric thermal-strain [%]	-	-	0.045
<b>With confining cell</b>			
Steel dummy (SS 316 L grade)	$4.80 \times 10^{-5}$	2356.19	6.78
Water inside the cell volume	$2.14 \times 10^{-4}$	2945.24	37.81
Change in the water-level in burette system	-	-	42.60
Column total internal volume	-	5301.4	1.99
Volumetric thermal-strain [%]	-	-	0.037

the calculated values in both tests (see Table 4.2). It clearly suggests that an expansion of the PVDF sample rings assembly occurred (about  $2.39 \times 10^3 \text{ mm}^3$  and  $1.99 \times 10^3 \text{ mm}^3$ ) which is about 0.04 % of the initial volume of the cell and hence can be considered insignificant in terms of its contribution to the interpretation of the test results.

#### 4.4.3 Test with fine sand

A test was performed with the Hostun sand to investigate the measurement abilities of TDR probes and the relative humidity sensors under applied hydraulic and temperature gradients, respectively. In the first test, the moist sand with 1 % water content was subjected to the stage-wise hydration under the capillary action from the bottom-end. In the second test, the moist sand column with 1 % water content was subjected to an applied thermal gradient (top-end = 80 °C and bottom-end = 20 °C). Figure 4.22 shows the schematic view of test set-up.

For the test under an applied hydraulic gradient, the RH sensors and TDR probes were installed prior to fill the moist sand in the cell. The moist sand was filled in total nine layers. Each layer was slightly compacted using a thick steel plate. The total weight of moist sand, which was filled in the cell was approximately 9.220 kg; hence, the mean dry

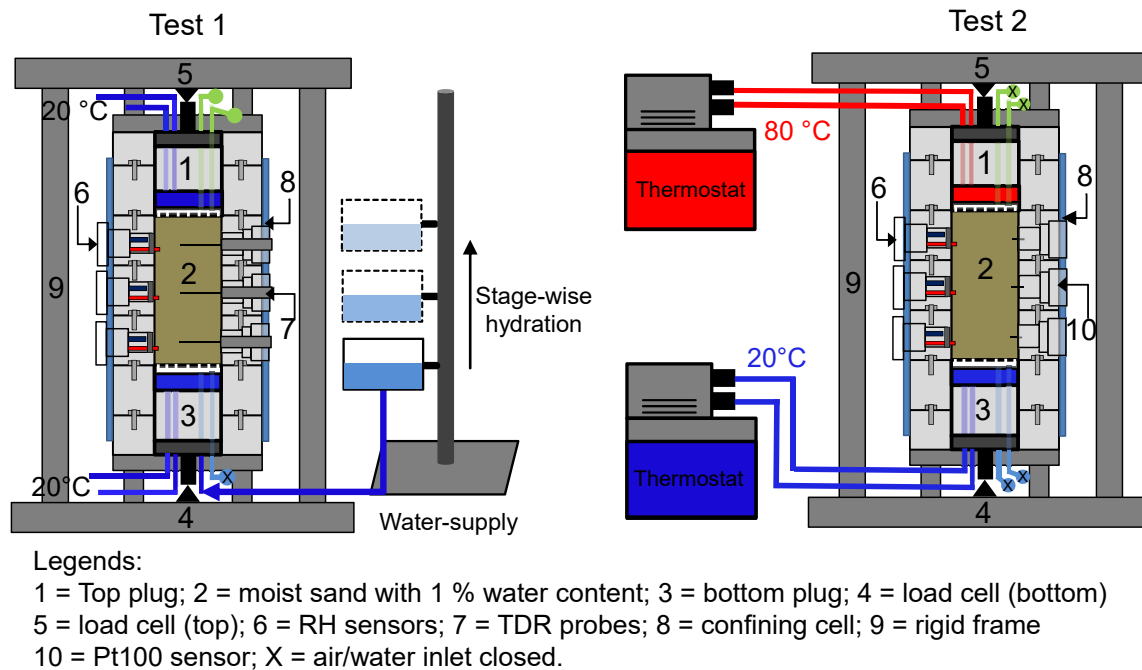


Figure 4.22: Schematic views of test set-up for testing the moist sand under an applied hydraulic gradient (test 1) and under an applied thermal gradient (test 2).

density was close to  $1.58 \text{ Mg/m}^3$ . In the next step, the sand-column was hydrated from the bottom end under the capillary action by rising the level of external water supply container as depicted in Figure 4.22. During the stage-wise hydration, the temperature at both the ends were kept constant at  $20 \text{ }^\circ\text{C}$ . The complete saturation of the sand column was achieved in three stages. During the test, TDR probes measured the transient water content values and the VAISALA-HMT337 probes measured the relative humidity at three measurement sections along the height of soil sample. Once the test was over, the samples were collected from the measurements sections for determining the water content to compare with the TDR measurements.

In the second test under an applied thermal gradient, the moist sand with 1 % water content was poured in the cell-volume similar to the first test. During the installation of test set-up, the RH sensors and Pt100 sensors were installed prior to sand pouring process. Once the experimental set-up was completely assembled, the temperature at the top-end was raised to  $80 \text{ }^\circ\text{C}$ , while at the bottom-end, the temperature was kept constant at  $20 \text{ }^\circ\text{C}$ . The relative humidity and temperature were measured at three measurement sections along the height of soil sample during the test and all the air/water inlets were kept closed. The test results are shown in Figures 4.23 and 4.24.

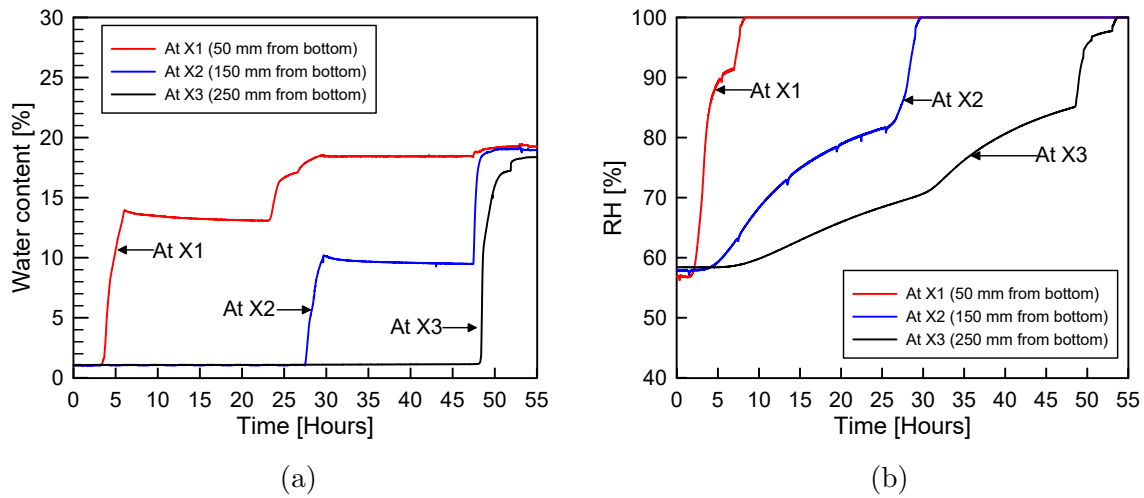


Figure 4.23: Test with fine sand under the applied hydraulic gradient (a) evolution of water content and (b) evolution of relative humidity over time along the height of soil sample.

In the first test, the water content at section X1 (50 mm from bottom) increased to 13-14 % in the first-stage. On the other hand, the water content at X2 (150 mm) and X3 (250 mm) did not show any changes. After 24 hours, the elevation of water supply container was raised to the next-level. In the second stage, the water content at section X1 further increased to 18 %. While at section X2, the water content increased to 10 % and the water content at section X3 was unchanged. After 24 hours, the third stage of hydration was initiated. In the third stage, full saturation of the sand column was achieved. The water content at section X3 was close to 18 %, which was more and less uniform along the entire sand column. In this test, the TDR sensors successfully captured the initial and final water content values which were later verified with the pre and post-experimental measurements. The relative humidity measurements also agreed well with the water content fluctuations. The initial relative humidity of the moist sand with 1 % water content was measured with the chilled mirror technique (58.5 %). The initial relative humidity profile along the moist sand column was not uniform. Hence, once the installation process was over, the sand-column was allowed to attain the equilibrium in terms of uniform relative humidity profile across the sample for 7 days. The measured relative humidity values after the equilibrium-period were close to 56-59 %, which were close to the chilled mirror measurements.

For the second test under an applied thermal gradient, the test results are shown in Figure 4.24. The temperature at section X3 close to the heating end reached to 48 °C. On the other hand, the temperature at section X2 and X1 increased to 28 °C and 22



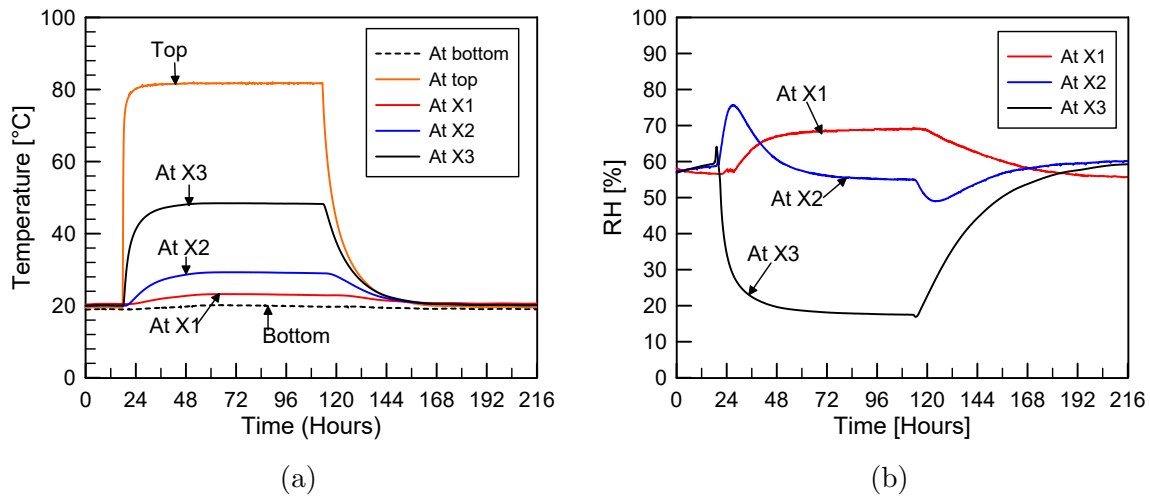


Figure 4.24: Test with fine sand under the applied temperature gradient (a) evolution of temperature and (b) evolution of relative humidity along the height of soil sample.

°C, respectively (Figure 4.24a). The effect of temperature rise and the resulting moisture migration towards the colder sections can be observed in the relative humidity evolution with the elapsed time (Figure 4.24a). The measured values at section X3 (close to the heating end) decreased with an increase in the temperature. As the moisture migrated towards the colder sections under the applied thermal gradient, the relative humidity increased at the section X1 close to the cooling end. As a result, the measured relative humidity at section X1 increased with the elapsed time and reached to 70 %. While at the measurement section X2, the relative humidity first increased due to the moisture migration from section X3 and then decreased due to the temperature rise.

The test results exhibit the satisfactory performance of TDR probes and RH sensors under an applied hydraulic and temperature gradients. However, the testing period was comparatively shorter than the associated saturation period of compacted expansive soil based materials. In this regard, a test was conducted with the compacted Calcigel bentonite sand mixture. The main objectives of the test were to investigate

- the device ability to capture the targeted processes in the engineered barrier, and
- the long-term performance of the monitoring sensors, instrumentation and cable-connections at high temperature levels.

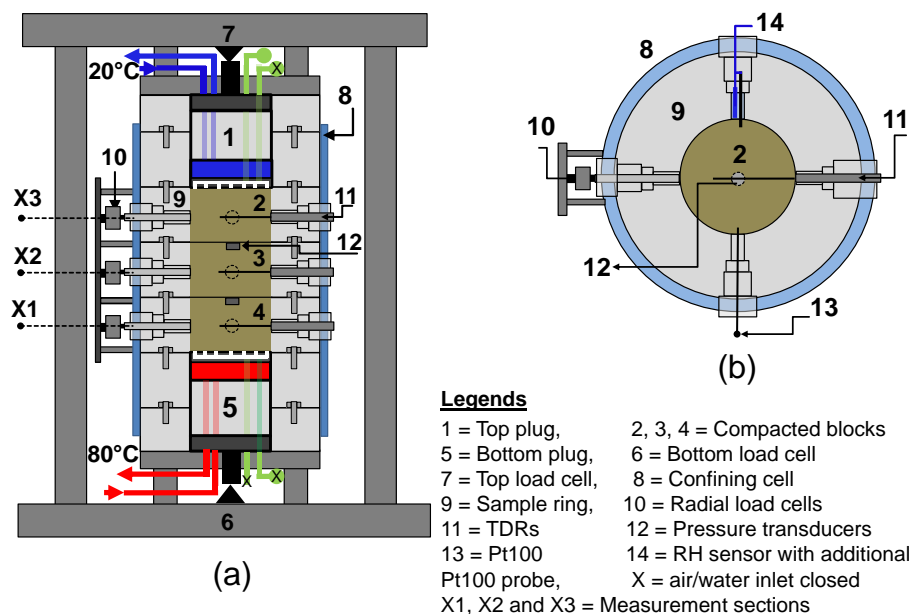


Figure 4.25: (a) A schematic view of test set-up in the presence of compacted bentonite-sand blocks and (b) monitoring sensors.

#### 4.4.4 Test with the compacted bentonite-sand blocks

A test was performed with compacted Calcigel bentonite-sand mixture (50:50) under an applied temperature gradient. The testing conditions mimic the early phase life time of underground repositories during which the thermal loading is considered significant and the vapor may escape from the disposal pits due to the presence of constructional gaps and technical voids.

Three compacted blocks to be accommodated in sample rings S1, S2 and S3, each with dia. 150 mm and height 100 mm, were prepared to form the sample to be tested. For preparing each compacted block, the mixture was statically compacted in a mould in three layers by applying a static compaction pressure of 30 MPa using a uniaxial static compaction machine to achieve a dry density of 1.80-1.85 Mg/m<sup>3</sup>. Prior to the compaction of the first layer in case of the blocks for S2 and S3 (Fig. 4.25), a steel dummy having similar dimensions to the pressure transducer was placed at the center of the base plate for creating the desired space for the miniature pressure transducer (KYOWA-BEC). The surface of the compacted layer was scarified prior to placing the next layer to ensure homogeneity. The compacted block was extruded from the mould. The dummy was removed for the installation of the pressure transducers. The compacted blocks were then prepared for installing the monitoring sensors. For installing the TDR wave-guides, two

holes (diameter = 3.5 mm and length = 110 mm) at predetermined positions were drilled. Similarly, two holes, each 10 mm length were also drilled for installing the Pt100 sensors. After assembling the experimental set-up with the compacted blocks in the sample rings and the monitoring sensors at the desired positions, all the air/water vents were closed. The sample was tested by applying a temperature of 80 °C at the bottom-end and 20 °C at the top-end. The test was conducted for a period of 92 days (35 days of equilibration-period and 57 days of heating-period). The equilibration-period was considered for achieving a homogeneous water content and relative humidity distributions along the height of sample. Although the data acquisition was made for the entire equilibration period, only the data for a period of seven days prior to the thermal loading are presented. Prior to applying the thermal loading, the air vent located at the top-end of the device was opened. This allowed a release of the moisture vapour from the sample during the test. Therefore, a constant moisture condition within the sample did not exist. Prior to commencement of the test, an initial seating stress of 50 kPa was applied in the axial direction. Similarly, the lateral load cells were adjusted to read a stress of 1-1.25 MPa for ensuring good contacts between the sample and the load cells.

Figure 4.26 shows the elapsed time vs. temperature plot under the applied temperature gradient of 0.2 °C/mm. The quasi steady state temperature distribution along the height of the sample was achieved in about twenty-four hours at all salient levels.

The temperature profiles and the calculated temperature gradients along the height of the sample at different testing periods (7, 9, and 64 days) are shown in Figure 4.27. The temperature gradient was found to be about 0.40 °C/mm at section X1 (50 mm from the heat source) which decreased to about 0.22 °C/mm nearer to the top-end (i.e., section X3 - 250 mm from the heat source). The results showed that temperature gradient decreased with an increase in the distance from the heat source. Similar trend for the temperature gradient has been reported by Tripathy et al. (2017) for tests at 85 and 150 °C. Figures 4.28a and 4.28b show the measured relative humidity (RH) and water content with elapsed time in the compacted bentonite-sand mixture sample at measurement sections X1, X2, and X3.

The data presented in Figure 4.29 correspond to test durations of 7, 9, and 64 days. Figures 4.29a and 4.29b show the profiles of relative humidity and water content, respectively. The RH of the sample decreased at sections X1 and X2 within about less than twenty-four hours from the commencement of the heating process, whereas the water content during this period remained nearly unchanged. This indicates that a decrease in the RH at X1 and X2 within a few hours after the commencement of the heating process was primarily

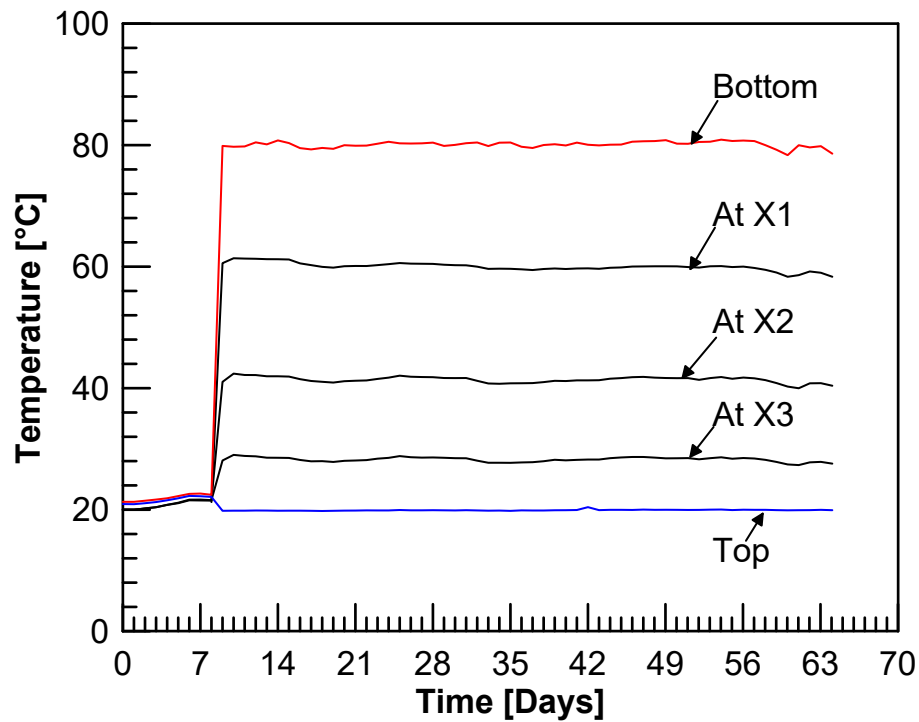


Figure 4.26: Elapsed time vs. temperature plot for the test with the compacted sand-bentonite mixture.

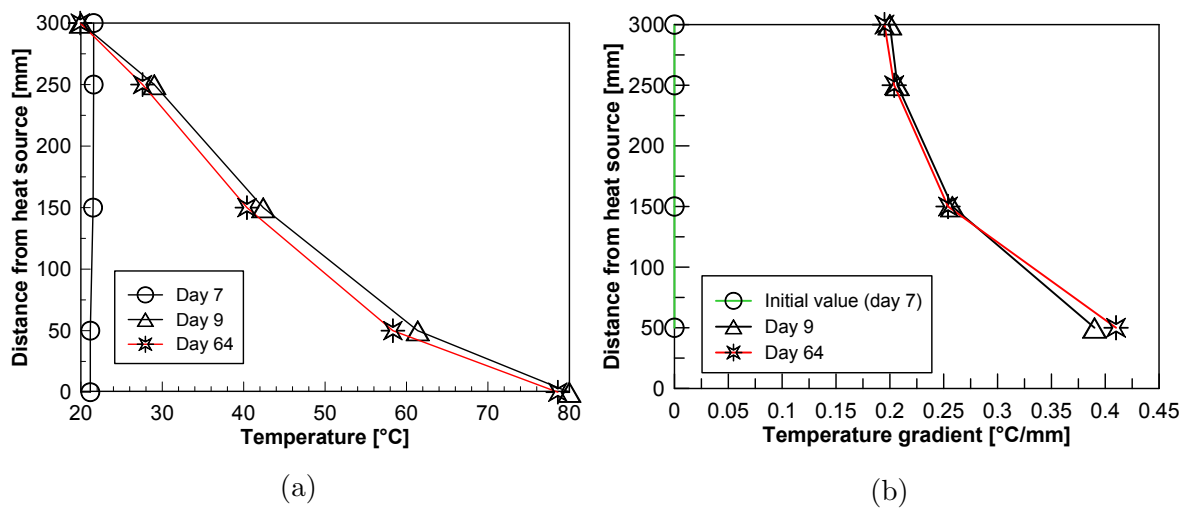


Figure 4.27: (a) Temperature profile and (b) temperature gradient at 7, 9 and 64 days.

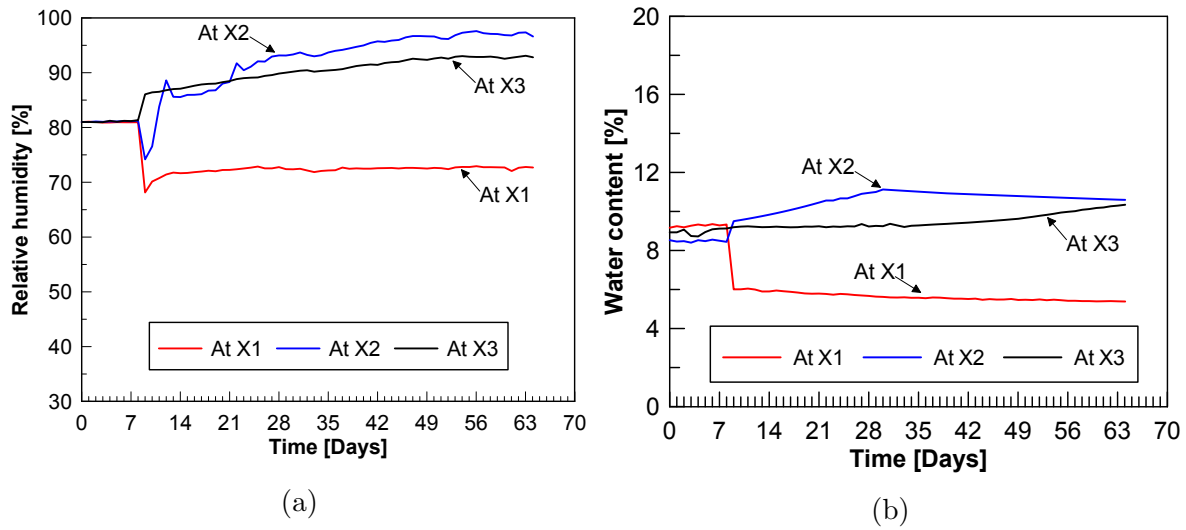


Figure 4.28: (a) Elapsed time vs. relative humidity and (b) elapsed time vs. water content plots at salient levels along the height of the sample.

due to an increase in the temperature. For elapsed times greater than twenty-four hours, the RH at X1 increased slightly and further remained constant (72 %), whereas a significant increase in the RH was noted at sections X2 and X3. A decrease in the water content at X1 and an increase of the same at X2 and X3 complement well the changes of the RH at these sections. Both the measured values of RH and water content at X2 and X3 were found to be greater than the initial values (RH = 81 % at compaction water content of 9 %) after about fourteen days indicating that the temperature gradient caused water vapour flow from the warmer to the cooler regions of the sample. At the time of termination of the test, the RH values at X2 and X3 were 97 and 93 %, respectively. Similarly, the water contents at X2 and X3 were 10.6 and 10.5 %, respectively. Higher values of RH and water content at X2 as compared that occurred at X3 can be attributed to two reasons, such as (i) a release of water vapour at the top of the sample since the top air vent was kept open during the test and (ii) the accuracies of the sensors. At X2 and X3 the values remained within the accuracies of the RH sensor (about  $\pm 3$  % above RH of 90 %) and the water content sensor used ( $\pm 2$  %).

The profiles of the temperature (Fig. 4.27a), relative humidity (Fig. 4.29a), and water content (Fig. 4.29b) clearly indicate that a steady state temperature profile was established much faster than the relative humidity and water content profiles. Similar test results have reported by other researchers in the past (Tripathy et al., 2015, 2017).

Figures 4.30a and 4.30b show the development of axial and lateral stresses at various salient levels of the sample tested. The development of axial stress at various levels (at

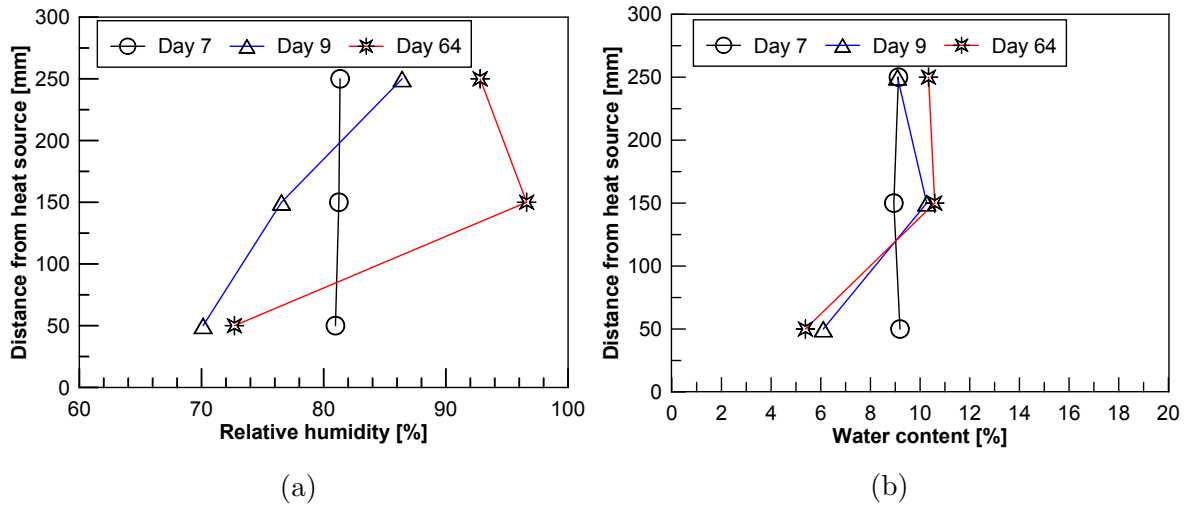


Figure 4.29: Profiles of (a) relative humidity and (b) water content at 7, 9, and 64 days.

top, bottom, and within the sample) showed similar trend. That is, the axial stress at any salient level increased due to an application of the temperature gradient and then decreased with an elapsed time. The measured axial stress at the top-end of the sample was found to be greater than that was measured at the bottom-end. The stresses measured by the embedded pressure transducers (at 100 and 200 mm from the heat source) were lower than that was measured by the load cell at the bottom of the sample.

Water vapour movement occurred from the warmer regions to cooler regions of the sample. Condensation of the water vapour, as evidenced by an increase in the water content, caused the development of swelling pressure at the top-end of the sample. Under confined condition and at equilibrium, it may be anticipated that the measured axial stress at both ends of the sample are equal. However, the axial stress developed at the top end of the sample did not get transmitted towards the bottom of the sample. This can be attributed to the following factors, such as (i) dissimilar compressibility characteristics along the height of the sample due to the difference in the water content in the warmer and cooler regions, (ii) the presence of construction joints meant for installing the pressure transducers, (iii) the side frictional resistance between the sample and the PVDF rings, and (iv) the composite nature of the sample due to the presence of sensors that created complex stress-deformation characteristics of the system.

The lateral stress at sections X1 and X2 increased and then decreased with an elapsed time, whereas at section X3, it decreased and further increased. The development of lateral stresses complements well to the water vapour movement and wetting of the bentonite sample, although close agreements between the trend exhibited by the measured water

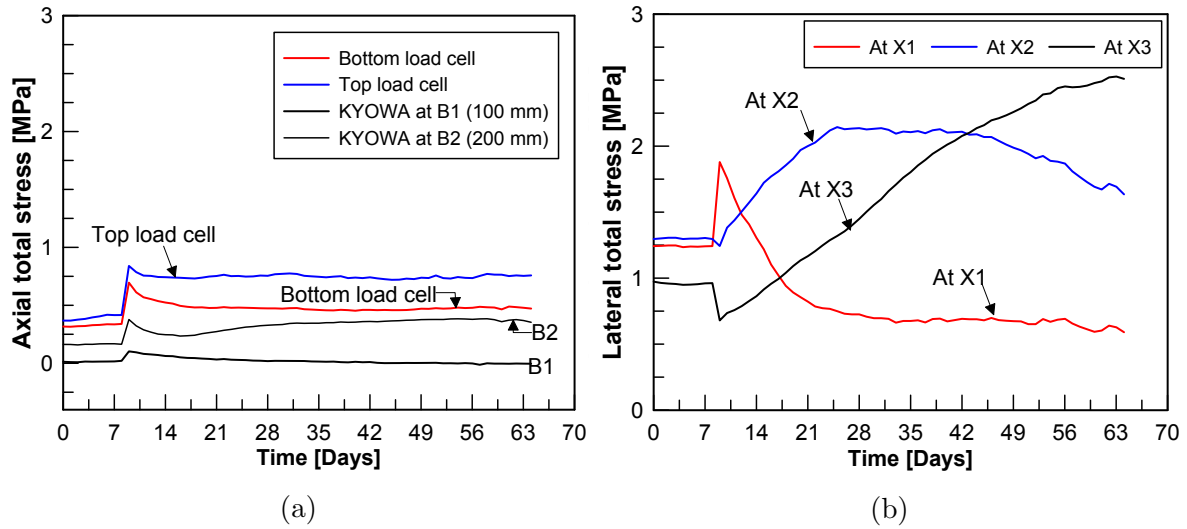


Figure 4.30: Development of (a) axial stress and (b) lateral stress at various salient levels of the sample.

content and lateral stress with an elapsed time was lacking at all levels. The lateral stress at X1 (50 mm from bottom of the sample) and the measured axial stress at bottom of the sample were similar (about 0.5 MPa). The measured lateral stress at X3 (250 mm from the bottom of the sample) at the time of the termination of the test was about 2.5 MPa, whereas the measured axial stress at 300 mm from the bottom was 0.75 MPa. Similarly, the measured lateral stress was 1.6 MPa at X2 (at mid height of the sample) at the time of termination of the test, whereas the measured axial stress by the pressure transducer located at a height of 200 mm was 0.4 MPa. The test results suggested that the sample exhibited greater magnitude of lateral stress than the axial stress towards the cooler regions. A higher magnitude of measured lateral stress as compared to the axial stress can attributed to a higher stiffness of the system in the lateral direction as compared to that in the axial direction and the impact of presence of sensors was more in the axial direction than in the lateral direction.

For the post-experimental observations, the heating was stopped, and the test set-up was allowed to cool down for 48 hours. After dismantling the test set-up, sensors and cable connections were checked visually for any possible damage due to the prolonged heating. It was observed that the cable for KYOWA pressure traducer installed at B1 (close to heating end) was deformed as depicted in Figure 4.31. The suitable preventive measures were taken to prevent it from further damage. The other sensors and respective cable connections were functioning well without any visual deformations.

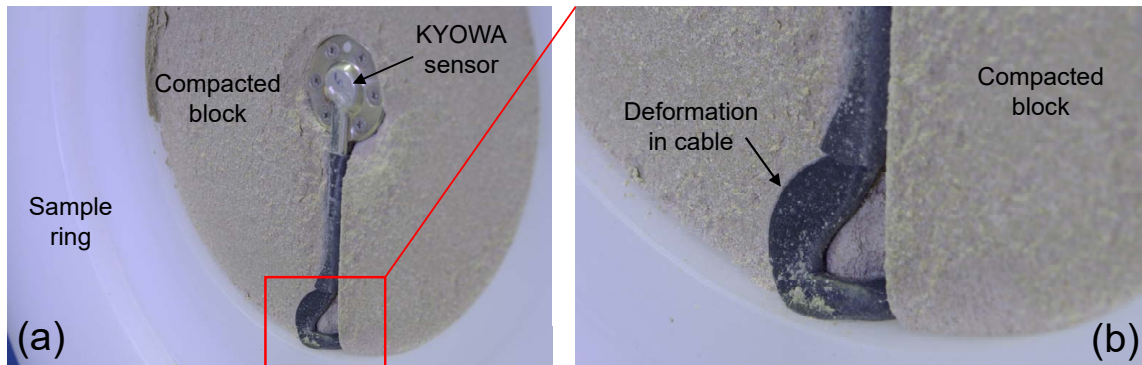


Figure 4.31: Post-experimental observation: deformation in cable connection of KYOWA miniature pressure transducer installed at position B1 (close to heating end).

## 4.5 Summary

A column-type experimental device is designed for investigating the soil behavior under a repository relevant thermal and hydraulic gradients. Sensors and monitoring instruments provide a continuous and non-destructive measurements of key state variables such as temperature, water content, relative humidity and total stress in both axial and lateral directions at various preselected locations. Prior to the main test with a sample of compacted bentonite-sand mixture, a series of tests were performed using the device to examine the air and water tightness of the constructional joints, to study the response of the load cells, and further for quantifying the temperature-induced volumetric deformation of the test set-up at an elevated temperature. These system compliance tests provided valuable information concerning the functionalities and sensitivities of various components within the device.

A test was performed with a compacted sample of bentonite-sand mixture (50:50) under an applied thermal gradient to mimic the initial heating phase of compacted buffer blocks in a repository. The test results can be summarized in following key points, such as:

- Water content redistribution occurred due to the applied temperature gradient that caused an increase in the relative humidity towards the cooler regions of the sample and a decrease of the same in the warmer regions. The relative humidity and water content at the opposite end of the heat source were found to be lesser than that were measured at the mid-height of the sample due to a release of the water vapour from the sample at the opposite end of the heat source.



- The measured axial stresses at both ends of the sample were found to be dissimilar. The difference in the axial stresses at both ends of the sample can be attributed to the dissimilar water content along the height of the sample that impacted the compressibility characteristics, the presence of construction joints, the side frictional resistance offered by the sample rings, and the presence of sensors that created a composite sample with varying stress-deformation characteristics.
- The measured lateral stress along the height of the sample was found to be higher than that measured in the axial direction and can be attributed to the dissimilar stiffness of the device in either direction and the presence of sensors in the sample that impacted the transmission of stress more in the axial direction than in the lateral direction.

The newly designed column-type experimental set-up seems promising for investigating the soil under repository relevant boundary conditions. In the next step, a water infiltration test is conducted for mimicking the transient hydration process of compacted bentonite sand blocks used as a backfill or sealing material at radioactive waste disposal galleries.



# 5 Water-infiltration test

## 5.1 Introduction

As a primary function, the backfill material creates a low-permeable zone around the waste and provides the mechanical stability to the entire disposal system. Figure 5.1 illustrates the application of bentonite-based materials as a backfill or a buffer material in a nuclear waste repository. In the field, the constructional gaps exist between the compacted blocks and also in between the blocks and host rock. The excavation activities and the resulting stress redistribution in the host rock create an excavation damaged zone (EDZ) around the underground openings. The EDZ acts as a preferential flow path, as a result the water may flow towards the waste. The bentonite-based materials have the ability to seal the excavation-induced preferential flow paths around the excavated openings. Once the constructional gaps are completely filled by the swollen bentonite, the swelling pressure develops in both axial and lateral directions. The rate of saturation and the resulting swelling pressure play a key role in the long-term safety of the entire disposal system. For instance, the swelling pressure must not be higher than the in-situ stresses in the host rock, at the same time it should be high enough to stabilize the excavation-induced mechanical and hydraulic disturbances in the entire disposal system.

Considering these aspects, a water infiltration test was conducted with a compacted Cal-cigel bentonite-sand mixture (50:50) at room temperature to mimic the transient hydration of a backfill material in repository. The effect of groundwater geochemistry on the bentonite hydration process is not considered in this test. Hence, the distilled water was supplied from the bottom-end under 15 kPa hydration pressure to mimic the water ingress from the host rock. The test was performed with the newly designed column-type experimental device, which facilitated the continuous and non-destructive measurements of temperature, relative humidity, water content and total stresses in both axial and lateral direction at various preselected locations along the sample height. The test was conducted for a period of 349 days.

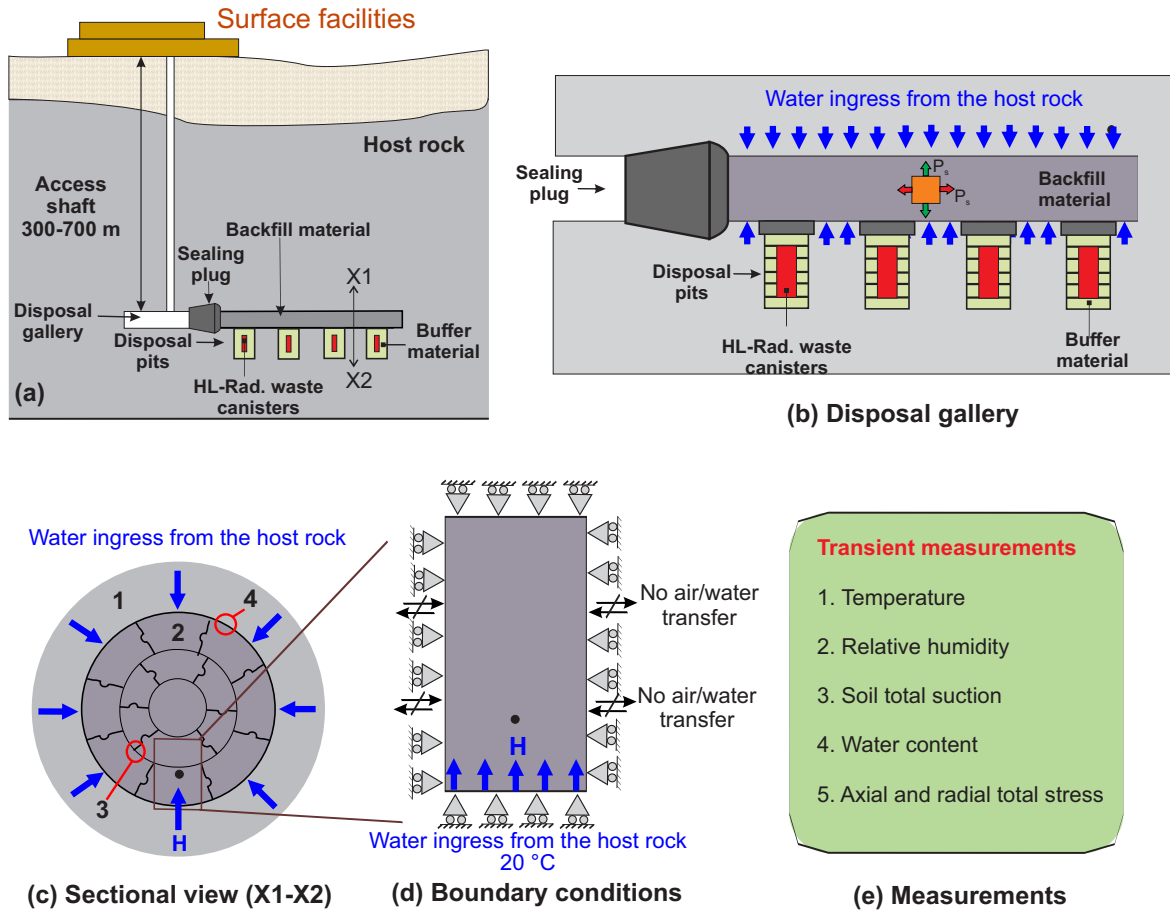


Figure 5.1: (a) Deep geological disposal concept for disposing the high level radioactive waste, (b) transient hydration of backfill material and resulting swelling pressure pressure in vertical and horizontal directions against the host-rock and sealing plugs ( $P_s$  = swelling pressure), (c) sectional view along the X1-X2 axis (legends: 1 = host rock, 2 = compacted blocks, 3 = constructional gaps between the compacted blocks, 4 = gap between the compacted blocks and host rock), (d) flow and displacement boundary conditions for the backfill element during the mock-up test, and (d) transient measurements during the mock-up test.

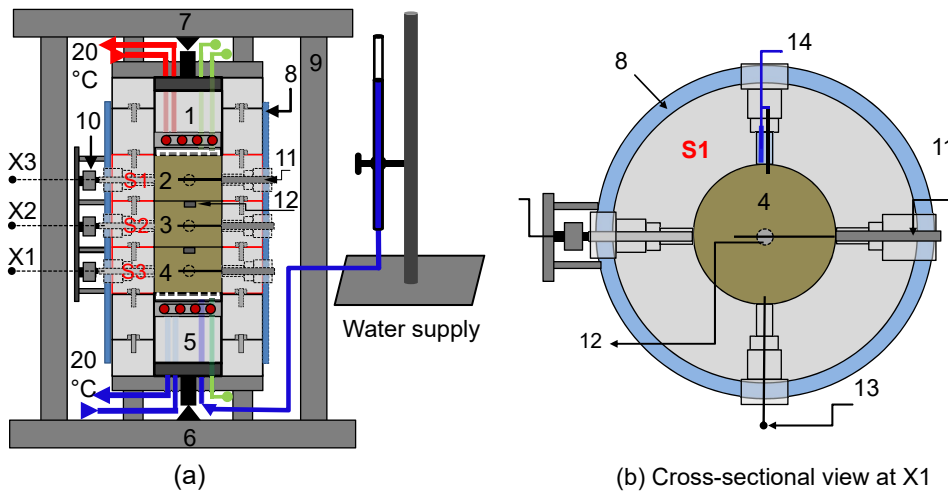
## 5.2 Sample preparation and testing program

The investigated material was a compacted mixture of Calcigel bentonite and sand with equal dry mass fractions. The mixture with 9 % initial water content was compacted in three layers using the uniaxial static compaction method under 30 MPa vertical stress. During the compaction process, the surface of the compacted layer was scarified prior to place the next layer to ensure a proper homogeneous connection between two layers. The initial suction (i.e., 26.9 MPa) was measured using the chilled mirror technique corresponding to 81 % initial relative humidity.

Once the compaction process was over, the compacted block was extruded from the mould. The achieved mean dry density of cylindrical blocks (dia. = 153 mm; height = 100 mm) were in the range of 1.80 to 1.85 Mg/m<sup>3</sup>. The compacted sample exhibited the post-compaction strains during the extrusion process. Consequently, the block diameter was slightly larger than the inner diameter of sample rings (150 mm). Hence, these blocks were prepared for installing inside the sample ring with monitoring sensors after the extrusion from the mould. For installing the TDR wave-guides in the soil block, two parallel holes were drilled (dia. = 3.5 mm; length = 110 mm). Additionally, two holes were also drilled for inserting the Pt100 sensor (dia. = 6 mm; length = 10 mm) associated with VAISALA relative humidity sensor and independent Pt100 sensor (dia. = 3 mm; length = 10 mm). For the installation of KYOWA miniature pressure transducers, a seating space was created during the compaction process using stainless steel dummy having dimensions identical to KYOWA pressure transducer. Total three blocks were compacted to achieve the required height of soil sample i.e., 300 mm.

The volume fractions of the sensors in the sample was only 0.14 % (six Pt100 sensors, three TDR probes and two miniature pressure transducers). The TDR sensor constitutes of two parallel waveguides made of stainless steel and are coated with polyvinyl chloride for waterproofing. For correct measurements of the water content, the entire length of the probes must be embedded in the soil sample. These wave-guides are sensitive to deformation. Hence, the sensor's embedment has insignificant effect on the sample response during the hydration under confined condition.

The test was conducted under a constant volume condition at room temperature; an air outlet at the bottom plug was kept closed, while an air outlet at top plug was kept open to evacuate the air during the hydration process. Sensors along with data logger continuously monitored temperature, relative humidity, water content and total stress in both lateral and axial directions at various preselected locations. The test was conducted



**Legends:**

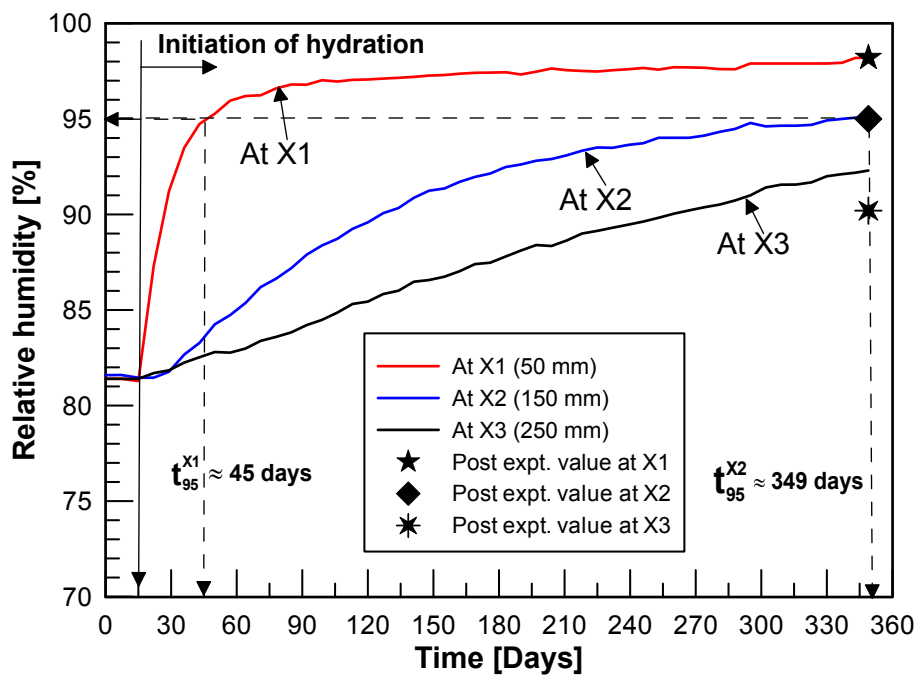
1 = Top plug; 2, 3, 4 = Compacted blocks; 5 = Bottom plug; 6 = Bottom load cell; 7 = Top load cell; 8 = Confining cell; S1, S2 and S3 = Sample rings; 9 = Rigid frame; 10 = Radial load cells; 11 = TDRs; 12 = Pressure transducers; 13 = Pt100 sensor; 14 = RH sensor with additional Pt100 probe; X1, X2 and X3 = Measurement sections; ●●●● = heating/cooling coil.

Figure 5.2: Schematic view, (a) test setup for water infiltration test and (b) cross sectional view and installation of monitoring sensors.

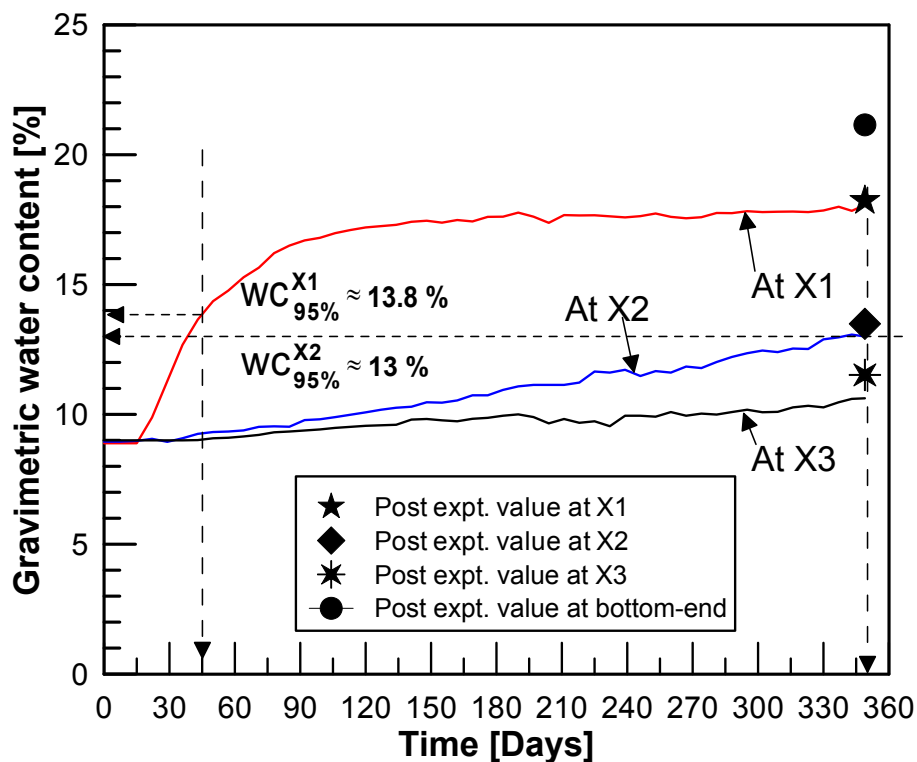
for a period of 349 days. For the post-experimental measurements, samples were collected from various locations along the height of soil sample during the dismantling of test set-up. The relative humidity was measured by Chilled Mirror technique, whereas the water content was measure using the oven-drying method. Figure 5.2 shows the test set-up and the installed sensors and monitoring instruments.

### 5.3 Test results

Figure 5.3a shows the relative humidity (RH) evolution over elapsed time for measurement sections X1, X2, and X3. The post-experimental measurements are also shown. The initial relative humidity of soil sample (i.e., 81.5 %) captured by the RH probes agreed well with the measured value (i.e., 81 %) using the chilled mirror technique. The RH measurements at section X1 exhibited a sharp increase before reaching to 95 % in 45 days. With further hydration, the relative humidity increased gradually to 98.3 % in 120 days and latter remained almost constant. A similar trend can be observed for measurement sections X2 and X3. The measured values increased linearly before reaching to 95 % at X2 and 93 % at X3 in 349 days.



(a)



(b)

Figure 5.3: (a) Elapsed time vs. relative humidity and (b) elapsed time vs. water content plots at salient levels along the height of the sample.

Figure 5.3b presents the evolution of water content with elapsed time at sections X1, X2 and X3 along with the post-experimental measurements. Similar to the relative humidity evolution at section X1, the water content increased rapidly before reaching to 13.8 % in 45 days. With further hydration, the water content at section X1 gradually increased to 17 % in 105 days and latter remained almost constant. The measurements at section X2 and X3 exhibited a lower incremental rate, particularly for section X3. The measured water content at section X2 reached to 13 % in 349 days. On the other hand, the measured water content at section X3 increased to 10.8 % from an initial value of 9 % in 349 days. The evolution of water content showed that the measured water content at X1 (13.8 %) was higher than the measured one at section X2 (13 %) at the same relative humidity level (95 %) or total suction (7 MPa).

The computed variables i.e., soil total suction and degree of saturation vs. elapsed time are shown in Figure 5.4. Based on the transient relative humidity measurements along with the measured temperature, soil total suction ( $s$ ) can be computed using Kelvin's equation:

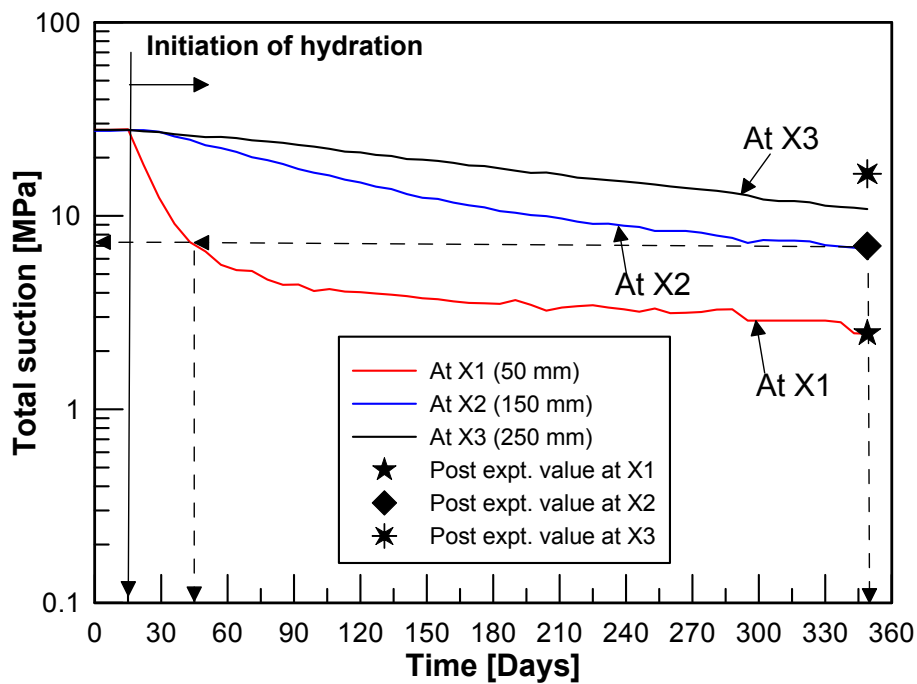
$$s = - \left( \frac{\rho_w RT}{M_w} \right) \ln \left( \frac{RH}{100} \right) \quad (5.1)$$

where,  $s$  is soil total suction,  $\rho_w$  is the water unit mass (1 Mg/m<sup>3</sup>);  $R$  is the universal (molar) gas constant (8.31432 J/mol-K);  $T$  is the absolute temperature (273.15 +  $t_{\text{measured}}$  °K);  $M_w$  is the molecular mass of water vapour (18.016 kg/kmol) and  $RH$  is the relative humidity in (%).

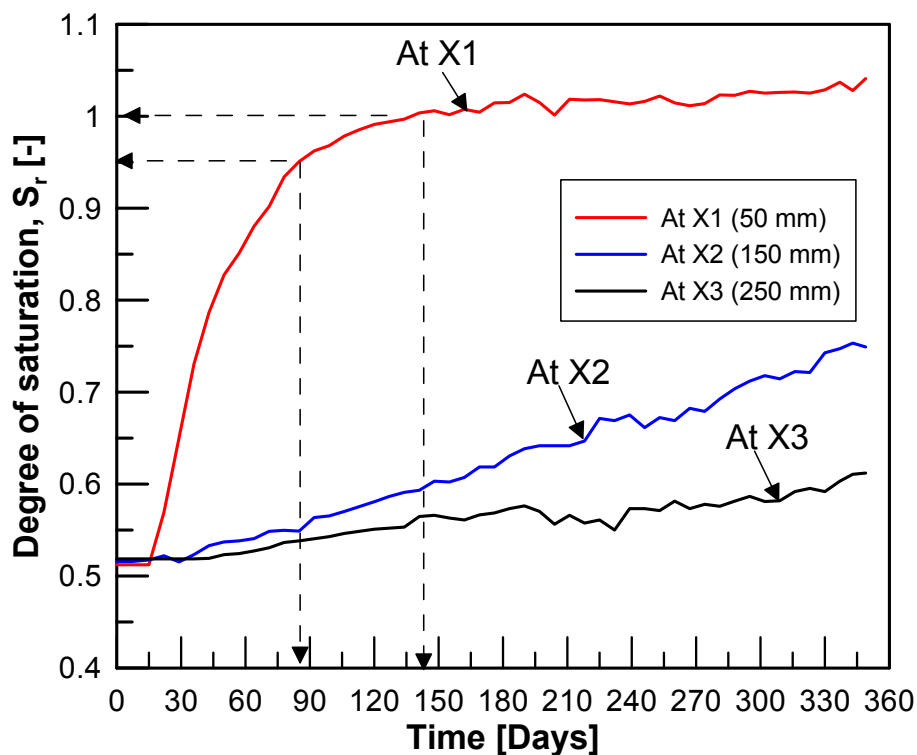
Figure 5.4a shows soil total suction evolution with elapsed time for measurement sections X1, X2 and X3 along with the post-experimental measurements. The soil total suction decreased rapidly close to the hydration-end (section X1) and reached to 7 MPa in 45 days. With further hydration, it decreased gradually to 2.43 MPa in 349 days. On the other hand, the total suction at section X2 and X3 exhibited successive decrease to 7 MPa and 10.54 MPa in 349 days, respectively.

The degree of saturation values during the transient hydration process were deduced from the water content measurements by assuming a constant void ratio (i.e., 0.47) along the height of soil sample. However, the assumption is not valid in case of expansive soils due to their swelling and collapse behavior during the hydration. Figure 5.4b shows the evolution of degree of saturation for three measurement sections. The initial degree of saturation was close to 0.51 for sample having approximately 9 % initial water content and a global void ratio of 0.47 along the height. The section X1 achieved 95 % saturation in 87 days and 100 % saturation in 142 days. Later, the computed degree of saturation values





(a)



(b)

Figure 5.4: (a) Elapsed time vs. soil total suction and (b) elapsed time vs. degree of saturation plots at salient levels along the height of the sample.

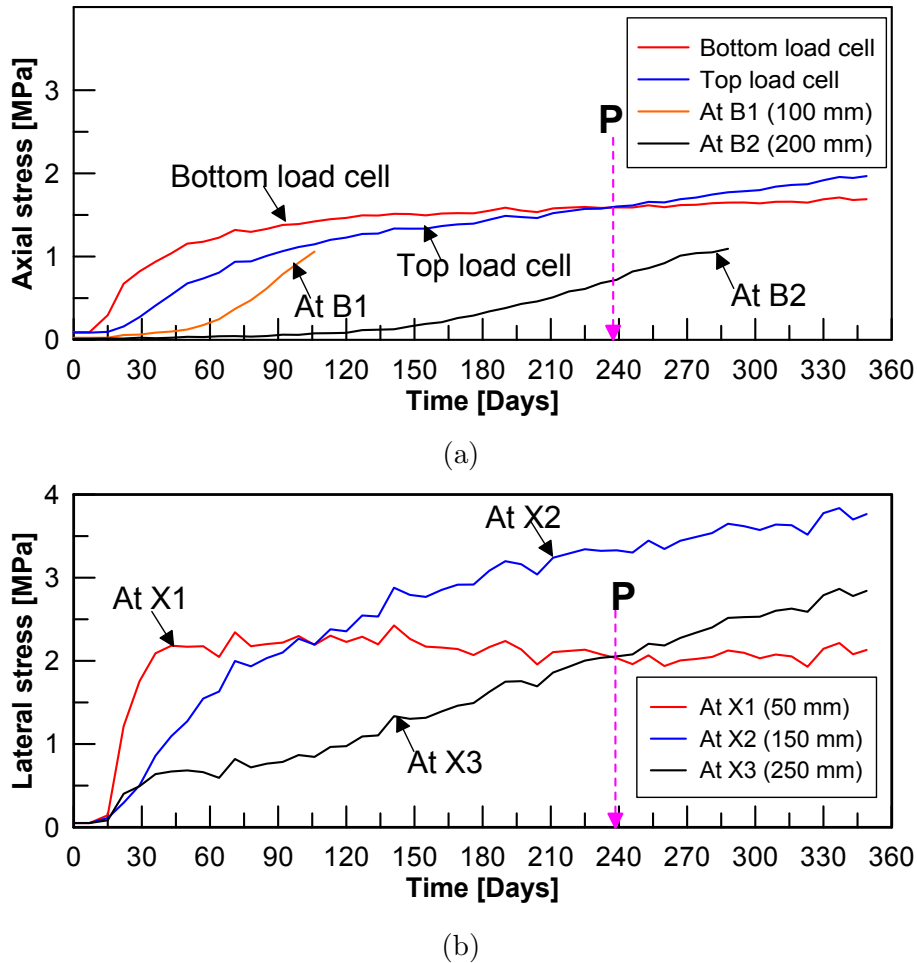


Figure 5.5: (a) Elapsed time vs. soil total suction and (b) elapsed time vs. degree of saturation plots at salient levels along the height of the sample.

greater than 1 was observed at section X1. While the sample away from hydration end remained in the unsaturated state within the entire testing period. The sample achieved close to 75 % and 60 % saturation at measurement sections X2 and X3 after 349 days of hydration, respectively.

Figure 5.5a shows the axial total stress evolution over elapsed time, the measurements were performed with the axial load cells and KYOWA miniature pressure transducers. The KYOWA miniature pressure transducers were installed between two compacted blocks (i.e., 100 mm and 200 mm from the bottom-end). Prior to initiate the hydration from the bottom-end, an initial siting stress of 50-60 kPa was applied during the installation of test set-up to ensure a proper connection between the sample and load cells. With the initiation of hydration, the bottom load cell responded quickly and reached to 1.1 MPa in 45 days. After time  $t = 45$  days, the axial total stresses measured with the bottom load

cell increased gradually before reaching 1.68 MPa in 349 days. The measured axial total stress with the top load cell remained lower than the measured one with the bottom load cell for a testing period of 238 days as shown by point P in Fig. 5.5a.

Figure 5.5b presents the evolution of lateral total stress at measurement sections X1, X2 and X3. In the current test, a cylindrical piston and load cell assembly measured the total stress in the lateral direction at section X1, X2 and X3. During the installation of test set-up, these pistons were kept in contact with the sample by applying some nominal siting stress. With the initiation of hydration from the bottom-end, the lateral total stress increased rapidly and exhibited higher values as compared to the measured axial total stresses with the top and bottom load cells. The measurements at section X1 showed a rapid increase and reached to 2.18 MPa in 45 days. With the further hydration, the measured values at X1 showed some oscillations before reaching to a value of 2.13 MPa in 349 days. The measurements at X2 showed a lower incremental rate as compared to the measured values at X1. The lateral stress at section X2 increased asymptotically and reached to 3.76 MPa in 349 days. On the other hand, the measured lateral stress at section X3 increased linearly during the entire testing period. The experimental results clearly exhibit the effect of distance from the hydration end on the lateral swelling pressure dynamics. The lowest rate of increase is observed at the farthest measurement section X3.

The miniature pressure transducer has  $4.15\text{E-}4\text{ m}^2$  pressure sensing area and 1 MPa rated capacity. These sensors were installed in a seating-space in the compacted block (see Fig. 5.6). The measurements revealed that these sensors have some initial gap between the pressure-sensing surface and the upper compacted block; this may be due to improper installation. The measurements showed that these sensors responded when the hydration front reached to the zone of their seating-space, the pressure transducer close to the bottom block at B1 reached to 1 MPa within 105 days. On the other hand, the sensor close to top block at B2 reached to 1 MPa within 285 days.

## 5.4 Discussion

The water infiltration test mimics the transient hydration of compacted bentonite-sand mixture (50:50) as a backfill material at the nuclear waste repository. The test was performed for a period of 349 days. The transient measurements revealed that the sample did not achieve full saturation within the testing period. However, the test results highlighted

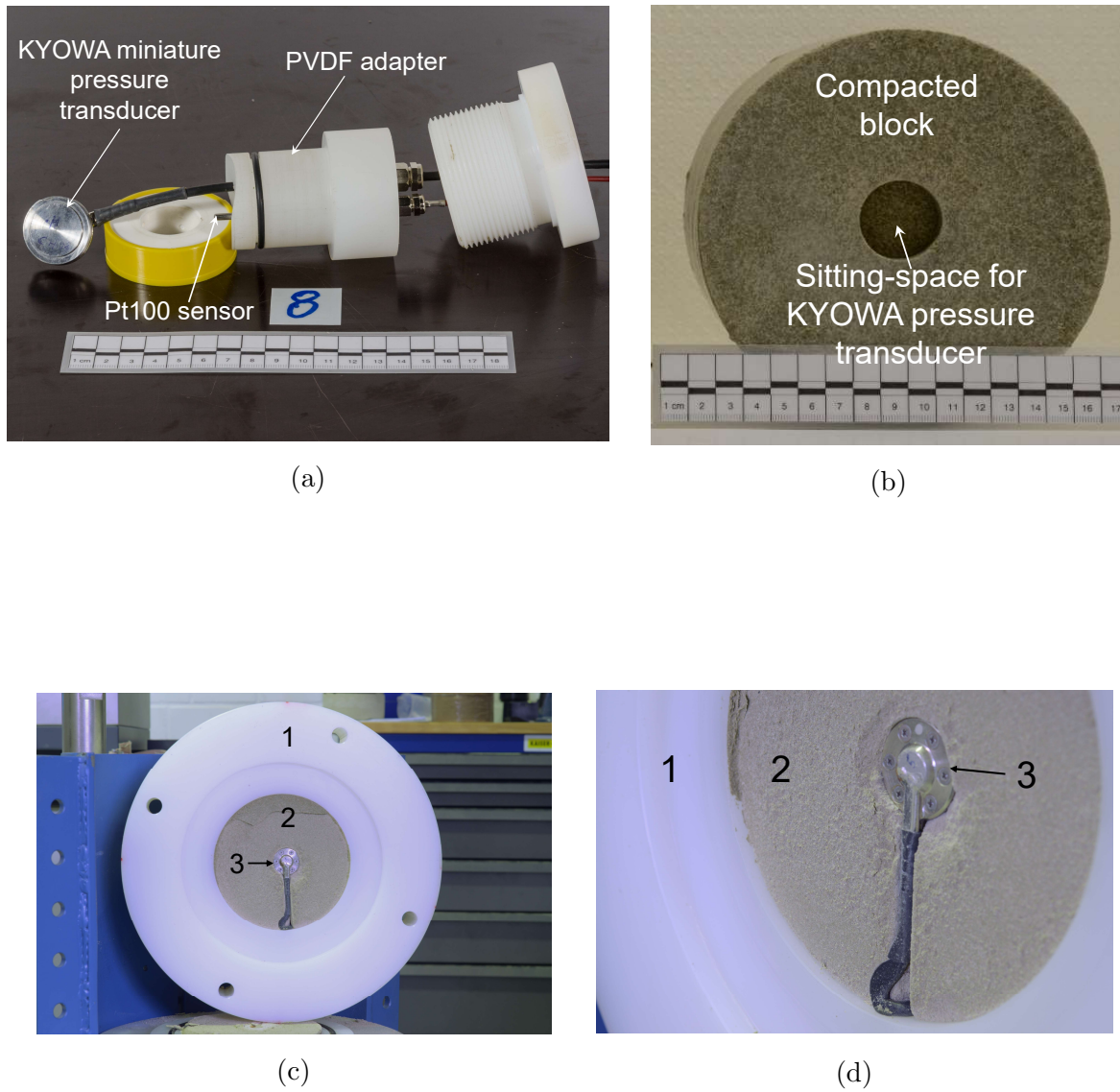


Figure 5.6: Installation of KYOWA miniature pressure transducer in floating condition, (a) KYOWA miniature pressure transducer with PVDF adapter (b) compacted block and sitting-space for installing the sensor, (c) and (d) installation of sensor between two blocks (legends: 1 = PVDF sample ring, 2 = compacted block, 3 = KYOWA sensor).

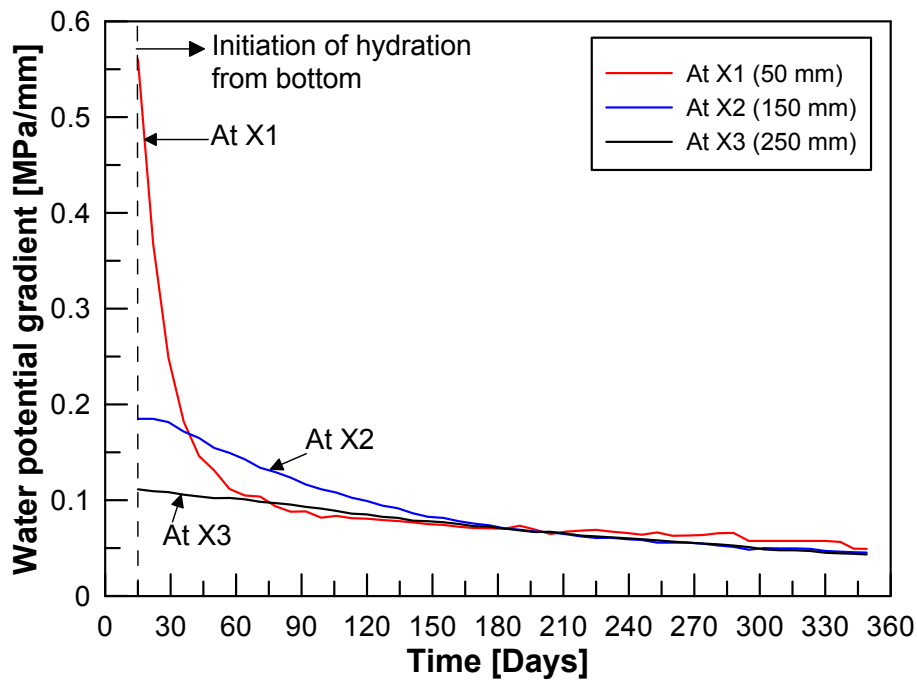


Figure 5.7: Elapsed time vs. water potential gradient along the height of soil sample.

several key features of coupled hydro-mechanical behavior of material. The observed test results are discussed in three subsections,

- Evolution of state variables,
- Swelling behavior, and
- Soil water retention behavior.

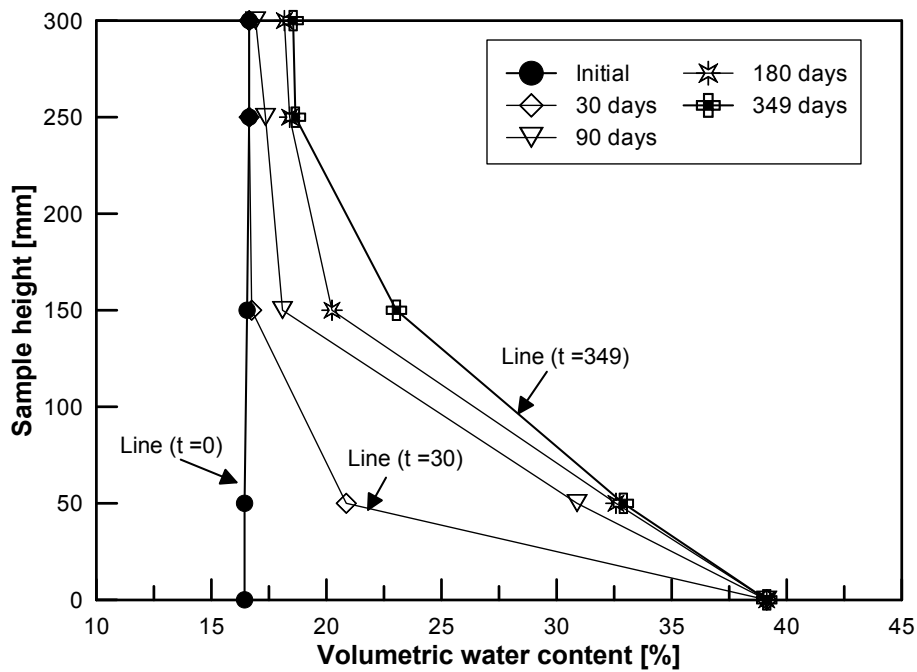
#### 5.4.1 Evolution of state variables

In the present test, the liquid water was supplied from the bottom-end under 15 kPa hydration pressure. The bottom-most layer of sample, which was in contact with the saturated porous stone achieved saturation immediately after the initiation of hydration. Pusch & Kasbohm (2001) investigated the effect of applied hydration pressure on the extension of the wetting zone in the highly compacted blocks of MX80 bentonite (dry density =  $1.51 \text{ Mg/m}^3$ ) by injecting water under a pressure of 0.650 MPa through a perforated injection pipe for 3 and 20 minutes. The test result revealed that the applied hydration pressure affected the rate of saturation only up to 10 mm distance from the injection point. In the present case with the applied hydration pressure of 15 kPa, the

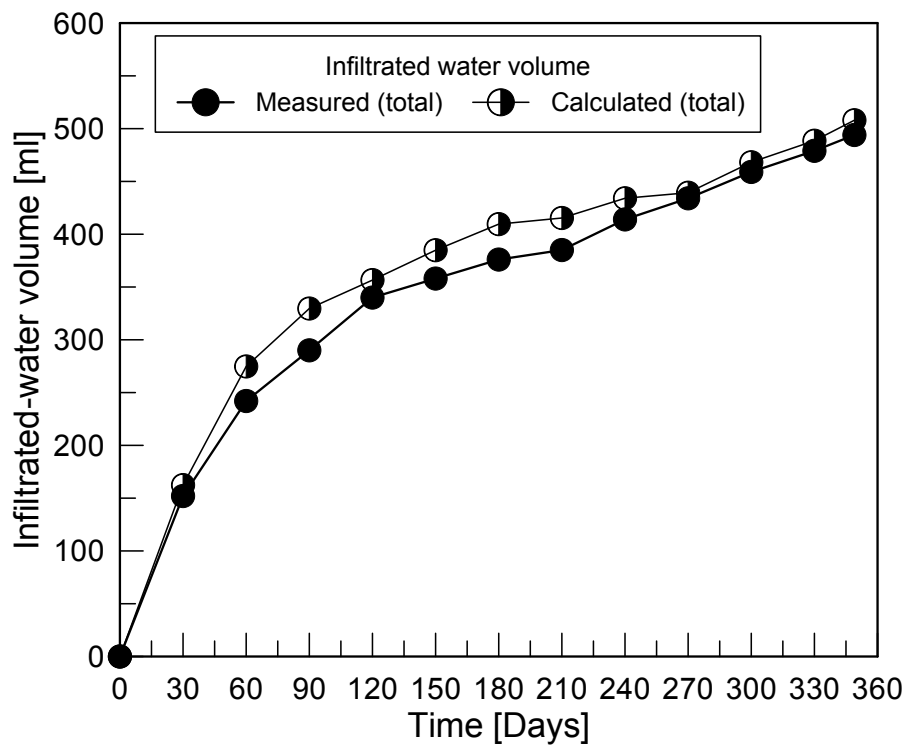
water migration took place due to the water potential gradient along the height of soil sample, which was higher in the beginning of test and decreased rapidly close to the hydration-end (see Fig. 5.7). As a result, the water content increased rapidly at section X1 with the initiation of hydration (see Fig. 5.3b). For the farther sections i.e., X2 and X3, the water migration process can be depicted as diffusion process where the concentration gradient is equivalent to the water content gradient.

In the further analysis of results, the water volume infiltrated into the soil sample was computed from the volumetric water content isochrones (see Fig. 5.8a). These isochrones were obtained from the transient water content measurements by assuming a constant dry density ( $1.85 \text{ Mg/m}^3$ ) along the height of soil sample. Prior to initiate the hydration, the mean volumetric water content along the height of soil sample was equal to 16.65 % (i.e.,  $9 \times 1.85$ ). With the initiation of hydration, soil total suction dissipated rapidly to zero at the bottom-most layer of the sample (i.e.,  $z = 0 \text{ mm}$ ). The corresponding volumetric water content (39.13 %) at  $z = 0 \text{ mm}$  was calculated from the measured water content during the post-experimental investigations and assigned to all the time steps. The transient water content measurements were not performed at the top-end (i.e.,  $z = 300 \text{ mm}$ ), the reported values in Figure 5.8a were obtained from the linear interpolation. The water volume infiltrated into the soil sample was computed at different time intervals and compared with the injected water volume, which was measured during the test (see Fig. 5.8b). A good agreement can be observed between the computed and the measured data.

However, the fact of having the same relative humidity corresponding to two different water content values at section X1 and X2 as observed in Figure 5.3 along with the different gravimetric water contents i.e., 21.15 % at the bottom end and 18 % at section X1 at full saturation stage indicate the redistribution of porosity along the height. Several researchers have observed the porosity redistribution during the hydration of compacted bentonite under confined conditions (Monroy et al., 2010; Romero et al., 2011; Villar et al., 2014). For instance, Villar et al. (2014) analyzed samples of compacted bentonite blocks, which were collected during the dismantling of isothermal hydration test (average temperature  $16 \text{ }^\circ\text{C}$ ) for 10.5 years. The post-mortem analyses revealed the increasing dry density from the hydration-end towards the inner sections. The porosity redistribution may lead to an error in the computed degree of saturation based on the assumption of constant initial void ratio (i.e., 0.47) along the height. In the present case, degree of saturation larger than one was obtained at the section X1 (50 mm from bottom end) at low suction values (see Fig. 5.4b), which may be attributed to the underestimation of the



(a)



(b)

Figure 5.8: (a) Volumetric water content isochrones at different selected time intervals and (b) measured and calculated infiltrated-water volume into the soil sample.

void ratio. Additionally, Jacinto et al. (2016) highlighted the effect of the density of water on the computed degree of saturation in the case of samples of expansive clays tested at constant volume condition. Villar & Lloret (2004) showed that the average density of water in saturated samples of compacted bentonite depends on the specimen density and gravimetric water content, and values higher than  $1.05 \text{ Mg/m}^3$  and up to  $1.22 \text{ Mg/m}^3$  were obtained for bentonite dry densities between  $1.3$  and  $1.8 \text{ Mg/m}^3$ .

### 5.4.2 Swelling behavior

The measured axial and lateral total stresses data were analyzed together with the transient water content and relative humidity measurements to better understand the coupled hydro-mechanical behavior of compacted Calcigel bentonite-sand mixture. The axial total stress evolution at the bottom-end showed a good resemblance with the relative humidity and water content evolution at section X1. With the initiation of hydration, it increases rapidly to  $1.1 \text{ MPa}$  in 45 days and later showed a gradual increase before reaching to  $1.68 \text{ MPa}$  in 349 days. During the clay-water interaction, the bentonite-based materials swells due to crystalline swelling and osmotic/double layer swelling mechanisms (van Olphen, 1977; Madsen & Müller-Vonmoos, 1989). The relative importance of these two mechanisms is different depending on the nature of exchangeable cations (i.e.,  $\text{Na}^+$  or  $\text{Ca}^{+2}$ ). For instance, Cases et al. (1997) found that the crystalline swelling during the adsorption was completed at a relative humidity of about 70 % in case of Ca-rich bentonite. On the other hand, Saiyouri et al. (2000, 2004) found that the crystalline swelling in Ca-rich bentonite completed at a suction of about  $4 \text{ MPa}$ , when a transition in the interlayer spacing from  $1.56 \text{ nm}$  (two monomolecular layers of water) to  $1.86 \text{ nm}$  (three monomolecular layers) took place. Ca-rich bentonite has a considerable range of stability with two molecular layer of water and it has substantially no expansion beyond an interlayer spacing of about  $1.9 \text{ nm}$  (Aylmore & Quirk, 1959). However, it may continue to accommodate more water on the particle's outer surfaces and result in to the inter-particle osmotic swelling (Madsen & Müller-Vonmoos, 1989; Segad et al., 2010).

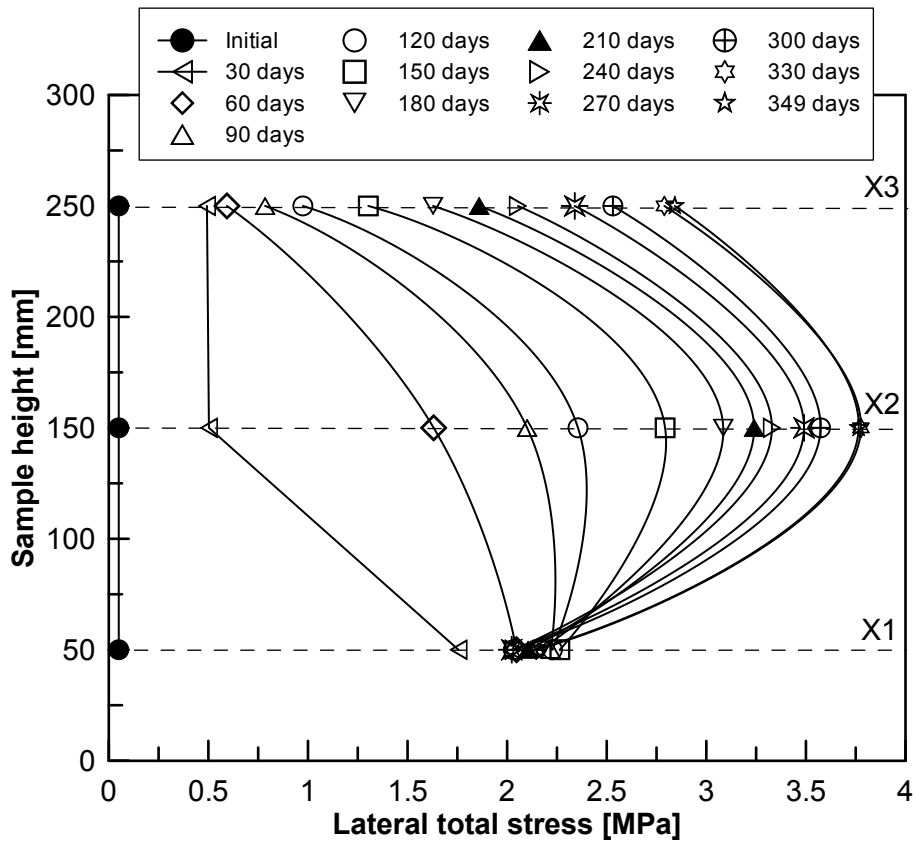
In the present case, the initial relative humidity of Calcigel bentonite-sand mixture was 81 %. At the relative humidity of 80 %, two monomolecular layers of water (d001 spacing =  $1.56 \text{ nm}$ ) exist in Ca-rich bentonites (Saiyouri et al., 2000, 2004; Ferrage et al., 2005). It signifies that the swelling of Calcigel bentonite-sand mixture (50:50) exposed to water (within 45 days) is due to the crystalline swelling which occurs because of the transition of interlayer spacing from two monomolecular to three monomolecular layers of water. As a result, the rapid increase in the axial swelling pressure at the bottom-end was



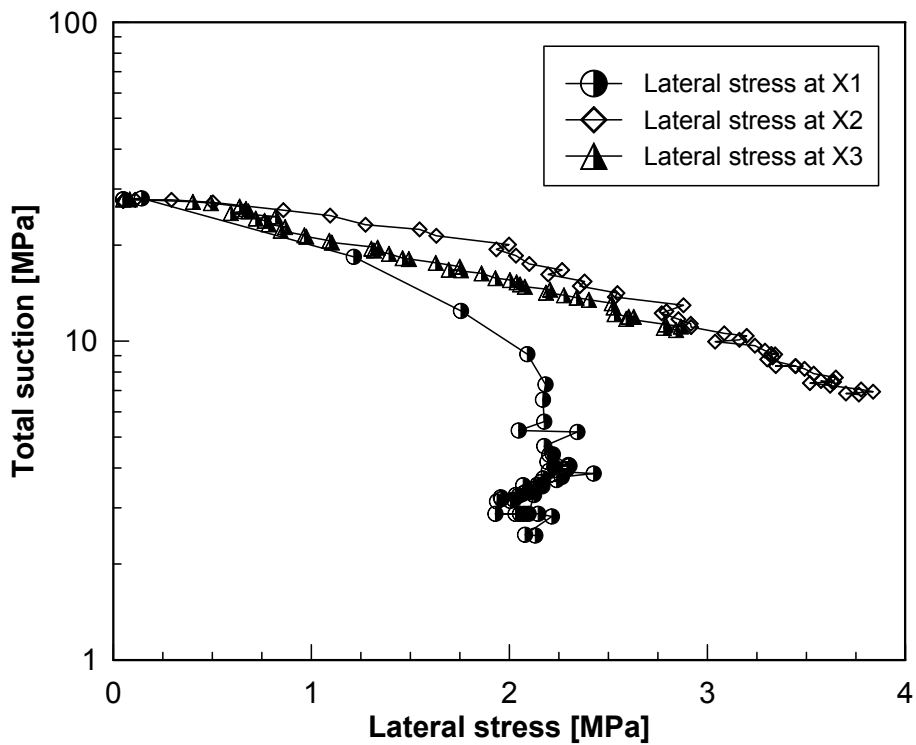
observed during the test. With the further hydration, the sample accommodated more water on the surfaces of clay particles. As the interlayer space can not exceed beyond 1.9 nm (Aylmore & Quirk, 1959), the gradual increase in the swelling pressure beyond the crystalline swelling was due to the osmotic phenomenon.

The aggregate swelling in the lower elements causes the compression of upper elements. Meanwhile, the top load cell measures the applied stress from the bottom elements. Under confined condition and at equilibrium, it may be anticipated that the measured axial stress at both ends of the sample are equal. However, the axial stress developed at the top end of the sample was not transmitted towards the bottom of the sample. This can be attributed to the following factors, such as (i) dissimilar compressibility characteristics along the height of the sample due to the difference in the water content along the height, (ii) the presence of construction joints meant for installing the pressure transducers, (iii) the side frictional resistance between the sample and the PVDF rings, and (iv) the composite nature of the sample due to the presence of sensors that created complex stress-deformation characteristics of the system. As shown in Figure 5.5a, the axial total stress measured at top end increases continuously and exceeds the bottom load cell measurement at time  $t = 238$  days as depicted by point P. This signifies the initiation of the swelling of the upper block under the influence of above-mentioned factors. Börjesson et al. (1995) investigated the effect of interfacial friction on the swelling-compression behavior of compacted bentonite-based specimens and found that the lateral stresses (corresponding to the normal stresses towards the rock surface) are higher than the stress in the swelling direction. It signifies that the swelling pressure is likely to be lower towards the sealing plug than on top of the canister due to the friction between the buffer and the rock.

The measured total stresses at section X1, X2 and X3 in lateral direction were higher than the measured total stress in the axial direction with top and bottom load cells. To gain a better understanding, the lateral stress profiles (see Fig. 5.9a) and the measured lateral stress vs. soil suction at respective measurement sections (see Fig. 5.9b) are presented, which indicate that the sample close to hydration-end exhibits elastoplastic behavior, while the measurement sections X2 and X3 show the elastic behavior. In the initial phase of hydration, the elastic swelling is dominant at section X1 close to the hydration-end. Due to the elastic swelling of the bottom part, the upper parts of the sample experience compression. It is worth to mention here that, the sample exhibits different stiffness values along the sample height due to the heterogeneity in the transient hydration process. Consequently, the sample exhibits different lateral total stress evolution rates along the



(a)



(b)

Figure 5.9: (a) Lateral total stress profiles along the height of soil sample and (b) lateral total stress vs. soil suction for measurement sections X1, X2 and X3.

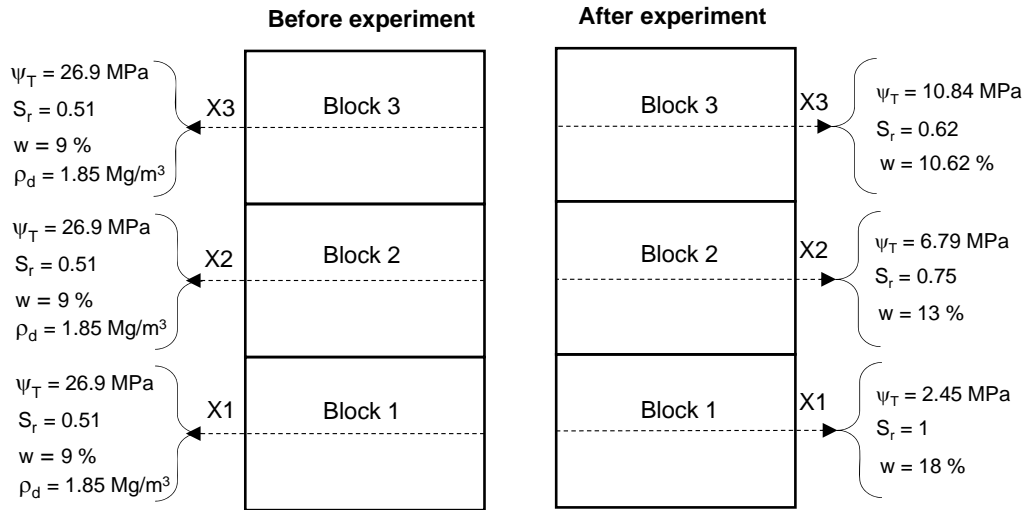
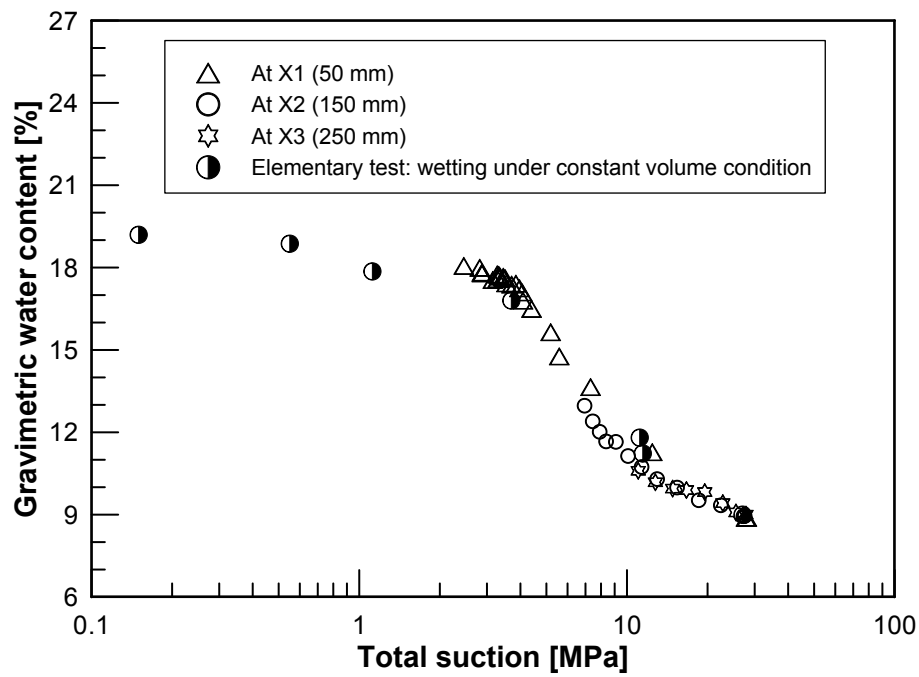


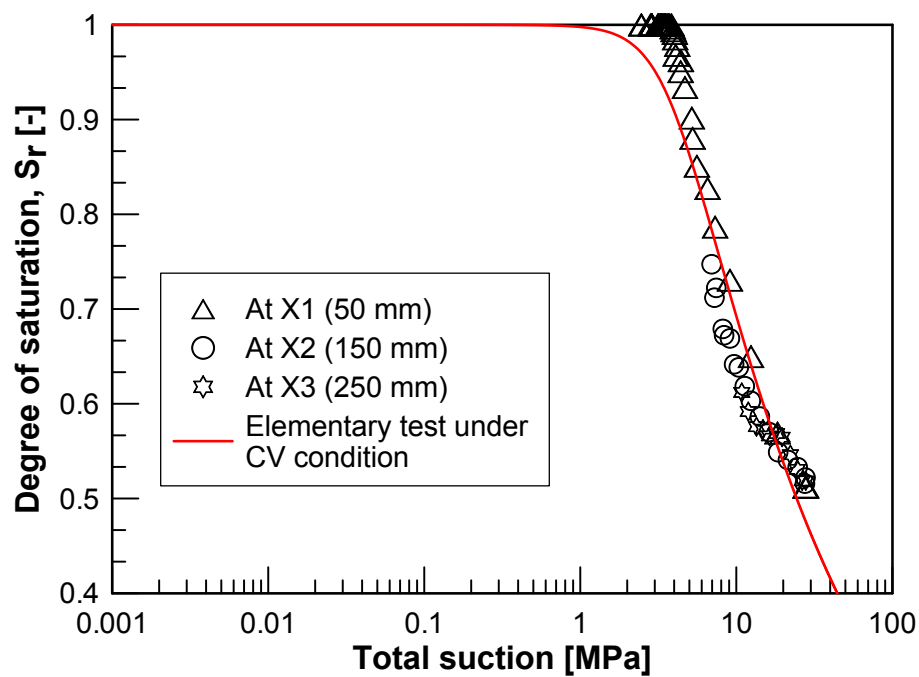
Figure 5.10: Material physical state before and after the test.

height. With the progressive hydration, the suction reduction leads to a decrease in the apparent preconsolidation pressure and consequently sample undergoes to plastic deformation, which is evident from the lateral total stress measurements at section X1. In addition to the heterogeneity in the transient hydration process, the presence of technical/construction joints meant for installing the sensors also affect the soil stiffness. In the present case, lateral total stress measurements were performed with a cylindrical piston (dia. = 20 mm) and a load cell assembly. These pistons were kept in contact with the sample at sections X1, X2 and X3 during the installation process. In the axial direction, top and bottom load cells measure the soil response during transient hydration process in the presence of interfacial friction (b/w the soil sample and cell wall) and the technical voids, which provide a higher stiffness of the system in the lateral direction as compared to that in the axial direction.

Hence, the saturation of compacted bentonite-sand mixture under applied hydraulic gradient involves various complex processes, such as soil swelling, interaction between different soil layers, and heterogeneity in the sample condition during the transient hydration. The physical state of soil sample before and after the test is shown in Figure 5.10, which depicts the hydration-induced heterogeneity in the sample along the height as a function of distance from the hydration-end.



(a)



(b)

Figure 5.11: Transient soil water retention profiles along the sample height during the hydration process, (a) gravimetric water content versus suction and (b) degree of saturation versus suction.

### 5.4.3 Soil water retention behavior

For investigating the soil water retention behavior in transient state, the measured water content were plotted against the computed soil total suction values ( $s$ ) as shown in Figure 5.11a. Similarly, the transient soil water retention curves ( $s - S_r$ ) were plotted by assuming the constant void ratio (0.47) along the height (see Fig. 5.11b). The measured data were compared with the water retention tests under constant volume condition. These tests were conducted with the isochoric cell, where the as-compacted sample (dia. = 50 mm; height = 15 mm) was subjected to multistage wetting by controlling the suction using the osmotic technique. As the water retention capacity of compacted bentonite-based materials is significantly affected by the initial dry density and the applied volume constraints imposed during the wetting process (Villar, 2007; Ye et al., 2009; Seiphoori et al., 2014; Gatabin et al., 2016), sample initial conditions (i.e., dry density = 1.80-1.85 Mg/m<sup>3</sup> and water content = 9 %) were kept similar to the water infiltration test.

The transient measurements (soil suction vs. gravimetric water content) agree well with the elementary test results in Figure 5.11a. On the other hand, the transient data ( $s - S_r$ ) at section X1 show some disagreement with the elementary test results and overestimates the degree of saturation at lower suction levels ( $s \leq 7$  MPa) as shown in Figure 5.11b. It may be attributed to the assumption of constant void ratio along the height of soil sample. As mentioned in the section 5.4.1, the fact of having the same relative humidity corresponding to two different water content values at section X1 and X2 (see Fig. 5.3) along with the different gravimetric water contents i.e., 21.15 % at the bottom end and 18 % at section X1 at full saturation stage indicate the redistribution of porosity close to the hydration-end. As a result, the assumption of constant void ratio (0.47) may lead to an underestimation of actual void ratio particularly at sections close to the hydration-end.

It is worth to discuss here the errors in soil total suction measurements using relative humidity sensors close to saturation levels ( $RH \geq 95\%$ ) due to the temperature gradient between the soil sample and the RH sensor. Agus & Schanz (2007) highlighted that if the error due to temperature gradient is limited, for instance, to 30 % of the measured value, the measurement of total suction will be limited to a value of about 850 kPa assuming that a 0.5 °C temperature gradient exists in the system. The temperature gradient of 0.5 °C can likely be maintained in temperature controlled laboratory, whereas the accurate measurement of total suction to as low as 100 kPa with 30 % error requires a means to control temperature within  $\pm 0.04$  °C.

In the present study, the test was conducted for 349 days. Due to the long duration of the experiment, it was not easy to repeat the test to evaluate the duplicability of the test results. However, the reliability of the reported data can be appreciated by its agreement with existing data available in the literature as discussed above.

## 5.5 Summary

A water infiltration test was conducted with a compacted Calcigel bentonite-sand mixture (50:50) at room temperature for investigating the coupled hydro-mechanical behavior. The test conditions mimic the transient hydration of backfill material under constant volume condition in a nuclear water repository. The geochemical aspects and the effect of ground water geochemistry were not considered in the test. Hence, the distilled water was supplied from the bottom-end for hydrating the compacted blocks. The test was performed with the newly designed column-type experimental device for a period of 349 days. The sensors and monitoring instruments facilitated the transient measurements of water content, relative humidity, temperature and total stresses in both lateral direction (along the height of soil sample) and in the axial direction (at the ends of soil sample) during the hydration process. The test results can be summarized in following key points, such as:

- The evolution of measured (water content and relative humidity) and computed variables (degree of saturation and soil total suction) over elapsed time exhibited the effect of distance from the wetting-end on the rate of saturation. For the measurement section X1 (50 mm from bottom), a progressive decrease in the water potential gradient was observed during the test, which was sharp at the beginning of hydration and later became smoother over elapsed time. The simultaneous measurements of water content and relative humidity along the hydration path revealed the porosity redistribution close to the hydrating-end during water infiltration. The post-experimental measurements revealed the state of material after 349 days of hydration.
- The total stress measurements indicated the effect of hydration-induced heterogeneities in the sample, the presence of constructional gaps or technical voids and the interfacial friction between soil sample and cell wall on the swelling pressure dynamics. The measured axial stresses at the ends were different during the test, which can be attributed to the presence of construction joints, the side frictional

resistance offered by the sample rings, and the presence of embedded sensors that creates a composite sample with varying stress-deformation characteristics.

- The data pertaining to soil water retention behavior (i.e., soil suction vs. gravimetric water content) indicated that the saturation of compacted blocks took place under constant volume condition. However, the transient data ( $s - S_r$ ) at section X1 showed some disagreement with the elementary test results and overestimates the degree of saturation at lower suction levels ( $s \leq 7$  MPa). It may be attributed to the assumption of constant void ratio along the height of soil sample, which results an underestimation of void ratio of soil close to the hydration-end.

Finally, the measurements of state variables such as water content, relative humidity, total stresses in lateral and axial direction which were performed during the water infiltration test are used to calibrate and validate the existing constitutive models to predict the coupled hydro-mechanical behavior of compacted bentonite sand mixture.





# 6 Numerical simulation of the water infiltration test

## 6.1 Introduction

A fully coupled hydro-mechanical analysis of water infiltration was performed using the finite element code LAGAMINE (Collin et al., 2002). The Barcelona Basic Model (BBM) (Alonso et al., 1990) is used to describe the elasto-plastic behavior of unsaturated soils. The BBM (Alonso et al., 1990) is a well-known elasto-plastic model, it is the extension of the Modified Cam-Clay Model (Roscoe & Burland, 1968) for the unsaturated state by considering soil suction as an additional stress variable. The model was developed in 1990 originally for soils with low to moderate expansivity. However, several extensions of the original BBM have been proposed to reproduce the swelling behavior of expansive soil-based material (Delahaye & Alonso, 2002; Vaunat & Gens, 2005; Zandarin et al., 2013; Sánchez et al., 2012). For the modeling of coupled flow and deformation problem, the indirect coupling is introduced by incorporating the soil water retention model, which features the description of soil suction and degree of saturation relationship in the mechanical constitutive model. In this regard, the double structure water retention model proposed by Dieudonne et al. (2017) is used in the simulation. The simulation results are compared with the classical soil water retention model (Van Genuchten, 1980). The main objectives of the simulation exercise were to investigate

- the ability of BBM with its extensions to reproduce the swelling behavior of compacted bentonite-sand mixture upon water saturation, and
- the influence of the soil water retention model on the simulation results.

Additionally, the parameters identification and calibration procedure for the Barcelona Basic Model and the Dieudonne water retention model are discussed in detailed.

## 6.2 Finite element formulation

In LAGAMINE, a bi-dimensional isoparametric finite element (MWAT) has been implemented for both 2D and 3D coupled flow and deformation analysis (Collin et al., 2002). The element for 2D-analysis possesses five degrees of freedom at each node: two displacements of the soil skeleton, a liquid water pressure, a gas (dry air + vapor) pressure and temperature. The number of nodes are variable (three, four, six or eight) and the element is isoparametric, which means that the coordinates, velocities, pore pressure (water and gas) and temperature are discretized by the same shape functions.

### 6.2.1 Balance equations

The theoretical framework is formulated using multiphase (solid, liquid and gas) multi-species (mineral, water, air) approach. The liquid water is assumed to be composed of liquid water and dissolved air, while the gas phase contains dry air and water vapor.

#### 6.2.1.1 Mass balance of water

The mass conservation equation of water species is obtained by summing the balance equation of liquid water and water vapour. The water vapor is one of the gas phase compounds and has two components: advective flux of the gaseous phase and the non-advective flux of water vapor related to vapor diffusion inside the gaseous phase. The mathematical expression for mass balance of water contains the variation of water storage and the divergence of water flows in both liquid and gas phases and reads

$$\frac{\partial}{\partial t} (\rho_w n S_{rw} + \rho_v n S_{rg}) + \nabla \cdot (\rho_w f_w + i_v \rho_v f_g) = 0 \quad (6.1)$$

where  $\rho_w$  is liquid water density,  $n$  is the porosity,  $S_{rw}$  is degree of water saturation,  $\rho_v$  is vapor density,  $S_{rg}$  is gas saturation,  $f_\alpha$  is the macroscopic velocity of phase  $\alpha$  ( $\alpha = w$  or  $g$ ),  $i_v$  is the non-advective flux of water vapor and  $t$  is the time.

#### 6.2.1.2 Mass balance of air

The dry air flows have two components: an advective flux related to gas phase motion and a non-advective flux corresponding to air diffusion in the gaseous mixture. The diffusion

of dissolved air in water is neglected. The mass balance of dry air contains the dry air and dissolved air in water and reads

$$\frac{\partial}{\partial t} (\rho_a n S_{rg} + H \rho_a n S_{rw}) + \nabla \cdot (\rho_a H f_w + i_a \rho_a f_g) = 0 \quad (6.2)$$

where  $\rho_a$  is dry air density,  $n$  is the porosity,  $S_{rw}$  is water saturation,  $H$  is Henry's coefficient,  $f_\alpha$  is the macroscopic velocity of phase  $\alpha$ ,  $i_a$  is the non-advective flux of dry air,  $\rho_v$  is vapor density,  $S_{rg}$  is gas saturation and  $t$  is the time. Henry's coefficient ( $H$ ) allows determining the dissolved air volume in liquid water. The dissolved air mass is supposed to be sufficiently low that water properties are not influenced.

### 6.2.1.3 Balance of heat

In the formulation of heat transfer in unsaturated porous medium, it was assumed that the different components are in a thermal equilibrium (i.e., temperature of soil solids ( $T_s$ ) = temperature of water in pores ( $T_w$ ) = temperature of vapor in pores ( $T_v$ ) = temperature of air in pores ( $T_a$ )). A unique temperature is defined for the medium and only one balance equation of energy is require. By neglecting the kinetic energy and pressure energy terms, the enthalpy balance equation can be expressed as

$$\frac{\partial \phi}{\partial t} + L \dot{E}_{H_2O}^{w \rightarrow v} + \nabla \cdot q - Q = 0 \quad (6.3)$$

where  $\phi$  is the enthalpy of the medium,  $L$  is the latent heat of water vaporisation,  $\dot{E}_{H_2O}^{w \rightarrow v}$  is the rate of water evaporation,  $q$  is the heat flux and  $Q$  is a volume heat source.

The rate of evaporation can be calculated from the water vapor balance equation using the following equation

$$\dot{E}_{H_2O}^{w \rightarrow v} = \frac{\partial}{\partial t} (\rho_v n S_{rg}) + \nabla \cdot (\rho_v f_g + i_v) \quad (6.4)$$

The enthalpy balance equation can be rewritten as

$$\underbrace{\frac{\partial \phi}{\partial t} + L \frac{\partial}{\partial t} (\rho_v n S_{rg})}_{\text{Heat storage}} + \underbrace{L \nabla \cdot (\rho_v f_g + i_v) + \nabla \cdot q - Q}_{\text{Heat transfer}} = 0 \quad (6.5)$$

#### 6.2.1.4 Momentum balance for the medium

The balance of momentum is expressed for the entire mixture. For quasi-static loading, the equation reduces to the equilibrium of stresses

$$\nabla \cdot \sigma_t + b = 0 \quad (6.6)$$

where  $\sigma_t$  is the total Cauchy stress tensor (with compressive stress taken as positive), and  $b$  is the body force vector. If the only body force is gravity,  $b$  is equal to  $\rho g$ , where  $\rho$  is the density of the mixture.

### 6.2.2 Constitutive equations: Mechanical behavior

The Barcelona Basic Model (Alonso et al., 1990) is used to describe the mechanical behavior of compacted bentonite sand mixture. The model is basically the extension of the Modified Cam-Clay Model (Roscoe & Burland, 1968) to the unsaturated state by considering soil suction as an additional stress variable. The complete formulation of the Barcelona Basic Model is presented in this section. For the sake of clarity, the model is first formulated for isotropic stress states. Later, the formulation is extended to a triaxial stress state.

#### 6.2.2.1 Formulation for isotropic stress states: saturated case

For an isotropic stress state (i.e.,  $\sigma_1 = \sigma_2 = \sigma_3$ ), the mechanical stress state is described using the net mean stress ( $p = \sigma_i - u_a$ ) and soil suction ( $s$ ), here  $\sigma_i$  is the total stress and  $u_a$  is the pore air pressure. For saturated conditions ( $u_a = 0$ ), the Barcelona Basic Model coincides with the Modified Cam-Clay Model (Roscoe & Burland, 1968), which belongs to the family of elastoplastic strain-hardening models. The total strain contains an elastic and a plastic component. For an isotropic stress state, the incremental total volumetric strain ( $d\varepsilon_v$ ) reads

$$d\varepsilon_v = d\varepsilon_v^e + d\varepsilon_v^p \quad (6.7)$$

where  $d\varepsilon_v^e$  and  $d\varepsilon_v^p$  are the elastic and plastic components of the incremental volumetric strain, respectively. In the elastic domain, the incremental volumetric strains are associated with the change in the mean net stress and can be expressed as

$$d\varepsilon_v^e = \frac{k}{1+e} \frac{dp}{p} = \frac{dp}{K} \quad (6.8)$$

where  $k$  is the slope of unloading-reloading curve and  $e$  is the void ratio. Material elasticity in the Modified Cam-Clay Model is non-linear as the bulk modulus  $K$  is a function of both the void ratio and the mean net stress, such as

$$K = \frac{(1 + e)p}{k} \quad (6.9)$$

Once the mean net stress exceeds the material preconsolidation stress (yield stress)  $p_0^*$ , plastic strains are generated. The evolution of plastic strains are governed by the hardening law as per following equation,

$$d\varepsilon_v^p = \frac{\lambda(0) - k}{1 + e} \frac{dp_0^*}{p_0^*} \quad (6.10)$$

### 6.2.2.2 Formulation for isotropic stress state: unsaturated case

An extension of the Modified Cam-Clay Model from a saturated to an unsaturated state considers soil suction ( $s$ ) as a hardening parameter (see Figs. 6.1a and 6.1b). The slope of virgin compression line ( $\lambda$ ) and the yield stress ( $p_0$ ) depend on the soil suction ( $s$ ). According to the original formulation of the BBM (Alonso et al., 1990), the slope of virgin compression line decreases with increasing suction as per following equation

$$\lambda(s) = \lambda(0) [(1 - r) \exp(-\omega s) + r] \quad (6.11)$$

where  $\lambda(s)$  is the slope of normal compression line in unsaturated state at suction  $s$ ,  $\lambda(0)$  is the slope of virgin compression line in saturated state,  $r$  and  $\omega$  are the material parameters,  $r$  is related to the maximum stiffness of the soil for an infinite suction and  $\omega$  controls the rate of increase of the soil stiffness with suction.

As the soil suction is considered as a hardening parameter, the elastic domain increases with an increase in soil suction. It signifies that the soil can sustain higher stress before yielding with an increase in suction level. The evolution of the preconsolidation pressure or yield stress with soil suction as per the original BBM formulation follows:

$$p_0(s) = p_c \left( \frac{p_0^*}{p_c} \right)^{\frac{\lambda(0) - k}{\lambda(s) - k}} \quad (6.12)$$

where  $p_0(s)$  is net preconsolidation pressure or yield stress in unsaturated state,  $p_c$  is a reference net pressure,  $p_0^*$  is net preconsolidation pressure or yield stress in saturated state and  $k$  is the slope of unloading-reloading line.

Equation 6.12 defines a yield curve in the ( $p$ - $s$ ) plane, which is known as Loading-Collapse (LC) curve (see Fig. 6.1b). This curve is a fundamental aspect of the Barcelona Basic

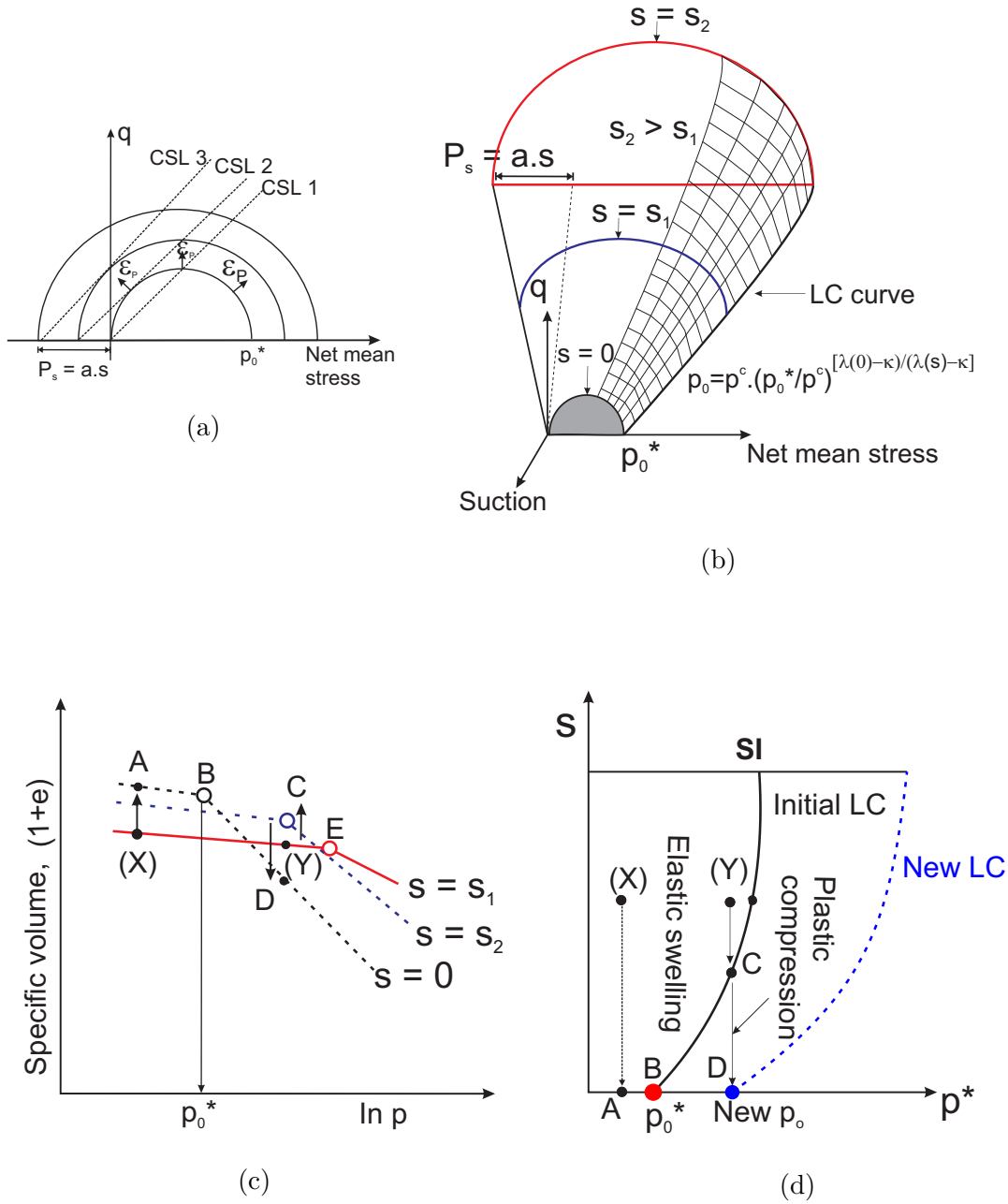


Figure 6.1: Characteristic features of Barcelona Basic Model (Alonso et., 1990), (a) extension of the Modified Cam-clay model for saturated to unsaturated state taking suction as a hardening parameters with the assumption of constant slope of critical state lines, (b) yield surface, (c) features of BBM (Alonso et al., 1990) and (d) loading path and collapse deformation of an unsaturated as-compacted sample.

Model. Owing for the dependence of the virgin compression line and the yield stress on soil suction level, the hardening law as per Equation 6.10 of the LC curve becomes,

$$d\varepsilon_v^p = \frac{\lambda(s) - k}{1 + e} \frac{dp_0}{p_0} \quad (6.13)$$

Using Eqs. 6.11 and 6.12, Eq. 6.13 reads

$$d\varepsilon_v^p = \frac{\lambda(0) - k}{1 + e} \frac{dp_0^*}{p_0^*} \quad (6.14)$$

### 6.2.2.3 Influence of suction change

In case of unsaturated expansive soils, suction change causes the volumetric strains in terms of soil swelling or shrinkage. As shown in Figure 6.1c, the unsaturated as-compacted sample (point X) undergoes to elastic swelling due to the suction reduction (point A) based on the applied mean net stress. Accordingly, the total strain increment in the elastic domain reads

$$d\varepsilon_v^e = d\varepsilon_{vp}^e + d\varepsilon_{vs}^e = \frac{k}{1 + e} \frac{dp}{p} + \frac{k_s}{1 + e} \frac{ds}{s + u_{atm}} = \frac{dp}{K} + \frac{ds}{K_s} \quad (6.15)$$

where  $d\varepsilon_{vp}^e$  and  $d\varepsilon_{vs}^e$  are the elastic increments of volumetric strain associated to the net stress and soil suction, respectively,  $k_s$  is the slope of the reversible wetting-drying line,  $u_{atm}$  is the atmospheric pressure and  $K_s$  is the bulk modulus for changes in suction, expressed as

$$K_s = \frac{(1 + e)(s + u_{atm})}{k_s}. \quad (6.16)$$

Along the drying path, there is a threshold suction  $s_0$  beyond which the irreversible plastic strains are created. The threshold suction  $s = s_0$  defines a second yield curve in the  $(p - s)$  plane, which is known as Suction-Increase (SI) curve. The SI surface is represented in Figure 6.1d.

$$f_{SI} \equiv s = s_0 \quad (6.17)$$

Once this suction  $s_0$  is reached, the incremental plastic volumetric strain produced by further increase of suction is given as

$$d\varepsilon_{vs}^p = \frac{\lambda(s) - k_s}{1 + e} \frac{ds_0}{s_0 + u_{atm}}. \quad (6.18)$$

The total increment of plastic volumetric strain  $d\varepsilon_v^p$  appears in Equations 6.14 and 6.18. Hence, the irreversible or plastic strains control the position of the new LC and SI yield

surfaces. For instance, if as-compacted sample is first subjected to elastic compression (point X to Y in Fig. 6.1c) followed by wetting under applied net stress (point Y to C in Fig. 6.1d), the sample may exhibit the initial swelling followed by plastic compression as shown in Figure 6.1d. Once the sample undergoes to plastic compression or collapse, the hardening takes place and sample attains new preconsolidation or yield stress as shown by point D in Figure 6.1d.

#### 6.2.2.4 Formulation for triaxial stress state

In the triaxial stress state ( $\sigma_1 \neq \sigma_2 = \sigma_3$ ), the mechanical stress state can be described by the net stress  $p$ , suction  $s$  and the deviatoric stress  $q = (\sigma_1 - \sigma_3)$ .

**6.2.2.4.1 Elastic strains in triaxial stress state** In the elastic domain, changes in the deviatoric stress  $q$  yield deviatoric deformation according to

$$d\varepsilon_d^e = \frac{1}{3}Gdq \quad (6.19)$$

where  $d\varepsilon_d^e$  is the elastic increment of deviatoric strain and  $G$  is the shear modulus, which may be chosen as a constant or as a function of the bulk modulus  $K$  as per the following equation

$$G = \frac{3(1-2\nu)K}{2(1+\nu)} \quad (6.20)$$

where  $\nu$  is Poisson ratio. In both cases, the shear modulus is assumed to be independent of suction.

**6.2.2.4.2 Yield surface** In the  $p - q$  plane, the BBM considers the modified Cam-clay yield surface according to

$$f_{LC} = q^2 - M_\theta^2 (p + p_s) (p_0 - p) = 0 \quad (6.21)$$

where  $M_\theta$  is the slope of the critical state line,  $p_s$  is the left intercept of yield surface and  $p_0$  is the apparent preconsolidation pressure at a suction  $s$ . The increase of the apparent cohesion with increase suction is included by considering  $p_s$  as an evolving function of suction according to

$$p_s(s) = \frac{c(s)}{\tan\phi} = \frac{c(0) + k \cdot s}{\tan\phi} \quad (6.22)$$

where  $c(0)$  is the cohesion under saturated conditions and  $k$  is a parameter controlling the increase of cohesion.



The slope of critical state line is linked to the soil friction angle by

$$M_\theta = \frac{6\sin\phi}{3 - \sin\phi} \quad \text{or} \quad \phi = \arcsin\left(\frac{3M_\theta}{6 + M_\theta}\right) \quad (6.23)$$

Finally, the SI surface is assumed to be independent of the stress level.

**6.2.2.4.3 Flow rules** For the BBM formulation in the triaxial state, non-associative flow rule is assumed. In particular, the following non-associated flow rule is defined,

$$\frac{d\varepsilon_d^p}{d\varepsilon_v^p} = \frac{2q\alpha}{M_\theta^2(2p + p_s - p_0)} \quad (6.24)$$

where  $\alpha$  is chosen in such a way that Equation 6.24 predicts zero lateral strain for stress states corresponding to Jacky's  $K_0$  values, that is

$$\alpha = \frac{M_\theta(M_\theta - 9)(M_\theta - 3)}{9(6 - M_\theta)} \frac{1}{1 - \frac{k}{\lambda(0)}}. \quad (6.25)$$

Accordingly, the flow surface is given by

$$g_{LC} \equiv \alpha q^2 - M_\theta^2(p + p_s)(p_0 - p) = 0. \quad (6.26)$$

## 6.2.3 Constitutive equations: Hydraulic behavior

The constitutive equations pertaining to the hydraulic behavior consider the fluid flow in both gaseous and liquid phase. Each phase constitutes a mixture of two components i.e., dry air and water vapor for the gas phase and liquid water and dissolved air for liquid phase. The compositional approach is used to write the balance equations. The fluid flow occurs in advective form for liquid phase and diffusive form for gaseous phase. The advective flow of fluid is described by the generalized Darcy's law. It reads

$$f_\alpha = -\frac{k_{int}k_{r,\alpha}}{\mu_\alpha} [\nabla p_\alpha + g\rho_\alpha \nabla y] \quad (6.27)$$

where  $\alpha$  is related to liquid or gas phase ( $\alpha = w$  or  $g$ ),  $\mu_\alpha$  is the dynamic viscosity of the fluid (gas/water),  $p_\alpha$  is the fluid pressure,  $g$  is the gravity acceleration,  $k_{int}$  is the intrinsic permeability of porous medium,  $k_{r,\alpha}$  is the relative permeability of fluid and  $y$  is the vertical upward directed co-ordinate. The tensor of intrinsic permeability  $K_{int}$  depends on the porosity according to the Kozeny-Carmen equation (Kozeny, 1936; Carman, 1938):

$$K_{int} = K_0 \frac{(1 - \phi_0)^M}{\phi_0^N} \frac{\phi^N}{(1 - \phi)^M} \quad (6.28)$$

where,  $\phi$  is the porosity,  $\phi_0$  is a reference porosity,  $K_0$  is the intrinsic permeability for matrix with porosity  $\phi_0$ . The relative permeability  $k_{r,\alpha}$  can be defined as a function of degree of saturation. In LAGAMINE, there are different ways to describe  $k_{r,\alpha}$  as a function of  $S_{r,\alpha}$ . Such as, the relative permeability  $k_{r,\alpha}$ , is derived from Mualem-van Genuchten closed-form model (Van Genuchten, 1980),

$$k_{rl,\alpha} = \sqrt{S_{r,\alpha}} \left( 1 - \left( 1 - S_{r,\alpha}^{1/\lambda} \right)^\lambda \right)^2 \quad (6.29)$$

where,  $\lambda$  is the parameter which controls the relative permeability value with degree of saturation.

The variation of degree of saturation with soil total suction is described by the shape of soil water retention curve. In LAGAMINE, different soil water retention models are implemented (Van Genuchten, 1980; Fredlund & Xing, 1994; Nuth & Laloui, 2008). For an example Van Genuchten (1980) model is described as below,

$$S_{r,\alpha} = S_{res,\alpha} + (S_{max,\alpha} - S_{res,\alpha}) \left( 1 + \left( \frac{s}{A} \right)^n \right)^{-(1-\frac{1}{n})} \quad (6.30)$$

where,  $S_{r,\alpha}$  is the current degree of saturation of phase  $\alpha$  (air or water),  $S_{res,\alpha}$  is the residual degree of saturation,  $S_{max,\alpha}$  is the maximum degree of saturation,  $A$  is the parameters related with air-entry / air-expulsion suction, and  $n$  is the fitting parameter which controls the shape of soil water retention curve. Recently a soil water retention model is developed by Dieudonne et al. (2017) based on the existence of dual porosity domains in the compacted clays. The model is implemented in LAGAMINE and discussed in section. 6.2.4.

In LAGAMINE, the vapor diffusion is linked to gradient of vapor density and follows the formulation proposed by Philip & De Vries (1957). It reads

$$i_v = -D_{atm} \tau_v \phi S_{r,g} \rho_g \nabla \omega_v \quad (6.31)$$

$$i_v = -D_{atm} \tau_v \phi S_{r,g} \nabla \rho_v \quad (6.32)$$

where,  $D_{atm}$  is the molecular diffusion coefficient and  $\tau_v$  is the tortuosity,  $\phi$  is the porosity,  $S_{r,g}$  is the degree of saturation,  $\rho_v$  is the vapor density and  $\omega_v$  is the molecular mass of water vapour.

The vapor is assumed to be in equilibrium with the liquid water and the vapor density  $\rho_v$  is expressed as:

$$\rho_v = \rho_{sat}(RH) \quad (6.33)$$

where,  $\rho_{sat}$  is the saturated water vapor density and  $RH$  is the relative humidity humidity.

The relative humidity takes into account of adsorption phenomenon and the capillary effect in soil. The Kelvin-Laplace equation relates soil suction with relative humidity and reads

$$RH = \exp\left(\frac{sM_w}{\rho_w R_v T}\right) \quad (6.34)$$

where,  $R_v$  is the gas constant of water vapor,  $s$  is the suction ( $p_g - p_w$ ) and  $T$  is the temperature.

Vapor is considered as a perfect gas and vapor pressure is computed using the ideal gas law,

$$p_v = \left(\frac{n}{V}\right) R_v T \quad (6.35)$$

or

$$p_v = \rho_v R_v T \quad (6.36)$$

The gradient of the water vapour density can now be developed using Equation 6.33 in order to compute the vapour flow:

$$\nabla \rho_v = \frac{\rho_0 g h}{R_v T} \nabla \frac{(p_w - p_g)}{\rho_w g} + (RH) \left[ \frac{\partial \rho_0}{\partial T} - \frac{\rho_0 (\rho_w - \rho_g)}{\rho_w R_v T^2} \right] \nabla T \quad (6.37)$$

The above equation signifies that the water vapour density gradient comprises two parts: an isothermal one related to hydraulic gradient and the another one related to thermal gradient.

Diffusion of dry air is related to dry air density gradient with the non-advective diffusive flow can be expressed as

$$i_a = -D_{atm} \tau_v \phi S_{r,g} \nabla \rho_a \quad (6.38)$$

#### 6.2.4 Clay-microstructure based water retention model

Based on the experimental observations at both micro-and macroscales, Dieudonne et al. (2017) proposed a phenomenological water retention model for the compacted bentonites. The model is developed to consider different water retention mechanisms in each structural level, namely the adsorption in intra-aggregate pore space (micro-scale) and the capillarity in inter-aggregate pore space (macro-scale). The consideration of different water retention mechanisms inside and between the aggregates allows for capturing the density effect on the soil water retention behavior. The model is formulated in terms of water void ratio ( $e_w$ ), which is expressed as the sum of micro ( $e_{wm}$ ) and macro water void ratio ( $e_{wM}$ ).

The water stored in the intra-aggregate pore space is based on the Dubinin's adsorption theory (Dubinin & Radushkevich, 1947) and it reads

$$\Omega_{wm} = \Omega_m \exp \left\{ - \left[ \frac{RT}{\beta_D E_0} \ln \left( \frac{\rho_v^0}{\rho_v} \right) \right]^{n_{ads}} \right\} \quad (6.39)$$

where  $\Omega_{wm}$  is the volume of water adsorbed in the micro-pores at relative pressure  $\rho_v/\rho_v^0$ ;  $\Omega_m$  is the total volume of the micro-pores;  $n_{ads}$  is a material parameter, called heterogeneity factor;  $\beta_D$  is termed similarity constant; and  $E = \beta_D E_0$  is the characteristic adsorption energy for the given system; and  $E_0$  is the characteristic energy of adsorption for a reference vapour for which  $\beta_D = 1$ .

The above equation can be expressed in term of water ratio by dividing both sides of the equation by the volume of solid particles  $\Omega_s$ . It yields

$$e_{wm} = e_m \exp \left\{ - \left[ \frac{RT}{\beta_D E_0} \ln \left( \frac{\rho_v^0}{\rho_v} \right) \right]^{n_{ads}} \right\} \quad (6.40)$$

with  $e_{wm}$  the water stored in the micropores and  $e_m$  the microstructure void ratio.

The Kelvin's equation relates the relative vapour pressure  $\rho_v/\rho_v^o$  with the soil total suction  $s$

$$RH = \frac{\rho_v}{\rho_v^o} = \exp \left( \frac{-sM_w}{RT\rho_w} \right) \quad (6.41)$$

where  $RH$  is the relative humidity,  $M_w$  is the molecular mass of water (0.018 kg/mol),  $R$  is the universal gas constant,  $T$  is the soil temperature and  $\rho_w$  is density of water.

Gathering the constant parameters, the following expression is finally adopted for the microstructural water retention domain

$$e_{wm} = e_m \exp [ - (C_{ads}s)^{n_{ads}} ] \quad (6.42)$$

where  $n_{ads}$  and  $C_{ads}$  are material parameters. The parameter  $n_{ads}$  controls the curvature of the water retention curve in the high suction range, while  $C_{ads}$  is related to the original Dubinin's adsorption theory, which can be expressed as

$$C_{ads} = \frac{M_w}{\rho_w \beta_D E_0} \quad (6.43)$$

For typical values of  $E = \beta_D E_0$  ranging between 1 and 10 kJ/mol,  $C_{ads}$  varies between 0.018 and 0.0018 MPa<sup>-1</sup>.

In the bentonite-based materials, the microstructural void ratio ( $e_m$ ) varies during the wetting or drying cycles. To account these microstructural changes in the bentonite, the

microstructural evolution model proposed by Della Vecchia et al. (2015) is adopted in the double-structure water retention model (Dieudonne et al., 2017). It reads

$$e_m = e_{m0} + \beta_0 e_w + \beta_1 e_w^2 \quad (6.44)$$

where  $e_{m0}$  is the microstructural void ratio for the dry material ( $e_w = 0$ ), whereas  $\beta_0$  and  $\beta_1$  are parameters that quantify the swelling potential of the aggregates. According to Eq. 6.44, the value of microstructural void ratio ( $e_m$ ) may exceed to total void ratio ( $e$ ) at higher water ratios. Hence to avoid such conditions, it is assumed that the microstructural void ratio will be equal to the total void ratio ( $e_m = e$ ), for a completely developed microstructure.

The macrostructural water retention model is based on the capillarity in inter-aggregate pore space. The Van Genuchten (1980) water retention model is used to model the water retention behavior in the larger inter-aggregate pores

$$S_r(s) = \left[ 1 + \left( \frac{s}{\alpha} \right)^n \right]^{-m} \quad (6.45)$$

where  $m$  and  $n$  are material parameters, and  $\alpha$  is related to the air-entry value. Alternatively, the van Genuchten equation may be expressed in terms of water ratio  $e_w$ .

$$e_w(s, e) = e \left[ 1 + \left( \frac{s}{\alpha} \right)^n \right]^{-m} \quad (6.46)$$

In the proposed model, the void ratio  $e$  is replaced by macrostructural void ratio  $e_M = e - e_m$ , hence the macrostructural water retention domain now can be expressed in terms of water void ratio  $e_w$

$$e_{wM}(s, e, e_m) = (e - e_m) \left[ 1 + \left( \frac{s}{\alpha} \right)^n \right]^{-m}. \quad (6.47)$$

Additionally, based on the mercury intrusion porosimetry (MIP) data (Della Vecchia et al., 2015), the air-entry value is supposed to vary with the macroscopic void ratio ( $e_M$ ) according to the following equation

$$\alpha = \frac{A}{e - e_m} \quad (6.48)$$

where parameter  $A$  controls the dependence of the air-entry suction on the macrostructural void ratio ( $e_M$ ). As mentioned earlier, the dependency of water permeability on porosity ( $\phi$ ) is described by Kozney-Carman relationship (Chapuis & Aubertin, 2003) as shown below:

$$K_{int} = K_0 \frac{(1 - \phi_0)^M}{\phi_0^N} \frac{\phi^N}{(1 - \phi)^M} \quad (6.49)$$

In the proposed double structure water retention model, the Kozeny-Carman law is extended for dual porosity domains in the aggregated soils, such as:

$$K_{int} = K_0 \frac{(1 - e_{M0})^M}{e_{M0}^N} \frac{e_M^N}{(1 - e_M)^M} \quad (6.50)$$

## 6.3 Identification and calibration of model parameters

The constitutive model parameters for a fully coupled hydro-mechanical analysis can be grouped into three categories: (i) parameters related to the mechanical behavior of soil (e.g., Barcelona Basic Model parameters), (ii) parameters related to the soil water retention behavior (e.g., van Genuchten or Dieudonne water retention model) and (iii) parameters related to the hydraulic behavior (saturated and unsaturated hydraulic conductivity functions). The parameter selection is one of the major challenge in the coupled hydro-mechanical analysis due the lack of standard procedures for calibrating the constitutive models for unsaturated soils. In this respect, a detailed and systematic procedure is presented for identifying and calibrating the model parameters for the compacted bentonite-sand mixture from the experimental results.

### 6.3.1 Parameter identification and calibration for BBM

The calibration of the BBM (Alonso et al., 1990) requires the selection of nine parameters. The isotropic material response is governed by six parameters ( $\beta$ ,  $\lambda(0)$ ,  $r$ ,  $p_c$ ,  $\kappa$  and  $\kappa_s$ ). The remaining three parameters ( $G$ ,  $k$  and  $M$ ) are needed to predict the deviatoric behavior. The parameter calibration is quite difficult because a single parameter controls more than one aspects of soil behavior. In the present case, the suction-controlled oedometer tests were performed with the compacted samples of bentonite-sand mixture (50:50). The sample initial conditions (i.e., dry density = 1.80 Mg/m<sup>3</sup>; water content = 9 %) were similar to the compacted blocks in the water infiltration test. Total four tests were performed with the high-pressure oedometer device by Lang (2019).

It should be noted here that the initial dry density of soil sample in the water infiltration was 1.85 Mg/m<sup>3</sup> with 9 % initial water content. After the compaction process, the samples were prepared for installing in PVDF sample ring with monitoring sensors such as TDR probes, Pt100 sensors and miniature pressure transducers with cable connections, as a result the sample initial dry density decreased to 1.80 Mg/m<sup>3</sup>. Hence, the sample initial

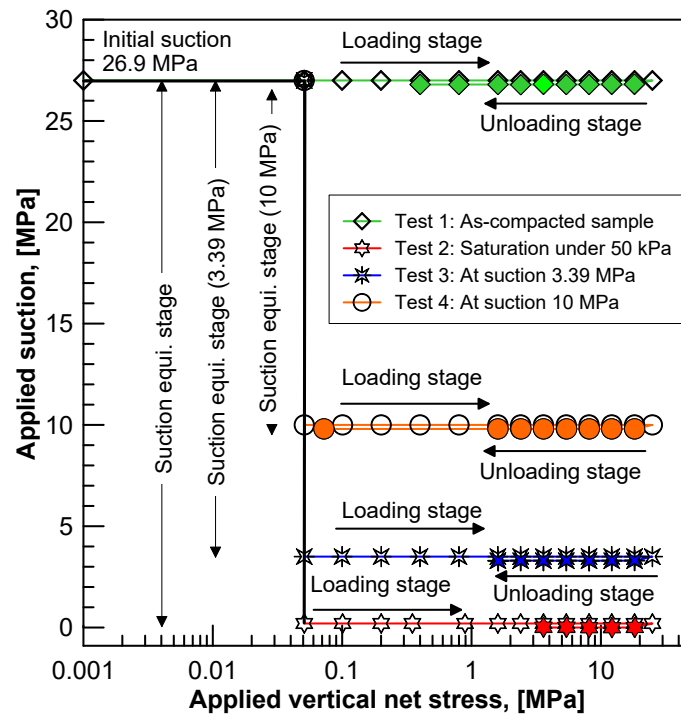


Figure 6.2: Stress paths for unsaturated oedometer tests on compacted sand-bentonite mixture

conditions (dry density =  $1.80 \text{ Mg/m}^3$ , water content = 9 % and initial suction = 26.9 MPa) were selected for the suction-controlled oedometer test by Lang (2019).

The tests were performed in two stages i.e., the suction-equilibrium stage and the one-dimensional compression-rebound stage as depicted in Figure 6.2. Prior to initiate the suction-equilibrium stage, the as-compacted samples were subjected to 50 kPa surcharge pressure. Later, the vapor equilibrium technique was used to impose the desired suction level (3.39 and 10 MPa) using the saturated salt solutions. During the suction-equilibrium stage, the vertical deformation of the samples were continuously monitored. Once the sample attained the desired suction level, the second stage i.e., one-dimensional compression-rebound was initiated. For the stress-deformation characteristics of the saturated sample, the distilled water was supplied from the bottom-end under 50 kPa surcharge load prior to initiate the loading-unloading stage. For the test with as-compacted state, the sample was directly subjected to the one-dimensional compression-rebound stage.

In the BBM, the yield surface in the saturated state (i.e.,  $s = 0$ ) increases with an increase in the soil total suction. The rate of increase is represented by the loading-collapse curve. The loading-collapse curve changes it's position when the sample undergoes to plastic

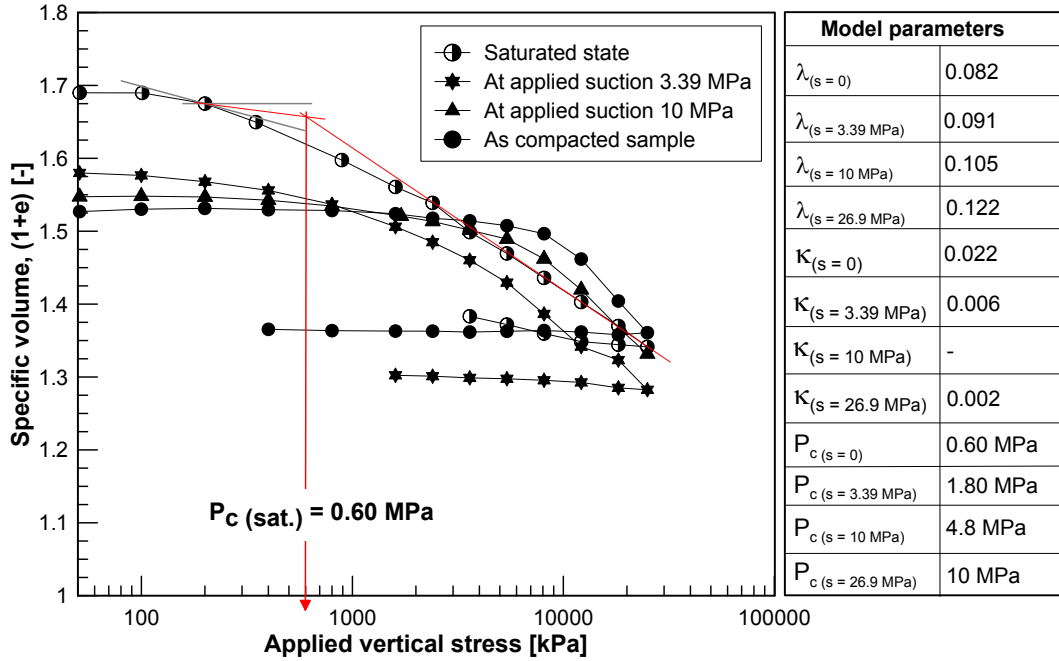


Figure 6.3: Suction-controlled oedometer tests results for compacted sand-bentonite mixture (50:50) with Barcelona Basic Model parameters.

deformations. The soil stress state in the  $(p - q - s)$  plane inside an elastic domain does not affect the position of loading-collapse curve (LC-curve). So, it is essential that the sample should remain in the elastic domain during the suction equilibrium-stage. In the present case, the sample was subjected to 50 kPa surcharge pressure and allowed to attain equilibrium at the imposed suction level (i.e., 3.39 or 10 MPa) under  $K_0$  condition (Figure 6.2). As the swelling was not prevented in the axial direction, the height of soil sample increased during the saturation process under the applied surcharge pressure of 50 kPa. To ensure the soil stress state with in the elastic domain during the saturation process, an applied surcharge pressure should be lower than the expected swelling pressure of the as-compacted sample during the saturation under constant volume condition. On the other hand, if the swelling is prevented at the global scale during the saturation, the stress state may hit the yield surface in the  $(p - q - s)$  plane due to an increase in the net mean stress and a decrease in the apparent preconsolidation stress during the saturation process. The suction-controlled oedometer test results are shown in Figure 6.3 along with the deduced BBM parameters. The slope of unloading-reloading path for sample at 10 MPa applied suction is not shown in the Figure 6.3 due to the power failure during the test.



The original formulation of BBM (Alonso et al., 1990) assumes that the slope of normal compression lines (NCLs) for different values of soil suction decreases with an increase in soil total suction. It signifies that the NCLs for different values of suction will diverge with increasing applied vertical stress. In the support of above statement, Alonso et al. (1990) presented the experimental results from García-Tornel (1988) (on compacted low plastic kaolin) and Maswoswe (1985) (on compacted sandy clay). While, the oedometer test results conducted by Wheeler & Sivakumar (1995) (on the compacted speswhite kaolin) revealed the converging behavior of normal compression lines under applied net mean stress levels. Wheeler et al. (2002) proposed a procedure for selecting the BBM parameter values ( $r$  and  $p_c$ ) to model the behavior of such soils where the NCLs converge with increasing vertical stress levels.

In the present case, the BBM parameters were selected in a sequential manner. In the first step, the model parameters ( $\lambda(0)$ ,  $\beta$  and  $r$ ) which control the slope of normal compression lines at different suction levels were determined. Figure 6.4a shows the predicted variation of  $\lambda(s)$  with the soil total suction according to the method suggested by Wheeler et al. (2002) with the  $r$  value higher than 1. In the second step, the model parameters related to the elastic behavior of soil ( $k$  and  $k_s$ ) were determined. Figure 6.4b presents the predicted variation of  $k$  with soil suction and the experimental values. The slope of the unloading/reloading line ( $k$ ) is supposed to vary according to

$$k = k_0 \left[ 1 + \alpha_1 s + \alpha_2 \ln \left( \frac{s + u_{atm}}{u_{atm}} \right) \right] \quad (6.51)$$

with  $k_0$  the elastic stiffness in saturated conditions;  $\alpha_1$  and  $\alpha_2$  model parameters and  $u_{atm}$  the atmospheric pressure.

For the slope of reversible wetting-drying line ( $k_s$ ), the experimental data from the suction-equilibrium stage (soil suction vs. specific volume) were used. Figure 6.4c shows the variation of  $k_s$  with soil suction under 50 kPa surcharge pressure. In the last step, the parameter  $p_c$  (reference stress) was selected to match the experimental data on preconsolidation pressure or yield stress values at different suction levels. Figure 6.4d shows the loading-collapse curve for the compacted bentonite-sand mixture with the fitting parameters according to

$$p_0(s) = p_c \left( \frac{p_0^*}{p_c} \right)^{\frac{\lambda(0)-k}{\lambda(s)-k}} \quad (6.52)$$

with  $p_0(s)$  the preconsolidation stress at soil suction ( $s$ ),  $p_c$  a reference net pressure,  $p_0^*$  preconsolidation stress for saturated condition and  $k$  the slope of unloading-reloading line for change in mean net stress.

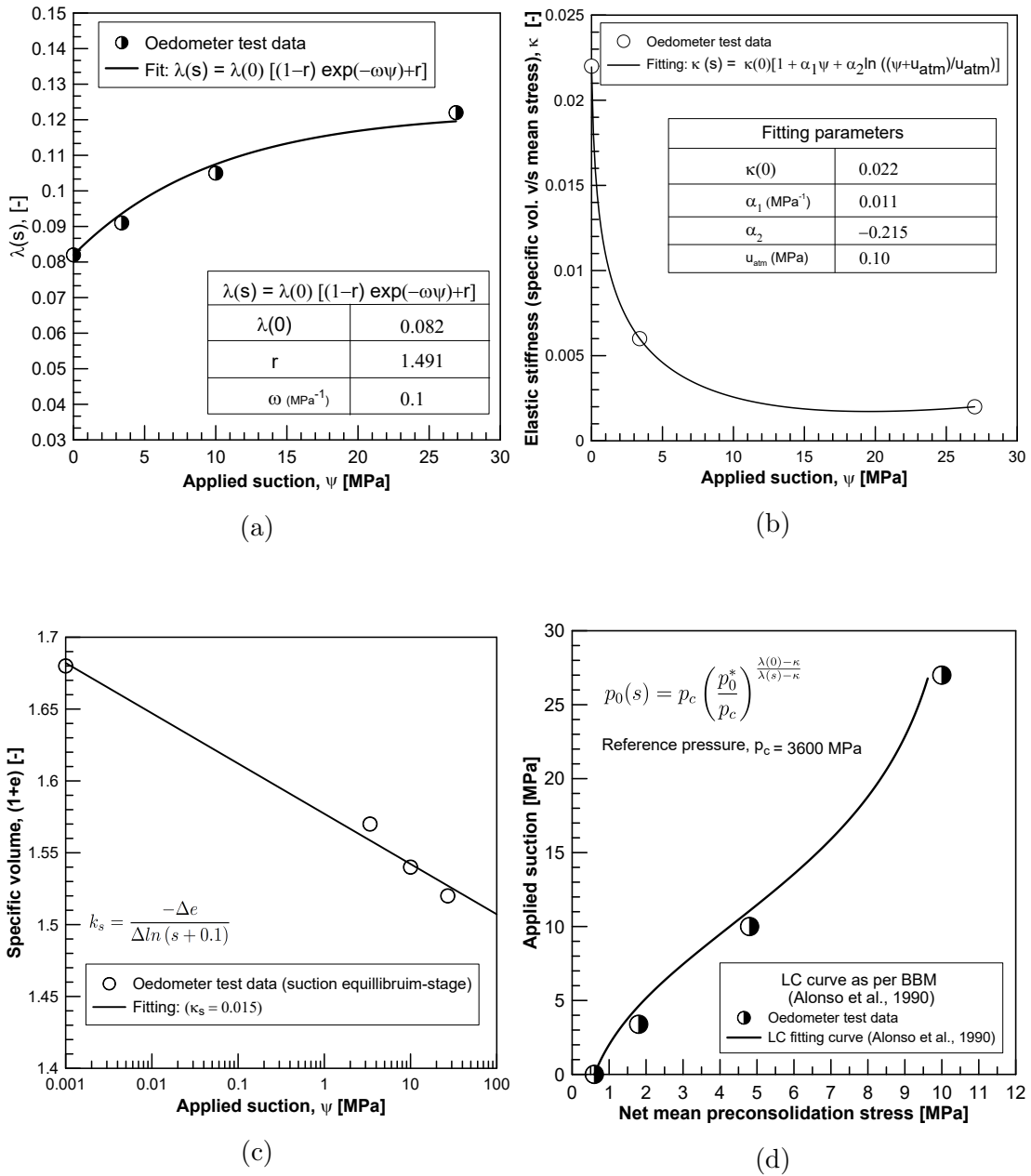


Figure 6.4: Determination of the BBM parameters, (a) slope of suction dependent normal compression lines, (b) applied net stress vs. specific volume at different applied suction-levels, (c) applied suction vs. specific volume at different applied net mean stress and (d) loading-collapse curve.

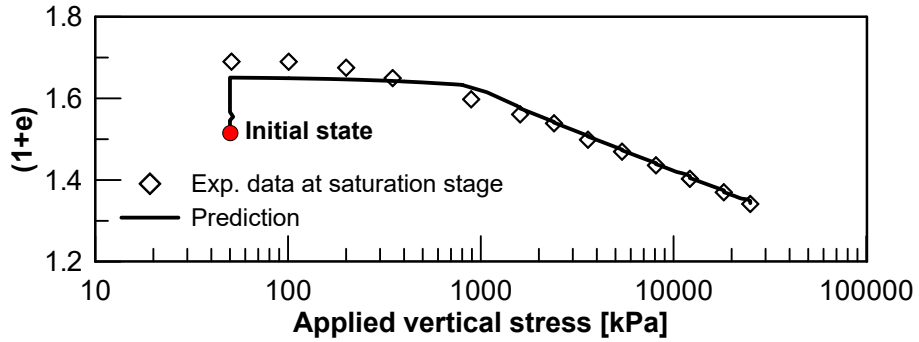
Table 6.1: Barcelona Basic Model parameters for compacted bentonite-sand mixture (50:50).

Parameters	Description	Value
<b>General parameters</b>		
$n_0$ [-]	Initial porosity	0.34
$\rho_s$ [Mg.m <sup>-3</sup> ]	Soild specific mass	2.725
$\psi_0$ [MPa]	Initial suction	26.9
<b>BBM plastic parameters</b>		
$\lambda(0)$ [-]	Slope of e-mean stress curve for saturated conditions	0.082
$p_0^*$ [MPa]	Preconsolidation pressure in saturated condition	0.6
$p^c$ [MPa]	Relative reference pressure	3600
$r$ [-]	First parameter defining the change in $\lambda(0)$ with suction	1.491
$\beta$ [MPa <sup>-1</sup> ]	Second parameter defining the change in $\lambda(0)$ with suction	0.10E-6
<b>BBM elastic parameters (relative to changes in net mean stress)</b>		
$k = k_0 \left[ 1 + \alpha_1 s + \alpha_2 \ln \left( \frac{s+u_{atm}}{u_{atm}} \right) \right]$		
$k_0$ [-]	Initial elastic slope	0.022
$\alpha_1$ [MPa <sup>-1</sup> ]	Parameter 1 related to elastic parameter	0.011
$\alpha_2$ [-]	Parameter 2 related to elastic parameter	-0.215
$G$ [MPa]	Shear modulus (for non-linear elasticity)	23.5E6
<b>BBM elastic parameter (relative to changes in suction)</b>		
$k_{s0}$ [-]	Initial elastic slope	0.015

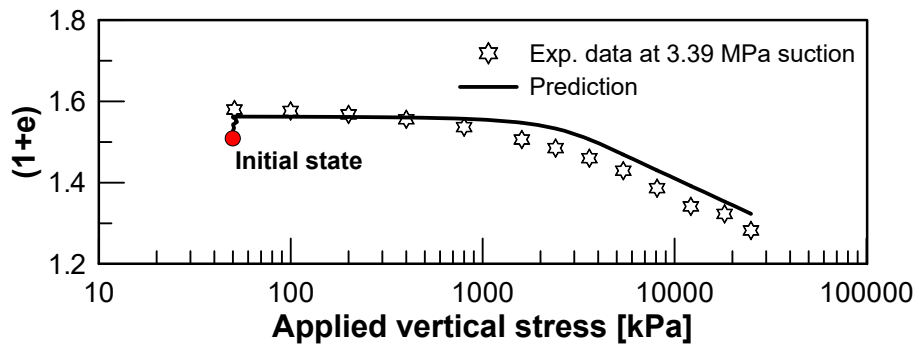
Table 6.1 summarizes the BBM parameters for compacted sand-Calcigel bentonite mixture (50:50). The selected BBM parameters were validated against the experimental data. Figure 6.5 shows the predicted vs. experimental data from the suction controlled oedometer tests on the Calcigel bentonite-sand mixture (50:50). It is evident from Figure 6.5 that the selected BBM parameters successfully predict the experimental results for both suction-equilibrium stage and the one dimensional compression stage.

### 6.3.2 Identification and calibration of double-structure water retention model parameters

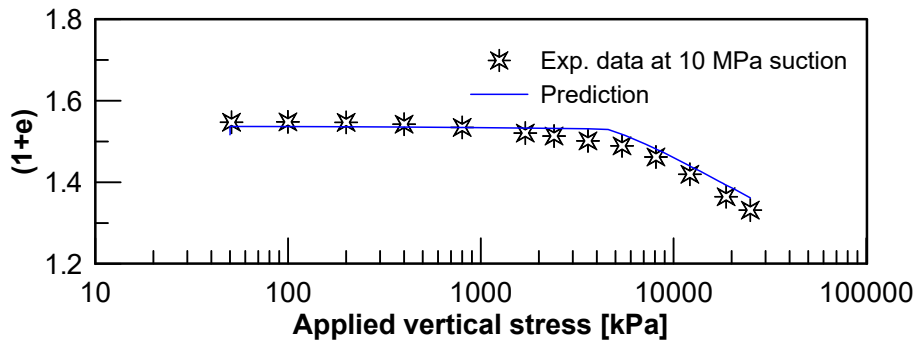
The double-structure water retention model proposed by Dieudonne et al. (2017) requires eight parameters, namely



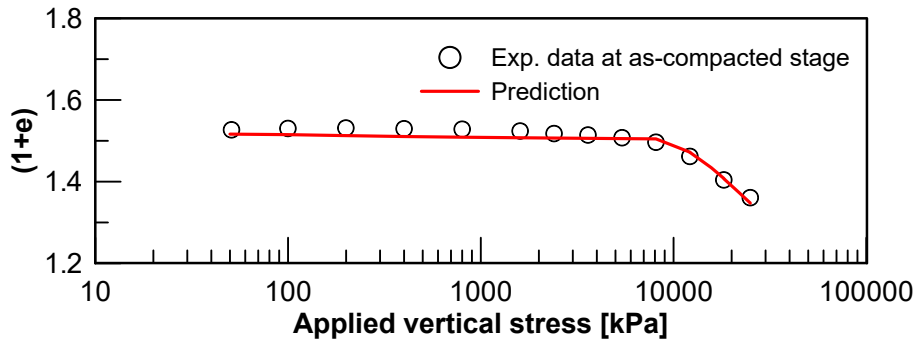
(a) Saturated sample



(b) Sample having 3.39 MPa total suction



(c) Sample having 10 MPa total suction



(d) As-compacted sample

Figure 6.5: Calibration of BBM model parameters using suction-controlled oedometer test results.

- $e_{m0}$ ,  $\beta_0$  and  $\beta_1$  characterize the evolution of the micro-structural void ratio ( $e_m$ ) with the water ratio ( $e_w$ ),
- $C_{ads}$  and  $n_{ads}$  describe the water retention response of the intra-aggregate pores, and
- $A$ ,  $n$ , and  $m$  describe the water retention response of the inter-aggregate retention region,

The identification of model parameters related to microstructure evolution can be estimated first, independently from the other parameters. It requires the pore size distribution (PSD) data of the compacted mixture of Calcigel bentonite-sand (50:50) at different water ratios. Additionally, the identification of  $e_{m0}$  requires the pore-size distribution of the oven-dried sample.

Agus (2005) obtained the PSD data from mercury intrusion porosimetry (MIP) tests on the sample having identical water ratio (i.e.,  $e_w = 0.245$ ). The MIP tests were conducted for the as-compacted, oven-dried and swollen sample. For the preparation of swollen sample, the as-compacted sample was allowed to swell in the axial direction only. The MIP test data for the as-compacted sample revealed that the intra-aggregate or micro-pore volume was 59 %, while the inter-aggregate pore volume was 41 % of the total pore volume. For the oven-dried sample, the intra-aggregate pore volume was 55 %, while the inter-aggregate pore volume was 45 % of the total pore volume. For the swollen sample, the intra-aggregate pore volume was 57 %, while the inter-aggregate pore volume was 43 % of the total pore volume.

Based on the above MIP test data the corresponding micro-and macro-void ratio were obtained for as-compacted samples ( $e_m = 0.30$ ,  $e_M = 0.21$  for  $e_w = 0.245$ ), for oven-dried sample ( $e_{m0} = 0.25$ ,  $e_M = 0.20$  for  $e_w = 0$ ) and for swollen sample ( $e_{m0} = 0.45$ ,  $e_M = 0.35$  for  $e_w = 0.80$ ). Figure 6.6 shows the evolution of microstructural void ratio with the water ratio, the obtained data were fitted with the model proposed by Della Vecchia et al. (2015).

In the second step, the micro-structural water retention parameters  $C_{ads}$  and  $n_{ads}$  were calibrated. The identification of these parameters requires water retention data for samples having different initial dry densities. In this regard, the as-compacted sample (initial dry density = 1.8 Mg/m<sup>3</sup>) was subjected to wetting under constant volume conditions (Lang, 2019). The water retention data for the sample with 2.0 Mg/m<sup>3</sup> were used from Agus (2005). The calibration of these parameters was performed by presenting water retention data in the ( $s - e_w$ ) plane. At high suction values, the data point in the ( $s - e_w$ )

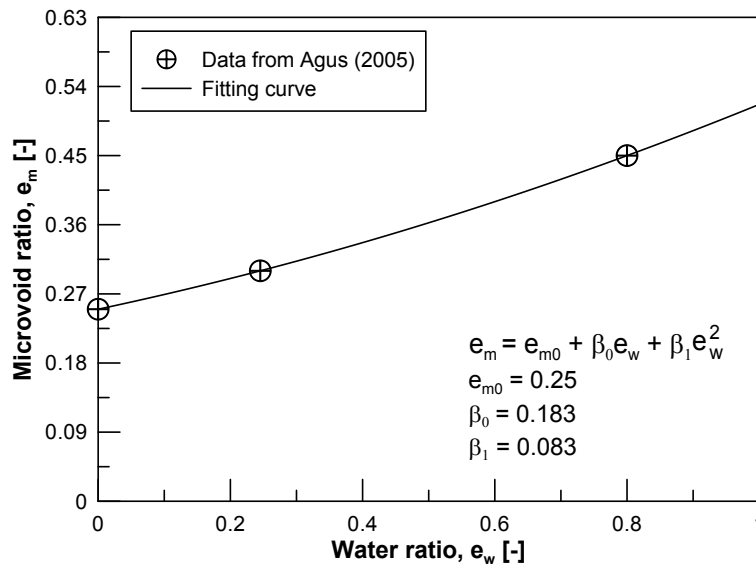


Figure 6.6: Evolution of micro-void ratio with water void ratio for compacted Calcigel bentonite-sand mixture (50:50) from Agus (2005).

plane became independent from the sample initial dry densities. A collection of points in this place is sufficient to calibrate the two parameters. In the final step, macro-structure water retention parameters were calibrated. The macroscopic parameter ( $A$ ) allows for tracking the dependency of the air-entry suction on the void ratio: it can reproduce the correct evolution of the air-entry (or air-occlusion) value with the sample dry density. The parameters  $n$  and  $m$  control the drying-wetting rate of the material in the low suction range. Figure 6.7 shows the calibration of Dieudonne water retention model and the van Genuchten model against the experimental data.

### 6.3.3 Identification and calibration of hydraulic parameters

The saturated permeability of the Calcigel bentonite-sand mixture (50:50) was determined by conducting a falling head permeability test in the oedometer. Prior to conduct the test, the as-compacted sample (initial density =  $1.8 \text{ Mg/m}^3$ ; water content = 9 %) was subjected to hydration under constant volume condition. Once the sample got saturation, the top inlet was connected to a manometer tube, while the bottom inlet was connect to the volume pressure controller for applying the water pressure and calculating the flow rate. Later, the saturated permeability was calculated.

The identification of parameters related to the Kozeny-Carman (Kozeny, 1936; Carman, 1938) formulation require the saturated permeability values at different initial porosity

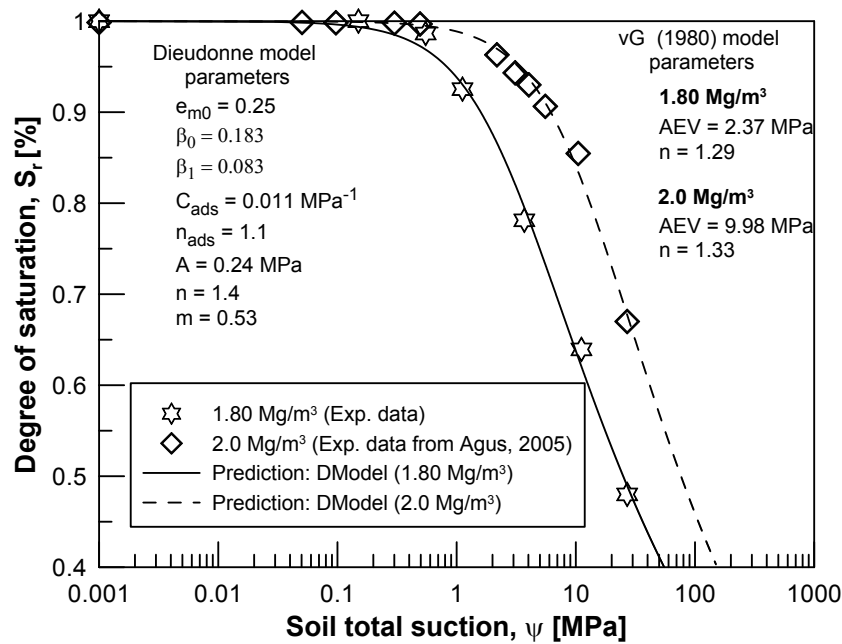


Figure 6.7: Calibration of water retention models against the experimental data on Cal-cigel bentonite-sand mixture (50:50) at two different dry densities (wetting path under confined condition).

values. These values were collected from Agus (2005) (initial dry density = 2.0 Mg/m<sup>3</sup>; water content = 9 %) and Long (2014) (initial dry density = 1.4 Mg/m<sup>3</sup>; water content = 9 %) on the similar bentonite-sand mixture (50:50). Using the measured and collected data, the parameters related to the Kozeny-Carman formulation were identified (see Fig. 6.8).

The parameter associated with the unsaturated hydraulic conductivity function proposed by Van Genuchten (1980) was computed the soil water retention data under constant volume condition. Table 6.2 summarizes the water retention parameters and the hydraulic parameters for the tested material.

## 6.4 Features of numerical simulation

A 2D axisymmetric model along Y-axis is selected for a fully coupled hydro-mechanical analysis. The model dimensions were selected according to the sample size in the water infiltration test (dimension along X-axis = 75 mm; dimension along Y-axis = 300 mm). The model geometry and initial boundary conditions are shown in Figure 6.9. The displacement in Y-direction was restricted along the line 1 and 3, while displacement in X-direction was restricted along the line 2 as depicted in Figure 6.9a. The initial to-

Table 6.2: Hydraulic parameters for compacted sand- Calcigel bentonite mixture having equal dry mass ratio.

Parameters	Description	Value
<b>van Genuchten (1980) model</b>	$S_e = \left(1 + \left(\frac{s}{A}\right)^n\right)^{-\left(1 - \frac{1}{n}\right)}$	
$A$ [MPa]	Air-entry suction	2.37
$n$ [-]	Shape function for retention curve	1.29
$S_{max}$ [-]	Max. field saturation	1
$S_{res}$ [-]	Residual field saturation	0
<b>Dieudonne et al. (2017): Microstructure water retention model</b>	$e_m = e_{m0} + \beta_0 e_w + \beta_1 e_w^2$ $e_{wm} = e_m \exp[-(C_{ads}s)]^{n_{ads}}$	
$e_{m0}$ [-]	Micro void ratio at $e_w = 0$	0.25
$\beta_0$ [-]	Parameter 1 for microstructure evolution	0.183
$\beta_1$ [-]	Parameter 2 for microstructure evolution	0.083
$C_{ads}$ [MPa <sup>-1</sup> ]	Parameter 1 for adsorption (Micro-level)	11.0E-3
$n_{ads}$ [-]	Parameter 2 for adsorption (Micro-level)	1.1
<b>Dieudonne et al. (2017): Macrostructure water retention model</b>	$e_{wM}(s, e, e_m) = (e - e_m) \left[1 + \left(\frac{s}{\alpha}\right)^n\right]^{-m}$	
$\alpha = \frac{A}{e - e_m}$ [MPa]	A (Macro-level parameter)	0.24
$m$ [-]	Shape parameter 1 for retention curve	0.53
$n$ [-]	Shape parameter 2 for retention curve	1.4
<b>Kozney-Carman formulation</b>	$K = K_0 \frac{(1 - \phi_0)^M}{\phi_0^N} \frac{\phi^N}{(1 - \phi)^M}$ for vG model $K = K_0 \frac{(1 - e_{M0})^M}{e_{M0}^N} \frac{e_M^N}{(1 - e_M)^M}$ for Dieudonne model	
$K_0$ [m <sup>2</sup> ]	Intrinsic permeability with matrix $\phi_0$ or $e_{M0}$	6.75E-20
$K$ [m <sup>2</sup> ]	Intrinsic permeability with matrix $\phi$ or $e_M$	-
$M$ [-]	Parameter 1 for KC formulation	3
$N$ [-]	Parameter 2 for KC formulation	1
<b>Relative permeability (water/air)</b>	$k_{rw} = \sqrt{S_{rw}} \left(1 - \left(1 - S_{rw}^{\frac{1}{\lambda}}\right)^\lambda\right)^2$	
$\lambda$ [-]	Parameter for water/air relative permeability	0.5



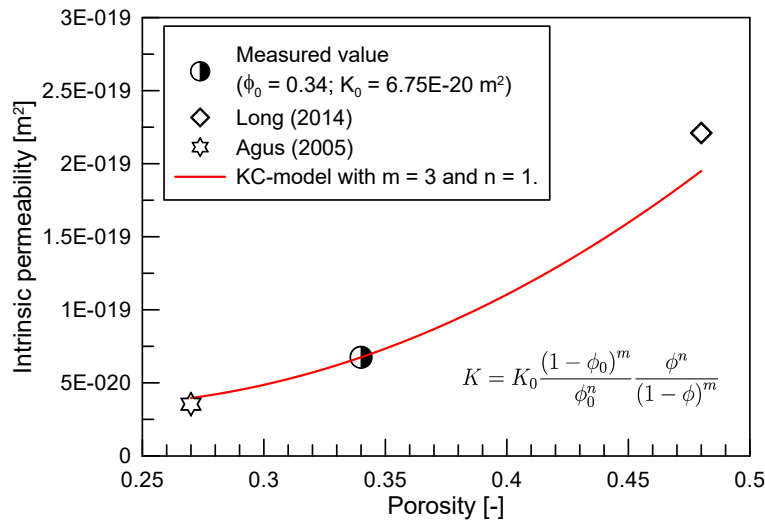


Figure 6.8: Sample initial porosity versus intrinsic permeability of compacted Calcigel bentonite-sand mixture (50:50): experimental data and the predicted values using Kozeny-Carman model.

tal stress in the material was assumed to be isotropic and equal to the 0.1 MPa. An isoparametric quadrilateral element (2D) with 8 nodes was selected for the analysis. The element for 2D case posses five degrees of freedom at each node: two displacements of the soil skeleton, a liquid water pressure, a gas (dry air+vapor) pressure and temperature. The temperature is kept constant at 20 °C. The initial total suction of the material was assigned as 26.90 MPa. It was assumed that the contact between the sample and the cell is frictionless. The hydration-pressure (i.e., 15 kPa) was applied by increasing the initial pore water pressure of the bottom nodes.

## 6.5 Results and discussion

### 6.5.1 Evolution of state variables

Figure 6.10 shows the comparison between the predicted and measured relative humidity values over the elapsed time along the height of soil sample. The predicted values show a good agreement with the experimental values. However, a minor deviation between the numerical and experimental results can be observed for the measurement sections X2 and X3.

Figure 6.11 shows the comparison between the predicted and measured water content over elapsed time for measurement sections X1, X2 and X3. Similar to the relative humidity

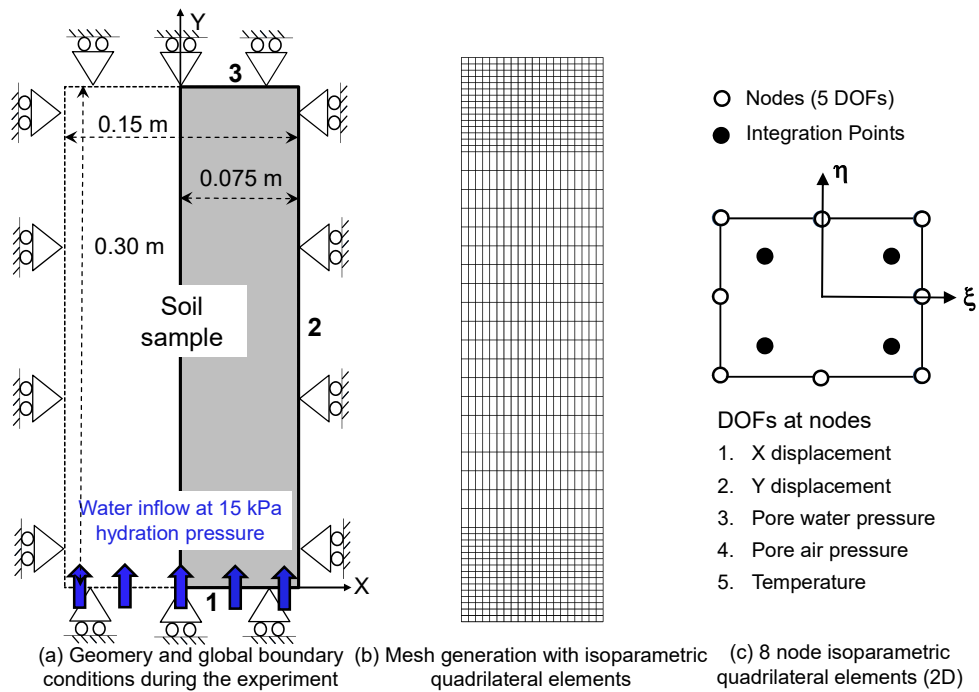


Figure 6.9: Features of numerical simulation, (a) geometry with global force and displacement boundary conditions, (b) mesh formation and (c) specifications of 2D isoparametric quadrilateral element with 5 degree of freedoms.

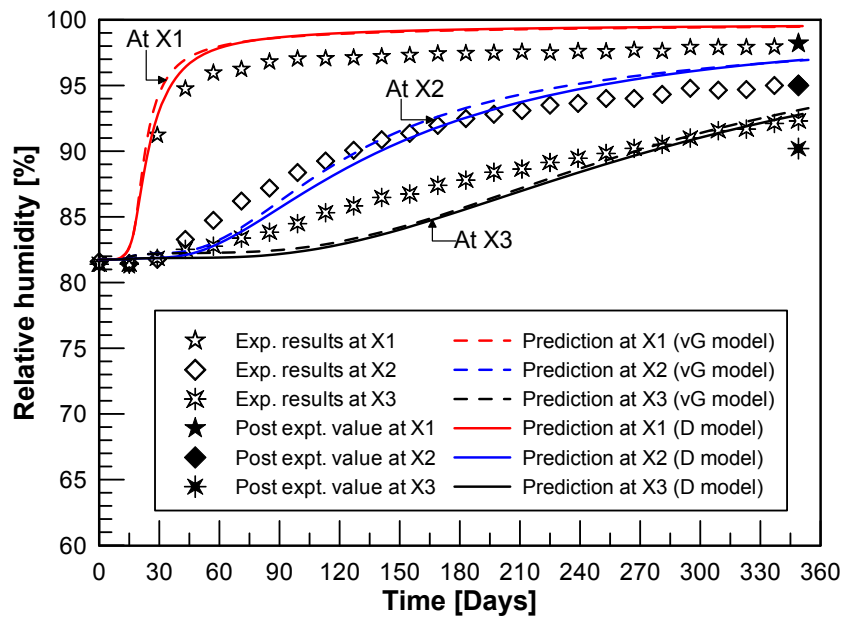


Figure 6.10: Experimental vs. simulation results: elapsed time vs. relative humidity values along the height of soil sample.

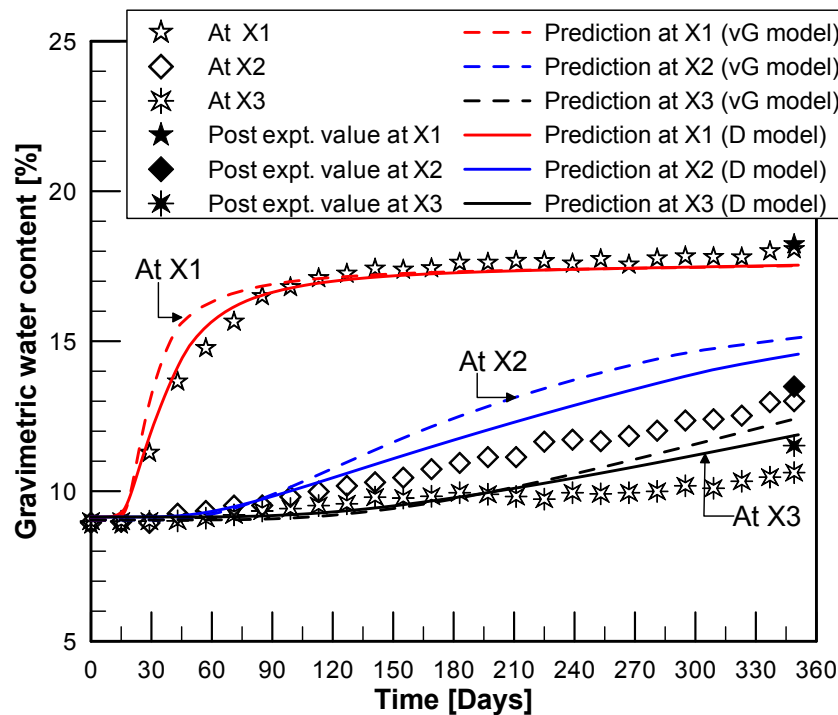


Figure 6.11: Experimental vs. simulation results: elapsed time vs. water content along the height of soil sample.

evolution, the effect of distance on the saturation rate is evident. Likewise, the relative humidity evolution at section X1, the water content increases rapidly with the initiation of hydration. The predicted values at section X1 agree well with the experimental results. The predicted values using Dieudonne water retention model showed a better agreement with the experimental values at measurement section X2 and X3. However, the predicted values of water content were slightly higher than the measured ones.

The predicted water volume infiltrated into the soil sample was compared with the measured volume during the water infiltration test (see Fig. 6.12). The figure also shows the calculated volume which infiltrated into the soil sample deduced from the transient water content measurements. The predicted values shows a good agreement with the measured and calculated water volume with some minor variations. A decrease in the flow rate with the elapsed is evident from the Figure 6.12, which signifies the effect of water potential gradient along the height of soil sample on the rate of saturation.

The Kozney-Carman (KC) equation (Kozeny, 1936; Carman, 1938) for the porosity dependent saturated hydraulic conductivity along with the Mualem-van Genuchten equation Van Genuchten (1980) provide a good estimation of material unsaturated hydraulic conductivity during the hydration process. The Mualem-van Genuchten closed-form equation

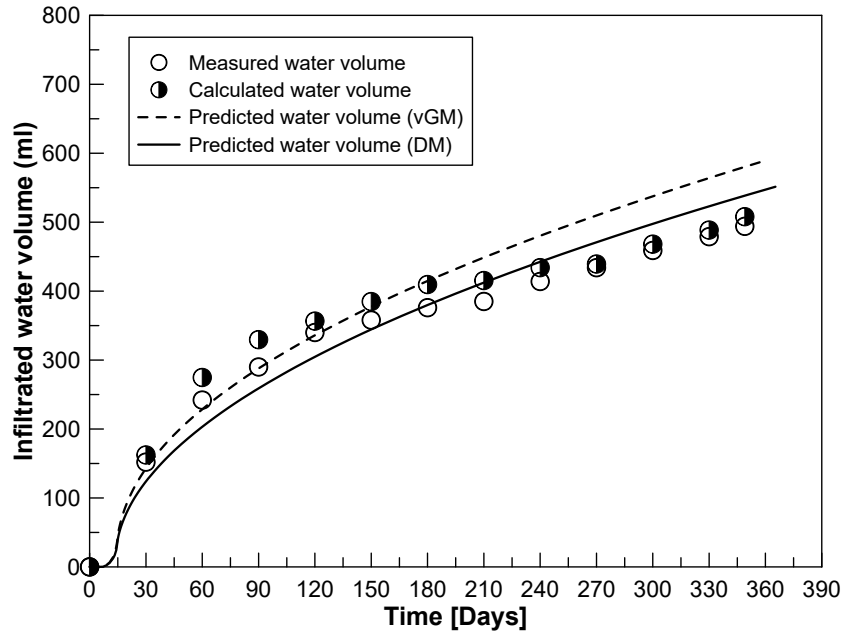


Figure 6.12: Experimental vs. simulation results: elapsed time vs. infiltrated water volume.

for unsaturated hydraulic conductivity function ( $k_{rl}$ ) is a non-linear function of degree of saturation ( $S_r$ ), which was calculated using the van Genuchten Van Genuchten (1980) and Dieudonne soil water retention model Dieudonne et al. (2017). The Kozney-Carman (KC) equation for the porosity dependent saturated hydraulic conductivity along with the Van Genuchten (1980) closed-form solution for the unsaturated hydraulic conductivity function provide a good prediction of water content and relative humidity evolution over elapsed time. The Mualem-van Genuchten closed-form equation for unsaturated hydraulic conductivity function ( $k_{rl}$ ) is a non-linear function of degree of saturation ( $S_r$ ), which was calculated using the Van Genuchten (1980) and Dieudonne et al. (2017) soil water retention model.

In the numerical simulation, the initiation of hydration from the bottom-end increased the void ratio at section X1 close to the hydration-end as shown in Figure 6.13a. Since the global swelling of the sample was kept constant, an increase in the porosity near the vicinity of the hydration-end was counterbalanced by an decrease in porosity for the measurement sections X2 and X3. According to the Dieudonne water retention model, the micro void ratio ( $e_m$ , initial value = 0.30) increased with an increase in the water void ratio or a decrease in the soil total suction during the hydration process (see Fig. 6.13b). As the macro void ratio ( $e_M$ ) was defined as the difference between the total void ratio  $e$  and the microstructural void ratio  $e_m$ . Hence, the macro void ratio progressively

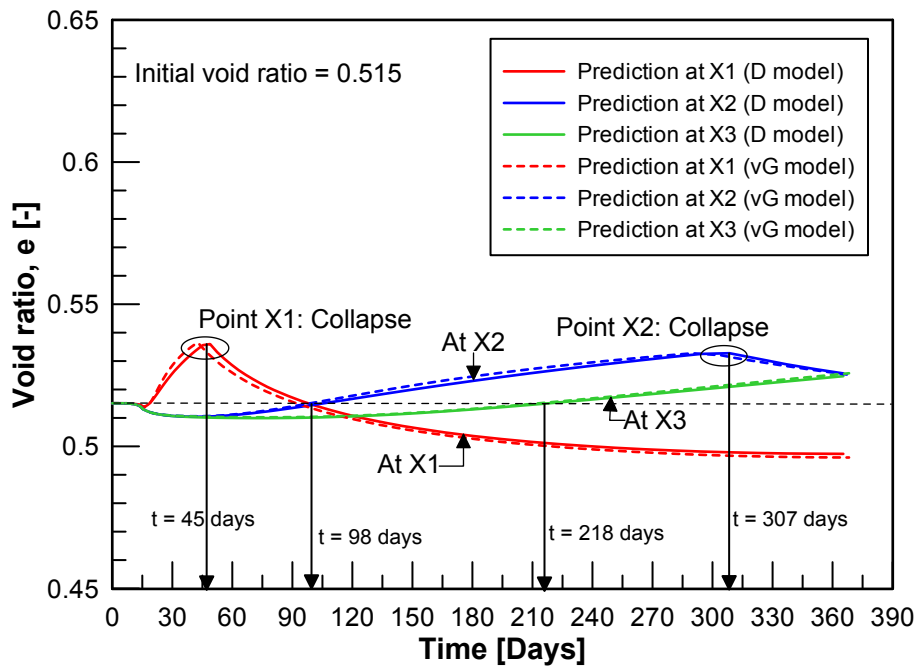
decreased during the hydration process, which results into the reduction in the saturated water permeability according to KC equation as depicted in Figure ??.

The evolution hydraulic conductivity is shown in Figure 6.14. It is evident from Figure 6.14 that the van Genuchten model provides slightly higher unsaturated hydraulic conductivity values than the Dieudonne model. Consequently, the predicted values (i.e., relative humidity, water content and flow rate) showed some minor variations (see Figs. 6.10, 6.11 and 6.12). In general, both models are capable to capture the water transfer mechanism and the permeability evolution in the compacted bentonite sand mixture during the hydration process under constant volume condition.

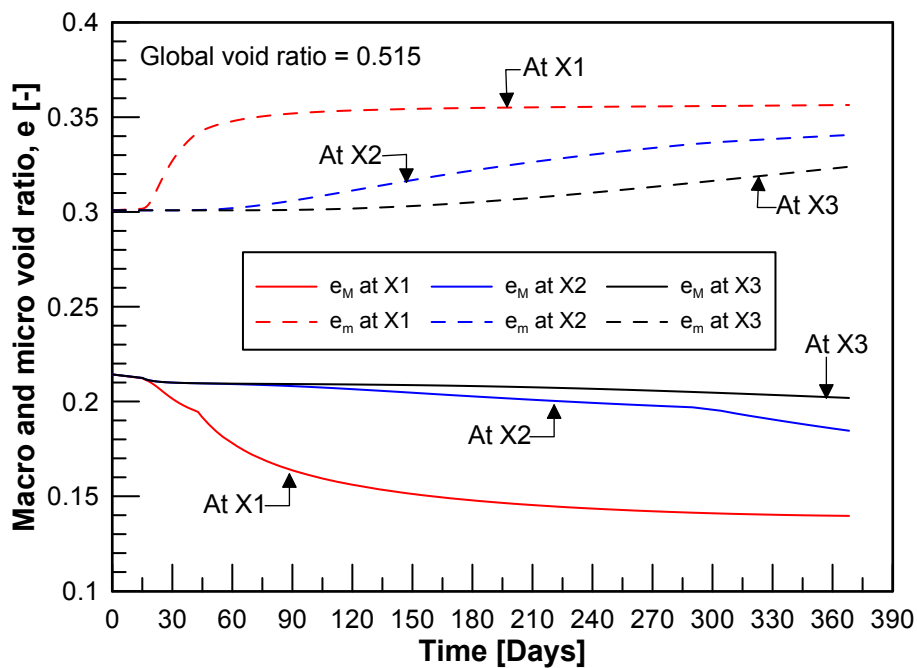
### 6.5.2 Material swelling behavior

The comparison between the predicted and measured axial total stress at the top and bottom ends is presented in Figure 6.15. The top load cell measured the applied stress from the bottom elements during the hydration process. Under the confined condition and at equilibrium, it may be anticipated that the measured axial stress at both ends of the sample are equal. However, it was observed that the axial stress developed at the top end of the sample was not transmitted towards the bottom of the sample, which can be attributed to factors, such as (i) dissimilar compressibility characteristics along the height of the sample due to variations in the water content, (ii) the presence of construction joints meant for installing the pressure transducers, (iii) the side frictional resistance between the sample and the PVDF rings, and (iv) the composite nature of the sample-sensors assembly that created complex stress-deformation characteristics of the system. These features were not considered during the simulation. However, a decent agreement can be observed between the experimental values and the model predictions at the bottom-end (see Fig. 6.15). The development of axial total stress at the bottom end exhibits a rapid increase before reaching to 1.1 MPa in 45 days. With the elapsed time, the axial swelling pressure at the bottom end increased gradually and reached to 1.68 MPa in 349 days. The simulation results successfully captured the trend, however the predicted values were slightly higher than the experimental measurements.

Figure 6.16 presents the comparison between the predicted and measured values of lateral swelling pressure for the measurement sections X1, X2 and X3. During the experiment, the lateral swelling pressure measurements were performed with the cylindrical-piston and a miniature load cell assembly. These PVDF pistons were kept in direct contact with the soil sample during the installation of test-setup. As soon as the hydration started, the



(a)



(b)

Figure 6.13: Numerical simulation results (a) evolution of void ratio and (b) evolution of micro and macro void ratio according to Dieudonne water retention model (Dieudonne et al., 2017).

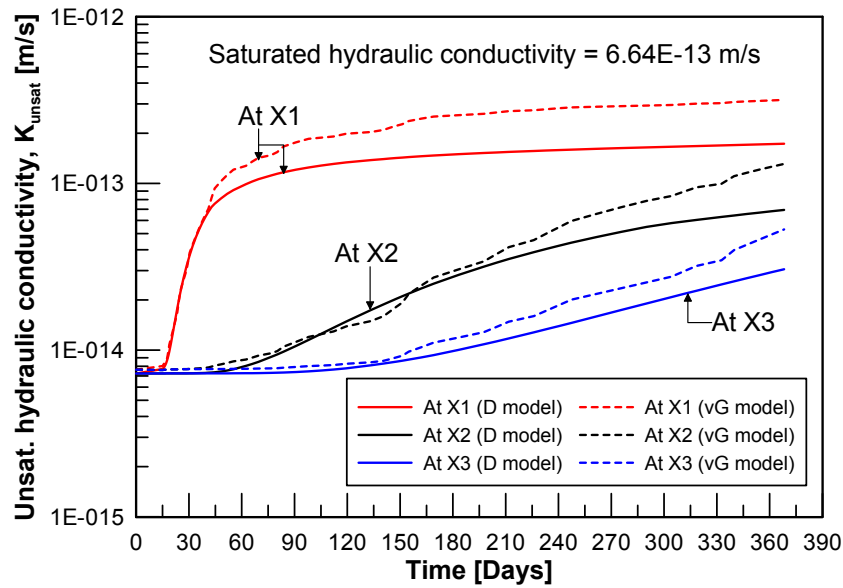


Figure 6.14: Numerical simulation results: evolution of hydraulic conductivity (m/s) over time for measurement section X1, X2 and X3.

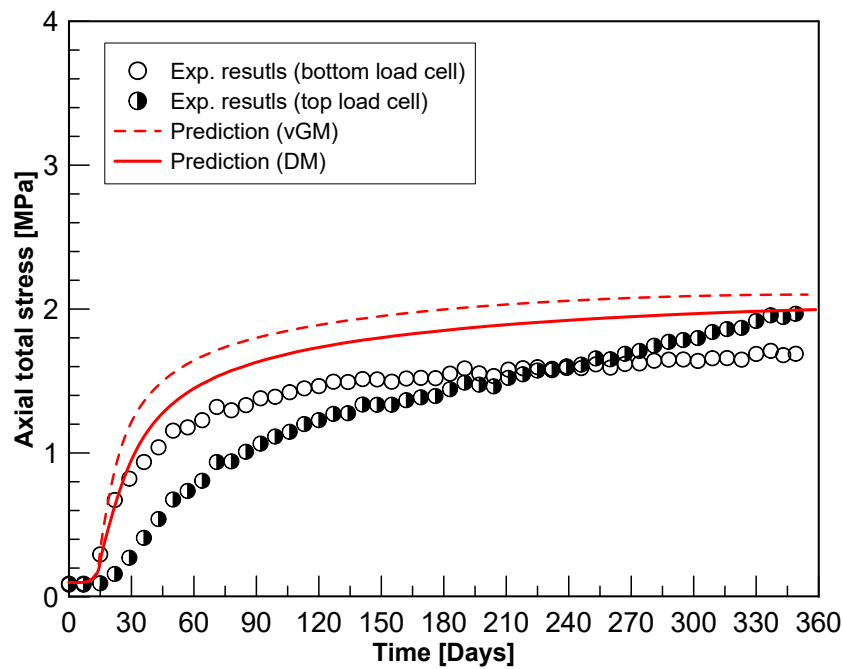
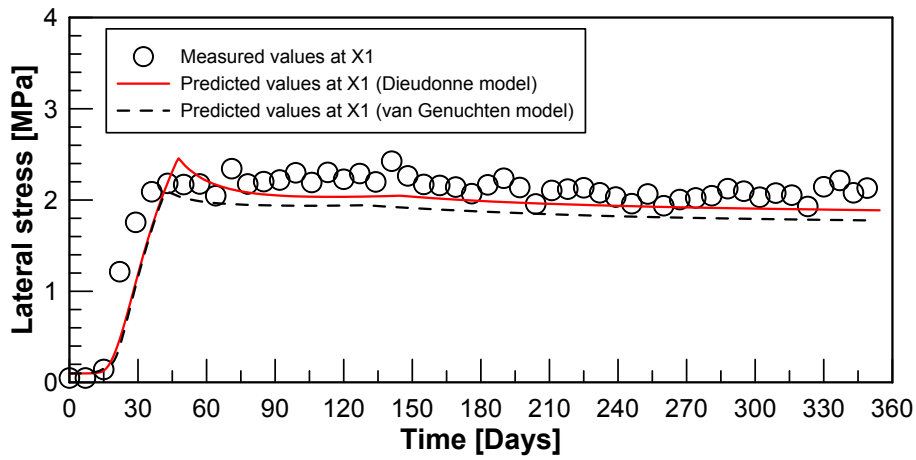
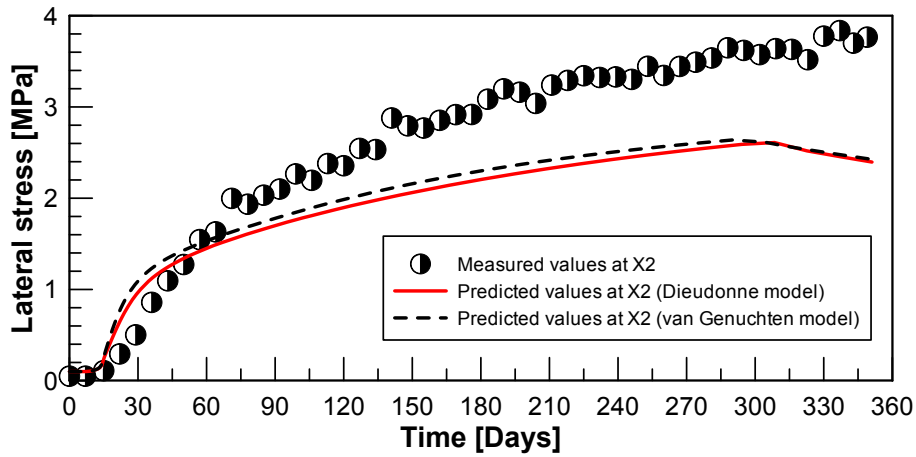


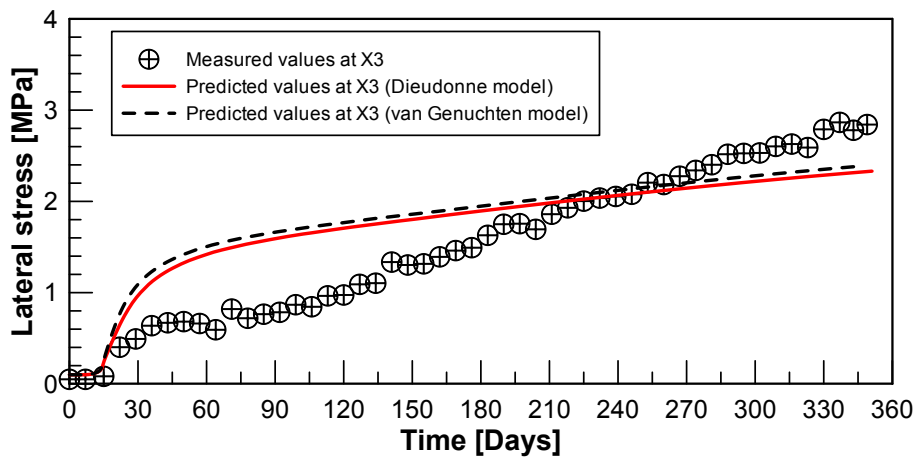
Figure 6.15: Experimental vs. simulation results: elapsed time vs. axial total stress.



(a) At section X1



(b) At section X2



(c) At section X3

Figure 6.16: Experimental vs. simulation results: elapsed time vs. lateral total stress.



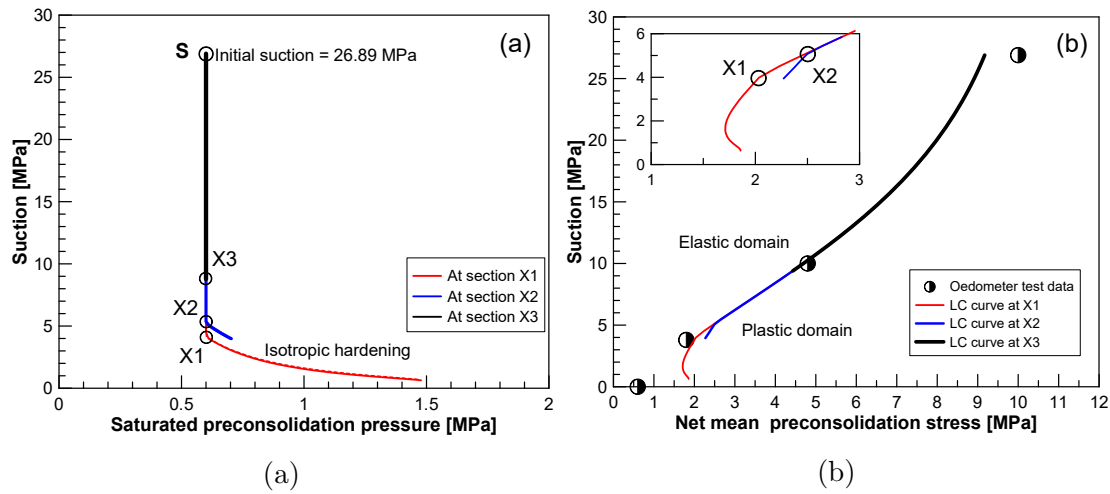


Figure 6.17: Numerical simulation results (a) saturated preconsolidation stress vs. soil suction and (b) evolution of loading-collapse curve along the sample height.

lateral total stress measurement system at the section X1 responded quickly and reached to 2.18 MPa within 45 days. With the further hydration, the measured values at the section X1 showed some oscillations before reaching to a value of 2.18 MPa within 349 days. The model predictions showed a good agreement with the experimental values at section X1. However, the numerical simulation did not reproduce the experimental data for measurement sections X2 and X3.

In further analysis, Figure 6.17a presents the variation in the saturated preconsolidation pressure with the soil total suction for measurement sections X1, X2 and X3. The yielding/collapse at section X1 and X2 along with an increase in preconsolidation stress in saturated state is evident at sections X1 and X2. While the stress-state at section X3 ( $p - s$ ) varies within the elastic domain of the loading-collapse (LC) curve. Figure 6.17b shows the evolution of LC curve along the height of soil sample, the data were obtained from the numerical analysis. Additionally, the oedometer tests data are also shown. The elastoplastic behavior of material at the measurement sections X1 and X2 and resulting increase in the preconsolidation pressure (i.e., isotropic hardening) can be observed from Figure 6.17b. The material at the section X3 exhibited the elastic swelling. Hence, the experimental results along with the numerical analysis indicated that the material stress-state in  $p - s$  plane evolves in elastic to elastoplastic domain during the hydration process.

In the numerical analysis, the sample was laterally and axially confined and the global porosity remained constant during the hydration. In particular, suction changes are assumed to yield only the volumetric strain. Accordingly, in the elastic domain, the total

strain increment is given by

$$d\varepsilon_v^e = d\varepsilon_{vp}^e + d\varepsilon_{vs}^e = \frac{k}{1+e} \frac{dp}{p} + \frac{k_s}{1+e} \frac{ds}{s + u_{atm}} = \frac{dp}{K} + \frac{ds}{K_s} \quad (6.53)$$

with  $d\varepsilon_{vp}^e$  and  $d\varepsilon_{vs}^e$  are the elastic increments of volumetric strain associated to changes in net stress and changes in suction, respectively,  $k_s$  is the slope of the reversible wetting-drying line,  $u_{atm}$  is the atmospheric pressure and  $K$  is the bulk modulus for changes in suction.

Since the global porosity is constant during the analysis, hence

$$d\varepsilon_v^e = 0. \quad (6.54)$$

Using Equation 6.53, Equation 6.54 yields

$$d\varepsilon_{vp}^e = -d\varepsilon_{vs}^e \quad (6.55)$$

hence,

$$dp = -\frac{k_s}{k} \frac{ds}{(s + u_{atm})} \cdot p \quad (6.56)$$

with  $dp$  the incremental change in the magnitude of net mean stress,  $k_s$  suction dependent soil elastic stiffness parameters,  $k$  stress dependent soil elastic stiffness parameter,  $ds$  the incremental change in the soil suction and  $p$  net mean stress.

The above equation indicates that an incremental change in the magnitude of net mean stress depends on the ratio of elastic stiffness ( $k_s/k$ ), an incremental change in soil suction ( $ds$ ), the current stress state ( $p$ ) and the soil suction. According to Figure 6.16, the observed incremental rates of total stress in lateral direction during the initial phase of hydration are similar at sections X2 and X3, which is mainly due to an insignificant change in the soil suction at X2 and X3 during the initial phase of hydration (i.e., 45 days). After 45 days, the suction at X2 decreases faster than the section X3, so the total stress in lateral direction at section X2 deviates from section X3. The total stress evolution in lateral direction at section X2 exhibits a collapse at  $t = 300$  days and the stress state in the  $(p - s)$  plane changes from an elastic to an elastoplastic domain (see Fig. 6.17). The above observations indicate that the soil stress-state during the hydration from one-end depends on several factors, such as soil swelling, interaction between different soil layers and non-uniform changes in the sample condition during the progressive hydration process. Additionally, the presence of technical/constructional gaps and non-uniform soil stiffness along the height of soil sample during the hydration are also responsible for a different axial and lateral swelling pressure dynamics.

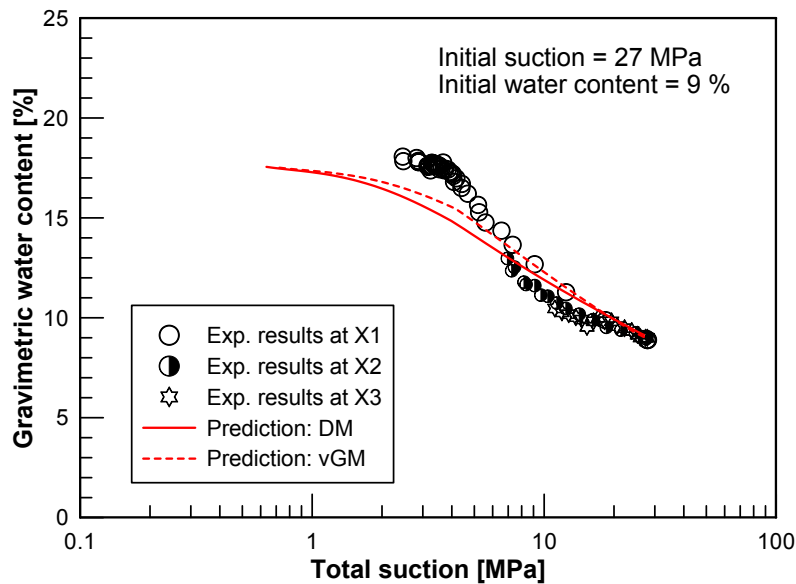


Figure 6.18: Comparison between the experimental and simulation results: soil suction vs. gravimetric water content.

### 6.5.3 Soil water retention behavior

In the water infiltration test, the experimental values of the degree of saturation were deduced from the transient water content measurements with an assumption of a constant void ratio along the height of soil sample. The test results revealed that the above assumption overestimated the degree of saturation particularly near the vicinity of hydration-end. Figure 6.18 compares the predicted and measured data (soil suction vs. gravimetric water content). The simulation results exhibited a unique relationship along the height of soil sample and showed a good agreement with the measured values within the range of soil suction from 27 MPa to 6 MPa. In the numerical simulation, the water content values are calculated from the updated void ratio and the current degree of saturation ( $S_r$ ) obtained from  $s - S_r$  relationship according to van Genuchten or Dieudonne water retention model. For the lower suction range (i.e.,  $RH \geq 95\%$ ), the predicted values slightly deviate from the experimental results and underestimate the water content.

## 6.6 Summary

A fully coupled hydro-mechanical analysis of the water infiltration test was performed using the finite element method. The Barcelona Basic Model along with the recently developed double structure water retention model Dieudonne et al. (2017) were used.

The suction-controlled oedometer tests were performed to identify the Barcelona Basic Model parameters for the Calcigel bentonite-sand mixture (50:50). It was observed that the collapse potential decreased with increasing the net mean vertical stress, the observed behavior was contrary to the assumption made by Alonso et al. (1990) during the formulation of the Barcelona Basic Model. The model parameters were identified in a sequential manner and calibrated against the suction-controlled oedometer test results. The model results were in a good agreement with the experimental measurements for the relative humidity and water content evolution over elapsed time. The predicted values of axial total stress at the hydration end also showed good agreement with the experimental measurements. However, some variations were observed in the predicted and measured values of the lateral total stresses.

# 7 Conclusions and recommendations

## 7.1 Summary and conclusions

The deep geological disposal concept is accepted worldwide as a promising solution for the safe disposal of heat-generating radioactive waste. In this concept, an effective isolation of radioactive waste relies on the long-term performance of the engineered barrier systems. Bentonite-based materials are considered as a key component of the engineered barrier systems due to having favorable engineering properties such as, low permeability, high swelling potential and good radionuclide retention properties. An adequate swelling potential ensures the effectiveness of hydraulic sealing around the waste canister. Indeed, the bentonite-based materials fill the constructional/technological gaps during the hydration process and create a zone of low-permeability to limit water flow around the underground openings. Once these gaps are completely filled, the further hydration process yields the development of swelling pressure against the global volume constraints. Hence, from the design point of view, the rate of saturation and the resulting swelling pressure are of prime importance. This dissertation intends to study the coupled hydro-mechanical behavior of a compacted bentonite-sand mixture (50:50) proposed to be used as a backfill material in repositories. To address the issue, the strategy adopted in this work follows a holistic approach combining the experimental, analytical and numerical investigations.

A new column-type experimental device is designed for testing the soil under the applied thermal and thermo-hydraulic gradients. For applying the thermal gradient, the temperature can be controlled in the range of 5 to 95 °C at both ends of the cylindrical soil sample. For applying the hydraulic gradient, water can be supplied externally to the top and bottom ends. The device facilitates the transient measurements of temperature, water content, relative humidity and stresses in both axial and lateral directions at various pre-selected locations. System compliance tests were performed at both room temperature and also at 80 °C to ensure the satisfactory performance of the device and monitoring sensors. A test was conducted with a compacted Calcigel bentonite-sand mixture (50:50)

under an applied thermal gradient (bottom-end = 80 °C ; top-end = 20 °C). The test conditions mimic the initial heating phase of the buffer material in a repository.

A water infiltration test was conducted to mimic the hydration of a proposed backfill material (a compacted Calcigel bentonite-sand mixture (50:50)) in pursuant to the German disposal concept. To imitate the water ingress and saturation process, the distilled water was supplied externally from the bottom-end under 15 kPa hydration-pressure. The test was conducted under a constant volume condition for a period of 349 days. The key process variables (i.e., temperature, relative humidity, water content and soil suction) were measured along with stresses in both axial and lateral directions as a function of time and space.

A fully-coupled hydromechanical analysis of the water infiltration test was conducted with finite element code LAGAMINE. The Barcelona Basic Model (Alonso et al., 1990) for describing the mechanical behavior of unsaturated expansive soils was adopted along with double structure water retention model (Dieudonne et al., 2017). A methodology is presented for the identification and calibration of constitutive model parameters. Based on the performed investigations and results obtained in this study, the following conclusions can be drawn:

- In the early lifetime of the buffer material, the moisture redistribution occurs due to the temperature difference (bottom-end = 80 °C ; top-end = 20 °C) that causes an increase in the relative humidity towards the cooler regions of the buffer material and a decrease of the same in the sections close to the waste canister. The temperature-induced redistribution of moisture content affects the stress distribution in axial and lateral directions. Additionally, the presence of construction/technological gaps, the friction at buffer/host-rock interface also affect the stress distribution in the buffer material.
- The rate of saturation of the backfill material depends on the soil-water potential gradient along the hydration-path. The soil-water potential gradient decreases rapidly close to the hydration-end as compare to the inner sections; consequently, the compacted blocks in the immediate vicinity of host rock achieve saturation faster than the inner sections.
- The hydration process initiates the redistribution of porosity within the backfill material. In the vicinity of host rock, the compacted blocks exhibit an increase in the porosity under free-swell condition during the initial phase of hydration. Once the exterior blocks have a tight contact with the host rock, the swelling pressure

yields the compression of the interior blocks; consequently, the boundary condition changes from a free-swell to constant-volume condition.

- In the water infiltration test, the measured axial stresses at the top and bottom ends were dissimilar. The total stress measurements in the lateral direction revealed anisotropic stress state due to the following possible reasons, (i) the hydration-induced heterogeneities along the hydration-path and the resulting changes in the soil stiffness, (ii) interactions between the swollen and non-swollen layers of material and (iii) presence of frictional stress at the soil/wall interface. These findings signify the role of a backfill-host rock interface in the swelling pressure distribution along the axis of disposal tunnel.
- The comparison between the measured data (soil suction vs. degree of saturation) in the water infiltration test and in the element test showed disagreement at the lower suction values. The observed disagreement was due to the porosity-redistribution in the vicinity of hydration-end during the hydration process; consequently, the assumption of a constant global void ratio may yield to an overestimation of the computed degree of saturation near the hydration-end.
- One of the major challenges in the application of the Barcelona Basic Model (BBM) is the identification of model parameters. To address this issue, a methodology is presented for parameter identification and calibration purpose using the suction-controlled oedometer tests.
- The simulation results showed good agreement with measured experimental data pertaining to the evolution of water content and relative humidity and captured the water transport mechanism and the permeability evolution in a compacted bentonite-sand mixture during the transient hydration process. Considering the mechanical behavior, the simulation results successfully predicted the measured axial and lateral total stresses close to the hydration-end. While for the inner sections, the simulation results was not able to predict the measured lateral total stress.
- The simulation results exhibited good agreement with the transient soil water retention profiles along the height of soil sample up to a soil suction of 6.94 MPa (RH = 95 %). In the lower suction range, the measured values deviated from the simulation results with an overestimation of the degree of saturation values particularly in the vicinity of the hydration-end, it can be attributed to an underestimation of the void ratio close to the hydration end.

- A comparative analysis of experimental and numerical investigations provides key inputs to improve the existing constitutive models for a coupled hydro-mechanical analysis. It is not only the anisotropy in the fabric during the compaction process, other factors such as presence of constructional/technological voids, the hydration-induced heterogeneities along the height of soil sample and the friction at the soil/wall interface are also responsible for anisotropic swelling behavior.

## 7.2 Recommendations

In conclusion, the following recommendations are suggested for further investigations in this field of study.

- Further tests should be conducted for investigating the effect of groundwater geochemistry on the observed test results.
- Microstructure investigations should be considered to study the effect of repository relevant boundary conditions on the clay microstructure characteristics and anisotropic behavior. Based on the systematic study of the relationship among micro characteristic parameters, hydro-mechanical indices, the swelling and permeability model of bentonite-based materials under the effect of thermal-hydro-mechanical-chemical (THMC) effects should be developed.
- The effect of different mechanical constitutive models such as the Barcelona Expansive Model (Gens & Alonso, 1992) and the hypoplasticity model (Mašín, 2014) on the simulation results should be investigated.
- The interaction between interfaces, constructional gaps and technical voids significantly affect the behavior of buffer/backfill material, their explicit modeling at the field-scale is cumbersome. In particular, the inter-facial friction between the compacted blocks and the host rock should be considered in the numerical simulation.



# Bibliography

- Agus, S., Arifin, Y., Tripathy, S. & Schanz, T. (2013), 'Swelling pressure-suction relationship of heavily compacted bentonite-sand mixtures', *Acta Geotechnica* **8**(2), 155–165.
- Agus, S. S. (2005), An experimental study on hydro-mechanical characteristics of compacted bentonite-sand mixtures, PhD thesis, Bauhaus-University Weimar.
- Agus, S. S. & Schanz, T. (2005), 'Comparison of four methods for measuring total suction', *Vadose Zone Journal* **4**(4), 1087–1095.
- Agus, S. S. & Schanz, T. (2007), Errors in total suction measurements, *in* 'Experimental Unsaturated Soil Mechanics', Springer, pp. 59–70.
- Agus, S. S. & Schanz, T. (2008), 'A method for predicting swelling pressure of compacted bentonites', *Acta Geotechnica* **3**(2), 125–137.
- Ahlneck, C. & Zografi, G. (1990), 'The molecular basis of moisture effects on the physical and chemical stability of drugs in the solid state', *International Journal of Pharmaceutics* **62**(2-3), 87–95.
- Åkesson, M., Jacinto, A., Gatabin, C., Sanchez, M. & Ledesma, A. (2009), 'Bentonite thm behaviour at high temperatures: experimental and numerical analysis', *Géotechnique* **59**(4), 307–318.
- Al-Badran, Y., Baille, W., Tripathy, S. & Schanz, T. (2017), 'Swelling behavior of bentonite-based backfilling materials in nuclear waste repository conditions', *Journal of Hazardous, Toxic, and Radioactive Waste* **21**(1).
- Albrecht, B., Benson, C. & Beuermann, S. (2003), 'Polymer capacitance sensors for measuring soil gas humidity in drier soils', *Geotechnical Testing Journal* **26**(1), 3–11.
- Alonso, E., Alcoverro, J., Coste, F., Malinsky, L., Merrien-Soukatchoff, V., Kadiri, I., Nowak, T., Shao, H., Nguyen, T., Selvadurai, A. et al. (2005), 'The febex benchmark

- test: case definition and comparison of modelling approaches', *International Journal of Rock Mechanics and Mining Sciences* **5**(42), 611–638.
- Alonso, E. E., Gens, A. & Josa, A. (1990), 'A constitutive model for partially saturated soils', *Géotechnique* **40**(3), 405–430.
- Assouline, S. (2006), 'Modeling the relationship between soil bulk density and the water retention curve contribution of the agricultural research organization, institute of soil, water and environmental sciences, bet dagan, israel, no. 607/05', *Vadose Zone Journal* **5**(2), 554–563.
- ASTM-D1557 (2007), Standard test methods for laboratory compaction characteristics of soil using modified effort (56,000 Ft-lbf/ft<sup>3</sup> (2,700 KN-m/m<sup>3</sup>)), Standard D698-07, ASTM International, West Conshohocken, PA.
- ASTM-D3977 (1997), Standard test methods for determining sediment concentration in water samples, Standard D3977-97, ASTM International, West Conshohocken, PA.
- ASTM-D422 (2007), Standard test method for particle-size analysis of soils, Standard D422-63, ASTM International, West Conshohocken, PA.
- ASTM-D4318 (2000), Standard test methods for liquid limit, plastic limit, and plasticity index of soils, Standard D4318-00, ASTM International, West Conshohocken, PA.
- ASTM-D698 (2007), Standard test methods for laboratory compaction characteristics of soil using standard effort (12 400 ft-lbf/ft<sup>3</sup> (600 kN-m/m<sup>3</sup>)), Standard D698-07, ASTM International, West Conshohocken, PA.
- ASTM-D854 (2002), Standard test methods for specific gravity of soil solids by water pycnometer, Standard D854-02, ASTM International, West Conshohocken, PA.
- ASTM-E104 (2007), Standard practice for maintaining constant relative humidity by means of aqueous solutions, Standard E104-02, ASTM International, West Conshohocken, PA.
- ASTMD2435-96 (1996), 'Standard test method for one-dimensional consolidation properties of soils', in 1998 Annual Book of ASTM Standards, Vol. 04.08.
- Avallone, E. & Baumeister, T. (2017), *Mark's standard handbook for mechanical engineers*, McGraw-Hill.
- Aylmore, L. & Quirk, J. (1959), 'Swelling of clay-water systems', *Nature* **183**, 1752–1753.

- Baille, W. (2014), Hydro-Mechanical Behaviour of Clays Significance of Mineralogy, PhD thesis, Ruhr-Universität Bochum.
- Bergaya, F. & Lagaly, G. (2013), *Basics*, Vol. 1 of *Handbook of Clay Science*, Elsevier Ltd., chapter 1.
- Bolt, G. (1956), 'Physico-chemical analysis of the compressibility of pure clays', *Géotechnique* **6**(2), 86–93.
- Börgesson, L., Chijimatsu, M., Fujita, T., Nguyen, T., Rutqvist, J. & Jing, L. (2001), 'Thermo-hydro-mechanical characterisation of a bentonite-based buffer material by laboratory tests and numerical back analyses', *International Journal of Rock Mechanics and Mining Sciences* **38**(1), 95–104.
- Börgesson, L., Johannesson, L., Sandén, T. & Hernelind, J. (1995), Modelling of the physical behaviour of water saturated clay barriers. laboratory tests, material models and finite element application, Technical report, Swedish Nuclear Fuel and Waste Management Co.
- Brooks, R. N. & Corey, A. T. (1964), 'Hydraulic properties of porous media', *Colorado State University, Hydro Paper* **3**, 27.
- Brunauer, S., Emmett, P. & Teller, E. (1938), 'Adsorption of gases in multi-molecular layers', *Journal of American Chemical Society* **60**, 309–319.
- Carman, P. (1938), 'Fundamental principles of industrial filtration (a critical review of present knowledge)', *Transactions of the Institution of Chemical Engineers* **16**, 168–188.
- Cases, J., Bérend, I., François, M., Uriot, J., Michot, L. & Thomas, F. (1997), 'Mechanism of adsorption and desorption of water vapor by homoionic montmorillonite: 3. the  $\text{mg}^{2+}$ ,  $\text{ca}^{2+}$ ,  $\text{sr}^{2+}$  and  $\text{ba}^{2+}$  exchanged forms', *Clays and Clay Miner* **45**(1), 8–22.
- Cerato, A. & Lutenegeger, A. (2002), 'Determination of surface area of fine-grained soils by the ethylene glycol monoethyl ether (EGME) method', *Geotechnical Testing Journal* **25**, 315–321.
- Chang, F.-R. C. & Sposito, G. (1996), 'The electrical double layer of a disk-shaped clay mineral particle: Effects of electrolyte properties and surface charge density', *Journal of Colloid and Interface Science* **178**(2), 555–564.
- Chapman, D. L. (1913), 'A contribution to the theory of electrocapillarity', *The London, Edinburgh, and Dublin philosophical magazine and journal of science* **25**(6), 475–481.

- Chapuis, R. P. & Aubertin, M. (2003), 'On the use of the kozeny carman equation to predict the hydraulic conductivity of soils', *Canadian Geotechnical Journal* **40**(3), 616–628.
- Cho, W.-J., Lee, J.-O. & Kang, C.-H. (2000), 'Influence of temperature elevation on the sealing performance of a potential buffer material for a high-level radioactive waste repository', *Annals of Nuclear Energy* **27**(14), 1271–1284.
- Colin Leung, David Holton, R. T. (2014), Review of the current status of work on enhanced bentonite buffer materials, RWMD Project RP51 TN-E2.2 103726-0008-UA00-TLN-0001 (Issue 2), Radioactive Waste Management Directorate, NDA.
- Collin, F., Li, X.-L., Radu, J.-P. & Charlier, R. (2002), 'Thermo-hydro-mechanical coupling in clay barriers', *Engineering Geology* **64**(2-3), 179–193.
- Cuevas, J., Villar, M., Fernández, A. M., Gómez, P. & Martín, P. (1997), 'Pore waters extracted from compacted bentonite subjected to simultaneous heating and hydration', *Applied Geochemistry* **12**(4), 473–481.
- Cui, Y., Loiseau, C. & Delage, P. (2002), Microstructure changes of a confined swelling soil due to suction controlled hydration, in 'Proceedings of the 3rd International Conference on Unsaturated Soils (UNSAT 2002), Recife, Brésil. Sous la direction de J. FT Jucá, TMP de Campos et FAM Marinho', Vol. 2, pp. 593–598.
- Cuisinier, O. & Masrouri, F. (2004), 'Testing the hydromechanical behavior of a compacted swelling soil', *Geotechnical Testing Journal* **27**(6), 1–9.
- De Boer, J. (1936), 'The influence of van der waals forces and primary bonds on binding energy, strength and orientation, with special reference to some artificial resins', *Transactions of the Faraday Society* **32**, 10–37.
- Delage, P., Cui, Y.-J. & Tang, A. M. (2010), 'Clays in radioactive waste disposal', *Journal of Rock Mechanics and Geotechnical Engineering* **2**(2), 111–123.
- Delage, P., Howat, M. & Cui, Y. (1998), 'The relationship between suction and swelling properties in a heavily compacted unsaturated clay', *Engineering Geology* **50**(1), 31–48.
- Delage, P., Marcial, D., Cui, Y. J. & Ruiz, X. (2006), 'Ageing effects in a compacted bentonite: a microstructure approach', *Géotechnique* **56**(5), 291–304.
- Delahaye, C. H. & Alonso, E. (2002), 'Soil heterogeneity and preferential paths for gas migration', *Engineering Geology* **64**(2-3), 251–271.

- Della Vecchia, G., Dieudonné, A.-C., Jommi, C. & Charlier, R. (2015), ‘Accounting for evolving pore size distribution in water retention models for compacted clays’, *International Journal for Numerical and Analytical Methods in Geomechanics* **39**, 702–723.
- Derjaguin, B. V. & Landau, L. D. (1941), ‘The theory of stability of strongly charged lyophobic sols and the adhesion of strongly charged particles in solutions of electrolyte’, *Acta Physicochimica (URSS)* **14**, 633–662.
- Dieudonne, A.-C., Della Vecchia, G. & Charlier, R. (2017), ‘Water retention model for compacted bentonites’, *Canadian Geotechnical Journal* **54**(7), 915–925.
- Dixon, D., Gray, M. & Thomas, A. (1985), ‘A study of the compaction properties of potential clay-sand buffer mixtures for use in nuclear fuel waste disposal’, *Engineering Geology* **21**(3-4), 247–255.
- Dohrmann, R. (1997), Kationenaustauschkapazität von Tonen. Bewertung bisheriger Analysenverfahren und Vorstellung einer neuen und exakten Silber-Thioharnstoff-Methode, PhD thesis, RWTH Aachen.
- Dubinina, M. & Radushkevich, L. (1947), The equation of the characteristic curve of the activated charcoal, in ‘Proceedings of the Union of Soviet Socialist Republics Academy of Sciences’, Vol. 55, pp. 331–337.
- Emmerich, K., Koeniger, F., Kaden, H. & Thissen, P. (2015), ‘Microscopic structure and properties of discrete water layer in Na-exchanged montmorillonite’, *Journal of Colloid and Interface Science* **448**, 24–31.
- Ferrage, E. (2004), Experimental investigation of smectite hydration from the simulation of 001 X-ray diffraction lines. Implications for the characterization of mineralogical modifications of the ‘argilite’ from the Meuse-Haute Marne site as a result of a thermal perturbation, PhD thesis.
- Ferrage, E. (2016), ‘Investigation of the interlayer organization of water and ions in smectite from the combined use of diffraction experiments and molecular simulations. a review of methodology, applications, and perspectives’, *Clays and Clay Minerals* **64**(4), 348–373.
- Ferrage, E., Lanson, B., Sakharov, B. A. & Drits, V. A. (2005), ‘Investigation of smectite hydration properties by modeling experimental x-ray diffraction patterns: Part i. montmorillonite hydration properties’, *American Mineralogist* **90**(8-9), 1358–1374.

- Fredlund, D. G. & Rahardjo, H. (1993), *Soil mechanics for unsaturated soils*, John Wiley & Sons.
- Fredlund, D. G. & Xing, A. (1994), 'Equations for the soil-water characteristic curve', *Canadian Geotechnical Journal* **31**(4), 521–532.
- Friedel, R. & Cundell, A. (1998), The application of water activity measurement to the microbiological attributes testing of nonsterile over-the-counter drug products, *in* 'Pharmacopeial Forum', Vol. 24, USPC United States Pharmacopeial Convention, pp. 6087–6090.
- Frydman, S. & Baker, R. (2009), 'Theoretical soil-water characteristic curves based on adsorption, cavitation, and a double porosity model', *International Journal of Geomechanics* **9**(6), 250–257.
- Gallipoli, D. (2012), 'A hysteretic soil-water retention model accounting for cyclic variations of suction and void ratio', *Geotechnique* **62**(7), 605–616.
- Gallipoli, D., Gens, A., Sharma, R. & Vaunat, J. (2003), 'An elasto-plastic model for unsaturated soil incorporating the effects of suction and degree of saturation on mechanical behaviour.', *Géotechnique* **53**(1), 123–136.
- Gallipoli, D., Wheeler, S. J. & Karstunen, M. (2003), 'Modelling the variation of degree of saturation in a deformable unsaturated soil.', *Géotechnique* **53**(1), 105–112.
- García-Tornel, A. J. (1988), Un modelo elastoplástico para suelos no saturados, PhD thesis, Universitat Politècnica de Catalunya.
- Gatabin, C., Talandier, J., Collin, F., Charlier, R. & Dieudonné, A.-C. (2016), 'Competing effects of volume change and water uptake on the water retention behaviour of a compacted mx-80 bentonite/sand mixture', *Applied Clay Science* **121**, 57–62.
- Gens, A. (1996), Constitutive modelling: Application to compacted soils, *in* E. E. Alonso & P. Delage, eds, 'Unsaturated Soils: proceedings of the First International Conference on Unsaturated Soils, UNSAT'95, Paris, France, 6-8 September 1995', Vol. 3, A. A. Balkema, Rotterdam/Brookfield, pp. 1179–1200.
- Gens, A. & Alonso, E. E. (1992), 'A framework for the behaviour of unsaturated expansive clays', *Can. Geotech. J.* **29**(6), 1013–1032.

- Gens, A., Sánchez, M., Guimarães, L. D. N., Alonso, E., Lloret, A., Olivella, S., Villar, M. & Huertas, F. (2009), 'A full-scale in situ heating test for high-level nuclear waste disposal: observations, analysis and interpretation', *Géotechnique* **59**(4), 377–399.
- Gens, A., Sánchez, M. & Sheng, D. (2006), 'On constitutive modelling of unsaturated soils', *Acta Geotechnica* **1**(3), 137.
- Goblet, P. & Marsily, G. d. (2000), Evaluation of the thermal effect in a kbs-3 type repository. a literary survey, Technical report, Swedish Nuclear Power Inspectorate.
- Goncalves, J., Adler, P. M., Cosenza, P., Pazdniakou, A. & De Marsily, G. (2015), Semipermeable membrane properties and chemomechanical coupling in clay barriers, in 'Developments in Clay Science', Vol. 6, Elsevier, pp. 269–327.
- Gouy, M. (1910), 'Sur la constitution de la charge électrique à la surface d'un électrolyte', *Journal de Physique Théorique et Appliquée* **9**(1), 457–468.
- Gray, M., Cheung, S. & Dixon, D. (1984), The influence of sand content on swelling pressures and structure developed in statically compacted na-bentonite, Technical Report 7825, Atomic Energy of Canada Limited, Mississauga, Ont.
- Grim, R. E. (1968), *Clay Mineralogy*, 2nd edition edn, McGraw-Hill Book Company.
- Guan, Y. & Fredlund, D. (1997), 'Use of the tensile strength of water for the direct measurement of high soil suction', *Canadian Geotechnical Journal* **34**(4), 604–614.
- Hand, L. (1994), 'Controlling water activity and ph in snack sticks', *Meat Marketing and Technology May* pp. 55–56.
- Hansen, J., Korkiala-Tanttu, L., Keski-Kuha, E. & Keto, P. (2009), 'Deposition tunnel backfill design for a kbs-3v repository', *Posiva Working Report* **129**.
- Herbert, H.-J. & Moog, H. (2002), Untersuchungen zur quellung von bentoniten in hochsalinaren lösungen, Technical Report GRS-179, Gesellschaft für Anlagen-und Reaktorsicherheit (GRS).
- Hilf, J. W. (1956), An investigation of pore water pressure in compacted cohesive soils, Technical report, US Department of Interior Bureau of Reclamation, Technical Memorandum.
- Houlsby, G. (1997), 'The work input to an unsaturated granular material', *Géotechnique* **47**(1), 193–196.

- Hu, R., Chen, Y., Liu, H. & Zhou, C. (2013), 'A water retention curve and unsaturated hydraulic conductivity model for deformable soils: consideration of the change in pore-size distribution', *Geotechnique* **63**(16), 1389.
- Huang, S., Barbour, S. & Fredlund, D. (1998), 'Development and verification of a coefficient of permeability function for a deformable unsaturated soil', *Canadian Geotechnical Journal* **35**(3), 411–425.
- IAEA (2006), *Fundamental Safety Principles: Safety Fundamentals No. SF1*, Vol. 1273, International Atomic Energy Agency.
- IAEA (2009), Classification of radioactive waste, General safety guides no. gsg-1, International Atomic Energy Agency Safety Standards.
- IAEA (2011), Disposal of radioactive waste, Specific Safety Requirements SSR-5, International Atomic Energy Agency.
- IMKO (2010), *TRIME-PICO IPH Manual*.
- Jacinto, A. C., Ledesma, A. & Demagistri, A. (2016), 'Effect of the clay–water interaction in the hydration of compacted bentonite used in engineered barriers', *Geomechanics for Energy and the Environment* **8**, 52–61.
- Jobmann, M., Flügge, J., Gazul, R., Hammer, J., Herold, P., Krone, J., Kuate Simo, E., Kühnlenz, T., Laggiard, E., Lommerzheim, A., Meleshyn, A., Müller, C., Rübél, A., Wolf, J. & Zhao, H. (2017), Investigation on long-term safety aspects of a radioactive waste repository in a diagenetic clay formation, Technical report, GRS BGR DBE TEC.
- Jobmann, M., Flügge, J., Hammer, J., Herold, P., Krone, J., Kühnlenz, T., Li, S., Lommerzheim, A., Meleshyn, A. & Wolf, J. (2015), Site-specific evaluation of safety issues for high-level waste disposal in crystalline rocks, Technical report, GRS BGR DBE TEC.
- Johannesson, L.-E., Börgesson, L. & Sandén, T. (1995), Compaction of bentonite blocks. development of technique for industrial production of blocks which are manageable by man, Technical report, Swedish Nuclear Fuel and Waste Management Co.
- Jommi, C. (2000), 'Remarks on the constitutive modelling of unsaturated soils', *Experimental Evidence and Theoretical Approaches in Unsaturated Soils* **153**, 139–153.
- Juvankoski, M. & Marcos, N. (2010), Design basis for buffer components, Working Report 2009-132, POSIVA OY, Olkiluoto FI-27160 EURAJOKI, Finland.



- Karube, D. & Kawai, K. (2001), 'The role of pore water in the mechanical behavior of unsaturated soils', *Geotechnical and Geological Engineering* **19**(3-4), 211–241.
- Kassiff, G. & Shalom, A. B. (1971), 'Experimental relationship between swell pressure and suction', *Géotechnique* **21**(3), 245–255.
- Kawai, K., Kato, S., Karube, D. et al. (2000), The model of water retention curve considering effects of void ratio., *in* 'Unsaturated soils for Asia. Proceedings of the Asian Conference on Unsaturated Soils, UNSAT-ASIA 2000, Singapore, 18-19 May, 2000', AA Balkema, pp. 329–334.
- Komine, H. & Ogata, N. (1996), 'Prediction for swelling characteristics of compacted bentonite', *Canadian Geotechnical Journal* **33**, 11–22.
- Komine, H. & Ogata, N. (1999), 'Experimental study on swelling characteristics of sand-bentonite mixture for nuclear waste disposal', *Soils and Foundations* **39**(2), 83–97.
- Komine, H. & Ogata, N. (2003), 'New equations for swelling characteristics of bentonite-based buffer materials', *Canadian Geotechnical Journal* **40**, 460–475.
- Komine, H. and Ogata, N. (1994), 'Experimental study on swelling characteristics of compacted bentonite', *Canadian Geotechnical Journal* **31**(4), 478–490.
- Kozeny, J. (1936), 'Über kapillare leitung des wassers im boden-aufstieg, versickerung und anwendung auf die bewässerung vol', *Wien: Sitzungsbericht Akademie der Wissenschaften* .
- Krahn, J. & Fredlund, D. G. (1972), 'On total, matric and osmotic suction', *Soil Science* **114**(5), 339–348.
- Lang, L. (2019), Hydro-mechanical behaviour of bentonite-based materials used for disposal of radioactive wastes, PhD thesis, Ruhr-University Bochum.
- Lee, J. O., Lim, J. G., Kang, I. M. & Kwon, S. (2012), 'Swelling pressures of compacted ca-bentonite', *Engineering Geology* **129**, 20–26.
- Lennemann, W. L. (1978), 'The management of high-level radioactive wastes', *IAEA Bulletin* **21**(4), 1–16.
- Leong, E.-C., Tripathy, S. & Rahardjo, H. (2003), 'Total suction measurement of unsaturated soils with a device using the chilled-mirror dew-point technique', *Géotechnique* **53**(2), 173–182.

- Lloret, A., Villar, M. V., Sanchez, M., Gens, A., Pintado, X. & Alonso, E. E. (2003), 'Mechanical behaviour of heavily compacted bentonite under high suction changes', *Géotechnique* **53**(1), 27–40.
- Long, N.-T. (2014), Coupled Thermo-Hydro-Mechanical Analysis: Experiment and Back Analysis, PhD thesis, Ruhr-Universität Bochum.
- Lorenz, P. M. (1999), 'Determination of the cation exchange capacity (cec) of clay minerals using the complexes of copper (ii) ion with triethylenetetramine and tetraethylenepentamine', *Clays and Clay Minerals* **47**, 386–388.
- Loret, B. & Khalili, N. (2002), 'An effective stress elastic–plastic model for unsaturated porous media', *Mechanics of Materials* **34**(2), 97–116.
- Lu, N. & Likos, W. (2004), *Unsaturated Soil Mechanics*, John Wiley & Sons, Inc., Hoboken, New Jersey.
- Madsen, F. (1998), 'Clay mineralogical investigations related to nuclear waste disposal', *Clay Minerals* **33**(1), 109–129.
- Madsen, F. & Müller-Vonmoos, M. (1989), 'The swelling behaviour of clays', *Applied Clay Science* **4**, 143–156.
- Martin, P. & Barcala, J. (2005), 'Large scale buffer material test: Mock-up experiment at ciemat', *Engineering Geology* **81**(3), 298–316.
- Mašín, D. (2014), 'Clay hypoplasticity model including stiffness anisotropy', *Géotechnique* **64**(3), 232–238.
- Maswoswe, J. (1985), Stress paths for compacted soil during collapse due to wetting, PhD thesis, Imperial College London (University of London).
- Mattson, E. (1980), Aluminum oxide as an encapsulation material for unreprocessed nuclear fuel waste-evaluation from the viewpoint of corrosion, Technical Report FR-90, Swedish Corrosion Institute, Stockholm, Sweden.
- Mattsson, E. (1981), Canister materials proposed for final disposal of high level nuclear waste-a review with respect to corrosion resistance, Technical Report 81-05, Swedish Corrosion Institute, Stockholm, Sweden.

- Mattsson, E., Ekbohm, L., Carlsson, R., Eklund, G., Grenthe, I., Hallberg, R., Henrikson, S., Vannerberg, N. & Wranglén, G. (1978), Copper as a canister material for unreprocessed nuclear waste: evaluation with respect to corrosion, Technical Report TR-90, Swedish Nuclear Fuel and Waste Management Company, Stockholm, Sweden.
- Meier, L. & Kahr, G. (1999), 'Determination of the cation exchange capacity (cec) of clay minerals using the complexes of copper(ii) ion with triethylenetetramine and tetraethylenepentamine', *Clays and Clay Minerals* **47**(3), 386–388.
- Mitchell, J. K. (1993), *Fundamentals of Soil Behaviour*, 2 edn, John Wiley & Sons, Inc.
- Mollins, L., Stewart, D. & Cousens, T. (1996), 'Predicting the properties of bentonite-sand mixtures', *Clay minerals* **31**(2), 243–252.
- Monroy, R., Zdravkovic, L. & Ridley, A. (2010), 'Evolution of microstructure in compacted london clay during wetting and loading', *Géotechnique* **60**(2), 105–119.
- Müller-Vonmoos, M., Kahr, G., Bucher, F. & Madsen, F. (1990), 'Investigation of kinnekulle k-bentonite aimed at assessing the long-term stability of bentonites', *Engineering Geology* **28**, 269–280.
- NEA (2000), Geological disposal of radioactive waste review of developments in the last decade, Technical report, Nuclear Energy Agency.
- NEA, O. (2008), *Moving Forward with Geological Disposal of Radioactive Waste, A Collective Statement by the NEA Radioactive Waste Management Committee (RWMC)*.
- Ng, C. W. & Pang, Y. (2000), 'Influence of stress state on soil-water characteristics and slope stability', *Journal of Geotechnical and Geoenvironmental Engineering* **126**(2), 157–166.
- Ninham, B. (1980), 'Long-range vs. short-range forces. the present state of play.', *Physical Chemistry* **84**(12), 1423–1430.
- Nitao, J. J. & Bear, J. (1996), 'Potentials and their role in transport in porous media', *Water Resources Research* **32**(2), 225–250.
- Nuth, M. & Laloui, L. (2008), 'Advances in modelling hysteretic water retention curve in deformable soils', *Computers and Geotechnics* **35**(6), 835–844.
- OECD (1995), 'The environmental and ethical basis of geological disposal of long-lived radioactive wastes'.

- Olson, R. E. & Langfelder, L. J. (1965), 'Pore water pressures in unsaturated soils', *Journal of the Soil Mechanics and Foundations Division* **97**(SM1).
- Overbeek, J. T. G. (1952), 'Kinetics of flocculation', *Colloid science* pp. 278–301.
- Philip, J. (1977), 'Unitary approach to capillary condensation and adsorption', *The Journal of Chemical Physics* **66**(11), 5069–5075.
- Philip, J. & De Vries, D. (1957), 'Moisture movement in porous materials under temperature gradients', *Transactions American Geophysical Union* **38**(2), 222–232.
- Pintado, X., Ledesma, A. & Lloret, A. (2002), 'Backanalysis of thermohydraulic bentonite properties from laboratory tests', *Engineering Geology* **64**(2-3), 91–115.
- Pleysier, J. & Juo, A. (1980), 'A single-extraction method using silver-thiourea for measuring exchangeable cations and effective cec in soils with variable charges', *Soil Science* **129**(4), 205–211.
- Poinsignon, C., C. J. & Fripiat, J. (1978), 'Electrical polarization of water molecules adsorbed by smectites: An infrared study', *The Journal of Physical Chemistry* **82**(16), 1855–1860.
- Potts, D. M., Zdravkovic, L. & Zdravković, L. (2001), *Finite element analysis in geotechnical engineering: application*, Vol. 2, Thomas Telford.
- Prost, R. (1975), Etude de l'hydratation des argiles: interactions eau-mineral et mecanisme de la retention de l'eau. ii. etude d'une smectite (hectorite), in 'Annales agronomiques'.
- Pusch, R. & Kasbohm, J. (2001), Can the water content of highly compacted bentonite be increased by applying a high water pressure?, Technical report, Swedish Nuclear Fuel and Waste Management Co.
- Pusch, R. & Yong, R. N. (2014), *Microstructure of smectite clays and engineering performance*, CRC Press.
- Rahardjo, H. & Leong, E. (2006), Suction measurements, in 'Unsaturated Soils 2006', pp. 81–104.
- Ridley, A. & Burland, J. (1993), 'A new instrument for the measurement of soil moisture suction', *Géotechnique*. **43**(2), 321–4.

- Ridley, A., Dineen, K., Burland, J. & Vaughan, P. (2003), 'Soil matrix suction: some examples of its measurement and application in geotechnical engineering', *Géotechnique* **53**(2), 241–253.
- Ridley, A. & Wray, W. (1996), Suction measurement: a review of current theory and practices, *in* 'Proceedings of the first international conference on unsaturated soils/UNSAT-95/Paris/France/6-8 September 1995. Volume 3'.
- RN, Y. (1999), 'Soil suction and soil-water potentials in swelling clays in engineered clay barriers', *Engineering Geology* **54**(1), 3–13.
- Romero, E., Della Vecchia, G. & Jommi, C. (2011), 'An insight into the water retention properties of compacted clayey soils', *Géotechnique* **61**(4), 313.
- Romero, E., Gens, A. & Lloret, A. (1999), 'Water permeability, water retention and microstructure of unsaturated compacted boom clay.', *Engineering Geology* **54**(1-2), 117–127.
- Romero, E. & Vaunat, J. (2000), Retention curves of deformable clays, *in* 'In Proceedings of the international workshop on unsaturated soils', CRC Press, pp. 91–106.
- Romero, E. & Vaunat, J. (2014), Retention curves of deformable clays, *in* 'Experimental evidence and theoretical approaches in unsaturated soils', CRC Press, pp. 99–114.
- Roscoe, K. & Burland, J. (1968), 'On the generalised stress-strain behaviour of wet clay', *Engineering Plasticity* pp. 535–609.
- Rothfuchs, T., Jockwer, N., Miehe, R. & Zhang, C. L. (2005), Self-sealing barriers of clay/mineral mixtures in a clay repository: Sb experiment in the mont terri rock laboratory, Technical report, Gesellschaft für Anlagen-und Reaktorsicherheit (GRS).
- Saba, S., Cui, Y.-J., Barnichon, J.-D. & Tang, A. M. (2014), 'Investigation of the swelling behaviour of compacted bentonite–sand mixture by mock-up tests', *Canadian Geotechnical Journal* **51**(12), 1399–1412.
- Saba, S., Cui, Y.-J., Barnichon, J.-D. & Tang, A. M. (2016), 'Infiltration column for studying the lateral swell behavior of expansive clay', *Geotechnical Testing Journal* **39**(3), 407–414.
- Saiyouri, N., Hicher, P. Y. & Tessier, D. (2000), 'Microstructural approach and transfer water modelling in highly compacted unsaturated swelling clays', *Mechanics of*

- Cohesive-frictional Materials: An International Journal on Experiments, Modelling and Computation of Materials and Structures* **5**(1), 41–60.
- Saiyouri, N., TESSIER, D. & HICHER, P. Y. (2004), ‘Experimental study of swelling in unsaturated compacted clays’, *Clay Minerals* **39**(4), 469–479.
- Salles, F., Beurroies, I., Bildstein, O., Jullien, M., Raynal, J., Denoyel, R. & Van Damme, H. (2008), ‘A calorimetric study of mesoscopic swelling and hydration sequence in solid na-montmorillonite’, *Applied Clay Science* **39**(3-4), 186–201.
- Sánchez, M., Gens, A. & Olivella, S. (2012), ‘Thm analysis of a large-scale heating test incorporating material fabric changes’, *International Journal for Numerical and Analytical Methods in Geomechanics* **36**(4), 391–421.
- Sato, T., Watanabe, T. & Otsuka, R. (1992), ‘Effects of layer charge, charge location, and energy change on expansion properties of dioctahedral smectites’, *Clays and Clay Minerals* **40**(1), 103–113.
- Schanz, T., Baille, W. & Tuan, L. N. (2010), ‘Effects of temperature on measurements of soil water content with time domain reflectometry’, *Geotechnical Testing Journal* **34**(1), 1–8.
- Schanz, T., Nguyen-Tuan, L. & Datcheva, M. (2013), ‘A column experiment to study the thermo-hydro-mechanical behaviour of expansive soils’, *Rock Mechanics and Rock Engineering* **46**(6), 1287–1301.
- Schanz, T. & Tripathy, S. (2009), ‘Swelling pressure of a divalent-rich bentonite: Diffuse double-layer theory revisited’, *Water Resources Research* **45**(5), W00C12.
- Segad, M., Jonsson, B., Åkesson, T. & Cabane, B. (2010), ‘Ca/na montmorillonite: structure, forces and swelling properties’, *Langmuir* **26**(8), 5782–5790.
- Seiphoori, A., Ferrari, A. & Laloui, L. (2014), ‘Water retention behaviour and microstructural evolution of mx-80 bentonite during wetting and drying cycles’, *Géotechnique* **64**(9), 721–734.
- Sellin, P. & Leupin, O. X. (2013), ‘The use of clay as an engineered barrier in radioactive-waste management—a review’, *Clays and Clay Minerals* **61**(6), 477–498.
- Sheng, D., Sloan, S. & Gens, A. (2004), ‘A constitutive model for unsaturated soils: thermomechanical and computational aspects’, *Computational Mechanics* **33**(6), 453–465.

- Sheng, D. & Zhou, A.-N. (2011), 'Coupling hydraulic with mechanical models for unsaturated soils', *Canadian Geotechnical Journal* **48**(5), 826–840.
- Simms, P. H. & Yanful, E. K. (2004), 'Estimation of soil–water characteristic curve of clayey till using measured pore-size distributions', *Journal of Environmental Engineering* **130**(8), 847–854.
- Sposito, G. et al. (1984), *The surface chemistry of soils.*, Oxford university press.
- Sridharan, A. (1968), Some studies on the strenght of partly saturated clays, PhD thesis, Purdue University.
- Sridharan, A. & Jayadeva, M. (1982), 'Double layer theory and compressibility of clays', *Géotechnique* **32**(2), 133–144.
- Sridharan, A., Rao, A. & Sivapullaiah, P. (1986), 'Swelling pressure of clays', *Geotechnical Testing Journal* **9**(1), 24–33.
- Stern, O. (1924), 'Zur theorie der elektrolytischen doppelschicht', *Zeitschrift für Elektrochemie und angewandte physikalische Chemie* **30**(21-22), 508–516.
- Steudel, A. & Emmerich, K. (2013), 'Strategies for the successful preparation of homoionic smectites', *Applied Clay Science* **75-76**, 13 – 21.
- Sun, D., Zhang, J., Zhang, J. & Zhang, L. (2013), 'Swelling characteristics of gmz bentonite and its mixtures with sand', *Applied clay science* **83**, 224–230.
- Tarantino, A. (2009), 'A water retention model for deformable soils', *Géotechnique* **59**(9), 751–762.
- Tarantino, A. & Mongiovi, L. (2003), 'Calibratoin of tensiometer for direct measurement of matric suction', *Géotechnique* **53**(1).
- Tessier, D. & Pedro, G. (1976), 'Les modalités de l'organisation des particules dans les matériaux argileux', *Science du Sol* **2**, 85–99.
- Topp, G. C., Davis, J. & Annan, A. P. (1980), 'Electromagnetic determination of soil water content: Measurements in coaxial transmission lines', *Water Resources Research* **16**(3), 574–582.
- Tripathy, S. & Rees, S. (2013), 'Suction of some polyethylene glycols commonly used for unsaturated soil testing', *Geotechnical Testing Journal* **36**(5), 1–13.

- Tripathy, S., Sridharan, A. & Schanz, T. (2004), 'Swelling pressures of compacted bentonites from diffuse double layer theory', *Canadian Geotechnical Journal* **41**, 437–450.
- Tripathy, S., Thomas, H. R. & Bag, R. (2015), 'Geoenvironmental application of bentonites in underground disposal of nuclear waste: Characterization and laboratory tests', *Journal of Hazardous, Toxic, and Radioactive Waste* **21**(1), D4015002.
- Tripathy, S., Thomas, H. R. & Stratos, P. (2017), 'Response of compacted bentonites to thermal and thermo-hydraulic loadings at high temperatures', *Geosciences* **7**(3), 53.
- Van Genuchten, M. T. (1980), 'A closed-form equation for predicting the hydraulic conductivity of unsaturated soils 1', *Soil science society of America journal* **44**(5), 892–898.
- van Olphen, H. (1963), *An introduction to clay colloid chemistry*, 1st edn, John Wiley & Sons, New York London Sydney Toronto.
- van Olphen, H. (1977), *An introduction to clay colloid chemistry: for clay technologists, geologists, and soil scientists*, 2nd edn, John Wiley & Sons, New York London Sydney Toronto.
- Vanapalli, S. K., Fredlund, D. G. & Pufahl, D. E. (1999), 'The influence of soil structure and stress history on the soil-water characteristics of a compacted till', *Géotechnique* **49**(2), 143–159.
- Vaunat, J. & Gens, A. (2005), 'Analysis of the hydration of a bentonite seal in a deep radioactive waste repository', *Engineering Geology* **81**(3), 317–328.
- Vaunat, J., Jommi, C. & Gens, A. (1997), A strategy for numerical analysis of the transition between saturated and unsaturated flow conditions, *in* 'Proceedings of 6th International Symposium on Numerical Models in Geomechanics, Montreal', pp. 297–302.
- Vazaios, I. & Vlachopoulos, N. (2017), The evolution of the excavation damage zone of tunnels in brittle rockmasses using a fem/dem approach, *in* 'Proceedings of the 70th Canadian Geotechnical Conference (GeoOttawa 2017)'.
- Verwey, E. & Overbeek, J. (1948), *Theory of the stability of lyophobic colloids: the interaction of sol particles having an electric double layer*, Elsevier Publishing Company.
- Villar, M. (2000), Caracterización termo-hidro-mecánica de una bentonita de Cabo de Gata Universidad Complutense, Madrid, Spain., PhD thesis, Universidad Complutense, Madrid, Spain.



- Villar, M. (2007), 'Water retention of two natural compacted bentonites', *Clays and Clay Minerals* **55**(3), 311–322.
- Villar, M., Campos, R. & Gutiérrez-Nebot, L. (2014), 'Long-term performance of engineered barrier systems pebs', *EB experiment Laboratory post-mortem analyses report, the Seventh Framework Programme of the European Atomic Energy Community (Euratom), DELIVERABLE* (D2.1-7), 1–34.
- Villar, M., García-Siñeriz, J., Bárcena, I. & Lloret, A. (2005), 'State of the bentonite barrier after five years operation of an in situ test simulating a high level radioactive waste repository', *Engineering Geology* **80**(3-4), 175–198.
- Villar, M. & Lloret, A. (2004), 'Influence of temperature on the hydro-mechanical behaviour of a compacted bentonite', *Applied Clay Science* **26**(1), 337 – 350.
- Villar, M. V., Martín, P. L., Romero, F. J., Iglesias, R. J. & Gutiérrez-Rodrigo, V. (2016), 'Saturation of barrier materials under thermal gradient', *Geomechanics for Energy and the Environment* .
- Wang, Q., Tang, A. M., Cui, Y.-J., Delage, P., Barnichon, J.-D. & Ye, W.-M. (2013a), 'The effects of technological voids on the hydro-mechanical behaviour of compacted bentonite-sand mixture', *Soils and Foundation* **53**(2), 232–245.
- Wang, Q., Tang, A. M., Cui, Y.-J., Delage, P. & Gatmiri, B. (2012), 'Experimental study on the swelling behaviour of bentonite/claystone mixture', *Engineering Geology* **124**(Supplement C), 59 – 66.
- Wheeler, S. (1996), 'Inclusion of specific water volume within an elasto-plastic model for unsaturated soil', *Canadian Geotechnical Journal* **33**(1), 42–57.
- Wheeler, S., Gallipoli, D. & Karstunen, M. (2002), 'Comments on use of the barcelona basic model for unsaturated soils', *International journal for numerical and analytical methods in Geomechanics* **26**(15), 1561–1571.
- Wheeler, S., Sharma, R. & Buisson, M. (2003), 'Coupling of hydraulic hysteresis and stress–strain behaviour in unsaturated soils', *Géotechnique* **53**(1), 41–54.
- Wheeler, S. & Sivakumar, V. (1995), 'An elasto-plastic critical state framework for unsaturated soil', *Géotechnique* **45**(1), 35–53.
- Wiederhold, P. R. (2012), *Water vapor measurement: methods and instrumentation*, CRC Press.

- Ye, W.-M., Cui, Y.-J., Qian, L.-X. & Chen, B. (2009), 'An experimental study of the water transfer through confined compacted gmz bentonite', *Engineering Geology* **108**(3), 169–176.
- Yigzaw, Z. G., Cuisinier, O., Massat, L. & Masrouri, F. (2016), 'Role of different suction components on swelling behavior of compacted bentonites', *Applied Clay Science* **120**, 81–90.
- Yong, R., Mohamed, A., Shooshpasha, I. & Onofrei, C. (1997), 'Hydro-thermal performance of unsaturated bentonite-sand buffer material', *Engineering Geology* **47**(4), 351–365.
- Zandarin, M. T., Alonso, E. & Olivella, S. (2013), 'A constitutive law for rock joints considering the effects of suction and roughness on strength parameters', *International Journal of Rock Mechanics and Mining Sciences* **60**, 333–344.
- Zhang, X.-W., Liu, X., Gu, D.-X., Zhou, W., Wang, R.-L. & Liu, P. (1996), 'Desorption isotherms of some vegetables', *Journal of the Science of Food and Agriculture* **70**(3), 303–306.

**Schriftenreihe des Lehrstuhls für Grundbau, Boden- und Felsmechanik der  
Ruhr-Universität Bochum**

*Herausgeber: H.L. Jessberger*

- 1 (1979) **Hans Ludwig Jessberger**  
Grundbau und Bodenmechanik an der Ruhr-Universität Bochum
- 2 (1978) **Joachim Klein**  
Nichtlineares Kriechen von künstlich gefrorenem Emschermergel
- 3 (1979) **Heinz-Joachim Gödecke**  
Die Dynamische Intensivverdichtung wenig wasserdurchlässiger Böden
- 4 (1979) **Poul V. Lade**  
Three Dimensional Stress-Strain Behaviour and Modeling of Soils
- 5 (1979) **Roland Pusch**  
Creep of soils
- 6 (1979) **Norbert Diekmann**  
Zeitabhängiges, nichtlineares Spannungs-Verformungsverhalten von gefrorenem Schluff unter triaxialer Belastung
- 7 (1979) **Rudolf Dörr**  
Zeitabhängiges Setzungsverhalten von Gründungen in Schnee, Firn und Eis der Antarktis am Beispiel der deutschen Georg-von-Neumayer- und Filchner-Station
- 8 (1984) **Ulrich Güttler**  
Beurteilung des Steifigkeits- und Nachverdichtungsverhaltens von ungebundenen Mineralstoffen
- 9 (1986) **Peter Jordan**  
Einfluss der Belastungsfrequenz und der partiellen Entwässerungsmöglichkeiten auf die Verflüssigung von Feinsand
- 10 (1986) **Eugen Makowski**  
Modellierung der künstlichen Bodenvereisung im grundwasserdurchströmten Untergrund mit der Methode der finiten Elemente
- 11 (1986) **Reinhard A. Beine**  
Verdichtungswirkung der Fallmasse auf Lastausbreitung in nichtbindigem Boden bei der Dynamischen Intensivverdichtung
- 12 (1986) **Wolfgang Ebel**  
Einfluss des Spannungspfades auf das Spannungs-Verformungsverhalten von gefrorenem Schluff im Hinblick auf die Berechnung von Gefrierschächten
- 13 (1987) **Uwe Stoffers**  
Berechnungen und Zentrifugen-Modellversuche zur Verformungsabhängigkeit der Ausbaubeanspruchung von Tunnelausbauten in Lockergestein
- 14 (1988) **Gerhard Thiel**  
Steifigkeit und Dämpfung von wassergesättigtem Feinsand unter Erdbebenbelastung

- 15 (1991) **Mahmud Thaher**  
Tragverhalten von Pfahl-Platten-Gründungen im bindigen Baugrund,  
Berechnungsmodelle und Zentrifugen-Modellversuche
- 16 (1992) **Rainer Scherbeck**  
Geotechnisches Verhalten mineralischer Deponieabdichtungsschichten  
bei ungleichförmiger Verformungswirkung
- 17 (1992) **Martin M. Bizialiele**  
Torsional Cyclic Loading Response of a Single Pile in Sand
- 18 (1993) **Michael Kotthaus**  
Zum Tragverhalten von horizontal belasteten Pfahlreihen aus langen Pfählen in Sand
- 19 (1993) **Ulrich Mann**  
Stofftransport durch mineralische Deponieabdichtungen:  
Versuchsmethodik und Berechnungsverfahren
- 20 (1992) **Festschrift anlässlich des 60. Geburtstages von  
Prof. Dr.-Ing. H. L. Jessberger**  
20 Jahre Grundbau und Bodenmechanik an der Ruhr-Universität Bochum
- 21 (1993) **Stephan Demmert**  
Analyse des Emissionsverhaltens einer Kombinationsabdichtung im Rahmen der  
Risikobetrachtung von Abfalldeponien
- 22 (1994) **Diethard König**  
Beanspruchung von Tunnel- und Schachtausbauten in kohäsionslosem Lockergestein  
unter Berücksichtigung der Verformung im Boden
- 23 (1995) **Thomas Neteler**  
Bewertungsmodell für die nutzungsbezogene Auswahl von Verfahren zur Altlastensanierung
- 24 (1995) **Ralph Kockel**  
Scherfestigkeit von Mischabfall im Hinblick auf die Standsicherheit von Deponien
- 25 (1996) **Jan Laue**  
Zur Setzung von Flachfundamenten auf Sand unter wiederholten Lastereignissen
- 26 (1996) **Gunnar Heibroek**  
Zur Rissbildung durch Austrocknung in mineralischen Abdichtungsschichten  
an der Basis von Deponien
- 27 (1996) **Thomas Siemer**  
Zentrifugen-Modellversuche zur dynamischen Wechselwirkung zwischen Bauwerken  
und Baugrund infolge stoßartiger Belastung
- 28 (1996) **Viswanadham V. S. Bhamidipati**  
Geosynthetic Reinforced Mineral Sealing Layers of Landfills
- 29 (1997) **Frank Trappmann**  
Abschätzung von technischem Risiko und Energiebedarf bei Sanierungsmaßnahmen  
für Altlasten
- 30 (1997) **André Schürmann**  
Zum Erddruck auf unverankerte flexible Verbauwände
- 31 (1997) **Jessberger, H. L. (Herausgeber)**  
Environment Geotechnics, Report of ISSMGE Technical Committee TC 5  
on Environmental Geotechnics

*Herausgeber: Th. Triantafyllidis*

- 32 (2000) **Triantafyllidis, Th. (Herausgeber)**  
Boden unter fast zyklischer Belastung: Erfahrung und Forschungsergebnisse (Workshop)
- 33 (2002) **Christof Gehle**  
Bruch- und Scherverhalten von Gesteinstrennflächen mit dazwischenliegenden Materialbrücken
- 34 (2003) **Andrzej Niemunis**  
Extended hypoplastic models for soils
- 35 (2004) **Christiane Hof**  
Über das Verpressankertragverhalten unter kalklösendem Kohlensäureangriff
- 36 (2004) **René Schäfer**  
Einfluss der Herstellungsmethode auf das Verformungsverhalten von Schlitzwänden  
in weichen bindigen Böden
- 37 (2005) **Henning Wolf**  
Zur Scherfugenbänderung granularer Materialien unter Extensionsbeanspruchung
- 38 (2005) **Torsten Wichtmann**  
Explicit accumulation model for non-cohesive soils under cyclic loading
- 39 (2008) **Christoph M. Loreck**  
Die Entwicklung des Frischbetondruckes bei der Herstellung von Schlitzwänden
- 40 (2008) **Igor Arsic**  
Über die Bettung von Rohrleitungen in Flüssigböden
- 41 (2009) **Anna Arwanitaki**  
Über das Kontaktverhalten zwischen einer Zweiphasenschlitzwand und nichtbindigen Böden

*Herausgeber: T. Schanz*

- 42 (2009) **Yvonne Lins**  
Hydro-Mechanical Properties of Partially Saturated Sand
- 43 (2010) **Tom Schanz (Herausgeber)**  
Geotechnische Herausforderungen beim Umbau des Emscher-Systems  
Beiträge zum RuhrGeo Tag 2010
- 44 (2010) **Jamal Alabdullah**  
Testing Unsaturated Soil for Plane Strain Conditions: A New Double-Wall Biaxial Device
- 45 (2011) **Lars Röchter**  
Systeme paralleler Scherbänder unter Extension im ebenen Verformungszustand
- 46 (2011) **Yasir Al-Badran**  
Volumetric Yielding Behavior of Unsaturated Fine-Grained Soils
- 47 (2011) **Usque ad finem**  
Selected research papers
- 48 (2012) **Muhammad Ibrar Khan**  
Hydraulic Conductivity of Moderate and Highly Dense Expansive Clays
- 49 (2014) **Long Nguyen-Tuan**  
Coupled Thermo-Hydro-Mechanical Analysis: Experimental and Back Analysis
- 50 (2014) **Tom Schanz (Herausgeber)**  
Ende des Steinkohlenbergbaus im Ruhrrevier: Realität und Perspektiven für die  
Geotechnik Beiträge zum RuhrGeo Tag 2014
- 51 (2014) **Usque ad finem**  
Selected research papers
- 52 (2014) **Houman Soleimani Fard**  
Study on the Hydro-Mechanical Behaviour of Fiber Reinforced Fine Grained Soils  
with Application to the Preservation of Historical Monuments
- 53 (2014) **Wiebke Baille**  
Hydro-Mechanical Behavior of Clays - Significance of Mineralogy
- 54 (2014) **Qasim Abdulkarem Jassim Al-Obaidi**  
Hydro-Mechanical Behavior of Collapsible Soils
- 55 (2015) **Veselin Zarev**  
Model Identification for the Adaption of Numerical Simulation Models - Application  
to Mechanized Shield Tunneling
- 56 (2015) **Meisam Goudarzy**  
Micro and Macro Mechanical Assessment of Small and Intermediate Strain Properties  
of Granular Material
- 57 (2016) **Oliver Detert**  
Analyse einer selbstregulierenden interaktiven Membrangründung für Schüttkörper  
auf geringtragfähigen Böden
- 58 (2016) **Yang Yang**  
Analyses of Heat Transfer and Temperature-induced Behaviour in Geotechnics

- 59 (2016) **Alborz Pourzargar**  
Application of Suction Stress Concept to Partially Saturated compacted Soils
- 60 (2017) **Hanna Haase**  
Multiscale Analysis of Clay-Polymer Composites for Geoenvironmental Applications
- 61 (2017) **Kavan Khaledi**  
Constitutive modeling of rock salt with application to energy storage caverns
- 62 (2017) **Nina Silvia Müthing**  
On the consolidation behavior of fine-grained soils under cyclic loading
- 63 (2017) **Elham Mahmoudi**  
Probabilistic analysis of a rock salt cavern with application to energy storage systems
- 64 (2017) **Negar Rahemi**  
Evaluation of liquefaction behavior of sandy soils using critical state soil mechanics and instability concept
- 65 (2018) **Chenyang Zhao**  
A contribution to modeling of mechanized tunnel excavation
- 66 (2018) **Tom Schanz (Herausgeber)**  
Innovationen im Spezialtiefbau und in der Umweltgeotechnik  
Geotechnik Beiträge zum RuhrGeo Tag 2018
- 67 (2019) **Linzhi Lang**  
Hydro-Mechanical Behaviour of Bentonite-Based Materials Used for Disposal of Radioactive Wastes
- 68 (2019) **Usama Al-Anbaki**  
Hydraulic Interaction of Soil and Nonwoven Geotextiles under Unsaturated Conditions
- 69 (2019) **Abhishek Rawat**  
Coupled Hydro-mechanical Behavior of a Compacted Bentonite-Sand Mixture: Experimental and Numerical Investigations







## curriculum vitae

Personal information	
Surname	Rawat
Name	Abhishek
E-mail	abhishek.rawat@rub.de
Nationality	Indian
Date of birth	18.07.1982

Education and training	
<b>Ph.D. (Under-process)</b>	
Duration	2014 to 2019
Name of Institute	Ruhr Universität Bochum, Germany
Principal subject	Geotechnical Engineering
Title of qualification awarded	Doktor der Ingenieurwissenschaften
<b>Post-Graduation</b>	
Duration	2007 to 2009
Name of Institute	Indian Institute of Technology Mumbai (IIT Bombay)
Principal subject	Civil Engineering with specialization in Geotechnical Engineering
Title of qualification awarded	Master of Technology
Final mark obtained	(CGPA) 8.65 out of 10
<b>Graduation</b>	
Date	2002 to 2006
Name of Institute	Jai Narain Vyas University, Faculty of Engineering, Jodhpur
Principal subject	Civil Engineering
Title of qualification awarded	Bachelor of Engineering
Final mark obtained	2781 out of 3875

Publications and articles submitted (In Journal)	
Author(s) and title	Rawat, A., Baille, W., Schanz, T. 2016, " Discussion of "Evaluation of the swelling characteristics of bentonite-sand mixtures".
Journal	<i>Engineering Geology</i>
Vol. and Pg. No.	209, 209-210.

Status	Published
Author(s) and title	Rawat, A., Al-Badran, Y., Schanz, T. 2016, " Discussion of "Exploring one-dimensional compression of compacted clay under constant degree of saturation paths".
Journal	<i>Geotechnique</i>
Vol. and Pg. No.	66(8), 86-90.
Status	Published
Author(s) and title	Rawat, A., Baille, W., Tripathy, S., & Schanz, T., 2018, "A Column-type Experimental Device for Investigating Coupled Thermo-Hydro-Mechanical Behavior of Expansive Soils".
Journal	<i>Geotechnical Testing Journal (ASTM)</i>
Vol. and Pg. No.	-
Status	Under First Revision
Author(s) and title	Rawat, A., Baille, W., & Tripathy, S., 2018, "Experimental investigation of swelling behavior of compacted sand-bentonite mixture with water infiltration test".
Journal	<i>Engineering Geology</i>
Vol. and Pg. No.	-
Status	Under First Revision
Author(s) and title	Rawat, A., Lang, L., Dieudonné, A-C., Baille, W., Collin, F., 2019, 'Coupled hydro-mechanical behavior of compacted expansive soil-based material: experimental and numerical investigations".
Journal	-
Vol. and Pg. No.	-
Status	Ready for Submission
<b>Publications and articles submitted (In Conference)</b>	
Author(s) and title	Rawat, A., Baille, W., Tripathy, S., & Schanz, T., 2018, "A novel thermo-hydro-mechanical column-device for testing compacted expansive soils".
Publication place	<i>The 7<sup>th</sup> International Conference on Unsaturated Soils, The Hong Kong University of Science and Technology (HKUST), Hong Kong</i>
Date of publication	03.08.2018
Author(s) and title	Schanz, T., & Rawat, A., 2016, "Transient boundary conditions in the frame of THM-processes at nuclear waste repositories".
Publication place	<i>3<sup>rd</sup> European Conference on Unsaturated Soil, Paris, France</i>
Date of publication	12.09.2016
Author(s) and title	Rawat, A., Rakesh, R. R. & Mandal, J. N., 2010, "A Study on Inclusion of Different Types of Fibers in Cover Soil for Low Level Radioactive Waste Disposal Facilities".
Publication place	<i>13<sup>th</sup> International Conference of the International Association for Computer Methods and Advances in Geomechanics, Melbourne, Australia</i>
Date of publication	13.05.2010
Author(s) and title	Rawat, A., Rakesh, R. R., & Mandal, J. N., 2010, "Effect of Inclusion of Glassgrid Geocell on Flexural Behaviour of Cover Soil".
Publication place	<i>6<sup>th</sup> International Congress on Environmental Geotechniques, New Delhi</i>
Date of publication	11.11.2010
Author(s) and title	Das, A., Rawat, A., Choudhury, D., & Chakraborty, D., 2008, "Seismic slope stability analysis using MSD model for different modes of movements".
Publication place	<i>Diamond Jubilee Conference on Landslide Management - Present Scenario &amp; Future Directions, February 10 - 12, 2008, CBRI, Roorkee, India</i>
Date of publication	12.02.2008

<b>Work experience, stages, studies abroad</b>		
Date (from – to)		2009 - 2014
Name of employer		<b>Bhabha Atomic Research Centre (BARC), Department of Atomic Energy</b>
Type of sector		Indian Premier Nuclear Research & Development Centre
Post		Scientific Officer (D)
R&D Activities		<ul style="list-style-type: none"> <li>• Site selection, performance and safety assessment studies for Near Surface Disposal Facilities (NSDFs) for Low Level/Intermediate Level radioactive waste.</li> <li>• Geotechnical aspect of deep geological disposal of high level radioactive waste.</li> <li>• Buffer material characterization studies on Indian Bentonite.</li> <li>• Design of Underground Research Laboratory (URL) based heater and tunnel sealing experiments (both surface and underground based).</li> </ul>
<b>Official Deputation Abroad</b>		
Date (from – to)		16.07.2012 – 15.01.2012
Name of institute		<b>ANDRA (The National Radioactive Waste Management Agency) Center for Meuse/Haute-Marne Underground Research Laboratory, Bure, France</b>
Purpose		Training on Underground Research Laboratory based experimental studies: <i>Design and Modeling</i> aspects
Main activities and responsibilities		Define the modalities and conditions regarding BARC's participation in the experiments to be conducted at the Meuse/Haute-Marne Underground Laboratory starting in early 2012. Two experiments are involved and are called the Thermo-hydro-mechanics (THM) and the clay core (NSC) sealing experiments, respectively.
<b>Research Stay</b>		
Date (from – to)		15.11.2016 – 09.12.2016
Name of institute		<b>University of Liege, Belgium</b>
Date (from – to)		23.07.2018 – 17.08.2018
Name of institute		<b>Technical University Delft, The Netherland</b>
Date (from – to)		01.10.2018 – 15.11.2018
Name of institute		<b>School of Engineering, Cardiff, United Kingdom</b>